Thèse de Doctorat de l'Université de Mons

UMONS
Université de Mons

Faculté
des Sciences

Spécialité :
Sciences Physiques

Study of the Confined and Deconfined Phases of QCD within Quasiparticle Approaches

présenté par

Gwendolyn LACROIX

pour l'obtention du grade de Docteur en Sciences.

Thèse soutenue le 4 décembre 2014 devant le jury composé de :

Dr. Nicolas BOULANGER, Université de Mons (Président)
Prof. Yves BRIHAYE, Université de Mons
Dr. Fabien BUISSERET, Université de Mons et HELHa (Codirecteur)
Dr. Daniel CABRERA, Goethe-Universität Frankfurt am Main
Dr. Jaume CARBONELL, Institut de Physique Nucléaire d'Orsay
Prof. Jean-Marc SPARENBERG, Université libre de Bruxelles
Prof. Claude SEMAY, Université de Mons (Directeur)

Année académique 2014–2015

Acknowledgements

Ne vous y méprenez pas ! La suite de ce manuscrit sera belle et bien dans la langue de Shakespeare, langue d'échange et de partage de toute la communauté scientifique. Néanmoins, dans la mesure où ce qui suit véhicule l'expression de ma gratitude envers des personnes ayant contribué au bon déroulement de ce travail, il me semble à propos de les exprimer dans leur langue maternelle.

Mes tout premiers remerciements vont donc naturellement vers mes deux promoteurs : Claude Semay et Fabien Buisseret. Une thèse, c'est le fruit d'une longue et laborieuse recherche qui s'étoffe au fil du temps. Tout au long de mon cheminement, j'ai pu trouver en mes promoteurs une guidance sans faille qui m'a permis de m'épanouir au sein d'un projet et d'une communauté scientifique. Merci à eux pour leur disponibilité, leur gentillesse, leur écoute, leurs conseils et tout le travail fourni à la bonne réalisation de cette thèse. Un merci tout particulier à Fabien pour avoir été l'initiateur de cette recherche, ainsi qu'à Claude pour l'accroissement de mes connaissances dans des domaines divers et variés allant de la science-fiction à la biologie cellulaire en passant par la politique, la BD et l'aérospatiale, tout cela autour d'un (bon) café. Merci également à lui pour cette maxime de vie : "Seuls les paranoïaques survivront".

J'aimerais aussi remercier mon "promoteur de voyage", Vincent Mathieu, pour m'avoir très souvent donné l'opportunité de faire des séjours scientifiques au sein des différents groupes dans lesquels il a travaillé ou travaille encore. Je remercie donc au passage l'ECT* de Trente ainsi que le centre de physique nucléaire théorique de l'université d'Indiana pour leur accueil. Merci à Vincent pour son aide et les nombreuses discussions intéressantes sur divers aspects de la physique des particules. Je lui souhaite très sincèrement une longue et fructueuse carrière dans ce domaine dont il ne cesse de parler avec passion.

También me gustaría desear lo mejor a Daniel Cabrera para su carrera científica. Gracias por la colaboración y las estancias, tanto en Madrid como en Frankfurt.

I would like also to thank all the members of my Ph.D. thesis jury to have devoted time to read and to criticize my work. Their useful remarks have, for sure, upgraded this text. De plus, merci à Nicolas Boulanger et Yves Brihaye, membres de mon comité d'accompagnement, pour l'attention qu'ils ont portée au suivi de ma formation doctorale.

Je remercie également toutes les personnes qui ont contribué à ce que ces quatre années de formation doctorale soient agréables. Il est évidemment bien difficile de toutes les citer. Je me contenterai donc d'énumérer de manière non exhaustive différentes activités plus ludiques, qui ont ponctué mes années de thèse, en remerciant en particulier les personnes qui les ont organisées et qui y ont participé. Merci pour les parties de cartes du temps de midi, les verres du vendredi, les tournois de belote, de poker et du roi des nains, les journées à la mer, les pronostics footballistiques, les soirées-jeux, les apéros sur la Grand Place de Mons, ...

Enfin, je remercie bien sûr ma famille de m'avoir toujours soutenue dans mes initiatives et projets. Un merci tout particulier à Quentin pour son écoute à toute heure et sa patience ainsi que pour ces surplus d'énergie insufflés, nécessaires à la finalisation de ce manuscrit.

Pour clore cette série de remerciements, je tiens naturellement à remercier le F.R.S-FNRS pour le soutien financier (bourse aspirant) apporté tout au long de ma formation doctorale.

Contents

Introduction **9**

1 Notions in QCD **13**
1.1 Theoretical principles . . . 13
1.1.1 A preliminary classification: the quark model . . . 13
1.1.2 Classical QCD Lagrangian . . . 16
1.1.3 Different ways of quantization . . . 18
1.1.4 QCD quantization within the path-integral formalism . . . 19
1.1.5 Regularization and renormalization . . . 21
1.1.6 QCD β-function: confinement and asymptotic freedom . . . 22
1.1.7 Chiral symmetry in QCD . . . 23
1.2 Lattice QCD . . . 25
1.2.1 The Wilson lines . . . 26
1.2.2 Discretization of the space-time . . . 26
1.2.3 Gluons and quarks on lattice . . . 27
1.2.4 QCD action on lattice . . . 27
1.2.5 Quantization of the QCD lattice action . . . 28
1.2.6 Monte Carlo simulations . . . 29
1.2.7 Progression in lattice QCD computations . . . 29
1.2.8 Lattice QCD versus the experiment . . . 29
1.3 Historical overview of the experiments . . . 31
1.3.1 The discovery of quarks . . . 31
1.3.2 The discovery of gluons . . . 34
1.3.3 The colour degrees of freedom . . . 35
1.3.4 The QCD running coupling constant . . . 36

2 QCD at Finite Temperature and Chemical Potential **39**
2.1 Theoretical principles . . . 39
2.1.1 Brief review in quantum statistical mechanics . . . 39
2.1.2 Partition function in the path-integral quantization formalism . . . 41
2.1.3 QCD partition function . . . 42
2.2 QCD phase transitions . . . 44
2.2.1 Chiral symmetry restoration . . . 44
2.2.2 Colour confinement/deconfinement phase transition . . . 44
2.2.3 The conjectured QCD phase diagram . . . 44

2.3 Lattice QCD . . . 45
2.3.1 Extension at finite temperature . . . 45
2.3.2 Polyakov loop . . . 46
2.3.3 Thermodynamic properties of the confinement/deconfinement phase transition . . . 47
2.3.4 Introduction of the chemical potential . . . 48
2.4 Heavy ion collision experiments . . . 49
2.4.1 Jet quenching . . . 50
2.4.2 Azimuthal anisotropy and elliptic flow . . . 50
2.4.3 J/ψ suppression . . . 51
2.4.4 Strange-particle production . . . 51
2.5 Quasiparticle approaches . . . 52

3 Thermodynamics of the Confined Phase **55**
3.1 Hadron Resonance Gas model and Hagedorn spectrum . . . 55
3.2 Thermodynamics of the 2 + 1 QCD plasma . . . 56
3.3 Thermodynamics of the pure-gauge sector . . . 58
3.4 Generalization to any gauge algebra . . . 59
3.4.1 Gauge-dependent quantities . . . 59
3.4.2 Linking $\boldsymbol{T_h}$ to $\boldsymbol{T_c}$ . . . 61
3.4.3 Numerical results . . . 61

4 QCD Spectrum within a $\boldsymbol{T}$-matrix Approach **63**
4.1 Non-relativistic scattering problems . . . 64
4.1.1 General description . . . 64
4.1.2 Schrödinger equation and its integral formulation . . . 65
4.1.3 Green's functions and its Lippmann-Schwinger equation . . . 66
4.1.4 $\boldsymbol{T}$-matrix and its Lippmann-Schwinger equation . . . 67
4.2 Bethe-Salpeter equation . . . 68
4.3 Solving the Lippmann-Schwinger equation for the T-matrix . . . 71
4.3.1 Blankenbecler-Sugar reduction scheme of the Bethe-Salpeter equation . . . 71
4.3.2 Interaction potential . . . 73
4.3.3 Masses and self-energies . . . 74
4.3.4 Partial wave decomposition of the T-matrix . . . 75
4.3.5 Haftel and Tabakin algorithm . . . 76
4.4 QCD spectrum at zero temperature . . . 76
4.4.1 Cornell potential and quasiparticle mass . . . 76
4.4.2 Glueball spectrum . . . 77
4.4.3 Meson spectrum . . . 78
4.5 QCD spectrum at finite temperature . . . 80
4.5.1 Two-body potential and quasiparticle thermal mass . . . 80
4.5.2 In-medium effects . . . 84
4.5.3 Glueball spectrum . . . 85
4.5.4 General QCD spectrum . . . 87

5 Thermodynamics of the QCD Deconfined Phase **93**
5.1 Dashen, Ma and Bernstein's formalism applied in QCD . . . 94
5.1.1 Generalities . . . 94
5.1.2 Application in QCD . . . 95
5.1.3 Born approximation . . . 97
5.2 Thermodynamics of the Yang-Mills plasma . . . 98
5.2.1 Model description . . . 98
5.2.2 Considerations about thermodynamic observables with SU(N_c) and G_2 . . . 99
5.2.2.1 SU(N_c) Case . . . 99
5.2.2.2 G_2 Case . . . 101
5.2.2.3 Scaling relations for SU(N_c) and G_2 . . . 101
5.2.3 Equations of state . . . 102
5.2.3.1 Pressure . . . 102
5.2.3.2 Trace anomaly . . . 105
5.3 Thermodynamics of the QGP . . . 107
5.3.1 Model description . . . 107
5.3.2 Criterion for selecting J^P channels . . . 108
5.3.3 Equations of state . . . 110
5.3.3.1 QGP with two light quark flavours . . . 110
5.3.3.2 2 + 1 QGP . . . 112
5.3.4 Adding baryonic potential . . . 113

6 The $\mathcal{N} = 1$ SUSY Yang-Mills Plasma **119**
6.1 General background . . . 119
6.1.1 $\mathcal{N} = 1$ SUSY Yang-Mills spectrum at $T = 0$ . . . 120
6.1.2 $\mathcal{N} = 1$ SUSY YM at finite temperature . . . 122
6.2 Thermodynamics of the $\mathcal{N} = 1$ SUSY Yang-Mills . . . 125
6.2.1 Model description . . . 125
6.2.2 Equations of state . . . 126
6.2.2.1 Pressure . . . 126
6.2.2.2 Trace anomaly . . . 128
6.2.3 Comparison to pure Yang-Mills theory . . . 128
6.2.4 Orientifold planar equivalence . . . 129

7 Large-N_c PNJL Model with Explicit Z_{N_c} Symmetry **133**
7.1 Polyakov-loop effective models for the pure-gauge sector . . . 133
7.1.1 Explicit Z_{N_c}-symmetry . . . 133
7.1.2 Numerical data . . . 136
7.2 PNJL model . . . 138
7.3 Phase diagram at large N_c . . . 140

Conclusions and Perspectives **145**

A Conventions **149**
A.1 Unit system . . . 149
A.2 Space-time characterization . . . 149
A.3 List of acronyms and abbreviations . . . 150

B Helicity Formalism for Spin-1/2 and Transverse Spin-1 Particles **153**
B.1 Generalities . . . 153
B.2 Two transverse spin-1 particles . . . 154
B.3 States containing one transverse spin-1 particle . . . 155

C Gauge Group Factors **157**
C.1 SU(N) gauge groups . . . 157
C.2 G_2 gauge group . . . 160

D Lagrange-Mesh Method **161**
D.1 Method in configuration space . . . 161
D.1.1 Lagrange functions . . . 161
D.1.2 Eigenvalue problems . . . 162
D.1.3 Mean values of radial observables . . . 164
D.1.4 Mean values of momentum-dependent observables . . . 164
D.1.5 Fourier's transform . . . 164
D.2 Method in momentum space . . . 165
D.2.1 Eigenvalue problems . . . 165
D.2.2 Mean values of momentum-dependent observables . . . 167
D.2.3 Mean values of radial observables . . . 168
D.2.4 Fourier's transform . . . 168

List of Publications **169**

List of Communications and Stays Abroad **171**

Introduction

Strong interaction: one of the four fundamental forces

According to our current knowledges, all phenomena in nature are well described by only four fundamental forces, namely the gravitation and the electromagnetic, weak and strong interactions. The theories underlying these three latter are part of the Standard Model while the gravitation is usually depicted by the Einstein's General Relativity. The ultimate dream of physicists is to build a unified and coherent framework in which all the physical aspects can be fully explained. Several candidates such as, for instance the String Theory, are nowadays studied.

The strong interaction is, as its name suggests it, the strongest one. It only acts at the nuclear level and on certain particles: the quarks, the antiquarks and the gluons. The residue of this force is responsible of the nuclei cohesion. Indeed, without it, the protons inside the nucleus should repel each other due to the electromagnetic forces. The theory underlying the strong interaction is the Quantum Chromodynamics (QCD).

QCD is a quantized non-abelian SU(3) gauge field theory. As in Quantum Electrodynamics (QED), the theory describing the electromagnetic interaction, the concept of conserved charge is a central point. The analogue of the electric charge is thus here the colour one, initially introduced by Fritzsch, Gell-Mann and Leutwyler [Frit73]. Mathematically, this concept is encoded in the associated gauge group. For QED, it is the abelian U(1) group. There are two states of electric charges ($+$ or $-$). In QCD, the associated gauge group is SU(3). It exists three colour-charged states (red, blue, green) and three anticolour-charged ones (antired, antiblue, antigreen). Quarks are the fundamental particles sensitive to the strong interaction. So, they carry a colour charge while antiquarks carry an anticolour one. Gluons are the gauge bosons of the interaction and have a colour and an anticolour charges. From a group point of view, the quarks (antiquarks) are in the fundamental (conjugate) representation of the gauge group; The gluons are in the adjoint one. The non-abelian feature of the gauge group gives a much more complex structure to the theory as we will see further.

QCD exhibits two essential features: the confinement and the asymptotic freedom. This latter was first proposed by Gross, Politzer and Wilczek [Gros73, Poli74]. Indeed, they realized that the behaviour of the QCD running coupling constant, which measures the strength of the interaction, is a decreasing function of the energy scale. This means that, provided that the energy increases, the interaction between colour-charged particles is weaker and weaker. These ones can thus feel almost free from each other, leading to the concept of the asymptotic freedom. On the other hand, at low energy, the strength of the interaction is so strong that colour particles are confined inside bigger structures called hadrons. This important particularity of QCD is expressed in the fact that observed particles are colourless.

Therefore, it naturally follows that the hadrons must be colourless combinations of colour particles. There exist two families experimentally observed: the baryons (combinations of three (anti)quarks) and the

mesons (combinations of one quark and one antiquark). Nevertheless, from a theoretical side, all colourless combinations can exist. In this thesis, the stress is thus also put on glueballs, bound states of gluons, even if they have not been detected for sure in the experiments up to now. Indeed, glueballs are extremely difficult to identify in particle accelerators, because they mix with other meson states. However, states like $f_0(1370)$, $f_0(1500)$ and $f_0(1710)$ could be good candidates.

Although so far, QCD appears as the most consistent theory to describe the strong interaction. Everything is not well understood. For example, the confinement is still a nebulous phenomenon by some aspects. Hadron spectra are far to be well known. QCD phase transitions require also a deeper understanding. All these opening directions and many others make that studying QCD and related phenomena is an attractive field of researches both theoretically and experimentally.

From a theoretical point of view, all these challenges are mainly due to the non-perturbative behaviour of QCD. Indeed, since at low energy, the QCD running coupling constant is large, the usual perturbative expansions can not be applied as well as in QED. That is the reason why several approaches, such as lattice QCD (lQCD), quasiparticle approaches, QCD sum rules *etc.*, are developed in order to predict results at this energy range. From the experimental side, the extreme smallness of the length scale ($\leq 10^{-18}$ fm) leads to build larger and larger accelerators and more and more precise detectors in order to probe matter in such a range.

Phase transitions in QCD

When a physicist is given a description of the matter at the microscopic level (elementary building blocks and interactions between them), the following relevant question that he has in mind, is: What could one build with that? For instance, water is made of molecules (building blocks in a relevant microscopic scale) that interact thanks to a residue of the electromagnetic interaction between electrons and protons, namely the van der Waals force. However, water can exist as ice, liquid or gas. These states of matter are different at a macroscopic level and, as we know, it is possible to reach these various phases by changing the thermodynamic variables.

Also in QCD, this question is meaningful. QCD exhibits two kinds of phase transitions: The confinement/deconfinement and the chiral ones. These two phases are driven by the change of two intensive thermodynamic variables: the temperature and the baryonic potential. At low value of these thermodynamic variables, the strongly-interacting matter is dominated by hadrons. We are in the confined regime. When the temperature and baryonic potential are increased and exceed a critical threshold, quarks and gluons are allowed to move quasi-freely. This is the deconfinement world. In parallel, the QCD chiral symmetry is broken at low value of these intensive parameters and then progressively restored, provided that they increase. Nevertheless up to now, there is no strong evidence that these two phase transitions coincide.

Studying such phenomena is thus particularly interesting for several reasons. First of all, it comes to investigate QCD under extremely high conditions and to develop, in other, thermal field theory. Next, since 1975, many scientists have thought that the core of the heaviest neutron stars should be in a state in which the density of neutrons is so high that they are overlapping [Coll75]. Therefore, the real degrees of freedom should be the quarks and the gluons. Moreover, from a cosmological point of view, our universe should go over a quark-gluon plasma (QGP) state few microseconds after the Big Bang. The temperature was then 100 000 times the one in the Sun core *i.e.* 10^{12} K. By cooling, quarks and gluons were sealed in hadronic matter. Finally, from the experimental side, QCD matter is probed under extremely high energy. Recently, the CERN has hold the record of the largest energy in the center-of-mass frame never reached (≈ 8 TeV) and RHIC (*Relativistic Heavy Ion Collider*) and LHC (*Large Hadron Collider*) experiments have probably

created a quark-gluon plasma.

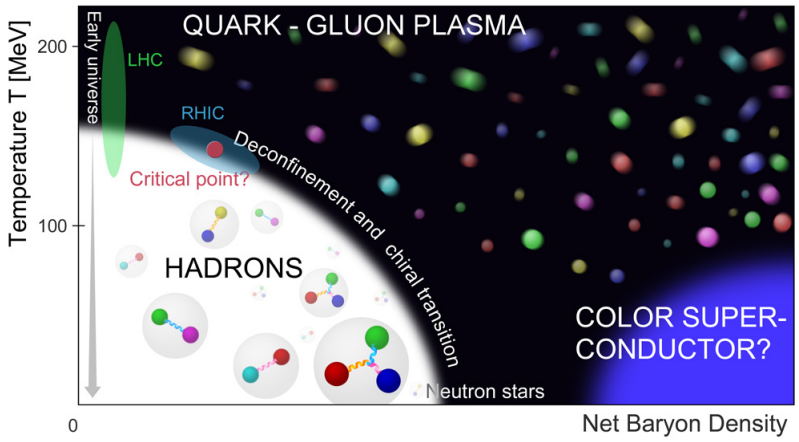

Figure 1: Conjectured QCD phase diagram [Coss11].

However, it is important to mention that the QCD phase diagram is poorly understood up to now. Fig. 1 is a conjecture: There are only few experimental data and the phase transition orders are not well identified. A lot of things remains to do and so, a lot of works are dedicated to better understand its structure.

Towards the quark-gluon plasma: quasiparticle approaches

In this thesis, the stress is mainly put on the study of the confined and deconfined phases of QCD thanks to quasiparticle approaches. Moreover, we essentially focus on the evolution in function of the temperature T. This does not prevent the fact that some parts of our research are also devoted to the effect of the baryonic potential μ and the study of the chiral transition.

Our quasiparticle approaches rely on the correct identification of the degrees of freedom. Below the critical temperature of deconfinement (T_c), the matter is seen as a gas of hadrons. Just above that, it is a strongly-interacting medium in which quarks and gluons are the relevant degrees of freedom. Well above T_c, it is an ideal gas of quarks and gluons.

The two first chapters of this thesis are of course dedicated to the state of art. The main concepts in QCD, useful to follow our further purposes, are summarized in Chapter 1 while a brief review of the knowledges about the QCD at finite temperature and baryonic potential is proposed in Chapter 2.

In Chapter 3, the Hadron Resonance Gas model (HRG) is discussed. This model is particularly interesting to describe matter below T_c. However, since the production of hadronic resonances is so abundant, approximations are needed and it is often assumed that their number follows an exponential growth in function of the hadron mass [Hage65, Hage68]. It thus results a limiting temperature T_h, for the description of the QCD matter in terms of hadrons. Maybe it is the temperature of deconfinement, maybe not. The question is still open.

A T-matrix approach based on [Cabr07] is then introduced to solve the QCD spectrum in Chapter 4. This approach is used to (re)produce the glueball and the meson spectra at $T = 0$ (seen as references) and at

finite temperature. Thanks to this study, we will be thus able to answer the question: Do QCD bound states survive above T_c?

In Chapter 5, the Dashen, Ma and Bernstein (DMB) formalism [Dash69] is applied to QCD in order to compute the QGP equations of state (EoS). This formalism is based on the T-matrix computations led in Chapter 4 and has the advantage to take explicitly into account the interactions between quasiparticles. First of all, the Yang-Mills (YM) sector as well as its extension to any gauge groups is studied and compared to current results in lQCD. Then, the EoS for the full plasma are presented and analysed. The effects due to the consideration of a small baryonic potential are also discussed.

In Chapter 6, we consider the $\mathcal{N} = 1$ SUSY extension of the YM theory. This latter is peculiarly interesting to draw some links with real QCD and is nowadays also investigated in lQCD. The bound-state sector of this theory is produced at zero and finite temperature following the ideas developed in Chapter 4 while the EoS are computed according to the formalism presented in Chapter 5. Moreover, the question of the orientifold equivalence is addressed.

In Chapter 7, the large-N_c QCD phase diagram is studied thanks to a Polyakov-Nambu-Jona-Lasinio (PNJL) model. Within this chapter, the order parameter of the confinement/deconfinement phase transition, the Polyakov loop, as well as the one of the chiral phase transition, the chiral condensate, are examined and allow us to draw the critical (T, μ) lines.

In order not to complicate the discussions during the lecture of this thesis, four appendices summarize some technical points. The conventions and a list of acronyms and abbreviations are given in Appendix A while the helicity formalism is introduced in Appendix B. The gauge-group factors are computed in Appendix C and the Lagrange-mesh method (LMM) is discussed in Appendix D.

Finally, our main results and findings are naturally summed up in our conclusions and several perspectives to our works are presented.

Chapter 1

Notions in QCD

The goal of this chapter is to give to the reader unfamiliar with QCD some useful and basic notions in order to sketch the background of this thesis and appreciate the extensions at finite temperature and chemical potential [1] that will be introduced in Chapter 2.

First of all, we will start by a theoretical description of QCD. A preliminary study on which QCD relies on is definitely the quark model. This work was essential because it exhibited for the first time the real degrees of freedom on which QCD field theory is based. That is the reason why it is the first point of our discussions. Then, the object of our second section will be obviously the classical formulation of QCD and its quantization. We will not miss to stress on two important QCD features: the confinement and the asymptotic freedom. Moreover, we will also briefly discuss the chiral symmetry of QCD with massless quarks. These characteristics are really the main notions to understand the QCD phase transition diagram presented in Chapter 2. The references used to achieve this theoretical description are essentially [Clos80, Muta10, Yagi05].

Amongst all the techniques used to compute observables in QCD, the lattice QCD (lQCD) is nowadays the most powerful framework to explore the QCD non-perturbative range starting from first QCD principles. In this thesis, we will systematically compare its predictions to our data. Therefore, it seems pertinent to dedicate some pages to its description. The key concepts given in this section are, in major part, extracted from [Yagi05].

Finally, we will close this chapter by relating, from a historical and experimental point of view, some observations that confirmed the validity of QCD theory. The discovery of quarks and gluons are addressed as well as the confirmation of their colour degrees of freedom and the behaviour of the strong coupling constant. The references used to feed this section are [Huss00, Fava12, Beth09].

1.1 Theoretical principles

1.1.1 A preliminary classification: the quark model

During early 1960s, physicists were faced with an impressive collection of particles emerging from collision experiments and cosmic rays. A classification as Mendeleev did for chemical elements seemed

1. The term "chemical potential" is conventionally used in statistical physics and designates the intensive variable associated to N, a number of particles. In the case of QCD, we talk more specifically of "baryonic potential", the intensive variable associated to the difference between the number of quarks and antiquarks.

to be more and more indispensable. In 1964, Gell-Mann and independently Zweig proposed a theoretical scheme of classification, the quark model.

The main idea of this model is to use the representations of symmetry groups under which the Lagrangian of strong interactions is invariant to classify hadrons (particles sensitive to strong interactions). Each hadron is then decomposed in terms of elementary pieces belonging to the fundamental representation of the underlying symmetry group and is described by quantum numbers resulting from the conserved charges, according to the Noether's theorem. These fundamental pieces were named quarks by Gell-Mann and were originally only mathematical tools before their real discovery in 1968 in deep inelastic scattering experiments of electrons on nucleons (see Section 1.3.1).

The first example of symmetry in which strong interactions obey is the proton/neutron SU(2) isospin (I) one. This symmetry was firstly noticed in 1932 by Heisenberg, well before the elaboration of the quark model. Indeed, experiments show that the neutron (n) and the proton (p) have nearly the same mass and that the strength of the interaction that apply between nn, pp and pn is practically the same, once the electromagnetic effects are removed. It can be thus deduced that, from the point of view of strong interactions, the neutron and the proton are two different representations of the same object, the nucleon. Their only difference lies in their electric charge. Therefore, including the electromagnetic interactions inside the Lagrangian breaks the isospin symmetry and defines a privileged direction in the isospin space (I_3). This mechanism is in pure analogy with the particle spin from which its name results.

Formally, a nucleon has an isospin, $I = 1/2$. This means that it belongs to the two-dimensional $(2I+1)$ representation of the SU(2) group which is the fundamental one [2]. The value of I_3 is $1/2$ for the proton and $-1/2$ for the neutron. We can also do the same for pions (light mesons) which have an $I = 1$ and belong to the adjoint representation of SU(2): (π^+, π^0, π^-) defines another multiplet of the symmetry group. Their projections on I_3 are respectively 1, 0 and -1. From these considerations, we can observe that particles are classified in terms of the representations of SU(2) Lie groups. This group was originally used because only hadrons with quark up and down were discovered at this time. Indeed, these quarks, although still unknown, are the only ones present in the nuclei structure. Nucleons and pions, as suggested by Yukawa, were (and still are) the fundamental degrees of freedom for describing the nuclear force, remaining part of the strong interaction at the nucleus level and only scale at which experiments had a quite easy access.

However in 1947, the picture got tougher because physicists discovered some "strange" hadrons, like kaons ($K^{\pm}$, K^0, $\bar{K}^0$, ...) and hyperons ($\Sigma^{\pm}$, Σ^0, ...), in cosmic rays and accelerators. They were strange because they did not obey to any decay rules known at this time. A first attempt of explanation were proposed in 1950s with the introduction of a new quantum number called strangeness which is conserved during strong interaction processes. Since a new conserved charge follows from a new symmetry of the Lagrangian, it is rather reasonable to think to extend the SU(2)-isospin symmetry into a SU(3) one: The quark model was born and this symmetry is called SU(3)-flavour. Patterns as in Fig. 1.1 were proposed by Gell-Mann and Zweig to classify hadrons.

Each hadron known at this time was therefore described in terms three flavours of quarks (cfr. Table 1.1): the up (u), the down (d) and the strange (s). Several associated quantum numbers as, for instance the isospin I, the strangeness S, the charge Q, were used (and are of course still used) to define all these hadrons.

As previously mentioned, quarks were firstly conjectured because the fundamental representation (*i.e.* the three-dimensional one) was missing from the classification scheme. This one represents the building block from which higher-dimensional representations can be obtained. However, from a tensor product point of view, only combinations with one quark (fundamental representation) and one antiquark (conjugate representation) as well as combinations with three quarks (or antiquarks) are observed in nature:

2. The fundamental representation of SU(2) is a doublet (↑,↓) with ↑ = (1,0) and ↓ = (0,1).

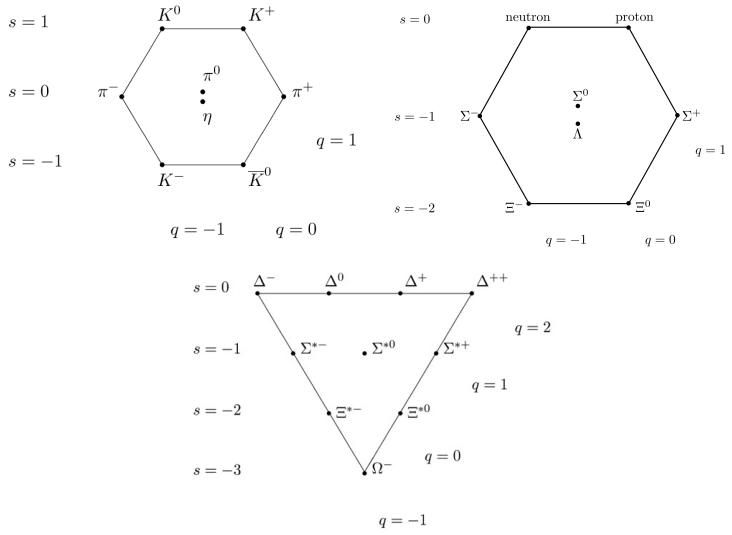

Figure 1.1: Meson octet, baryon octet and baryon decuplet from *Wikipedia*.

$$q\bar{q} \quad \Rightarrow \quad 3 \otimes \bar{3} = 1 \oplus 8, \tag{1.1.1}$$

$$qqq \quad \Rightarrow \quad 3 \otimes 3 \otimes 3 = 1 \oplus 8 \oplus 8 \oplus 10. \tag{1.1.2}$$

This leads to two groups of hadrons:

- the mesons: particles made of a quark-antiquark pair,
- the baryons: particles made of three (anti)quarks.

From (1.1.1) and (1.1.2), we understand the patters presented in Fig. 1.1: the meson and baryon octet as well as the baryon decuplet. One of the most beautiful predictions of the quark model, other than quarks, was the experimental observation of Ω^- in the baryon decuplet.

To finish this section and bounce on the next one, it is worth pointing two facts. Firstly, the SU(3)-flavour symmetry is not an exact one of the QCD Lagrangian. There is a mass gap between the u- and d-quarks (few MeV) and the s-one (around 100 MeV) that breaks it. Secondly, some quark decomposition proposed in Table 1.1 were disturbing. In fact, if we take into account all the degrees of freedom known at this time, the symmetry of the wave function associated to some hadrons does not respect the Pauli's principle: Bosons (fermions) have a (anti)symmetric wave function. For instance, Δ^{++} seemed to be a fermion with symmetric wave function. Either the Pauli's principle was not correct, either there was another degree of freedom in order to cure this anomaly. This last assertion was true and the colour was introduced and observed in experiment (see Section 1.3.3). Since, because of the confinement, the colour degree of freedom produces an antisymmetric contribution to the wave function, the Pauli's principle was restored. The SU(3)-colour

Mesons				
Quarks	Charge	Spin	Strangeness	Examples
$u\bar{d}$	1	0	0	π^+
$\bar{u}d$	-1	0	0	π^-
$u\bar{u}, d\bar{d}$	0	0	0	π^0
$u\bar{s}$	1	0	1	K^+
$\bar{u}s$	-1	0	-1	K^-
$d\bar{s}$	-1	0	1	K^0
Baryons				
Quarks	Charge	Spin	Strangeness	Examples
uud	1	1/2	0	p
udd	0	1/2	0	n
uuu	2	3/2	0	Δ^{++}
uud	1	3/2	0	Δ^+
udd	0	3/2	0	Δ^0
ddd	-1	3/2	0	Δ^-
uus	1	1/2	-1	$\Sigma^{\star+}$, Σ^+
uds	0	1/2	-1	$\Sigma^{\star0}$, Σ^0, Λ^0, Λ
dds	-1	1/2	-1	$\Sigma^{\star-}$,Σ^-
uss	0	1/2	-2	$\Xi^{\star0}$,Ξ^0
dss	-1	1/2	-2	$\Xi^{\star-}$,Ξ^-
sss	-1	3/2	-3	Ω^-

Table 1.1: Quark decomposition of some hadrons.

symmetry is nowadays at the heart of the gauge field theory describing QCD.

1.1.2 Classical QCD Lagrangian

QCD is a non-abelian gauge theory describing the interaction between quarks (massive fermions) through gluons (gauge bosons). The gauge group for the physical QCD is SU(3), but arbitrary semi-simple, compact Lie groups will be also considered in this thesis. The classical QCD Lagrangian is then given by

$$\mathcal{L}_{QCD} = \mathcal{L}_g + \mathcal{L}_q, \tag{1.1.3}$$

with

$$\mathcal{L}_g = -\frac{1}{4} F^a_{\mu\nu} F_a^{\mu\nu}, \tag{1.1.4}$$

$$\mathcal{L}_q = \sum_{f=1}^{N_f} \bar{\psi}^\alpha_f (i\gamma^\mu D_\mu - m_f)_{\alpha\beta} \psi^\beta_f. \tag{1.1.5}$$

This compact notation hides a lot of implicit information that must be clarified.

Firstly, $F^a_{\mu\nu}$ is the field strength. This tensor depends on the gauge fields A^a_μ, through the relation

$$F^a_{\mu\nu} = \partial_\mu A^a_\nu - \partial_\nu A^a_\mu + g f^{abc} A^b_\mu A^c_\nu, \tag{1.1.6}$$

where a, a colour index, runs over 1 to the dimension of the adjoint representation of the gauge group. For SU(N_c), $a = 1, \ldots, N_c^2 - 1$. g is the strong coupling constant and f^{abc} are the structure constants of the associated gauge algebra.

Secondly, D_μ is the covariant derivative and is defined by

$$D_\mu = \partial_\mu - ig A^a_\mu t_a, \tag{1.1.7}$$

where t_a are the gauge algebra generators obeying the commutation relations

$$[t^a, t^b] = i f^{abc} t_c, \tag{1.1.8}$$

and where $A_\mu = A^a_\mu t_a$.

Finally, ψ^α_f and $\bar{\psi}^\alpha_f = \psi^{\dagger\alpha}_f \gamma_0$ are the quark and antiquark fields with f, the flavour index, running over 1 to N_f (number of quark flavours in the theory) and α, a colour index, running over 1 to the dimension of the representation in which the quark and the antiquarks belong (usually, the fundamental and the conjugate representation of the gauge group). ψ^α_f and $\bar{\psi}^\alpha_f$ also carry Dirac spinor indices but they are omitted here not to overload the notation. m_f is the mass associated to f-quark and γ_μ are the Dirac γ-matrices (see Appendix A).

It is worth noting that the QCD Lagrangian is obtained by imposing the respect of the Lorentz invariance, the invariances under space and time reversal and the local gauge invariance. For this latter, the Lagrangian must be invariant under the transformation,

$$\Omega(x^\nu) = e^{i\theta^a(x^\nu) t_a}, \tag{1.1.9}$$

where $\theta^a(x^\nu)$ is an infinitesimal parameter which depends on the space-time point x^ν. Quarks, antiquarks and gluons respect respectively the following transformation laws:

$$\psi(x^\nu) \rightarrow \Omega(x^\nu)\psi(x^\nu) \quad \text{(fundamental representation)}, \tag{1.1.10}$$

$$\bar{\psi}(x^\nu) \rightarrow \bar{\psi}(x^\nu)\Omega^\dagger(x^\nu) \quad \text{(conjugate representation)}, \tag{1.1.11}$$

$$A_\mu(x^\nu) \rightarrow \Omega(x^\nu)\left(A_\mu(x^\nu) + \frac{i}{g}\partial_\mu\right)\Omega^\dagger(x^\nu) \quad \text{(adjoint representation)}. \tag{1.1.12}$$

At the infinitesimal level, $\Omega(x^\nu) \approx 1 + i\theta^a(x^\nu)t_a$, we have

$$\psi(x^\nu) \rightarrow \psi(x^\nu) + i\theta^a(x^\nu)t_a\psi(x^\nu), \tag{1.1.13}$$

$$\bar{\psi}(x^\nu) \rightarrow \bar{\psi}(x^\nu) + i\theta^a(x^\nu)(-t_a^*)\bar{\psi}(x^\nu), \tag{1.1.14}$$

$$A_\mu^c(x^\nu) \rightarrow A_\mu^c(x^\nu) + \theta^a f_{ab}^c A_\mu^b(x^\nu) + \frac{1}{g}\partial_\mu\theta^c(x^\nu). \tag{1.1.15}$$

However, these invariance principles are not sufficient to get an unique $\mathcal{L}_{QCD}$. Indeed, adding terms of higher powers of $F_{\mu\nu}^a$ and ψ do not spoil Lorentz, space and time reversal and local gauge invariances. The additional requirement of renormalizability (see Section 1.1.5) may eliminate all the irrelevant terms and fix the Lagrangian to that given by (1.1.3).

A remarkable feature of $\mathcal{L}_{QCD}$ that can be immediately noticed is that it allows pure-gauge vertices like

- the three-gluon (3-g): $A_\mu^a A_\nu^b A_\rho^c$,
- the four-gluon (4-g): $A_\mu^a A_\nu^b A_\rho^c A_\sigma^d$.

These ones are represented in terms of Feynman diagrams in Fig. 1.2 together with the quark/antiquark/gluon ($q\bar{q}g$) vertex: $\psi^a A_\mu^b \bar{\psi}^c$.

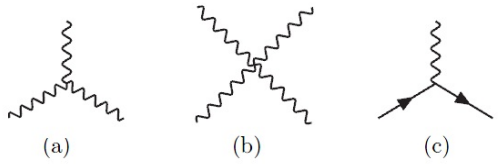

Figure 1.2: (a) 3-g vertex, (b) 4-g vertex and (c) $q\bar{q}g$ vertex.

1.1.3 Different ways of quantization

As mentioned in the previous section, the Lagrangian given by (1.1.3) is the one of a classical field theory. Quantization is thus needed. However, it is not an unique procedure and several equivalent methods can be used. There are two well-known ways:

- Canonical operator formalism [Heis29],
- Path-integral formalism [Feyn48],

The most traditional one is the canonical operator formalism in which fields are seen as operators obeying to canonical commutation relations and in which all the building blocks of the theory, the n-point Green's functions, may be calculated as vacuum expectation values of the product of these field operators:

$$\langle 0|T[\hat{\phi}(x_1)\dots\hat{\phi}(x_n)]|0\rangle \tag{1.1.16}$$

where $\hat{\phi}(x_i)$ is a field operator at position x_i, T is the time-ordered product and $|0\rangle$ is the vacuum of the underlying theory.

In the Feynman formulation of quantum mechanics, the n-point Green's functions are written in terms of path integrals,

$$\langle 0|T[\hat{\phi}(x_1)\dots\hat{\phi}(x_n)]|0\rangle = \frac{\int [d\phi]\phi(x_1)\dots\phi(x_n)\, e^{i\mathcal{S}}}{\int [d\phi]\, e^{i\mathcal{S}}}. \tag{1.1.17}$$

They are obtained by integrating over all possible classical field configurations $\phi(t,\vec{x}\,)$, with a weight factor $e^{i\mathcal{S}}$, given by the classical action,

$$\mathcal{S} = \int d^4x\, \mathcal{L}\,, \tag{1.1.18}$$

evaluated in that field configuration.

This formulation of quantum mechanics is much more intuitive than the canonical one. Indeed, this is a natural generalization of the two-slit experiment: Even if it is known where the particle originates from and where it hits on the screen, the slit in which the particle came, can not be determined. The path integral formalism is an infinite-slit experiment.

In this thesis, we will use the results of the path-integral quantization method for two main reasons. Firstly, this method is the one used in lQCD to compute observables (see section 1.2.5). Secondly, it can be easily applied to compute statistical partition functions and thus, to develop QCD at finite temperature (see section 2.1.2).

1.1.4 QCD quantization within the path-integral formalism

In the path-integral quantization formalism, all the Green's functions of a theory can be computed thanks to the concept of the functional derivative with respect to an external source. This procedure was first introduced by Schwinger [Schw51].

The main principles of this technique is to consider an external source $J(x^\nu)$ and introduce an artificial source term $\phi(x^\nu)\, J(x^\nu)$ in the functional integral:

$$Z[J] = \int [d\phi] e^{\,i\int d^4x\,(\mathcal{L}+\phi J)}. \tag{1.1.19}$$

$Z[J]$ is called the generating functional for Green's functions. Indeed, it generates all the Green's functions of the underlying theory by functional differentiation and by setting, at the end of the computation, J to 0:

$$\langle 0|T[\hat{\phi}(x_1)\dots\hat{\phi}(x_n)]|0\rangle = \frac{(-i)^n}{Z[0]}\frac{\delta^n Z[J]}{\delta J(x_1)\dots\delta J(x_n)}\bigg|_{J=0}. \tag{1.1.20}$$

If we apply straightforwardly (1.1.19) to gauge fields, we have

$$Z[J^a_\mu] = \int \prod_{\mu,a} [dA^a_\mu]\, e^{\,i\int d^4x\,(\mathcal{L}_g + A^a_\mu J^\mu_a)}. \tag{1.1.21}$$

The integration in (1.1.21) is over the set of all the configurations of the gluon field A^a_μ. This set is called the gauge space. However, gauge invariance principle imposes that all the gluon fields are not independent.

Indeed, because of the relation (1.1.12), A^a_μ is equivalent to all $A'^a_\mu(\theta)$. A^a_μ and $A'^a_\mu(\theta)$ lie on the same gauge orbit. Eventually, we remain with a problem of over-counting the gauge-field path in the integration.

The conventional approach to solve this problem is to make the following restriction on A^a_μ,

$$G^\mu A^a_\mu = B^a, \tag{1.1.22}$$

where G^μ and B^a should be chosen in an appropriate way. This is a gauge-fixing condition that must be applied before the quantization. The goal is to include only one configuration of each gauge orbit. Several gauge-fixing scheme can be used. For instance:

- Coulomb gauge: $G^\mu = (0, \vec{\nabla})$,
- Covariant gauge: $G^\mu = \partial^\mu$,
- Axial gauge: $G^\mu = n^\mu$ with n^μ is a space-like constant 4-vector,
- Temporal gauge: $G^\mu = (1, 0, 0, 0)$.

The standard procedure to implement this constraint at the level of the path-integral is not explained here. Further explanations can be found in [Muta10]. The result is the appearance of a jacobian det M_G, and of a gauge-fixing term with a gauge parameter ξ, in the exponent within the generating-functional formula,

$$Z[J^a_\mu] = \int \prod_{\mu,a} [dA^a_\mu] \det M_G \, e^{\,i \int d^4x \, (\mathcal{L}_g - \frac{1}{2\xi}(G^\mu A^a_\mu)^2 + A^a_\mu J^\mu_a)}. \tag{1.1.23}$$

It is det M_G which makes the quantization of gauge fields non-trivial. Of course, its computation depends on the gauge-fixing scheme. For axial and temporal gauges, M_G is independent of A^a_μ and det M_G is simply a constant. For covariant gauges, M_G depends on A^a_μ and a way to compute det M_G is to introduce fictitious fields called Faddeev-Popov ghost [Fade67].

After having applied all this machinery to quantize our theory, we remain with gauge-dependent n-point Green's functions since (1.1.23) depends on the gauge-fixing scheme. Thus, they can not be physical quantities. They are only building blocks of the underlying theory. Indeed, we need to combine them in such a way that they are gauge-independent. This is what we call observables in physics. Let us mention for example the S-matrix of a particle system (defined in the following section). Only the physical observables can be measured in experiments.

To close this section, quarks and antiquarks must be added and so, the generating functional including fermion fields is given by

$$\begin{aligned} Z[J^a_\mu, \eta, \bar{\eta}] &= \int \prod_{\mu,a} [dA^a_\mu] \prod [d\psi] \prod [d\bar{\psi}] \det M_G \\ &\times \; e^{\,i \int d^4x \, (\mathcal{L}_{QCD} - \frac{1}{2\xi}(G^\mu A^a_\mu)^2 + A^a_\mu J^\mu_a + \psi\bar{\eta} + \bar{\psi}\eta)}, \end{aligned} \tag{1.1.24}$$

where η and $\bar{\eta}$ are anticommuting sources for anticommuting fermion fields $\bar{\psi}$ and ψ. The mathematical tool to deal with anticommuting fields is the Grassmann algebra. Some cares must be taken with the differentiation and integration within this context. We will not enter into details here. Interested readers will find further information in [Bere66, Ohnu78, Fade80].

1.1.5 Regularization and renormalization

From the equation (1.1.3), we know that QCD depends on N_f + 1 parameters that must be fixed by experiments: the masses of the N_f quarks and the coupling constant g. For example, we could set them by using the experimental mass measurements of some hadrons like the ρ- or the π-mesons. Then, we can normally predict the all QCD spectrum by applying the aforementioned QCD theory. However, even if the procedure seems simple, it is not the case and some subtleties quickly appear. The purpose of the following discussion is to highlight them without entering into the deep technical aspects.

From an experimental point of view, the way to access to information about particles is via scattering or disintegration. In such processes, a good approximation of asymptotic states (well before and after the scattering or the disintegration) is the free-particle ones. Indeed, the effect of the interactions is limited in space and time. The probability amplitude for these processes is the transition probability between these two asymptotic states, $|in\rangle$ and $|out\rangle$, the link being ensured by the S-matrix:

$$\langle out|S|in\rangle. \tag{1.1.25}$$

These matrix elements are the physical observables. They can be computed within the formalism described in Section 1.1.4 and thus depend on Green's functions.

The traditional way to compute the Green's functions of an interactive field theory is to use a perturbative expansion: The interaction terms inside the Lagrangian are treated like perturbations relative to the free fields. In QED, it works well since the electromagnetic coupling constant is small at the energy scale of interest. On the other side, in QCD, g is quite large and we do not know the validity of the perturbation theory until we perform practical computation. A second problem, this time in both theories, is that some integrals in the perturbative expansion are divergent. These divergences are not necessary the sign of inconsistency in the theory: The contribution of one Feynman diagram [3] has not a physical sense. Only the S-matrix elements have one. We thus need a formulation of perturbative expansion which has finite S-matrix elements and well-defined Green's functions at each perturbative order.

This task can be accomplished by using a regularization and renormalization scheme. It means that we have to redefine fields and QCD parameters in order to eliminate the divergences. Several regularization ways can be used as the cut-off method, the Pauli-Villars regulator method, the analytic regularization, the dimensional regularization *etc.*. The choice of the regularization scheme depends on which physical principles is important to preserve in the problem. There also exists several renormalization procedures as, for instance, the on-shell subtraction, the off-shell subtraction, the minimal subtraction (MS), the modified minimal subtraction ($\overline{MS}$). Again, this scheme is not unique but it is worth mentioning and rather logical to ask that, at the end of the computation, physical observables must be independent of it. That is the case in QCD: QCD is thus a renormalizable theory. We will not enter here into the details of these mathematical procedures: Interesting readers can refer to [Muta10]. The main interests for us are the following. The renormalizability of QCD implies, as already addressed in Section 1.1.2, the form of the QCD Lagrangian given in (1.1.3). Moreover, all the QCD parameters finally depend on an energy scale μ. Especially, we are interested in the behaviour of the β-function which encodes the dependence of the coupling parameter g, on the energy scale μ. This is discussed in what follows.

3. A Feynman diagram is a schematic representation of one Green's function at a given order.

1.1.6 QCD β-function: confinement and asymptotic freedom

The β-function of a theory is given by the following expression emerging from the renormalization group theory:

$$\beta(g) = \frac{\mathrm{d}g(\mu)}{\mathrm{d}\ln\mu}. \tag{1.1.26}$$

The sign of this function is crucial. The different subsequent cases can be encountered:

- $\beta(g) < 0$; g decreases with the energy scale,
- $\beta(g) > 0$; g increases with the energy scale,
- $\beta(g) = 0$; g is independent of the energy scale (conformal theory).

It can be shown from renormalization group method that the β-function at two-loop order has the following form:

$$\beta(g) = -\beta_0 g^3 - \beta_1 g^5 + O(g^7), \tag{1.1.27}$$

with

$$\beta_0 = \frac{1}{(4\pi)^2}\frac{11C_A - 4\,T_R N_f}{3}, \tag{1.1.28}$$

and

$$\beta_1 = \frac{1}{(4\pi)^4}\left[\frac{34}{3}C_A^2 - 4\left(\frac{5}{3}C_A + C_R\right)T_R N_f\right]. \tag{1.1.29}$$

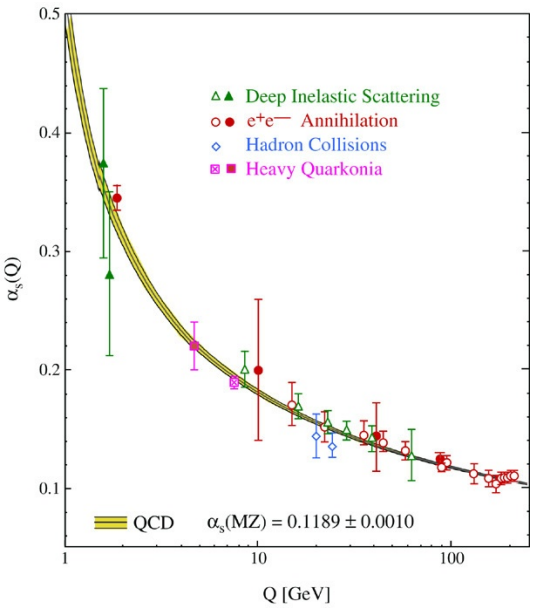

Figure 1.3: Behaviour of the running coupling constant of QCD [Beth07].

In the formulas (1.1.28) and (1.1.29), C_A, C_R and T_R are coefficients depending on the gauge group:

- C_A is the quadratic Casimir of the gauge-group adjoint representation,
- C_R is the quadratic Casimir of the gauge-group R representation,
- d_A is the dimension of the gauge-group adjoint representation,
- d_R is the dimension of the gauge-group R representation,
- T_R is the Dykin index of the gauge-group R representation given by $\frac{C_R\, d_R}{d_A}$.

For a SU(N_c) gauge group and (anti)quarks in their usual representations, we have

$$C_A = N_c, \qquad C_R = \frac{N_c^2 - 1}{2N_c}, \qquad d_A = N_c^2 - 1, \qquad d_R = N_c, \qquad T_R = \frac{1}{2}. \tag{1.1.30}$$

In QCD, we are in the case $\beta(g) < 0$ because $N_c = 3$ and $N_f \leq 6$. At low energy, the coupling constant is thus quite large. A perturbative expansion is not justified. We are in the confinement world. By increasing the energy, the coupling constant comes smaller and smaller and then, the strength of interaction decreases. We are therefore in the region of the asymptotic freedom.

In Fig. 1.3, it is represented the behaviour of the running coupling constant of QCD. Let us define:

$$\alpha_s(\mu) = \frac{g^2(\mu)}{4\pi} = \frac{4\pi}{\beta_0 L}\left[1 - \frac{\beta_1 \ln L}{\beta_0^2 L}\right], \tag{1.1.31}$$

with $L = \ln\frac{\mu^2}{\Lambda_{QCD}^2}$ and $\Lambda_{QCD} \approx 200$ MeV [PDG]. This Λ_{QCD} is a typical energy scale below which perturbative expansion fails. The experimental determination of α_s will be addressed in Section 1.3.4.

1.1.7 Chiral symmetry in QCD

The QCD classical Lagrangian given in (1.1.3) exhibits more symmetries than the local SU(3) gauge one in some limit cases . For example, we can think of

- SU(2) isospin symmetry: $m_u = m_d$,
- SU(3) flavour symmetry: $m_u = m_d = m_s$,
- chiral symmetry: $m_u = m_d = m_s = 0$.

In this section, we will briefly focus on this last one. For this purpose, the $\mathcal{L}_{QCD}$ can be divided in the following way:

$$\mathcal{L}_{QCD} = \mathcal{L}_{QCD}^{\text{chiral}} + \mathcal{L}_{QCD}^{\text{mass}}, \tag{1.1.32}$$

where

$$\mathcal{L}_{QCD}^{\text{chiral}} = -\frac{1}{4}F_{\mu\nu}^{a}F_{a}^{\mu\nu} + \sum_{f}^{N_f}\bar{\psi}_{f}^{\alpha}(i\gamma^{\mu}D_{\mu})_{\alpha\beta}\psi_{f}^{\beta}, \tag{1.1.33}$$

$$\mathcal{L}_{QCD}^{\text{mass}} = -\sum_{f}^{N_f}\bar{\psi}_{f}^{\alpha}(m_f)_{\alpha\beta}\psi_{f}^{\beta}. \tag{1.1.34}$$

In the chiral limit, $\mathcal{L}_{QCD}^{\text{mass}}$ is naturally absent. If we decompose the Dirac spinor representing the (anti)quark into a right- and left-handed parts, we have

$$\psi = \psi_R + \psi_L, \tag{1.1.35}$$

with

$$\psi_R = \frac{1+\gamma_5}{2}\psi, \tag{1.1.36}$$

$$\psi_L = \frac{1-\gamma_5}{2}\psi, \tag{1.1.37}$$

and with $\gamma_5 = i\gamma_0\gamma_1\gamma_2\gamma_3$.
ψ_R (ψ_L) is an eigenstate of the chirality operator with the eigenvalue 1 (-1). Since the chirality is equivalent to the helicity h for massless quarks,

$$h = \frac{\vec{S}.\vec{p}}{|\vec{p}|}, \tag{1.1.38}$$

where $\vec{S}$ is the spin, $\vec{p}$ the momentum, and ψ_R (ψ_L) represents a quark with spin and momentum aligned (opposite). The next decomposition is therefore allows:

$$\mathcal{L}_{QCD}^{\text{chiral}} = \mathcal{L}_{QCD}^{R}(\psi_R, A_\mu) + \mathcal{L}_{QCD}^{L}(\psi_L, A_\mu). \tag{1.1.39}$$

Right- and left-handed are completely decoupled in the limit of massless quarks. $\mathcal{L}_{QCD}^{\text{chiral}}$ for three quark flavours is thus invariant under the $\text{U(3)}_L \times \text{U(3)}_R$ = $\text{SU(3)}_L \times \text{SU(3)}_R \times \text{U(1)}_V \times \text{U(1)}_1$ global transformations:

$$\psi_R \rightarrow e^{i\theta_R^a\lambda^a}\psi_R \quad \text{U(3)}_R, \tag{1.1.40}$$

$$\psi_L \rightarrow e^{i\theta_L^a\lambda^a}\psi_R \quad \text{U(3)}_L, \tag{1.1.41}$$

where $\lambda^a = 2t_a$ (for $a = 1, \ldots, 8$) are the Gell-Mann matrices and $\lambda^0 = 1/2$.

Note that $\text{SU(3)}_R \times \text{SU(3)}_L$ can also be rewritten $\text{SU(3)}_V \times \text{SU(3)}_A$ associated respectively to vector and axial currents. Because of the Noether's theorem, the vector and the axial currents,

$$V_\mu^a = \bar{\psi}\gamma_\mu\lambda^a\psi, \tag{1.1.42}$$

$$A_\mu^a = \bar{\psi}\gamma_\mu\gamma_5\lambda^a\psi, \tag{1.1.43}$$

are conserved in the chiral limit ($\partial^\mu V_\mu^a = 0$ and $\partial^\mu A_\mu^a = 0$) and associated to conserved charges, Q_V^a and Q_A^a.

However, it happens that a conservation law at the classical level can be broken spontaneously by quantum effects. This is called an anomaly. The axial current is affected by this anomaly, $\partial^\mu A^0_\mu \neq 0$.

Moreover, the action of the vector and the axial vector charges on the ground state of QCD, the vacuum $|0\rangle$, is

$$Q^a_V|0\rangle = 0, \qquad Q^a_A|0\rangle \neq 0, \tag{1.1.44}$$

which is called the Nambu-Goldstone realization of the chiral symmetry. Note, for further purposes that

$$Q^a_V|0\rangle = 0, \qquad Q^a_A|0\rangle = 0, \tag{1.1.45}$$

is called the Wigner-Weyl realization.

The $SU(3)_A$ and $U(1)_A$ symmetries are thus not preserved by the QCD vacuum. We speak over a spontaneous breaking of the chiral symmetry. Such spontaneously broken symmetries of the QCD vacuum have some consequences on the QCD spectrum. They generate for instance the non-degeneracy of chiral partner multiplets and massless particles in the QCD spectrum according to the Goldstone's theorem. Indeed, this theorem mentions that if a charge associated to a global symmetry of the Lagrangian is conserved, but that the vacuum is not invariant under the action of the corresponding charge, then a new massless particle appears in the theory spectrum with the same quantum numbers as the corresponding charge. For example in QCD, the spontaneous breaking of $SU(3)_A$ symmetry generates eight Goldstone's bosons: π^0, $\pi^\pm$, K^0, $\bar{K}^0$, $K^\pm$ and η.

Nevertheless, it is worth adding that in experiments, these eight bosons have a mass. This is due to the fact the the chiral symmetry is explicitly broken at the level of the QCD Lagragian since the quarks have a mass. However, the masses of the Goldstone's bosons are weaker than the masses of other hadrons, reflecting so the spontaneously chiral symmetry breaking.

To finish, we will introduce an important notion that will be useful to understand the chiral phase transition: the chiral condensate $\langle\bar{q}q\rangle$. This last one has a zero value in the Wigner-Weyl phase (chiral symmetry) and a non-zero one in the Nambu-Goldstone phase (chiral symmetry spontaneously broken). It is associated to the faculty of the QCD vacuum at low energy to generate quark-antiquark pair. Indeed, from

$$\partial^\mu A^0_\mu = -\sqrt{2N_f}\frac{g^2}{32\pi^2}\epsilon_{\mu\nu\lambda\rho}F^{\mu\nu}_a F^{\lambda\rho\,a}, \tag{1.1.46}$$

we can notice that, when g is strong (at low energy), the chiral symmetry is spontaneously broken and that it is progressively restored when the energy increases since $g \to 0$ (cfr. Fig. 1.3).

1.2 Lattice QCD

Lattice QCD is a powerful approach of QCD in which non-perturbative phenomena like the confinement or the QGP can be studied. Indeed, as already addressed, perturbative expansions are not allowed at low energy in QCD because of its too huge coupling constant (cfr. Fig. 1.3). Therefore, it is difficult (even impossible) to get analytical solutions and so, lQCD is really helpful to compute observables in the QCD non-perturbative regime. Its formulation was originally proposed by Wilson in 1974. The basic ideas are the discretization of QCD on a space-time lattice and the concept of Wilson lines.

1.2.1 The Wilson lines

To compute QCD on a lattice, it is not enough to discretize the QCD action since we need to preserve gauge invariance. So, a special variable is introduced for representing the gauge field: the Wilson line. Starting from the QCD gauge theory in Euclidean continuous space-time, we consider a path Γ (parametrized by the variable s, $s \in [0,1]$) going from $x = \Gamma(0)$ to $y = \Gamma(1)$ space-time points:

$$U(y,x) = \mathcal{P}\{\exp[\, ig \int_\Gamma dz^\mu A_\mu(z)]\}, \tag{1.2.1}$$

where $\mathcal{P}$ orders the product of operators according to the value of a chosen parameter along the path (path-ordering operator) and $A_\mu(z)$ is the gauge field.

The main property of the Wilson line is that under a local gauge transformation $\Omega(x)$ defined in (1.1.9), it transforms covariantly. Indeed,

$$U'(y,x) = \Omega(y)U(y,x)\Omega^\dagger(x). \tag{1.2.2}$$

The Wilson line is therefore an useful tool that allows us to define non-local gauge invariant objects which will be building blocks of the QCD action on the lattice.

1.2.2 Discretization of the space-time

In lQCD, space-time is no longer continuous but discretized on a hyper-cubic lattice. Space-time coordinates are then given by

$$x_\mu = a\, n_\mu, \text{ with } n_\mu \in \mathbb{Z} \text{ et } \mu \in [0,3], \tag{1.2.3}$$

where a is the lattice spacing. Naturally, the more a is small, the more the precision is high.

The elementary components of a lattice are

- the sites of the lattice,
- the links: the shortest Wilson line connecting two neighboring lattice sites, n and $n + \hat{\mu}$,

$$U_{\hat{\mu}}(n) = \exp[ig\, a\, A_\mu(n)], \tag{1.2.4}$$

  where $\hat{\mu}$ is a vector pointing in the direction μ with length a,

- the plaquette: the smallest oriented closed paths on the lattice,

$$\mathrm{Tr}\, U_{\hat{\mu}\hat{\nu}}(n) = \mathrm{Tr}\left[U^\dagger_{\hat{\nu}}(n)\, U^\dagger_{\hat{\mu}}(n+\hat{\nu})\, U_{\hat{\nu}}(n+\hat{\mu})\, U_{\hat{\mu}}(n) \right], \tag{1.2.5}$$

  where $U^\dagger_{\hat{\mu}}(n) = U_{-\hat{\mu}}(n+\hat{\mu})$.

It is worth mentioning that $U_{\hat{\mu}\hat{\nu}}(n)$ transforms covariantly under a local gauge transformation, $\Omega(n)$,

$$U_{\hat{\mu}\hat{\nu}}(n) \to U^\Omega_{\hat{\mu}\hat{\nu}}(n) = \Omega(n) U_{\hat{\mu}\hat{\nu}}(n) \Omega^\dagger(n). \tag{1.2.6}$$

The plaquette is so a gauge-invariant object. This notion will be crucial to define the gluon action in Section 1.2.4.

1.2.3 Gluons and quarks on lattice

Now that we have defined the main objects in lQCD, we have to connect them to the main ones in real QCD: gluons and quarks. Quarks and antiquarks are simply represented by their field value on the different lattice sites :

$$\psi(x^\mu) \rightarrow q(n), \tag{1.2.7}$$
$$\bar{\psi}(x^\mu) \rightarrow \bar{q}(n). \tag{1.2.8}$$

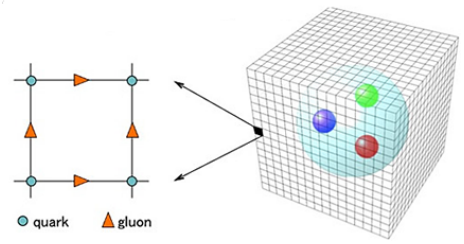

Figure 1.4: Representation of quarks and gluons on lattice [Kura14].

Concerning the gluon field, it is a bit more involved. It is expressed by a link between two sites:

$$U_{\hat{\nu}}(n) = \mathcal{P}\{\exp ig \int_n^{n+\hat{\nu}} dz^\rho A_\rho(z)\}, \tag{1.2.9}$$

where $\hat{\nu}$ is the direction in which the field is integrated over. For instance, we have integrated here the gauge field on the link going from n to $n + \hat{\nu}$.

1.2.4 QCD action on lattice

In order to build the QCD action, we need pieces that combine them in a gauge-invariant way. Let us focus first in the pure-gauge sector. We can obtain the SU(N_c) gluon action from the plaquettes since they are gauge-invariant (cfr. Section 1.2.2). The lattice gluon action is then given by

$$\mathcal{S}_W = \frac{2N_c}{g^2} \sum_p \left[1 - \frac{1}{N_c} \text{Re } [\text{Tr } U_{\hat{\mu}\hat{\nu}}(n)]\right], \tag{1.2.10}$$

where $\sum_p$ denotes the summation over all plaquettes with a definite orientation.

$\mathcal{S}_W$ is called the Wilson action. The only requirement for building such action is that, at the continuum limit,

$$\mathcal{S}_W \xrightarrow[a\to 0]{} \frac{1}{4} \int d^4x \, F^b_{\mu\nu} F^{\mu\nu}_b. \tag{1.2.11}$$

It is thus evident that (1.2.10) is not unique in the sense that we can add arbitrary non-minimal terms which vanish when $a \to 0$. The main interest of such terms is to increase the convergence to the continuum limit. A lattice action with non-minimal terms is called an improved action.

For completeness and by analogy with the pure-gauge case, the fermion action can also be built with small-size gauge-invariant objects like

$$\bar{q}(n)q(n), \;\; \bar{q}(n+\hat{\mu})\, U_{\hat{\mu}}(n)\; q(n), \;\; \bar{q}(n-\hat{\mu})\, U_{-\hat{\mu}}(n)\; q(n). \tag{1.2.12}$$

One may put any γ-matrices between $\bar{q}$ and q without spoiling the gauge invariance. The Wilson fermion action is then given by

$$\begin{aligned} \mathcal{S}_{W,f} &= a^4 \sum_n \Bigg[m\, \bar{q}(n)q(n) - \frac{1}{2a} \sum_\mu \bar{q}(n+\hat{\mu})\, \Gamma_\mu\, U_{\hat{\mu}}\, q(n) \\ &- \frac{r}{2a} \sum_\mu \Big(\bar{q}(n+\hat{\mu})\, U_{\hat{\mu}}\, q(n) - \bar{q}(n)q(n) \Big) \Bigg], \end{aligned} \tag{1.2.13}$$

where the summation over μ is taken for both positive and negative directions and Γ_μ are the Euclidean γ-matrices [Yagi05]. Naturally, $\mathcal{S}_{W,f}$ has to reduce to the QCD fermion action at the continuum limit and it is not unique.

Note that a more convenient way to give the Wilson fermion action is

$$\mathcal{S}_{W,f} = \sum_{m,n} \bar{\Psi}(m) F_W(m,n) \Psi(n), \tag{1.2.14}$$

where the field Ψ and $\bar{\Psi}$ are a rescaling of q and $\bar{q}$ in terms of lattice parameters and $F_W(m,n)$ is the Wilson fermion kernel. (1.2.14) is a general way to write an arbitrary lattice fermion action with a particular kernel $F(m,n)$.

1.2.5 Quantization of the QCD lattice action

Once a QCD classical lattice action is fixed, we have of course to quantize it. The path-integral quantization formalism, described in Section 1.1.4, imposes itself since it shares the same conceptual picture with the lattice description. In lQCD, it writes

$$\mathcal{Z} = \int [dU][d\bar{\Psi}][d\Psi]\, e^{-\mathcal{S}_g(U) - \mathcal{S}_f(\bar{\Psi},\Psi,U)}, \tag{1.2.15}$$

where $\mathcal{S}_{g,f}$ are respectively the pure-gauge and fermion lattice action. Since the gauge fields are represented by the group element U, the symbolic notation $\int [dU]$ hides an integration over the Haar measure. We will not enter into these technical details here, interested reader could refer to [Dies14]. The quark (Ψ) and antiquark (Ψ) fields are Grassmann (anticommutating) variables that can be integrated out to arrive to a more suitable computational form:

$$\mathcal{Z} = \int [dU] \mathrm{Det}\, F(U)\, e^{-\mathcal{S}_g(U)}, \tag{1.2.16}$$

where Det $F(U)$ encodes the fermionic part. This compact notation takes into account all indices of F, namely colour, flavour, spin and space-time coordinates. Det $F(U)$ represents the effects of quark loops. If Det $F(U)$ has a constant value, we work in the quenched approximation. This means that all virtual quark and antiquark excitations are ignored. Otherwise, we are in an unquenched lattice computation.

1.2.6 Monte Carlo simulations

In order to compute (1.2.16), lQCD resorts to a Monte Carlo (MC) integration, which is a statistical way of evaluating integrals. Indeed, usual numerical integration methods as Simpson method, Gaussian quadrature, *etc.* are not well-efficient to support the large number of necessary dimensions. If we suppose a lattice with a number of temporal sites N_t, and spatial sites N_s, the total number of gluon integrations will be

$$(N_s^3 \times N_t) \times 4_{\text{links}} \times 8_{\text{colour}}. \tag{1.2.17}$$

A moderate lattice ($N_t = N_s = 32$) leads to a dimension of the order of 10^7.

The MC method can be divided into two steps. First, we generate a Markov chain of N gauge configurations [4]:

$$U^{(1)} \to U^{(2)} \to \ldots \to U^{(N)}, \tag{1.2.18}$$

where a configuration $U^{(i)}$ is a set of links on the lattice distributed according to a probability,

$$W(U) = \frac{1}{\mathcal{Z}} \text{Det}\, F(U) e^{-\mathcal{S}_g(U)}. \tag{1.2.19}$$

Once the configurations are generated, expectation values $\langle A \rangle$, can be calculated by averaging over those configurations:

$$\langle A \rangle = \frac{1}{N} \sum_{n=1}^{N} A(U^{(n)}). \tag{1.2.20}$$

Obviously, when N increases, the statistical errors are reduced as $1/\sqrt{N}$ as long as the configurations are generated independently.

The most challenging and fastidious part of all this procedure is the inclusion of fermions and so, the computation of Det $F(U)$. Several methods such as the pseudo-fermion and the hydride MC ones has been developed. We will not enter into details here.

1.2.7 Progression in lattice QCD computations

It is also important to mention the progression followed by lQCD computations since its beginning [Hash11]. Indeed, until the 1990s, most of lattice simulations were done in the pure-gauge sector within the quenched approximation. Systematic errors were still important.

During the 1990s, improvements were carried out by including non-constant Det $F(U)$ but with unphysical quark masses ($\sim$ 50 - 100 MeV). Extrapolations to physical quark masses were then a source of large systematic errors. With the progresses in both algorithms and computers, simulations have involved smaller and smaller quark masses up to nowadays, wherein the physical light quark masses are reached. It comes that presently, lQCD is really a reliable and efficient approach to study QCD even if it has also its limits, see Section 2.3.4.

1.2.8 Lattice QCD versus the experiment

Since lQCD is a computational framework built from first QCD principles, a mandatory test is the comparison with experimental data. In this section, we will focus only on one aspect that QCD exhibits: the

4. Passing from U to $U^{'}$ in (1.2.18) is called an updating. Typical used method is, for instance, the Metropolis algorithm [Metr53]

confinement. The way to see whether lQCD leads to quark confinement or not is by studying the behaviour of the Wilson loop defined by

$$\langle W(C)\rangle = \langle \mathrm{Tr} \prod_{\mathrm{link}\in C} U_{\hat{\mu}}(n)\rangle. \tag{1.2.21}$$

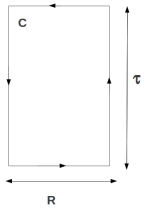

Figure 1.5: Rectangular Wilson loop C, with temporal size τ and spatial size R.

The Wilson loop is thus the expectation value of the product of links delimiting the closed path C (see Fig. 1.5).

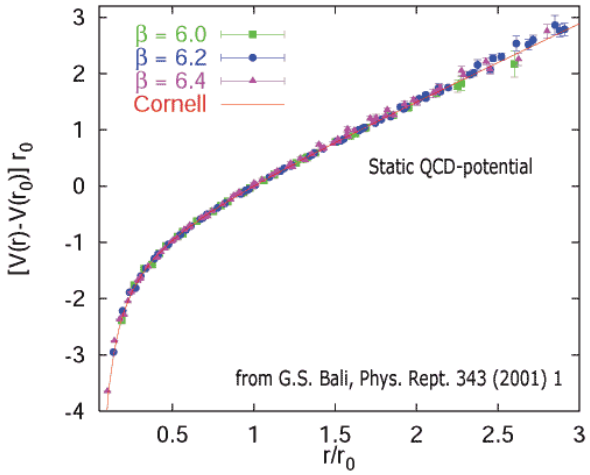

Figure 1.6: Dimensionless potential between a heavy quark and antiquark pair in function of their dimensionless spatial separation r/r_0 with r_0, the Sommer scale. β corresponds to different lattice spacings [Yagi05].

If we consider the physical situation in which a heavy quark and antiquark pair is embedded in the non-perturbative QCD vacuum, we can extract from a computation of the correlation function [Yagi05], that the potential between them is linked to the Wilson loop by the following relation:

$$V(R) = -\lim_{\tau\to\infty}\left[\frac{1}{\tau}\ln\langle W(C)\rangle\right]_{\tau\gg R}, \tag{1.2.22}$$

where R is the spatial distance between the quark and the antiquark and τ, the time scale of the interaction.

Lattice numerical simulations, displayed in Fig. 1.6, clearly show that $V(R)$ behaves like

$$V(r) = ar - \frac{b}{r} + c, \tag{1.2.23}$$

which is the Cornell potential. This potential is composed by a linear confining part at long distance and an attractive Coulombic part at short distance. It comes that the confinement is sketched by lQCD.

Another main prediction of lQCD related to confinement is, without doubt, the hadron spectrum. The lQCD hadron spectrum is richer than the one produced by experiments. It includes glueballs (bound states made of gluons) and exotic hadrons that are not observed yet. In Fig. 1.7, the lQCD light hadron spectrum is presented and compared to experiments.

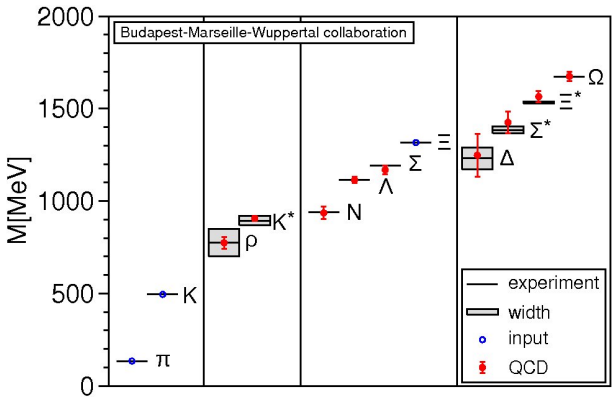

Figure 1.7: The light hadron spectrum of QCD. Horizontal lines and bands are the experimental values with their decay widths. lQCD results are shown by solid circles [BMW08].

1.3 Historical overview of the experiments

The question that naturally comes in mind after having elaborated a theory is: Does it encounter successful agreements when one tries to compare it to experiments? In this section, we will pay a particular attention to the description of main experiments that have highlighted the quarks, the gluons and some QCD important features.

1.3.1 The discovery of quarks

As we have seen it in Section 1.1.1, quarks were first theoretical tools to classify the hadron zoo observed in experiments since the beginning of particle physics. It was only some years later that the experimental evidences came to crown the success of the quark model.

In 1968-69, deep inelastic scattering experiments at the Stanford Linear Accelerator Center (SLAC) showed that electrons appeared to be bouncing off small hard cores inside the nucleon. An analyse of the scattering data carried out by Bjorken and Feynamn concluded that the nucleon contained much smaller, point-like objects and was therefore not an elementary particle. These point-like objects were foremost called partons by Feynman and some years later identified as quarks.

This experiment consists to collide electrons (considered as elementary and so, as clear probe) on nucleons at very high energy in order to probe their structure. The philosophy is the same as the pioneer experiments of probing the atom structure by Rutherford. Hydrogen and deuterium liquid are used as nucleon targets and electrons are accelerated at 20 GeV. Reaching such energy is really a key point because the principle is the following: The more the energy of the electron beam is huge, the more the wave length is small and the more the nucleon structure can exhibit sharp details.

Figure 1.8: SLAC at Stanford (USA) [SLAC].

By the early 1970s, detailed analyses of the distribution of the scattered electrons revealed three scattering centres inside the nucleon. This is the first experimental evidence of quarks. Friedman, Kendall, and Taylor received the Nobel Prize for this discovery in 1990. From this fact, physicists started progressively to admit the real existence of quarks.

However, the story of quarks was not finished. Without entering into the details, the existence of a fourth quark became quickly necessary to accord electroweak theory with experiments but also to satisfy the symmetry desire of physicists. Quarks are of course sensitive to the strong interaction but likewise to the electromagnetic and the weak ones. The leptons like electrons, muons and neutrinos are also sensitive to these two last ones. From a symmetry point of view, two generations of leptons was known at this time: the electron and its neutrino (e, ν_e) and the muon and its neutrino (μ, ν_μ). Concerning the quark, we had (u, d) and (s, ?). A quark was thus missing. Its discovery (again driven by theoretical predictions) was done in 1974. Two teams of physicists directed respectively by Ting (Brookhaven National Laboratory, BNL) and Richter (Stanford, SPEAR), independently highlighted a new particle: the J/ψ [5]. This J/ψ is made of two elementary particles whose mass is around 1.5 GeV. We could thus deduce the existence of this new heavier quark. It was called "charm" (c) because thanks to it, all the theoretical problems seemed magically disappear. Nevertheless, because of the "hidden charm" of the J/ψ (indeed, it is a combination of $c\bar{c}$), physicists wanted to observe the charm quark in a bare combination like in mixed meson ($c\bar{u}$), ($c\bar{s}$) or ($c\bar{d}$). This was done by the discovery of D-meson family at CERN in 1976.

It is worth remembering at this stage that quarks can not be observed as free states. The explanation results from the QCD property of colour confinement. If we try to extract a single quark out of a nucleon, a new $q\bar{q}$ pair will be suddenly created from the vacuum and will generate new hadrons. This is known as the hadronization. In order to obtain such phenomena, we need to hit the nucleon (or more generally the hadron) with an energy of about 30 GeV. Indeed, a common description for a meson (the simplest hadron) is done by a pair of quark-antiquark linked by a flux tube (representing the strength field lines). When the

5. The particle was named J by Ting's team and ψ by Richter's one.

energy goes up, the flux tube starts to stretch up to the breaking. Because of the confinement, we need more and more energy to stretch this tube and at the moment of the breaking, the energy is sufficient to create a new $q\bar{q}$ pair from the vacuum. At minimum, we remain with two mesons, more generally, with two jets of particles because a cascade of disintegrations starts from this $q\bar{q}$ pair. The process can be generalized to any hadron.

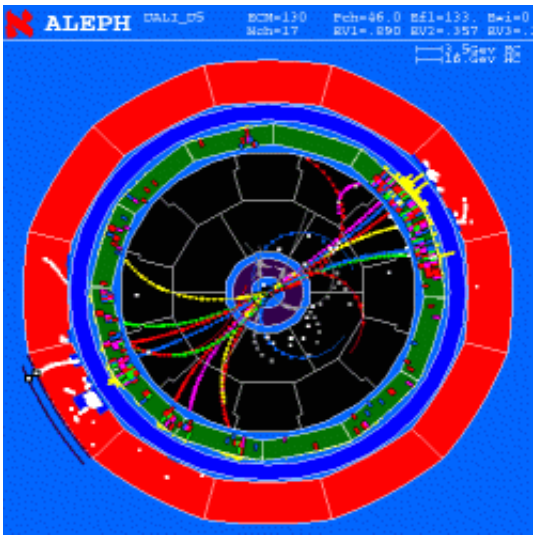

Figure 1.9: A radiative 2-jet event detected in the Large Electron Positron (LEP) collider by the ALEPH collaboration at CERN [Surf].

In the experiments, it is possible to precisely identify the quark flavour that starts the jet thanks to its lifetime or the disintegration chain that generates. This ability was a precious tool to discover the two last quarks known up to now: the bottom (or the beauty) b, and the top (or the truth) t .

As often in particle physics, the quarks b and t were first theoretically needed. Indeed, to explain the CP-violation [6] observed in the decay of neutral kaons (1964), Kobayashi and Maskawa had to introduce, at minimum, a third generation of quarks and the Cabibbo-Kobayashi-Maskawa (CKM) matrix, which defines the mixing parameters between quarks, was the result of their work (1973). The flavour of quarks can change during a weak interaction process.

The quark b was then discovered at the Fermi National Accelerator Laboratory (Fermilab) by Lederman's team in 1977. The experiment consisted to accelerate protons on fix target (of copper for instance) at very high energy (400 GeV) and to analyse mainly the channel producing muon pairs, privileged decay channel for the upsilon Υ, a meson made of a $b\bar{b}$ pair. The b mass is around 4 GeV. Hadrons with a combination of b and other quarks flavours were also observed thereafter.

The t story is just a matter of repulsing the energy limit of accelerators. The Tevatron (build by the Fermilab) was the first one to reach an energy of 1.8 TeV at the collision point. Here, two proton beams collided on each other to increase the energy in the center-of-mass frame. The quark t were highlighted in 1995 with a mass of about 174 GeV.

6. C refers to the charge conjugation symmetry and P to the parity symmetry. CP-symmetry states that the laws of physics should be the same if a particle is interchanged with its antiparticle (C-symmetry), and if its spatial coordinates are inverted (mirror or P-symmetry).

To conclude this section, we summarize in Table 1.2 some data we have about quarks from experiments [PDG].

Flavour	J^P	Q (e)	I	I_3	S	C	B	T	Mass
u	$(1/2)^+$	2/3	1/2	1/2	0	0	0	0	$2.3^{+0.7}_{-0.5}$ MeV
d	$(1/2)^+$	-1/3	1/2	-1/2	0	0	0	0	$4.8^{+0.7}_{-0.3}$ MeV
s	$(1/2)^+$	-1/3	0	0	-1	0	0	0	95 ± 5 MeV
c	$(1/2)^+$	2/3	0	0	0	1	0	0	1.275 ± 0.025 GeV
b	$(1/2)^+$	-1/3	0	0	0	0	-1	0	4.18 ± 0.03 GeV
t	$(1/2)^+$	2/3	0	0	0	0	0	1	173.5 ± 1.4 GeV

Table 1.2: Properties of quarks. J^P is the spin-parity. Q is the charge with e, the elementary charge (the proton one). I is the isospin with the projection I_3. S, C, B and T are respectively the strange, charm, bottom and top charges.

1.3.2 The discovery of gluons

Another important discovery in QCD was the one of the gluon. In the mid-1970s, QCD was considered as a serious candidate for describing the strong interaction. However, the gluon, the particle that mediates this interaction, was not still observed. The first experimental evidence of this essential QCD building block,

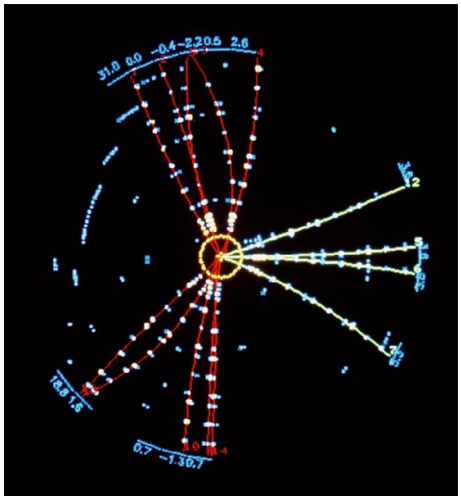

Figure 1.10: A three-jet event, registered at the PETRA storage ring (DESY) [CERNco].

were obtained in 1979 within the particle accelerator PETRA (Positron-Electron Tandem Ring Accelerator)

at DESY (Deutsches Elektronen-Synchrotron) in Hamburg. Three-jet events were produced. An even number of jets is well understood thanks to a $q\bar{q}$ pair at the origin of the hadronization while the third jet signs inevitably the presence of one gluon. The allowed and more likely reactions are then the following:

$$e^+e^- \rightarrow q\bar{q} \rightarrow 2 \text{ jets of hadronization,} \tag{1.3.1}$$
$$e^+e^- \rightarrow q\bar{q}g \rightarrow 3 \text{ jets of hadronization.} \tag{1.3.2}$$

1.3.3 The colour degrees of freedom

The experimental evidence of the colour degrees of freedom was done by studying the cross-section of the e^+e^- annihilation into hadrons, given by:

$$\sigma(e^+e^- \rightarrow \text{hadrons}) = \sum_{i=1}^{N_f} \sigma(e^+e^- \rightarrow q_i\bar{q}_i), \tag{1.3.3}$$

with the summation goes up to the number of present flavours at the reaction energy *i.e.* $2\,m_f < \sqrt{s}$ where $\sqrt{s}$ is the center-of-mass energy and m_f the mass of f-flavour quark.

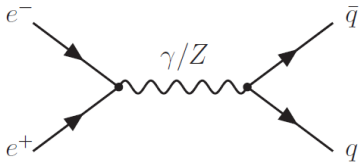

Figure 1.11: Annihilation of e^+e^- in a $q\bar{q}$ pair.

The cross-section of the $q\bar{q}$-pair production by the annihilation of e^+e^- in a photon (or if the energy is sufficiently high, a Z^0) is the same as the one that produces fermion-antifermion pairs. The only difference results in the counting of the electric charge Q in presence.

At high energy, we have [Fava12]:

$$\sigma(e^+e^- \rightarrow \text{hadrons}) = N_c \frac{4\pi\alpha^2}{3s} \sum_{i=1}^{N_f} Q_i^2, \tag{1.3.4}$$
$$\sigma(e^+e^- \rightarrow \mu^+\mu^-) = \frac{4\pi\alpha^2}{3s}. \tag{1.3.5}$$

Defining the ratio:

$$R = \frac{\sigma(e^+e^- \rightarrow \text{hadrons})}{\sigma(e^+e^- \rightarrow \mu^+\mu^-)} = N_c \sum_{i=1}^{N_f} Q_i^2, \tag{1.3.6}$$

we can see that R depends explicitly of the colour number N_c, and thus signs the existence of three colours:

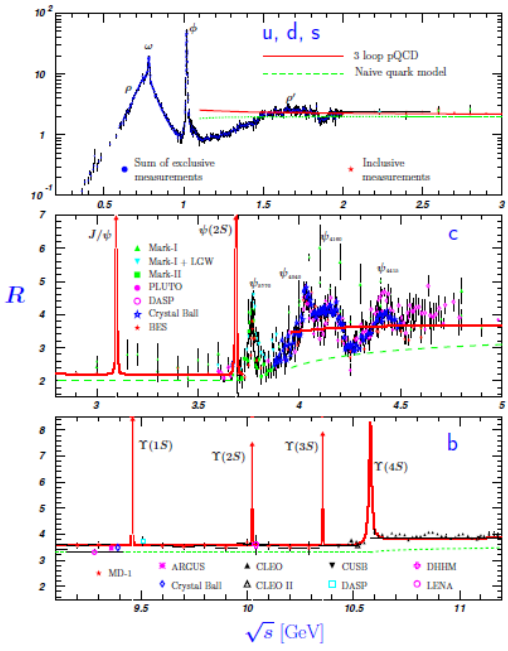

Figure 1.12: R in the light-flavour, charm, and beauty threshold regions. The full list of references to the original data and the details of the R-ratio extraction from them can be found in [arXiv:hep-ph/0312114].

- if $2\,m_s < \sqrt{s} < 2\,m_c$ then $R = 2$,
- if $2\,m_c < \sqrt{s} < 2\,m_b$ then $R = 10/3$,
- if $2\,m_b < \sqrt{s} < 2\,m_t$ then $R = 11/3$.

In Fig. 1.12, the comparison with experimental data validate $N_c = 3$. The theoretical predictions are right if we exclude resonance peak and hadronization effects at low energy which are out of the scope of the formula (1.3.6).

1.3.4 The QCD running coupling constant

An important parameter in QCD that must be extracted from experiments, is the strong coupling constant $\alpha_s = g^2/(4\pi)$. Only its knowledge at one energy (μ) is needed since its behaviour is given by the renormalization group equation (1.1.26).

Thanks to perturbative expansions, physical observables can be expanded in power of α_s. Some of these

observables are used in its experimental determination [Beth09]. For instance, we can think of

- the τ-decay,
  The hadronic branching fraction of τ-decays,

$$R_\tau = \frac{\sigma(\tau \to \text{hadrons})}{\sigma(\tau \to \nu_\tau\, e^-\, \bar{\nu}_e)}, \tag{1.3.7}$$

  is theoretically given by (for memory)

$$R_\tau = N_c\, S_{EW} |V_{ud}|^2 (1 + \delta'_{EW} + \delta_p + \delta_{np}), \tag{1.3.8}$$

  with $S_{EW} = 1.0189(6)$ and $\delta'_{EW} = 0.001(1)$ are electroweak corrections, $|V_{ud}|^2 = 0.97418(27)$, δ_p and δ_{np} are perturbative and non-perturbative QCD corrections. δ_p was calculated to complete N^{3}LO perturbative order $O(\alpha_s^4)$. Based on the operator product expansion (OPE), the non-perturbative corrections are estimated to be small, $\delta_{np} \approx -0.007 \pm 0.004$. The final result from τ-decays, leads to

$$\alpha_s(M_\tau) = 0.330 \pm 0.014.$$

- heavy quarkonia ($c\bar{c}$ or $b\bar{b}$),
  Heavy quarkonia masses and decay rates are observables which can be accurately measured and predicted by QCD perturbation theory and lQCD calculations:

$$\begin{aligned} \alpha_s(M_{Z_0}) &= 0.119^{+0.006}_{-0.005} \text{ from radiative } \Upsilon\text{-decays}, \\ \alpha_s(M_{Z_0}) &= 0.1183 \pm 0.0008 \text{ from lQCD}. \end{aligned}$$

- jet production in deep inelastic scattering,
  Measurements at HERA determine α_s from fits of NLO QCD predictions to data of inclusive jet cross-sections in neutral current deep inelastic scattering at high Q^2. The result is

$$\alpha_s(M_{Z_0}) = 0.1198 \pm 0.0032.$$

- hadronic event shapes and jet production in e^+e^- annihilation,
  Data from the PETRA and the LEP collider which operated from 1979 to 1986 and from 1989 to 2000, respectively were re-analyzed in the light of new theoretical improved calculations:

$$\alpha_s(M_{Z_0}) = 0.1224 \pm 0.0039.$$

- ...

The QCD running coupling constant has been already presented in Fig. 1.3. It is a really important feature that will be in the centre of the QCD phase diagram understanding.

Chapter 2

QCD at Finite Temperature and Chemical Potential

Now that we have rapidly reviewed the main aspects of QCD, formally at zero temperature, we are able to approach its extensions at finite temperature (T) and chemical potential (μ). Studying these extensions will be thus the goal of this chapter.

Firstly, we will briefly recall some basic principles in quantum statistical mechanics [Kapu06, LeBe96]. The most important mathematical tool, *i.e.* the partition function, will be formulated within the framework of the path-integral quantization. Then, the QCD partition function, from which the whole QCD thermodynamics can be derived, will be built. Note that thermal quantum field theory has been formulated in the imaginary as well as real time. In this thesis, we focus on the imaginary time formulation since it is well-suited for computing time independent quantities such as the partition function. However, for time dependent quantities, the real time formulation is a more convenient framework. This latter case will be not considered within this thesis. Interested readers can refer to [Kapu06, LeBe96].

Secondly, we will discuss the phase transitions that QCD exhibits: the confinement/deconfinement and the chiral ones [Yagi05]. A conjectured QCD phase diagram is presented to close this section.

Again, the most powerful technique to get results at finite temperature is lQCD because strongly-interacting effects are still present, mostly around the critical temperature of the phase transitions. However, as we will partially address, lQCD has some troubles to compute at finite chemical potential [Yagi05].

Then, some aspects of heavy ion experiments, which are used to explore the QCD phase diagram, are introduced in order to give a general overview of the main directions investigated nowadays to characterize the QGP [Yagi05].

Finally, a brief state of art in quasiparticle approaches is proposed. This section is intended to highlight our original contributions in the field.

2.1 Theoretical principles

2.1.1 Brief review in quantum statistical mechanics

At a macroscopic level, thermodynamics is used to describe the bulk properties of matter in or near equilibrium. Several quantities like the temperature (T), the pressure (p), the entropy (S), *etc.* can be

defined and have to respect thermodynamic laws. At a microscopic stage, motion is dictated by quantum mechanics (even if classical mechanics can be a correct approximation for several problems). Unfortunately, because of the large number of particles considered in thermodynamic systems, it is of course impossible to solve simultaneously the numerous equations of motion. This is even more true that they are generally coupled. That is the reason why we resort to quantum statistical mechanics.

There are usually three types of ensemble in equilibrium statistical mechanics:

- The microcanonical ensemble (used to describe an isolated system with a fixed energy E, a fixed particle number N, and a fixed volume V),
- The canonical ensemble (used to describe a system in contact with a heat reservoir at temperature T; The temperature, the number of particles and the volume of the system are fixed),
- The grand canonical ensemble (used to describe a system that can exchange energy and particles with a reservoir; The temperature, the volume and the chemical potential of the system are fixed).

In our case, we restrict ourself to a description of thermodynamics in the grand canonical ensemble. Indeed, in a relativistic quantum system, particles can be created and destroyed and so, their number can not be fixed.

Let us thus consider a system described by a Hamiltonian $\hat{H}$, and a set of conserved numbers $\hat{N}_i$ [1]. For instance in QCD, a possible conserved number is the difference between the number of quarks and antiquarks inside the system. Indeed, they always emerge in pairs from the vacuum. The central object in equilibrium statistical mechanics is the statistical density matrix $\hat{\rho}$, given by

$$\hat{\rho} = e^{-\beta(\hat{H}-\sum_i \mu_i \hat{N}_i)}, \tag{2.1.1}$$

where $\beta = 1/T$.
This statistical density matrix is used to compute the ensemble average of any observable A:

$$A = \langle \hat{A} \rangle = \frac{\mathrm{Tr}\, \hat{A}\hat{\rho}}{\mathrm{Tr}\, \hat{\rho}}, \tag{2.1.2}$$

where Tr denotes the trace over all the accessible states of the system.

The partition function is the most important function to link statistical mechanics to thermodynamics and is defined, in the grand canonical ensemble, as

$$\mathcal{Z} = \mathcal{Z}(V, T, \mu_i) = \mathrm{Tr}\, \hat{\rho}, \tag{2.1.3}$$

and the grand canonical potential Ω, is given by

$$\Omega = -T \ln \mathcal{Z}. \tag{2.1.4}$$

From (2.1.3), all thermodynamic quantities can be expressed:

1. The hat is to emphasize the fact that the quantity is an operator.

$$p = \left.\frac{\partial(T\ln\mathcal{Z})}{\partial V}\right|_{T,\mu_i}, \tag{2.1.5}$$

$$N_i = \left.\frac{\partial(T\ln\mathcal{Z})}{\partial \mu_i}\right|_{T,V}, \tag{2.1.6}$$

$$S = \left.\frac{\partial(T\ln\mathcal{Z})}{\partial T}\right|_{V,\mu_i}, \tag{2.1.7}$$

$$E = -pV + TS + \sum_i \mu_i N_i. \tag{2.1.8}$$

2.1.2 Partition function in the path-integral quantization formalism

In this section, the partition function is expressed in terms of the path-integral quantization formalism. Formally, (2.1.3) becomes

$$\mathcal{Z} = \mathcal{Z}(V,T,\mu_i) = \mathrm{Tr}\, e^{-\beta(\hat{H}-\sum_i \mu_i \hat{N}_i)} = \sum_a \int d\Phi_a \langle \Phi_a | e^{-\beta(\hat{H}-\sum_i \mu_i \hat{N}_i)} | \Phi_a \rangle, \tag{2.1.9}$$

where the sum runs over all the states Φ_a, accessible to the system [Kapu06].

The integrand of (2.1.9) is similar to the transition amplitude in quantum mechanics,

$$\langle \Phi_b | e^{-i\hat{H}t_f} | \Phi_a \rangle, \tag{2.1.10}$$

for going from a state $|\Phi_a\rangle$ at time $t = 0$ to a state $|\Phi_b\rangle$ at $t = t_f$. In the path-integral quantization formalism, this transition amplitude is given by [Kapu06]

$$\begin{aligned} \langle \Phi_b | e^{-i\hat{H}t_f} | \Phi_a \rangle &= \int [d\pi] \int_{\Phi_a(0,\vec{x})}^{\Phi_b(t_f,\vec{x})} [d\Phi] \\ &\times e^{\left[i \int_0^{t_f} dt \int d^3x \left(\pi(t,\vec{x}) \frac{\partial \Phi(t,\vec{x})}{\partial t} - \mathcal{H}(\pi(t,\vec{x}), \Phi(t,\vec{x})) \right) \right]}, \end{aligned} \tag{2.1.11}$$

with

$$\hat{H} = \int d^3x\, \mathcal{H}(\hat{\pi}(t,\vec{x}), \hat{\Phi}(t,\vec{x}))\,, \tag{2.1.12}$$

and $\hat{\Phi}(t,\vec{x})$ is a Schrödinger-picture field operator and $\hat{\pi}(t,\vec{x})$, its conjugate momentum operator. Through the Legendre transformation, we can relate the argument of the exponential with the Lagrangian density of the system. Indeed,

$$\mathcal{L} = \pi \frac{\partial \Phi}{\partial t} - \mathcal{H}. \tag{2.1.13}$$

In order to connect the transition amplitude to statistical quantum mechanics, we need to exploit the similarity between the Boltzmann operator $e^{-\beta H}$ and the time evolution operator in quantum mechanics. Two main things have to be carried out. First, we perform an analytical continuation from real to imaginary

time (Wick rotation): $\tau = it$. This means that we go from Minkowski space to Euclidean one, since the metric becomes euclidean (up to a sign):

$$t^2 - \vec{x}^2 \to -(\tau^2 + \vec{x}^2). \tag{2.1.14}$$

Then, we impose two types of boundary conditions in (2.1.11):

- If the system returns to its initial state after a time t_f (periodic conditions, bosonic-like system):

$$\Phi(\tau, \vec{x}) = \Phi(\tau + \beta, \vec{x}), \tag{2.1.15}$$

  with $\beta = it_f$.

- If the system returns to its initial state with an opposite sign after a time t_f (anti-periodic conditions, fermionic-like system):

$$\Phi(\tau, \vec{x}) = -\Phi(\tau + \beta, \vec{x}). \tag{2.1.16}$$

Moreover, if the system admits conserved numbers, we must make the substitution

$$\mathcal{H} \to \mathcal{H} - \sum_i \mu_i \mathcal{N}_i, \tag{2.1.17}$$

where $\mathcal{N}$ is the particle number density.

Finally, we arrive at the following expression [2]

$$\mathcal{Z} = \int_{B.C.} [d\Phi]\, e^{-S_E}, \tag{2.1.18}$$

where $B.C.$ are the aforementioned boundary conditions and

$$S_E = \int_0^\beta d\tau \int d^3x\, \mathcal{L}_E, \tag{2.1.19}$$

is the Euclidean action. The equivalent to (1.1.20) for finite temperature quantum field theory is

$$\langle 0|T[\hat{\Phi}(\tau_1, \vec{x}_1) \dots \hat{\Phi}(\tau_n, \vec{x}_n)]|0\rangle = \frac{(-i)^n}{Z[\beta, 0]} \frac{\delta^n Z[\beta, J]}{\delta J(\tau_1, \vec{x}_1) \dots \delta J(\tau_n, \vec{x}_n)}\bigg|_{J=0}, \tag{2.1.20}$$

which allows to calculate the Green's functions.

The equation (2.1.18) can be interpreted as a field theory in a four-dimensional "box". Indeed, the spatial size is infinite while the temporal one is $1/T$. We recover the four-dimensional Euclidean space when $T \to 0$.

2.1.3 QCD partition function

The QCD classical partition function is given by the following expression:

$$\mathcal{Z}_{QCD} = \int_{B.C.} [dA_\mu]\, [d\bar{\psi}]\, [d\psi]\, e^{-S_E^g(A_\mu)}\, e^{-S_E^f(A_\mu, \psi, \bar{\psi})}, \tag{2.1.21}$$

2. Note that the integration over conjugate momenta π, gives a multiplicative constant that will not change the thermodynamics of the system. This constant is simply rescaled to one here.

with

$$S_E^g(A_\mu) = \int_0^\beta d\tau \int d^3x \, \frac{1}{4} F^a_{\mu\nu} F_a^{\mu\nu} \tag{2.1.22}$$

$$S_E^f(A_\mu, \psi, \bar{\psi}) = \int_0^\beta d\tau \int d^3x \sum_{f=1}^{N_f} \bar{\psi}_f^\alpha (\Gamma^\nu D_\nu + m_f - \mu_f \, \Gamma^0)_{\alpha\beta} \psi_f^\beta, \tag{2.1.23}$$

and where μ_f is the chemical potential for the f-quark [3]. This extra-term containing μ_f comes from the substitution (2.1.17) and is aimed to count the difference between the number of quarks and antiquarks inside the plasma while the Γ^0-matrix is introduced to take into account the fact that the quark and the antiquark have an opposite chemical potential. The boundary conditions for the fields in (2.1.21) are

$$A_\mu(\tau, \vec{x}) = A_\mu(\tau + \beta, \vec{x}), \tag{2.1.24}$$

$$\psi_f(\tau, \vec{x}) = -\psi_f(\tau + \beta, \vec{x}). \tag{2.1.25}$$

The simple case that it is possible to compute from (2.1.21) is the black body radiation for a non-interacting gas made of quarks and gluons [Yagi05]. That means that $g = 0$ in the QCD action. The grand potential is then given by

$$\begin{aligned} \Omega_0(T, V, \{\mu_f\}) &= -T \ln \mathcal{Z}^0_{QCD}, \\ &= V \int \frac{d^3k}{(2\pi)^3} \Bigg[2(N_c^2 - 1) \left(\frac{E_g(k)}{2} + T \ln(1 - e^{-E_g(k)/T}) \right) \\ &\quad + 2N_c \sum_{f=1}^{N_f} \left(-\frac{E_{q_f}(k)}{2} - T \ln(1 + e^{-(E_{q_f}(k) - \mu_f)/T}) \right) \\ &\quad + 2N_c \sum_{f=1}^{N_f} \left(-\frac{E_{\bar{q}_f}(k)}{2} - T \ln(1 + e^{-(E_{\bar{q}_f}(k) + \mu_f)/T}) \right) \Bigg], \end{aligned} \tag{2.1.26}$$

where E_g, E_{q_f} and $E_{\bar{q}_f}$ are respectively the energy of the gluon, the f-quark and the f-antiquark; $E = \sqrt{k^2 + m^2}$ where m is the mass of the considered particle. Each line of (2.1.26) is composed by the zero-point energy [4] and the associated statistics. For the gluon (first line), we have a degeneracy factor $2(N_c^2 - 1)$, depending on the (spin) $\times$ (colour) degrees of freedom and we recognize the Bose-Einstein statistics. For the f-quark (second line) and the f-antiquark (third line), we have $2N_c$ degrees of freedom ((spin) $\times$ (colour)) and the Fermi-Dirac statistics with respectively μ_f and $-\mu_f$ as chemical potential.

If we assume massless particles and $\mu_f = 0$ in (2.1.26), we remain with

$$\frac{\Omega_0(T, V, \{0\})}{V} = -\frac{\pi^2}{90} T^4 \left[2(N_c^2 - 1) + \frac{7}{8} 4 N_c N_f \right]. \tag{2.1.27}$$

This equation is usually referred as the Stefan-Boltzmann (SB) limit and is conventionally used as a normalization for the thermodynamic quantities.

3. Remember that Γ_ν are the euclidean γ-matrices.
4. This latter can be fixed in an *ad hoc* manner and set to zero for convenience.

2.2 QCD phase transitions

2.2.1 Chiral symmetry restoration

Let us recall the equation (1.1.32):

$$\mathcal{L}_{QCD} = \mathcal{L}_{QCD}^{\text{chiral}} + \mathcal{L}_{QCD}^{\text{mass}}. \tag{2.2.1}$$

We have seen in Section 1.1.7 that the classical $\mathcal{L}_{QCD}$ is invariant under the $U_L(N_f) \times U_R(N_f)$ symmetry if the mass term is set to zero. Therefore, the chiral condensate $\langle \bar{q}q \rangle = \langle \bar{\psi}_L \psi_R + \bar{\psi}_R \psi_L \rangle$, which is proportional to the mass term, can be used as order parameter of the chiral symmetry restoration. Two cases can occur:

- If $\langle \bar{q}q \rangle = 0$, we are in the Wigner-Weyl phase and the chiral symmetry is restored,
- If $\langle \bar{q}q \rangle \neq 0$, we are in the Nambu-Goldstone phase and the chiral symmetry is broken.

At low temperature and baryonic potential, the QCD vacuum is made of quark/antiquark pairs which condensate. It is in analogy with Cooper pairs in superconductivity. As the magnitude of these quantities increase, these pairs are dissolved inside the medium and $\langle \bar{q}q \rangle \to 0$. The chiral symmetry is then restored. The estimated critical temperature T_χ, for this transition is between 165 and 190 MeV according to lQCD simulations while the value of μ_χ can not be obtained in lQCD up to now (see Section 2.3.4). Several approaches, as PNJL models, can be then used to characterize it. Such models will be discussed in Chapter 7.

2.2.2 Colour confinement/deconfinement phase transition

As mentioned in Chapter 1, QCD relies on two main features: the confinement and the asymptotic freedom. These two characteristics, encoded in the behaviour of the running coupling constant (see Fig. 1.3), are at the centre of our understanding of the confinement/deconfinement phase transition.

A deconfined phase can be reached either by increasing the temperature, or by increasing the baryonic potential. At low temperature and/or baryonic potential, hadrons such as pions, kaons *etc.*, govern the thermodynamics (confined phase). When these intensive variables increase and exceed some critical values, gluons and quarks becomes the real thermodynamic degrees of freedom (deconfined phase).

In order to understand what happens with an increase of the temperature, let us assume that it can be seen as a measure of the average energy inside the medium. When the energy (or an average of it) increases, the running coupling constant becomes smaller and smaller. At a certain point, called the critical temperature T_c, the strength of the interaction is no more sufficient to keep quarks and gluons confined. So, they can move freely. We are faced to new degrees of freedom inside the medium and the quark-gluon plasma (QGP) is formed.

In the baryonic potential case, it is more an effect of compression of the QCD matter that drives us to a deconfinement state. Indeed, increasing the baryonic potential means increasing the baryon density. Let us consider a large number of hadrons within a certain volume and let us start to compress it adiabatically at $T = 0$. The hadrons begin to overlap at a certain baryon density ρ_c. The distance between quarks and gluons are then really small. The running coupling constant is therefore in the asymptotic-freedom regime. A state of degenerate quark matter is reached.

2.2.3 The conjectured QCD phase diagram

A representation of the QCD phase diagram is given in Fig. 2.1.

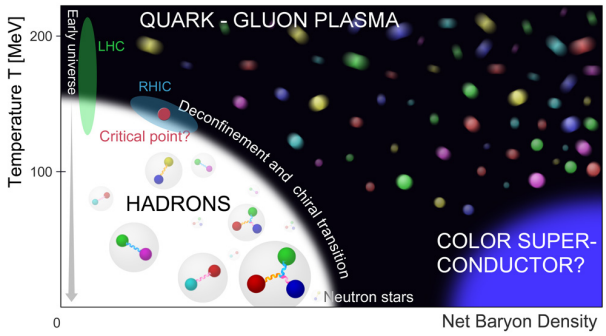

Figure 2.1: Conjectured QCD phase diagram [Jicf].

It is important to stress on the fact that it is a theoretical conjecture since only few points are given by heavy ion experiments (see Section. 2.4). The quantitative features as well as the orders of the phase transitions for the different regimes (T, μ) are not well-determined. Several phases are expected as the QGP at large temperature and the neutron-star core and colour superconductor regimes at large baryonic potential.

2.3 Lattice QCD

In the section, we will summarily introduce lQCD at finite temperature and chemical potential following [Yagi05, Gatt10]. We will be much more interested in the results for the confinement/deconfinement phase transition since it will be a comparison point for the approach that we have developed in Chapter 5.

2.3.1 Extension at finite temperature

We have seen in Section 1.2 how the QCD action is discretized on a lattice. The extension at finite temperature is based on the same procedure apart from the fact that the time-integration has finite boundaries in order to reproduce the QCD partition function given in (2.1.21).

In this vision, working in QCD as described in Chapter 1, formally at $T = 0$, means that we are interested in results in the infinite space-time volume limit. The finite size effects are just deviations of what we would like to obtain. At finite temperature, the space volume is still formally infinite, but the physical extent of the euclidean time is limited to $1/T$.

The temperature and the spatial volume can be defined, in terms of lattice parameters, by the following relations

$$\frac{1}{T} = N_t\, a, \qquad V = (N_s\, a)^3, \tag{2.3.1}$$

where a is the lattice spacing of the hyper-cube with N_t (N_s) temporal (spatial) sites. It comes naturally from (2.1.24) and (2.1.25) that the link variable and the quark field have to respect the following boundary conditions:

$$U_\mu(n_0 + N_t, \vec{n}) = U_\mu(n_0, \vec{n}), \tag{2.3.2}$$

$$q(n_0 + N_t, \vec{n}) = -q(n_0, \vec{n}). \tag{2.3.3}$$

The fact that the temporal extent is kept finite implies discrete Matsubara frequencies [LeBe96]. Indeed, if we apply a Fourier transformation to the finite time direction, we remain with discrete energy levels:

$$\omega_n = 2n\,\pi T \quad \text{for gluons,} \tag{2.3.4}$$
$$= (2n+1)\,\pi T \quad \text{for quarks and antiquarks.} \tag{2.3.5}$$

On lattice, the Matsubara frequencies are not only discrete but also limited to the range $[-\pi/a, \pi/a]$.

2.3.2 Polyakov loop

Let us first focus on the SU(N_c) gauge theory without dynamical quarks (*i.e.* $N_f = 0$). We introduce here an important observable: the Polyakov loop $L(\vec{x})$ defined by

$$L(\vec{x}) = \mathcal{P} e^{ig\int_0^{1/T} d\tau A_0(\tau,\vec{x})}, \tag{2.3.6}$$

and discretized on lattice as [5]

$$\phi = \frac{1}{N_c}\mathrm{Tr}\prod_{j=0}^{N_t-1} U_0(j,\vec{x}). \tag{2.3.7}$$

The expectation value of the Polyakov loop can be interpreted as the probability to observe a single static infinitely heavy quark at point $\vec{x}$ in a pure-gauge system. It is proportional to

$$|\langle\phi\rangle| \sim e^{-F_q/T}, \tag{2.3.8}$$

where F_q is the free energy of the quark. This one thus acts as a probe to see if the system is in a confined or a deconfined phase. Indeed, in the confined phase, the probability to observe a single quark is nul since its free energy tends to infinite. In the deconfined phase, the quark free energy is finite and $|\langle\phi\rangle| \neq 0$.

In summary, the Polyakov loop can be used as an order parameter to characterize the confinement/deconfinement phase transition in pure-gauge theory:

Confined phase	$T < T_c$	$\lvert\langle\phi\rangle\rvert = 0$	$F_q \to \infty$
Deconfined phase	$T > T_c$	$\lvert\langle\phi\rangle\rvert \neq 0$	F_q is finite

Usually, the change in value of an order parameter is associated to a change of the symmetry underlying the system; This latter can be broken or restored in function of it. As we see hereafter, we can also interpret the QCD pure-gauge phase transition in terms of the breaking or not of the $Z(3)$ centre symmetry of SU(3).

Let us consider the SU(N_c) gauge transformation Ω:

$$\Omega(\tau + 1/T, \vec{x}) = z\,\Omega(\tau,\vec{x}), \tag{2.3.9}$$

5. On lattice, the Polyakov loop is traced over colour indices. (2.3.6) and (2.3.7) will be indifferently called Polyakov loop.

where z is an element of the centre [6] of SU(N_c), that is to say an element of $Z(N_c)$ [7]. So, we have

$$\begin{aligned} A^{\Omega}_{\mu}(\tau + 1/T, \vec{x}) &= \Omega(\tau + 1/T, \vec{x}) \left(A_{\mu}(\tau + 1/T, \vec{x}) - \frac{i}{g}\partial_{\mu} \right) \Omega^{\dagger}(\tau + 1/T, \vec{x}), \\ &= z\, A^{\Omega}_{\mu}(\tau, \vec{x})\, z^{\dagger} - \frac{i}{g} z\, \partial_{\mu} z^{\dagger}, \\ &= A^{\Omega}_{\mu}(\tau, \vec{x}). \end{aligned} \tag{2.3.10}$$

The gauge field is thus invariant under (2.3.9). However, the Polyakov loop is not since

$$L(\vec{x}) \rightarrow z\, L(\vec{x}). \tag{2.3.11}$$

A zero value of the Polyakov loop means that the $Z(N_c)$ centre symmetry is realized unlike a non-zero value means that this symmetry is broken. Two cases for the pure-gauge phase transition can be then imagined: either first or second-order [8] phase transition. It can be shown that the situation depends on the colour number [Yagi05]. If $N_c = 2$, it is a second-order phase transition, while if $N_c \geq 3$, it is a first-order one.

When quarks are added, the $Z(N_c)$ symmetry is explicitly broken at the level of the action. The Polyakov loop can not be formally used as order parameter. The confinement/deconfinement phase transition is much more seen as a crossover.

2.3.3 Thermodynamic properties of the confinement/deconfinement phase transition

On lattice, some thermodynamic quantities can be computed such as the pressure p, the energy density ϵ, the entropy s, or the trace anomaly $\Delta = \epsilon - 3\,p$, by using a discretized version of the usual relations given in Section 2.1.1. Several comments can be done from the results.

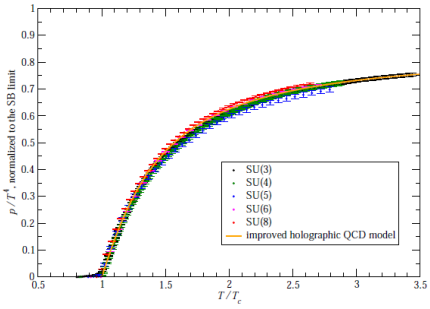

Figure 2.2: Pressure normalized to the SB limit p/p_{SB} versus T/T_c, obtained from simulations of SU(N_c) lattice gauge theories on $N_t = 5$ lattices. Error bars denote statistical uncertainties only. The results corresponding to different gauge groups are presented by different colours, according to the legend [Pane09].

In Fig. 2.2 and Fig. 2.3, we can notice that the pressure is far from the SB limit (see (2.1.27)) in the considered temperature range, meaning far from the non-interacting gas with massless particles. The SB

6. The centre of a group is the set of elements in the group which commute with all the elements of the group.
7. $Z(N_c)$ is the group of unity roots: $z = e^{2\pi i\, n/N_c}\mathbb{1}$ with $n = 0, 1, \ldots, N_c - 1$.
8. A first (second) order phase transition is a discontinuity in the first (second) derivative of the partition function.

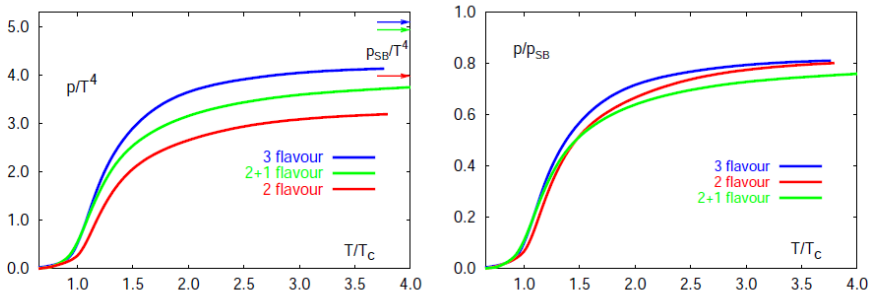

Figure 2.3: (Left) Pressure normalized to T^4 and determined from lattice simulations [Kars00] for QCD with two or three light quarks or two light and one heavy quarks (2 + 1) calculated with the p4-action versus T/T_c. The arrows indicate the SB limit for two- and three-flavour QCD with quarks of mass $m/T = 0.4$ as well as the case of two-flavour QCD with $m/T = 0.4$ and an additional heavier quark of mass $m_s/T = 1$. (Right) p/p_{SB} versus T/T_c.

pressure is expected to be reached at very high temperature as it is suggested by the asymptotic-freedom property. In Fig. 2.3, we can observe that the hierarchy of the pressure naturally follows the number of degrees of freedom present inside the plasma. However, when the pressure is normalized to the SB limit, the situation changes and the curves are nearly superimposed. It is also worth mentioning the determination of T_c, which depends of the number of quark flavour present inside the plasma. Indeed, for the pure-gauge sector, lattice computations find that $T_c \approx 270$ MeV, while when quarks are added, T_c is between 130 and 200 MeV.

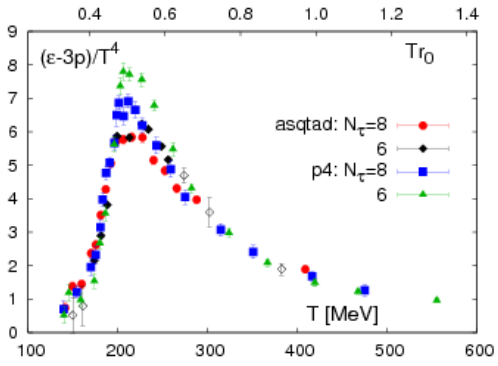

Figure 2.4: Δ/T^4 calculated on lattices with temporal extent $N_t = 6, 8$. Asqtad and p4 are two different prescriptions for the fermionic action. The upper x-axis shows the temperature scale in units of the scale parameter r_0 which has been determined in studies of the static quark potential. The lower x-axis gives the temperature in MeV [Baza09].

In Fig. 2.2, the pure-gauge pressure is computed for different SU(N_c) gauge groups. Normalized quantities seem to be superimposed. This behaviour will be also investigated within our approach in Chapter 5.

It suggests that the role of the gauge structure leads mainly to an overall statistical factor given by a correct counting of the freedom degrees.

Finally, let us conclude this section by an analysis of the trace anomaly. In the SB case, this latter must be simply equal to zero. In Fig. 2.4, we can observe that it has its maximum of deviation from the SB limit around T_c and tends to zero at high temperature. It enforces the fact that strongly-interacting effects play an important role around T_c and that the interactions are gradually turned off at high temperature. This is expected since the running coupling constant of QCD is small at large temperature and a picture of non-interacting gas of quarks and gluons should be justified [Buis10a].

2.3.4 Introduction of the chemical potential

The chemical potential is introduced within the fermionic euclidean action given in (2.1.23). For our purposes, we schematically rewrite it [Yagi05] :

$$\mathcal{L}_E^f = \sum_{f=1}^{N_f} \bar{\psi}_f \left[\Gamma^0(\partial_0 - i(gA_0 - i\mu_f)) + \Gamma^i D_i + m_f\right] \psi_f. \tag{2.3.12}$$

It implies that the temporal gauge potential acquires an extra imaginary part. Indeed,

$$gA_0 \to gA_0 - i\mu_f. \tag{2.3.13}$$

Although it is formally simple to introduce the chemical potential, the task is hard on lattice. Because of the replacement (2.3.13), the fermionic lattice determinant Det $F(U;\mu_f)$, becomes complex for $N_c = 3$. MC simulations are thus not well-justified since the probability given in (1.2.19) is not well-defined. We are faced of what we call *the complex phase problem*.

Also for $\mu_f = 0$, we have some troubles with Det $F(U;\mu_f)$ since it can be either a positive or a negative real. It is called *the sign problem*. However, when N_f is even and the quark masses (m) are degenerate, we have $(\text{Det } F(U;0))^{N_f}$ and the sign problem does not appear. Also when $m \gg \mu$, Det $F(U;\mu_f)$ barely changes its sign and computations at low chemical potential are still possible. This is not the case at finite and large μ_f.

Several approaches are used to overcome the problem. We can mention, for the record, the reweighting method or the imaginary-μ_f computations, for instance (see [Yagi05] and references therein).

2.4 Heavy ion collision experiments

Heavy ion collisions are experiments that consist to collide heavy ion beams in order to produce a thermalized partonic [9] medium and so, to study QGP. Such experiments started at the end of 1980s at BNL-AGS (Alternating Gradient Synchrotron) and at CERN-SPS (Super Proton Synchrotron). During these first experimental rounds, AGS accelerated beams of ^{28} Si at 14 GeV per nucleon, while SPS reached an energy of 200 GeV per nucleon for ^{32} Si, and then, 158 GeV per nucleon with ^{208} Pb. These conditions were already favourable to produce QGP. During 2000s, BNL-RHIC supplanted these preliminary experiments and gold ions were used. The center-of-mass energy per nucleon pair was around 200 GeV. Nowadays CERN-LHC holds the energy record with Pb-Pb collisions and almost 8 TeV per nucleon.

The main difficulty in such experiments, other than to reach higher and higher center-of-mass energy, lie in the manner of extracting the information. Indeed, the QGP is confined in a really small space volume and

9. The term “parton”was originally used by Feynman. It is a generic word to designate quarks and gluons.

the lifetime does not exceed 10^{-23} s. It is thus not possible to directly observe the QGP. However, the QGP leaves us some signatures of its formation as, for example, the jet quenching, the azimuthal anisotropy, the J/ψ suppression and the strange-particle production. Without entering into too much technical details (since it is not the purpose of this thesis), we will try to give a brief overview of the main experimental results in this section. For more details, interested readers can refer to [Frim11, Sark10].

2.4.1 Jet quenching

We have seen in Section 1.3 that collisions of ultra-high-energy particles involving partons produce jets. This is due to the hadronization. However, during heavy-ion collisions, if the QGP is created, these jets interact strongly with the hot and dense partonic medium: High-momentum partons produced in the initial state of the nucleus-nucleus collision undergo multiple interactions and lose energy. It leads to a remarkable reduction of the jet energy. This phenomenon is called the *jet quenching*.

RHIC experiments observed the first evidences of this parton energy loss from the suppression of high-p_T (transverse momentum) particles, while in November 2010, CERN announced its first direct observation of jet quenching after only three weeks of runs (see Fig. 2.5).

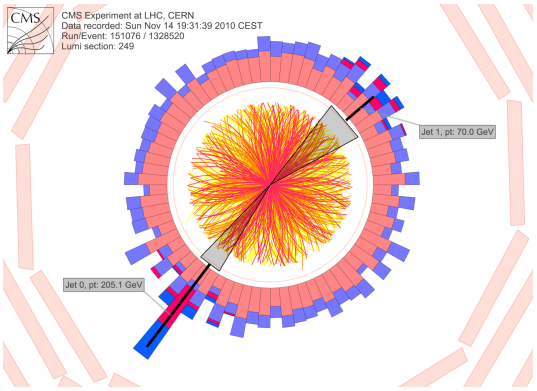

Figure 2.5: LHC lead-lead collision in the CMS detector showing particles (yellow and red tracks) radiating from the collision point. The particles deposit their energy in the calorimeters (salmon, mauve, red and blue towers, with a height proportional to energy). Two back-to-back jets are seen with a large energy asymmetry, as expected from the jet-quenching mechanism [CERN] (2010).

2.4.2 Azimuthal anisotropy and elliptic flow

In relativistic heavy-ion collisions, a very huge number of particles are produced in all directions. The momentum, the energy and the particle distributions naturally vary with the direction and give us some important experimental information about the behaviour of matter.

To study QGP, we are particularly interested in non-central heavy-ion collisions. In this case, the ions do not collide face to face and only some nucleons participate in the collision while the others are spectators. Moreover, such collisions generate asymmetries in the geometry of the system and these initial spatial asymmetries within the nuclear overlap affects the transverse momentum distribution of particles. In such experiments, an azimuthal momentum space anisotropy of the particle emissions in the plane transverse to

the ion beam is observed. It can be characterized by the second harmonic coefficient of the azimuthal Fourier decomposition v_2, which is called the elliptic flow.

Since the elliptic flow directly reflects the initial spatial anisotropy, it is especially sensitive to the early stages of the system evolution, that is to say the formation of the QGP. The elliptic flow is thus a fundamental observable to characterize QGP and it is one of the key observations done by RHIC and LHC.

Using relativistic hydrodynamics and transport coefficient, it was extracted from elliptic flow measurements that the QGP behaves like a nearly perfect liquid with a small ratio shear viscosity over entropy (η/s) around T_c. This means that the strong interactions remain important in this region of temperature. Indeed, instead of dissipating randomly, as expected in a gas, the particles tend to move collectively (like a liquid flow) in response to the pressure gradient generated by the initial spatial asymmetry. Moreover, unlike ordinary liquids, in which individual molecules move about randomly inside the collective modes, QGP seems to move in a way in which a high degree of coordination among the particles is required. It is the notion of "nearly perfect fluid".

It is also worth adding that the connection between the $\mathcal{N} = 4$ supersymmetric $SU(N)$ Yang-Mills theory at large N and the classical ten-dimensional gravity on the background of black three-branes allows one to perform analytical calculations in a strongly coupled four-dimensional gauge theory. In particular, the ratio η/s has been computed in [Poli01]. Moreover, η/s has been also calculated using the AdS/CFT correspondence [10]. It suggests that in all thermal field theories in the regime described by gravity duals [Kovt04],

$$\frac{\eta}{s} = \frac{1}{4\pi}. \tag{2.4.1}$$

More generally, all known fluids or gas in nature are expected to follow

$$\frac{\eta}{s} \geq \frac{1}{4\pi}. \tag{2.4.2}$$

2.4.3 J/ψ suppression

In the usual proton-proton collisions, c and $\bar{c}$ are bound together in order to form the J/ψ. The mean lifetime of such bound states is at the order of 10^{-21} s. This is quite huge for strong interaction processes ($\sim 10^{-23}s$). This can be explained by the fact that the hadronic decay modes of the J/ψ are strongly suppressed because of the OZI Rule. Therefore, electromagnetic decays begin to compete with hadronic ones. This is why the J/ψ has a significant branching fraction to leptons and annihilates in a lepton/antilepton pair (whose $\mu^+\mu^-$).

At the energy range in which we are interested in heavy-ion collisions, $c\bar{c}$ pairs can be quite easily created. However, they are produced inside a medium which screens the colour interaction. This causes the J/ψ suppression [Mats86] since it will be more difficult for a c and a $\bar{c}$ to bound together. This phenomenon were observed in NA38 and NA50 experiments at CERN.

2.4.4 Strange-particle production

In heavy-ion collision regime, the energy density is sufficiently high to produce heavier quarks as s and c. As explained in the previous section, the strong interaction is screened by the medium and such particles are then able to move quasi-freely inside the medium up to the beginning of the hadronization phase (*i.e.*

10. The AdS/CFT correspondence is a conjectured duality between closed string theory in Anti-de Sitter (AdS) space and conformal field theory (CFT) in Minkowski space [Mald98].

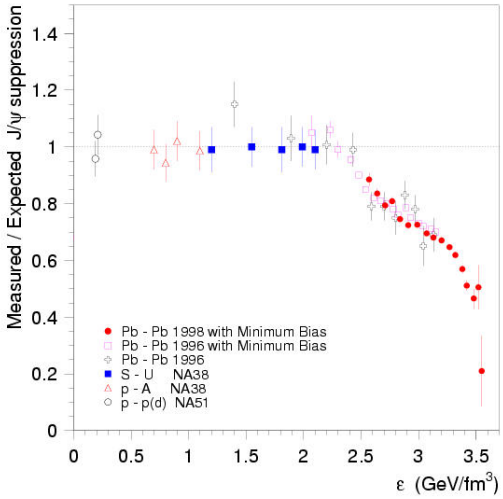

Figure 2.6: Measure of the J/ψ production normalized by the ordinary nuclear absorption as a function of the energy density (Abreu *et al.*, 2000)

when the medium is cooled). Since the strange production is higher within the QGP, the strange hadrons are then expected to be more numerous [Rafe82]. This phenomenon were observed in heavy-ion experiments.

2.5 Quasiparticle approaches

As we have just seen, the QCD phase transitions are intensively studied in experiments through heavy ion collisions while lQCD deeply investigates QCD at finite temperature and baryonic potential. Among all the other approaches used to study QCD under extreme conditions, quasiparticle ones will deserve our attention. Indeed, they are part of phenomenological models used to describe the different QCD phases. Such models have the advantage to give some intuitions concerning the physics underlying the different regions of the QCD phase diagram.

Quasiparticle approaches have their origin in the experience gained from the study of phase transitions in solid state physics. In these models, the particles acquire effective masses generated through the interactions with the other constituents inside the medium. The basic idea is the following: If a large part of the interactions can be included into the effective masses, then the matter under study can be described thanks to a gas of quasiparticles moving freely or interacting only weakly.

This assumption was applied in QCD within many studies such as [Gore95, Leva98, Pesh96]. In these latter references, the used thermal masses are usually based on perturbative calculations carried out in the Hard Thermal Loop (HTL) scheme [Braa90]. The gluon and quark thermal masses are thus given by

$$m_g^2(T) = (N_c + T_R N_f)\frac{g^2 T^2}{6} + T_R N_f \frac{g^2 \mu^2}{2\pi^2}, \tag{2.5.1}$$

$$m_q^2(T) = \frac{C_R g^2}{4}(T^2 + \frac{\mu^2}{\pi^2}), \tag{2.5.2}$$

where all the symbols entering its formula are detailed in Section 1.1.6. Note that in [Buis10a], such thermal masses were also used to build a quasiparticle approach allowing to compute the EoS of a generic gauge theory with gauge group $SU(N_c)$ and quarks in an arbitrary representation.

However, these quasiparticle models are only expected to correctly reproduce the physics of the QCD matter at very high temperature. Indeed, according to experimental evidences, such as collective flow [Stoe05], the non-perturbative interactions are still important around T_c. Moreover, it has be shown in [Plum11] that the behaviour of the quasiparticle thermal masses directly extracted from lQCD EoS is compatible with perturbative HTL calcultations ($m \sim T$) from $T \approx 2T_c$ while an increase of the thermal masses is observed when the temperature is down, reaching T_c.

In order to account non-perturbative effects, some quasiparticle models are completed by adding a so-called bag constant to the pressure [Leva98]. Such a constant has to be temperature-dependent, in order to ensure the thermodynamic consistency. Indeed, when a quasiparticle thermal mass is introduced at the level of the Hamiltonian of the system, thermodynamic relations must be adapted in order to ensure the respect of the thermodynamic laws, as for instance (2.1.8). Different procedures have been proposed to treat such systems, see for instance [Golo93, Gore95]. Their common point is to keep invariant one of the thermodynamic relations, for example the pressure or the entropy, and to modify the other thermodynamic quantities in order to respect the thermodynamic laws. It is worth adding that in [Brau09], the authors briefly reviewed these different procedures and proposed a new formulation where the expression of the thermodynamic quantities remain invariant but where the Lagrange's multiplier β is no longer equal to T^{-1}. Ensuring the thermodynamic consistency of the results is a procedure that is not uniquely defined and is still a matter of debate.

On another hand, there exists some works in which the thermodynamics of the strongly-coupled region around the phase transition, is studied by taking into account the possible existence of bound states beyond T_c [Bann95, Gelm06, Liao06, Shur04]. In particular, in [Shur04], they have studied the different binary bound states (mostly coloured) that can be formed in the plasma beyond T_c: gg, gq, qq, on top of the usual $\bar{q}q$ mesons. The study was done by using Klein-Gordon equation whose the potential is the internal energy directly extracted from the lQCD free energy between heavy quarks in the singlet channel (obtained by the Bielefeld group) and by assuming a Casimir scaling in order to deal with all the other coloured states. Then, they have estimated their contributions to the bulk thermodynamics by adding bound states as free additional species to the EoS. A good agreement with lQCD data was found. The contribution of bound states seems to be significant between 1-3 T_c even if the main contribution to the total pressure is due to unbound quasiparticles.

Within Chapter 5, we propose to the reader a new quasiparticle approach to describe the QCD medium beyond T_c. Its peculiarity is to explicitly and non-perturbatively take into account the interaction between quasiparticles thanks to the use of the Dashen, Ma and Bernstein formalism of statistical mechanics; This interaction may lead to the formation of bound states within the plasma.

Chapter 3

Thermodynamics of the Confined Phase

Now that we have sketched the background of this thesis, we can get into the various approaches we have studied and/or developed in order to better understand the different regions of the conjectured QCD phase diagram presented in Section 2.2.3. In this chapter, we will be interested in what happens below T_c and we will mainly focus on a thermodynamic description of the confined phase.

As we will show it, it is possible to describe the equations of state (EoS) provided by lQCD thanks to the use of a Hadron Resonance gas (HRG) model. This will be discussed in the pure-gauge and in the 2 + 1 QCD plasma following respectively the papers of [Meye09] and [Bors10, Kars03].

Then, we will present our original work [Buis11b]. This latter consists to generalize to an arbitrary simple gauge algebra the Meyer's proposal [Meye09] of modelling the Yang-Mills (YM) matter by an ideal glueball gas in which the high-lying glueball spectrum is approximated by a Hagedorn spectrum of closed-bosonic-string type.

3.1 Hadron Resonance Gas model and Hagedorn spectrum

At low temperature, in the confined phase, the low-lying glueballs are the relevant degrees of freedom of the YM matter while the QCD matter is dominated by pions. As the temperature T increases (but still below T_c), heavier states become more relevant and need to be taken into account. These two situations can be modelled in a first approximation by an ideal gas of hadrons and their resonances, assuming that the residual interactions between the colour-singlet [1] states are weak enough to be neglected [Dash69]. For the pion gas, this assumption is supported by the Goldstone's theorem which implies weak interactions between pions at low energies. For the glueball one, it emerges from a strong coupling expansion in the case of large-N_c SU(N_c) YM theory [Lang10], where glueballs are exactly non-interacting since their scattering amplitude scales as $1/N_c^2$ [Witt79].

To compute thermodynamic quantities with a HRG model, we have to express the partition function $\mathcal{Z}(T,V,\mu)$ (see (2.1.3)) with the above hypothesis. Thus, $\ln \mathcal{Z}(T,V,\mu)$ is a sum over one-particle partition functions $\ln \mathcal{Z}^1(T,V,\mu)$,

$$\ln \mathcal{Z}(T,V,\mu) = \sum_i \ln \mathcal{Z}_i^1(T,V,\mu), \tag{3.1.1}$$

1. The colour-singlet representation, appearing in some peculiar tensor products of the (anti)quark and gluon representations, is the only gauge-group representation allowed below T_c because of the confinement property.

where the summation over i means that we have formally to include all the hadrons and their resonances. For a hadron of mass m_i and d_i degrees of freedom, $\ln \mathcal{Z}_i^1(T,V,\mu)$ reads

$$\ln \mathcal{Z}_i^1(T,V,\mu) = \frac{d_i\, V}{2\pi^2} \int_0^\infty dp\, p^2 \eta \ln(1+\eta e^{-\beta(E_i-\mu)}), \tag{3.1.2}$$

with $E_i = \sqrt{p^2+m_i^2}$ and $\eta = -1$ for bosons and $+1$ for fermions.

Of course, it is difficult to properly count all the states. Indeed, from experimental point of view, information about resonances above 3 GeV is still lacking. That is the reason why a Hagedorn spectrum is often used to describe the high-lying hadronic matter [Hage65]. Such spectrum has the following form:

$$\rho(m) \propto m^a\, \mathrm{e}^{m/T_h} \text{ with } a, \text{ real.} \tag{3.1.3}$$

So, the number of hadrons with a certain mass m is found to increase as $\rho(m)$ and the thermodynamic quantities, using such spectrum, are then undefined for $T > T_h$, the Hagedorn temperature. Therefore, T_h is a limiting temperature for a gas with hadronic degrees of freedom. Other degrees of freedom are then needed at higher temperatures, it is thus tempting to guess that $T_h \approx T_c$ and that the new degrees of freedom are deconfined quarks and gluons.

Although the current lattice studies agree on a value of T_c in the range $(150-200)$ MeV when $2+1$ light quark flavours are present [Bors10, Chen06], there is currently no consensus concerning the value of T_h. Indeed, to reach values of T_h as low as 200 MeV demands an *ad hoc* modification of $\rho(m)$: By introducing an extra parameter m_0 and setting $\rho(m) \propto (m^2+m_0^2)^{a/2}\, \mathrm{e}^{m/T_h}$, one can reach values of T_h in the range $(160-174)$ MeV, that agree with lattice computations, see *e.g.* [Cley11, Hage68]. However, by taking the original form $m_0 = 0$, one rather ends up with values of T_h around $(300-360)$ MeV, see [Bron04, Dien94]. Moreover, it has been observed in some pure-gauge lattice simulations with the gauge algebra $\mathfrak{su}(N_c)$ that $T_c \lesssim T_h$ [Brin06, Luci05] as intuitively expected. It has to be said that the value of T_h and its relation to T_c are still a matter of debate.

Finally, it is worth mentioning that open strings as well as closed strings naturally lead to a Hagedorn spectrum, see *e.g.* [Zwie04]. Modelling mesons as open strings is a way to make appear a Hagedorn spectrum in QCD [Cohe06]. The question of showing that a Hagedorn spectrum arises from QCD itself is still open but, under reasonable technical assumptions, it has recently been found in the large-N_c limit of QCD [Cohe10]; Glueballs and mesons have a zero width in this limit.

3.2 Thermodynamics of the 2 + 1 QCD plasma

In this section, we summarize the results of different lattice collaborations that compare their thermodynamic observables with the ones obtained within a HRG model. The point of this discussion is to illustrate the compatibility between lQCD data and such models.

The first analysed results are the ones proposed in [Kars03]. In this paper, they compare their data for 2 + 1 quark flavours with a HRG model in which meson and baryon resonances are taken into account up to 1.8 and 2 GeV respectively [PDG]. This means 1026 resonances. As it can be observed in Fig. 3.1, their results match very well with the HRG model previously described. However, it is important to point out that since this study dates from 2003, physical quark masses were not yet reached by lQCD.

This is nowadays the case. That is the reason why we also analyse [Bors10]. In this paper, the lQCD data obtained by the BMW (Budapest-Marseille-Wuppertal) collaboration, in which physical quark masses are reached, are compared with the hotQCD collaboration ones using a HRG model including meson and

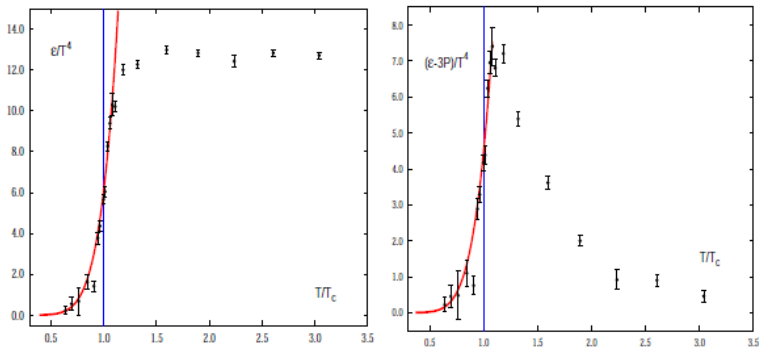

Figure 3.1: (Left) The figure shows the energy density ϵ in units of T^4 calculated on the lattice with (2+1) quark flavours as a function of the T/T_c ratio. The vertical lines indicate the position of the critical temperature. (Right) The figure represents the corresponding results for the reduced trace anomaly $(\epsilon - 3p)/T^4$. The full lines are the results of the HRG model that accounts for all mesonic and baryonic resonances. This figure is extracted from [Kars03].

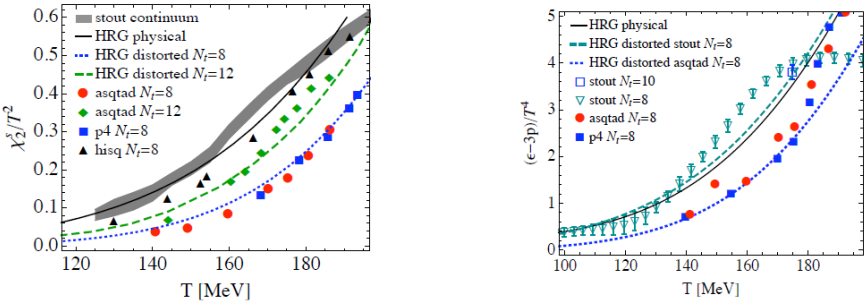

Figure 3.2: (Left) Strange quark susceptibility as a function of T. Full symbols correspond to results obtained with the asqtad, p4 and hisq actions [Baza09, Baza10]. The continuum result [Bors10] is indicated by the gray band. The solid line is the HRG model result with physical masses. The dashed and dotted lines are the HRG model results with distorted masses corresponding to $N_t = 12$ and $N_t = 8$, which take into account the discretization effects and heavier quark masses, which characterize the results of the hotQCD Collaboration. (Right) $(\epsilon - 3p)/T^4$ as a function of T. Open symbols are the results from [Bors10]. Full symbols are the results for the asqtad and p4 actions at $N_t = 8$ [Baza09]. Solid line: HRG model with physical masses. Dashed lines: HRG model with distorted spectra. This figure is extracted from [Bors10].

baryon resonances up to 2.5 GeV. As it can be shown in Fig. 3.2, the BMW results are in agreement with this HRG model while for hotQCD data, some distorted one has to be used in order to take into account lattice artefacts as discretization effects and heavier quark masses.

Finally, the lesson of all this is that with a HRG model, lQCD thermodynamic observables are well interpolated. Non-interacting gas models of hadrons seem to reproduce the main features of the confined phase computed by lQCD.

3.3 Thermodynamics of the pure-gauge sector

In the pure-gauge sector, the SU(3) EoS computed on the lattice have been shown to be compatible with a glueball gas model in which the high-lying spectrum is modelled by the density of states of a closed bosonic string [Meye09].

As mentioned in Section 3.1, the glueball gas picture implies that the total pressure p, should be given by

$$p = \sum_{J^{PC}} p_0(2J+1, T, M_{J^{PC}}), \tag{3.3.1}$$

where the sum runs on all J^{PC} glueball states of the SU(3) YM theory and where [Meye09]

$$p_0(d, T, M) = \frac{d}{2\pi^2} M^2 T^2 \sum_{j=1}^{\infty} \frac{1}{j^2} K_2(j\, M/T) \tag{3.3.2}$$

is the pressure associated with a single bosonic species with mass M and d degrees of freedom. K_2 is a modified Bessel function.

Performing the sum $\sum_{J^{PC}}$ demands the explicit knowledge of all the glueball states, not only the lowest-lying ones that can be known from lattice computations or from effective approaches. To face this problem, it has been proposed in [Meye09] to express the total pressure of SU(3) YM theory as

$$p = \sum_{M_{J^{PC}} < 2M_{0^{++}}} p_0(2J+1, T, M_{J^{PC}}) + \int_{2M_{0^{++}}}^{\infty} dM\; p_0(\rho(M), T, M), \tag{3.3.3}$$

where the high-lying glueball spectrum (above the two-glueball threshold $2M_{0^{++}}$) is approximated by a closed-string Hagedorn density of states. In four dimensions [Zwie04, Meye09], this density reads

$$\rho(M) = \frac{(2\pi)^3}{27 T_h} \left(\frac{T_h}{M}\right)^4 \mathrm{e}^{M/T_h}. \tag{3.3.4}$$

The idea of modelling glueballs as closed fundamental strings was actually already present in the celebrated Isgur and Paton's flux-tube model, inspired from the Hamiltonian formulation of lQCD at strong coupling [Isgu85]. Moreover, it has also been shown within a constituent picture that, in the SU(3) case, a many-gluon state (typically more than three gluons in a Fock-space expansion) tends to form a closed gluon chain [Buis09].

In (3.3.4), T_h is the Hagedorn temperature, which reads in this case

$$T_h^2 = \frac{3}{2\pi} \sigma^{(f)}, \tag{3.3.5}$$

where $\sigma^{(f)}$ is the fundamental string tension, here defined as the slope of the static energy between two sources in the fundamental representation of a given gauge algebra.

Meyer has computed the entropy density, $s = \partial p / \partial T$, which is presented in Fig. 3.3. Several cases are displayed. If we only consider the low-lying glueballs, the curve is consistent at very low temperature

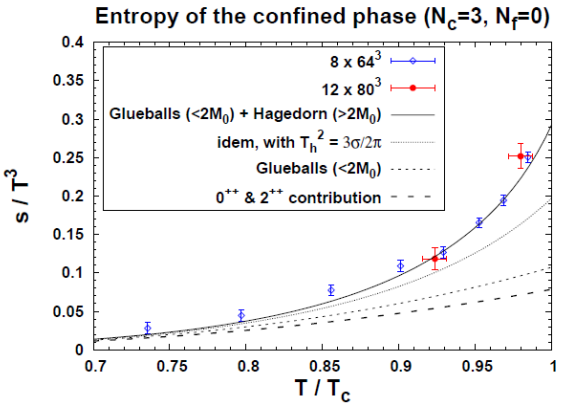

Figure 3.3: The entropy density in units of T^3 as a function of T/T_c [Meye09].

and fails to reproduce s when $T \to T_c$. We can also notice that the 0^{++} and the 2^{++} states account for about three quarters of the glueball contribution below the threshold. In this figure, we see in particular the importance of the high-lying spectrum inclusion. Lattice data are correctly interpolated by the addition of this spectrum to the low-lying glueballs. It appears that the best agreement is reached for $T_h/T_c = 1.069(5)$. What is striking is that the high-lying spectrum analytic form is completely predicted by free bosonic closed-string theory. The main thermodynamic features of the YM matter below T_c are thus well described with a non-interacting glueball gas and its resonances.

3.4 Generalization to any gauge algebra

Besides the SU(3) case, YM thermodynamics with an arbitrary gauge group is challenging too. A clearly relevant case is the one of $\mathfrak{su}(N_c)$-type gauge algebras, linked to the large-N_c limit of QCD. Moreover, a change of gauge algebra may lead to various checks of the hypothesis underlying any approach describing SU(3) YM theory. To illustrate this, let us recall the pioneering work [Svet82], suggesting that the phase transition of YM theory with gauge algebra $\mathfrak{g}$ is driven by a spontaneous breaking of a global symmetry related to the centre of $\mathfrak{g}$. Effective $Z(3)$-symmetric models are indeed able to describe the first-order phase transition of SU(3) YM thermodynamics [Pisa00]. However, a similar phase transition has also been observed in lattice simulations of G_2 YM theory [Pepe07] even though the centre of G_2 is trivial, meaning that the breaking of centre symmetry is not the only mechanism responsible for the deconfinement [2]. In this case, still under active investigation, studying different gauge algebras helps to better understand the general mechanisms of (de)confinement in YM theory.

3.4.1 Gauge-dependent quantities

In this section, we generalize to an arbitrary simple gauge algebra the aforementioned Meyer's proposal. We have thus to correctly identify the quantities that depend on the gauge group. There are essentially two things: the number of glueballs and the string tension.

2. For example, it is argued in [Diak11] that the YM phase transition for any gauge group is rather driven by dyons contributions.

For this latter, the Casimir scaling, which is an analytic prediction from the strong coupling expansion of the Wilson loop, says that the string tension is given by [Deld02, Shos03]

$$\sigma^R = C_2^R \, \Theta, \tag{3.4.1}$$

where the colour sources are in a given representation R of the gauge algebra, C_2^R is thus the value taken by the quadratic Casimir in the R-representation, and where Θ reads, in a lattice formulation of the theory [Deld02],

$$\Theta = \frac{g^2(a\Lambda)}{2a}. \tag{3.4.2}$$

a is the lattice spacing and $g(a\Lambda)$ is the running coupling with the renormalization scale Λ. Following well-known two-loop calculations, one can extract the explicit gauge-algebra dependence in the running coupling as follows: $g^2(a\Lambda) = \lambda(a\Lambda)/C_2^{adj}$ [Casw74], where λ is nothing else than the 't Hooft coupling when the gauge algebra is $\mathfrak{su}(N_c)$. One can finally define

$$\sigma^R = \frac{C_2^R}{C_2^{adj}} \, \sigma_0, \tag{3.4.3}$$

where σ_0, that can be interpreted as the adjoint string tension, does not depend explicitly on the gauge algebra. However, an implicit dependence in the renormalization scale Λ may be present. Throughout this work we consider a gauge-algebra independent value for Λ.

The structure of the low-lying glueball spectrum for an arbitrary simple gauge algebra has been discussed in detail in [Buis11a] within a constituent picture. Let us recall here those results:

- The lightest glueballs are the scalar, pseudoscalar and tensor ones, whose masses are ordered as $M_{0^{++}} < M_{2^{++}}$, $M_{0^{-+}}$ in agreement with lattice results in the $\mathfrak{su}(N_c)$ case [Morn99, Luci10]. Those states are found to be lighter than $2\,M_{0^{++}}$ in these last works. Note that it has been proved in [West96] that the 0^{++} glueball is always the lightest one in YM theory.

- At masses typically around (3/2)$M_{0^{++}}$, states that can be seen as mainly three-gluon ones in a Fock-space expansion appear: They can have $C = +$ for any gauge algebra, but $C = -$ for $\mathrm{A}_{r\geq 2}$ ($\mathfrak{su}(N_c \geq 3)$) only. In this last case, the 1^{+-} glueball is still lighter than $2\,M_{0^{++}}$ [Morn99, Luci10].

- Higher-lying states (containing more than three gluons in a Fock space expansion) obviously exist, but their exhaustive study cannot be performed explicitly, eventually justifying the use of a Hagedorn spectrum. An important remark has nevertheless to be done: If all the representations of a given gauge algebra are real, the gluonic field A_μ is its own charge-conjugate, forbidding $C = -$ glueball states. This happens for the algebras A_1, $\mathrm{B}_{r\geq 2}$, $\mathrm{C}_{r\geq 3}$, $\mathrm{D}_{\mathrm{even}-r\geq 4}$ [3], E_7, E_8, F_4, and G_2.

It is worth noticing that a closed-string picture for high-lying glueballs is not only a consequence of Isgur and Paton's flux-tube-like approaches but may also be compatible with constituent approaches such as the one used in [Buis11a]: An excited closed string is then alternatively viewed as a closed chain of quasigluons where the quasigluons are linked by fundamental strings. In the case of E_8, the lowest-dimensional representation, that we have called fundamental before, is the adjoint one, so the closed-string picture seems less justified by comparison to a constituent picture. We therefore prefer not to investigate further the case of E_8 in the following.

3. Another nomenclature can be used. Indeed, the algebra class A_r can be also written $\mathfrak{sl}(r+1)$, $\mathrm{B}_{r\geq 2}$ is $\mathfrak{so}(2r+1)$, $\mathrm{C}_{r\geq 3}$ is $\mathfrak{sp}(2r)$ and $\mathrm{D}_{r\geq 4}$ is $\mathfrak{so}(2r)$.

3.4.2 Linking T_h to T_c

To continue, the link between T_h and T_c has to be fixed. A straightforward way to do it is to briefly recall Meyer's results in the pure-gauge SU(3) case [Meye09] (see Section 3.3). We have seen that the best agreement is reached for $T_h/T_c = 1.069(5)$. Finding $T_h > T_c$ is actually an indication that a metastable, superheated, hadronic phase of matter exists at temperatures between T_c and T_h; This phase has actually been studied on the lattice in [Brin06], where, for example, $T_h/T_c = 1.116(9)$ has been found for the gauge algebra $\mathfrak{su}(12)$, and discussed within the framework of an open-string model in [Cohe06].

From the above discussion, we realize that an accurate determination of the ratio T_h/T_c is of great phenomenological interest. However, such a study is not the main purpose of the present study, where we aim at giving reliable predictions for the EoS of YM theory with an arbitrary gauge algebra. As observed in [Meye09], typical values $T_h \approx T_c$ give very good results in fitting the lattice data. Setting $T_c = T_h$, as we will do in the rest of this work, means that the deconfinement temperature may be identified with the maximal allowed temperature for the confined hadronic phase. This assumption has two advantages. First, it will reproduce accurately the latest SU(3) lattice data of [Bors11] (see next section), and it is not in strong disagreement with current SU(N_c) results, where T_h is at most far from around 10% of T_c [Brin06, Luci05]. Second, it is applicable to any gauge algebra without having to guess a value for T_h/T_c, that can not be fitted on lattice results since no EoS is available for gauge algebras different from $\mathfrak{su}(N_c)$ so far. The drawback of this choice is that it forbids any discussion about a superheated hadronic phase in generic YM theories. Such a refinement of the model will rather be the topic of a separate study.

For completeness, we notice that the somewhat surprising value $T_h = 2.8\,T_c \gg T_c$ has been found in [Megi07] by using a Hagedorn picture too. The difference with our approach comes from the fact that, in [Megi07], T_h is fitted by assuming that the low-lying glueballs currently known from lattice simulations should exhibit a Hagedorn-type spectrum. On the contrary, we think here that the Hagedorn-like behaviour only appears in the high-lying sector, that mostly concerns the glueballs that are not known so far by lattice calculations, see (3.3.3).

3.4.3 Numerical results

According to standard SU(3) studies, it is relevant to set $\sigma_0 \approx (9/4)\ 0.2$ GeV^2, leading to T_h =309 MeV. The masses of the lightest glueballs are proportional to $\sqrt{\sigma_0}$ [Buis11a], so they can be thought as constant with respect to a change of gauge algebra in our approach. Consequently, the sum $\sum_{M_{JPC}<2M_{0^{++}}}$ should run on all the states below 3.46 GeV found in the SU(3) lattice work [Morn99]. There is an exception however: The 1^{+-} glueball, whose mass is below the two-glueball threshold, only exists when the gauge algebra is $\mathrm{A}_{r\geq 2}$ [Buis11a]; Hence its contribution will be omitted in the other cases. Concerning the Hagedorn spectrum, it is worth recalling that the density (3.3.4) is able to reproduce the SU(3) lattice EoS with $T_c \approx T_h$ [Meye09]. But $\rho(M)$ accounts for both the $C = +$ and $C = -$ glueballs. When the gauge algebra has only real representations, the $C = -$ sector is absent as said before. So in such cases, the substitution $\rho(M) \to \rho(M)/2$ will be done. The validity of this prescription has been explicitly checked in [Case11] by computing the EoS of $2+1$-dimensional YM theory below T_c with $\mathfrak{su}(N_c)$ gauge algebras: $\rho(M)$ correctly describes the data for $\mathfrak{su}(3-6)$, while $\rho(M)/2$ must be used for $\mathfrak{su}(2)$ in order to compensate for the absence of $C = -$ states in the theory.

We are now in position of explicitly computing the pressure (3.3.3) for any gauge algebra, E_8 excepted. We actually compute from p the trace anomaly using

$$\Delta = T^5 \partial_T \left(\frac{p}{T^4} \right). \tag{3.4.4}$$

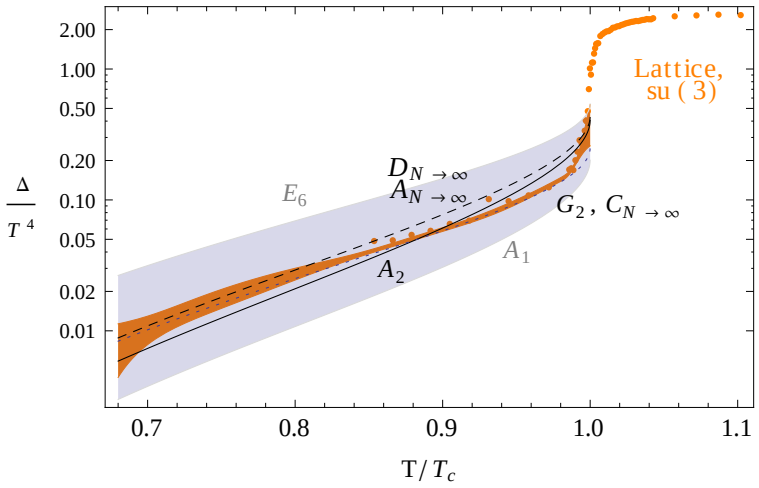

Figure 3.4: (Colour online) Trace anomaly below T_c, computed using Eqs. (3.3.3) and (3.4.4) with $T_h = T_c$ and $\sigma_0 = (9/4)0.2$ GeV^2, for the gauge algebras A_2 (solid line), $A_{N_c\to\infty}$ and $D_{N_c\to\infty}$ (dashed line), G_2 and $C_{N\to\infty}$ (dotted line). All the possible cases are located within the grey area, whose upper and lower borders are E_6 and A_1 respectively. SU(3) lattice data from [Bors11] are plotted for comparison (orange points and area). The orange points correspond to $N_t = 8$ data.

This above expression can be easily derived from the Euler relation (remember (2.1.8)) and is preferentially used in our computations. Our results are compared to the recent and accurate $\mathfrak{su}(3)$ lattice data of [Bors11], displayed in Fig. 3.4.3.

As a first check, we can see that the proposed model compares well with the SU(3) lattice data of [Bors11]. In a first approximation, the choice $T_c = T_h$ thus gives good results. A generic feature of p and Δ is that they are finite in T_h, and mostly located between the E_6 and A_1 cases at any T. This finiteness is due to the M^{-4} factor in (3.3.4) [Frau71], which is a consequence of the closed-string picture used here. Note that this finiteness is present in $2+1$ dimensions too [Case11]. An interesting feature is that the large-N_c limits of the A_{N_c} and D_{N_c} (when N_c is odd) cases are equivalent, in agreement with the large-N_c orbifold equivalence between $\mathfrak{su}(N_c)$ and $\mathfrak{so}(2N_c)$ YM theories, see *e.g.* [Cher11]. The large-N_c limit of the C_{N_c} ($\mathfrak{sp}(2N_c)$) case is however inequivalent to the A_{N_c} one, but equal to the G_2 case. The observed significant numerical differences between the gauge algebras are moreover relevant from a physical point of view since they come from changes in the structure of the glueball spectrum, mainly at the level of the allowed quantum numbers. Remember that the density of state $\rho(M)$, is divided by two for a class of gauge algebra that forbids $C = -$ glueballs.

To summarize, we have discussed a picture of YM matter that allows to compute its thermodynamic properties for any gauge algebra. In the confined phase, the relevant degrees of freedom are glueballs, whose low-lying states can be separately described, while the high-lying states are modelled by a closed bosonic string Hagedorn spectrum. Such a spectrum exhibits a Hagedorn temperature, above which hadronic matter ceases to exist: The partition function of a glueball gas with Hagedorn spectrum is not defined above T_h, suggesting a phase transition to a deconfined regime. The study of such regime for the YM matter as well as the full QGP will be in the centre of the following chapters.

Chapter 4

QCD Spectrum within a T-matrix Approach

The main goal of this chapter is to study and to solve two-body relativistic scattering problems in order to obtain the glueball and the meson spectra of QCD at zero and finite temperature.

The first section will aim to familiarize the reader with scattering problems. To make it simple, we will place in the framework of non-relativistic quantum mechanics and we will analyse the textbook case of a light particle that scatters on a heavy fix target. This study will allow us to define some central concepts as, for instance, the S-matrix, the T-matrix and the total cross-section. All these important notions will be introduced following [Tayl83]. Then, we will derive from the integral formulation of the usual Schrödinger equation, the Lippmann-Schwinger (LS) equations. Solving such equations is one of the possible ways to deal with scattering problems. It will be the main technical part of our work. Note that initially, we thought to address such problems by using the Lagrange-mesh method (LMM) and performing the resulting R-matrix elements. This way was finally given up. Nevertheless, it led us to develop the LMM in momentum space and to publish two referenced articles [Lacr11, Lacr12] summarized in Appendix D.

In the next section, we will study the two-body relativistic scattering problems. Formally, these ones are described within the quantum field theory. Feynman diagrams are used to represent schematically the interactions between particles and the scattering amplitudes are usually computed in perturbation theory. Unfortunately in QCD, the strength of the interaction is so strong that, at low energy (*i.e.* an energy at the order of the hadron masses), the perturbation theory fails. This problem is increased when one wants to analyse the hadron spectrum. Indeed, since particles are supposed to interact infinitely together in bound states, higher perturbative orders have to be considered. The formal way for addressing such processes is given by the Bethe-Salpeter (BS) equation. This one will be introduced following [Grei99].

Although the BS equation is exactly derived from the quantum field theory, it is really difficult to solve in practice. That is the reason why approximations must be done. We have chosen to work here within the Blankenbecler-Sugar (BbS) three-dimensional reduction scheme [Blan66]. This latter procedure leads to the resolution of a LS equation that will be computed thanks to the Haftel-Tabakin algorithm [Haft70]. These technical considerations will be explained in the third section.

Finally, our results for glueball and meson spectra will be presented in the fourth and fifth sections. The fourth one will be dedicated to the zero-temperature spectra while the fifth one will deal with temperature effects.

4.1 Non-relativistic scattering problems

4.1.1 General description

Let us consider the simple following process [Tayl83]: the elastic scattering of a spinless particle by a fixed target. Obviously, it is not a situation that happens inside a plasma since the particles are in random motion and multiple interactions can occur. However, it will help us to define the most important concepts encountered in all scattering problems without complicating them by taking into account too much details.

In quantum mechanics, the evolution of a particle within a potential $V(\vec{x})$, generated here by a fixed target is given by the time-dependent Schrödinger equation,

$$i\frac{\partial}{\partial t}|\Psi\rangle = H|\Psi\rangle, \tag{4.1.1}$$

where H is the Hamiltonian of the system. If H is time-independent, (4.1.1) admits stationary states of the form

$$|\Psi\rangle = e^{-iHt}|\psi\rangle \equiv U(t)|\psi\rangle, \tag{4.1.2}$$

where $U(t)$ is the evolution operator and $|\psi\rangle$ is a vector in the Hilbert space.

In a scattering problem, three different regions can be distinguished:

- the infinite-past region (before the collision, $t \to -\infty$),
- the interaction region (during the collision, $t \approx 0$),
- the infinite-future region (after the collision, $t \to +\infty$).

Well before the scattering, the particle is represented by a free wave packet since it is far from the interaction range. Therefore, $U(t)|\psi\rangle$ has to follow the infinite-past constraint:

$$U(t)|\psi\rangle \underset{t\to-\infty}{\longrightarrow} U^0(t)|\psi_{in}\rangle, \tag{4.1.3}$$

where $U^0(t) = e^{-iH_0t}$ with H_0, the free Hamiltonian and $|\psi_{in}\rangle$ is any incoming free state.
Similarly, after the scattering, the particle is also free and so, in the infinite-future region, we have

$$U(t)|\psi\rangle \underset{t\to+\infty}{\longrightarrow} U^0(t)|\psi_{out}\rangle, \tag{4.1.4}$$

with $|\psi_{out}\rangle$, any outgoing free state.

In the aforementioned case, we do not consider the possible formation of a bound state (*i.e.* here, the absorption of the particle by the target), it will be discussed later in Section 4.2. We assume that the potential $V(\vec{x})$ falls off sufficiently fast in order to admit the asymptotic free states, (4.1.3) and (4.1.4), as boundary conditions. Since $U(t)$ is an unitary operator, we can rewrite these boundary conditions as

$$|\psi\rangle = \lim_{t\to-\infty} U^\dagger(t)U^0(t)|\psi_{in}\rangle \equiv \Omega_+|\psi_{in}\rangle, \tag{4.1.5}$$

$$|\psi\rangle = \lim_{t\to+\infty} U^\dagger(t)U^0(t)|\psi_{out}\rangle \equiv \Omega_-|\psi_{out}\rangle, \tag{4.1.6}$$

where $\Omega_\pm$ are called the Møller wave operators.

Let us now define the scattering operator S as

$$|\psi_{out}\rangle = S|\psi_{in}\rangle. \tag{4.1.7}$$

Naturally $S = \Omega_-^\dagger \Omega_+$. S contains all the information about the scattering process and its matrix elements are linked to the probability w that a particle with an ingoing state $|\psi_{in}\rangle$, emerges in the detector with an outgoing state $|\psi_{out}\rangle$:

$$w\left(|\psi_{in}\rangle \to |\psi_{out}\rangle\right) = |\langle\psi_{out}|S|\psi_{in}\rangle|^2. \tag{4.1.8}$$

In practice, $w(|\psi_{in}\rangle \to |\psi_{out}\rangle)$ can not be directly observed. Indeed, it is impossible to produce a wave packet with a well-defined quantum state and it is also impossible to identify the outgoing state with an infinite precision. The quantity that is experimentally an observable is the differential cross-section *i.e.* the section of the plane at infinity that scatters $|\psi_{in}\rangle$ in the solid angle $d\Omega$. In the experiments, $|\psi_{in}\rangle$ (resp. $|\psi_{out}\rangle$) is so a wave packet with a momentum peaked around $\vec{k}_0$ (resp. $\vec{k}$) and the differential cross-section is defined as

$$\frac{d\sigma}{d\Omega}(\vec{k}_0 \to \vec{k}) = |f(\vec{k}_0 \to \vec{k})|^2, \tag{4.1.9}$$

with $f(\vec{k}_0 \to \vec{k})$ the scattering amplitude.

Now, the point is to link the theoretical S-matrix elements with the experimentally-measured scattering amplitude. Conventionally, S is decomposed as $S = 1 + R$ with R representing the difference between the values of S with and without interactions. The R-matrix elements are given in momentum space by

$$\langle\vec{q}|R|\vec{p}\rangle = -2\pi i\,\delta(E_{\vec{q}} - E_{\vec{p}})\,t(\vec{p} \to \vec{q}), \tag{4.1.10}$$

and it follows that,

$$\langle\vec{q}|S|\vec{p}\rangle = \delta(\vec{q} - \vec{p}) - 2\pi i\,\delta(E_{\vec{q}} - E_{\vec{p}})\,t(\vec{p} \to \vec{q}). \tag{4.1.11}$$

In the first term of (4.1.11), $\delta(\vec{q} - \vec{p})$ obviously expresses the fact that the particle is not scattered while, in the second term, $\delta(E_{\vec{q}} - E_{\vec{p}})$ ensures the energy conservation. The factor $-2\pi i$ is for convenience and the function $t(\vec{p} \to \vec{q})$ depends on the interaction process. The second term is thus only defined for $E_{\vec{q}} = E_{\vec{p}}$ or equivalently, on the shell $\vec{q}^2 = \vec{p}^2$ [1]. We will see thereafter that it is convenient to introduce an operator T for all momenta $\vec{p}$, $\vec{q}$ and coinciding with $t(\vec{p} \to \vec{q})$ on the shell. The matrix elements $\langle\vec{q}|T|\vec{p}\rangle$, with(out) the condition $\vec{q}^2 = \vec{p}^2$ define then the on-(off-) shell T-matrix.

The on-shell function $t(\vec{p} \to \vec{q})$, is related to the scattering amplitude in the non-relativistic case by

$$f(\vec{p} \to \vec{q}) = -(2\pi)^2 m\,t(\vec{p} \to \vec{q}), \tag{4.1.12}$$

where m is the mass of the particle. From (4.1.12), we understand that knowing $t(\vec{p} \to \vec{q})$ is equivalent to solve the scattering problem. We thus need a way to extract it from the theory. The purpose of the following subsections will be to put to the foreground $t(\vec{p} \to \vec{q})$ from the foundation of quantum mechanics.

4.1.2 Schrödinger equation and its integral formulation

In order to fix a situation for the discussion below, let us start by expressing the time-independent Schrödinger equation for a central potential in configuration space [Tayl83], *i.e.*

$$\left[-\frac{1}{2m}\Delta_{\vec{r}} + V(\vec{r})\right]\psi(\vec{r}) = E\psi(\vec{r}), \tag{4.1.13}$$

1. The on-shell condition is of course modified if relativistic processes are considered.

where $\Delta_{\vec{r}}$ is the Laplacian in spherical coordinates, m is the particle mass and $V(\vec{r})$ is the potential.

Since this equation is a corner stone of quantum mechanics, a lot of methods have been developed to solve it. Here, we are mainly interested in its integral formulation because we want to easily connect it to $t(\vec{p} \to \vec{q})$. Therefore, (4.1.13) can be rewrite as

$$(E + \frac{1}{2m}\Delta_{\vec{r}})\,\psi(\vec{r}) = V(\vec{r})\psi(\vec{r}). \tag{4.1.14}$$

Mathematically, (4.1.14) is equivalent to the following problem [2]:

$$\mathcal{D}\phi(x) = j(x), \tag{4.1.15}$$

where $\mathcal{D}$ is a linear differential operator and $j(x)$ is a given function called "source of $\phi(x)$".
Let us define the Green's function $G_0(x)$, as the solution of

$$\mathcal{D}G_0(x) = \delta(x). \tag{4.1.16}$$

If $G_0(x)$ is known, the solution of (4.1.15) is given by

$$\phi(x) = \phi_0(x) + \int G_0(x-y)\,j(y)\,dy, \tag{4.1.17}$$

where $\phi_0(x)$ is the solution of $\mathcal{D}\phi_0(x) = 0$.

In our case, $\mathcal{D}$ is the operator $(E + \frac{1}{2m}\Delta_{\vec{r}})$ and $j(x)$ is $V(\vec{r})\psi(\vec{r})$. It naturally comes the integral equation:

$$\psi(E,\vec{r}) = \psi_0(E,\vec{r}) + \int G_0(E,\vec{r},\vec{r}^{\,'})\,V(\vec{r}^{\,'})\psi(E,\vec{r}^{\,'})\,d\vec{r}^{\,'}. \tag{4.1.18}$$

$G_0(E,\vec{r},\vec{r}^{\,'})$ is thus a Green's function associated to the linear operator $E + \frac{1}{2m}\Delta_{\vec{r}}$ since it satisfies the equation:

$$\left[E + \frac{1}{2m}\Delta_{\vec{r}}\right] G_0(E,\vec{r},\vec{r}^{\,'}) = \delta(\vec{r}-\vec{r}^{\,'}). \tag{4.1.19}$$

$G_0(E,\vec{r},\vec{r}^{\,'})$ is called the free propagator of the system. We can also define $G(E,\vec{r},\vec{r}^{\,'})$ by

$$\left[E + \frac{1}{2m}\Delta_{\vec{r}} - V(\vec{r})\right] G(E,\vec{r},\vec{r}^{\,'}) = \delta(\vec{r}-\vec{r}^{\,'}). \tag{4.1.20}$$

$G(E,\vec{r},\vec{r}^{\,'})$ is the full propagator of the system.

From the aforementioned mathematical manipulations, we bring out another fully equivalent way to solve the Schrödinger equation. (4.1.18) is called the Lippmann-Schwinger equation for the wave function.

4.1.3 Green's functions and its Lippmann-Schwinger equation

In the previous subsection, we have just extracted from quantum mechanics a crucial tool that we have already met in the context of quantum field theory: the two-point Green's functions or equivalently, the propagator. As seen in Section 1.1.3, such functions are the building blocks of any quantum field theory.

2. The problem is well-posed once the boundary conditions have been specified.

The link between these ones and the scattering problems is thus an important connection to establish. In what follows, we will continue to study it in the framework of the non-relativistic quantum mechanics in order to make this link easier.

Let us rewrite (4.1.19) and (4.1.20) in momentum space by doing a Fourier's transformation and by making complex the variable E ($E \to z$):

$$(z - H_0)\, G_0(z) = \mathbb{1}, \tag{4.1.21}$$
$$(z - H)\, G(z) = \mathbb{1}. \tag{4.1.22}$$

If $(z - H_0)$ and $(z - H)$ are invertible, $G_0(z)$ and $G(z)$ are Green's operators [3] defined by

$$G_0(z) = (z - H_0)^{-1}, \tag{4.1.23}$$
$$G(z) = (z - H)^{-1}. \tag{4.1.24}$$

Nevertheless, it is worth noticing that the inverses of $z - H_0$ and $z - H$ are not defined for any value of z. The values for which $z - H_0$ and $z - H$ are not invertible are precisely the eigenvalues of the associated Hamiltonian. Therefore, its spectrum coincides with the poles of the corresponding Green's operator. Unfortunately, this observation does not make easier the resolution of the eigenvalue problem. Only for H_0, the spectrum is well-known. That is the reason why it is useful to have a relation that links the unknown analytic structure of $G(z)$ to the well-known one of $G_0(z)$. This link is given by the LS equation for the propagator and it is derived for the simple operator identity,

$$A^{-1} = B^{-1} + B^{-1}(B - A)A^{-1}, \tag{4.1.25}$$

that becomes, if $A = z - H$ and $B = z - H_0$,

$$G(z) = G_0(z) + G_0(z)VG(z). \tag{4.1.26}$$

4.1.4 T-matrix and its Lippmann-Schwinger equation

In scattering theory, it is also convenient to define another operator $T(z)$, by the relation

$$T(z) = V + VG(z)V. \tag{4.1.27}$$

It is obvious that $T(z)$ as the same analytic structure as $G(z)$. So, $T(z)$ has poles that correspond to the eigenvalues of the associated Hamiltonian. After some algebraic manipulations, it is also possible to write a LS equation for $T(z)$. That is to say,

$$T(z) = V + VG_0(z)T(z). \tag{4.1.28}$$

Note that (4.1.28) is particularly simple to compute when V is sufficiently weak. In this case, we can hope to have a satisfactory solution of the problem by iteration in which the Born approximation, $T \approx V$, can be used as a starting point. The procedure can be then refined by expanding the other terms of the infinite series,

$$T = V + VG_0V + \dots\ . \tag{4.1.29}$$

3. It is worth mentioning the fact that here, the notation $G_0(z)$ and $G(z)$ defined operators. In the section 4.1.2, $G_0(E, \vec{r}, \vec{r}^{\,'})$ and $G(E, \vec{r}, \vec{r}^{\,'})$ are the functions associated with the matrix elements $\langle \vec{r}^{\,'}|G_0(E)|\vec{r}\rangle$ and $\langle \vec{r}^{\,'}|G(E)|\vec{r}\rangle$, expressed in the configuration space.

However, the most important advantage to introduce $T(z)$, is that it can be proved that the on-shell $t(\vec{p} \to \vec{q})$ is given by [Tayl83]

$$t(\vec{p} \to \vec{q}) = \lim_{\epsilon \to 0} \langle \vec{q}|T(E_{\vec{p}} + i\epsilon)|\vec{p}\rangle, \tag{4.1.30}$$

where $\langle \vec{q}|T(z)|\vec{p}\rangle$ are the off-shell T-matrix elements expressed in momentum space. From (4.1.28), we have

$$\langle \vec{q}|T(z)|\vec{p}\rangle = \langle \vec{q}|V|\vec{p}\rangle + \int d\vec{p}^{\,'} \frac{\langle \vec{q}|V|\vec{p}^{\,'}\rangle}{z - E_{\vec{p}^{\,'}}} \langle \vec{p}^{\,'}|T(z)|\vec{p}\rangle. \tag{4.1.31}$$

This equation is precisely the one we will solve to get information about the Hamiltonian spectrum. It is important to notice that (4.1.31) requires the knowledge of the entire off-shell T-matrix since it is only at the end of the computation that the on-shell condition can be applied.

With (4.1.30), the link between the experimental differential cross-section (introduced in Section 4.1.1) and the theoretical tools is now fully-determined. We are thus equipped to extend these concepts to the two-body relativistic scattering.

4.2 Bethe-Salpeter equation

Let us now have a look to the full two-particle propagator. Schematically, it can be represented by Fig. 4.1 at first approximation. It connects four lines depicting the propagation of four fields. By using the Feynman rules, Fig. 4.1 can be mathematically translated into [Grei99]

$$\begin{aligned} S^{ab}(x_3, x_4; x_1, x_2) &= iS_a^0(x_3, x_1)\, iS_b^0(x_4, x_2) \\ &+ \int d^4x_5 d^4x_6 \left[iS_a^0(x_3, x_5)\, iS_b^0(x_4, x_6) \right] \\ &\times (-ig\gamma_\mu^a) iD_F^{\mu\nu}(x_5, x_6)(-ig\gamma_\nu^b) \left[iS_a^0(x_5, x_1)\, iS_b^0(x_6, x_2) \right] + \dots , \end{aligned} \tag{4.2.1}$$

where S^0 represents the free one-particle fermion propagator and D_F is the free one-particle boson propagator. a and b are spinor indices. For simplicity, the vertices used in (4.2.1) are the ones of QED.

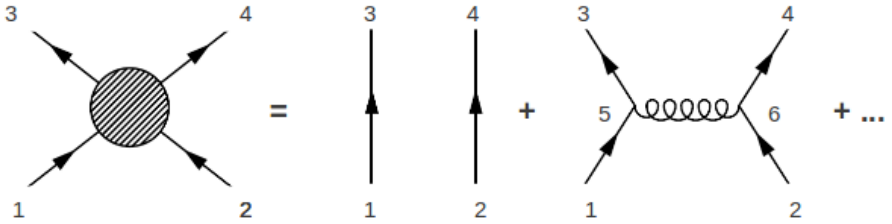

Figure 4.1: Pertubation expansion of the full two-particle propagator. The blob represents the full two-particle propagator.

Nevertheless, in many situations, we need a better description for the interaction between two particles than the one provides by the perturbation expansion. It is especially right in the non-perturbative range of

QCD because the strength of the interaction is too strong but also when one wants to deal with bound states, regardless of the interaction strength of the underlying theory. In the following subsection, we will focus on this latter case.

Let us take back the example given in Fig. 4.1 and let us formally consider the impact of the infinite series by the schematic view displayed in Fig. 4.2, which explicitly reads [Grei99],

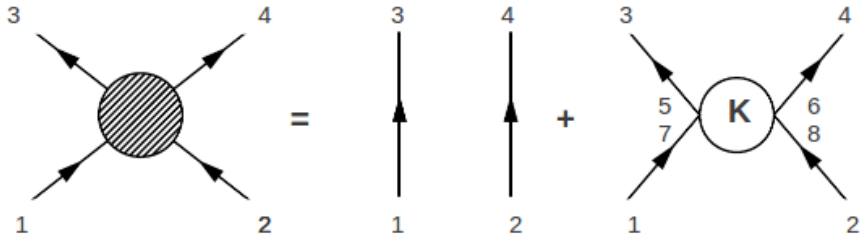

Figure 4.2: The blob represents the full two-particle propagator. The empty circle stands for the impact of the infinite series of interactions.

$$
\begin{aligned}
S^{ab}(x_3,x_4;x_1,x_2) &= iS_a^0(x_3,x_1)\,iS_b^0(x_4,x_2) \\
&+ \int d^4x_5\,d^4x_6\,d^4x_7\,d^4x_8\,\left[iS_a^0(x_3,x_5)\,iS_b^0(x_4,x_6)\right] \\
&\times K^{ab}(x_5,x_6;x_7,x_8)\left[iS_a^0(x_7,x_1)\,iS_b^0(x_8,x_2)\right].
\end{aligned}
\tag{4.2.2}
$$

$K^{ab}(x_5,x_6;x_7,x_8)$ is called the interaction kernel.

At the first perturbation order, $K^{ab}(x_5,x_6;x_7,x_8)$ is given by

$$
K^{ab}(x_5,x_6;x_7,x_8) = (-ig\gamma_\mu^a)iD_F^{\mu\nu}(x_5,x_6)(-ig\gamma_\nu^b)\delta(x_5-x_7)\delta(x_6-x_8), \tag{4.2.3}
$$

as seen in the previous section. (4.2.3) is a rather good approximation if the interaction is weak. One can naturally improve its computation by adding any subset of diagrams to K but the whole infinite series has formally to be considered, especially if we want to describe bound states.

However, a minor condition can be applied in order to get the bound-state spectrum. It consists to only take into account some diagrams at any order. This last option is computationally manageable if all the diagrams are sorted in an clever way. Indeed, among all the diagrams, two types can be distinguished : the reducible and the irreducible ones. A reducible diagram is characterized by the fact that it can be split into two unconnected parts by cutting two fermion lines. On the other hand, an irreducible one is so deeply interwoven that it is impossible to cut (see examples in Fig. 4.3).

Thanks to this classification, the interaction kernel K can be expressed as a sum of a reducible and an irreducible interaction kernels. This splitting make sense if we realize that each reducible diagram can be obtained from irreducible pieces. Therefore, the schematic view displayed in Fig. 4.2 can be rearranged as

Figure 4.3: (Left) Irreducible diagram. (Right) Reducible diagram. [Grei99]

shown in Fig. 4.4, and (4.2.2) can be rewritten

$$\begin{aligned} S^{ab}(x_3,x_4;x_1,x_2) &= iS_a^0(x_3,x_1)\,iS_b^0(x_4,x_2) \\ &+ \int d^4x_5\,d^4x_6\,d^4x_7\,d^4x_8\,\left[iS_a^0(x_3,x_5)\,iS_b^0(x_4,x_6)\right] \\ &\times \overline{K}^{ab}(x_5,x_6;x_7,x_8)S^{ab}(x_7,x_8;x_1,x_2), \end{aligned} \tag{4.2.4}$$

where $\overline{K}^{ab}(x_5,x_6;x_7,x_8)$ is the irreducible interaction kernel.

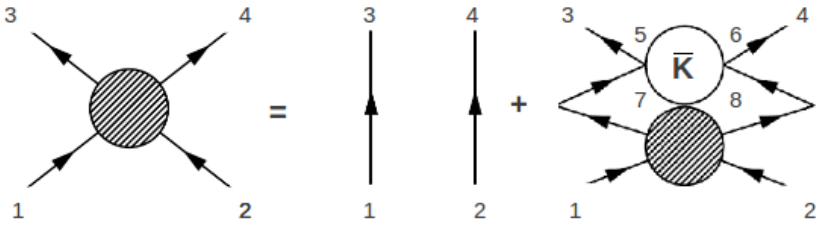

Figure 4.4: Rearrangement of Fig. 4.2 by using the irreducible interaction kernel.

Of course, (4.2.4) is fully equivalent to (4.2.2). It is particularly obvious if we represent it iteratively. However, $\overline{K}$ is still difficult to evaluate since it is an infinite sum of irreducible diagrams. The main advantage of (4.2.4) is the following: Even if $\overline{K}$ is computed within the perturbation theory, the solution of (4.2.4) contains an infinite series of interactions. As seen previously, this is the crucial point for obtaining bound states. Moreover, the unitarity of the expressions is always preserved, regardless of the chosen kernel.

(4.2.4) is thus the master idea from which all Bethe-Salpeter equations are established. Note that, as for the LS equations, a BS equation can be expressed for different quantities as, for instance, the wave function, the vertex or the T-matrix. This last case is the one that deserves interests for us.

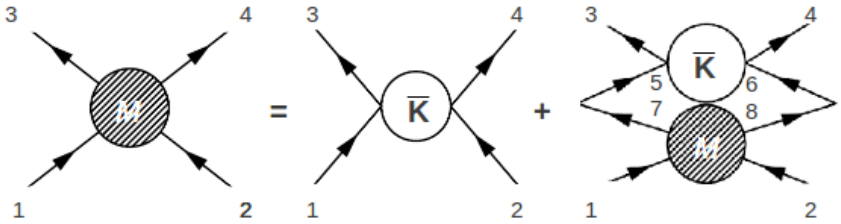

Figure 4.5: LS equation for the amplitude $\mathcal{M}$.

As seen in Section 4.1.1, the T-matrix is the interaction part of the S-matrix since S can be decomposed in $1 + R$ and R depends on the T-matrix. If we do this substitution within (4.2.4) and drop out the free part, we remains with

$$\mathcal{M} = \overline{K} + \overline{K} G_0 \mathcal{M}, \tag{4.2.5}$$

where $\mathcal{M}$ is the amplitude that describes the process and G_0 is the two-body Green's functions. In Fig 4.5, $G_0 = (iS^0)(iS^0)$. From (4.2.5), the on-shell T-matrix elements can be then schematically defined as [Cabr07]

$$T \equiv \langle out|\mathcal{M}|in\rangle, \tag{4.2.6}$$

where $|in\rangle$ and $|out\rangle$ are respectively the appropriate in-going and out-going states. In the example of Fig. 4.5, they are Dirac spinors on free shell. A LS equation for the off-shell T-matrix elements as (4.1.31) can be thus established from (4.2.6). The way to solve it will be the purpose of the next section.

4.3 Solving the Lippmann-Schwinger equation for the T-matrix

Up to now, we have exposed the main theoretical framework associated to scattering problems and the useful equations that result from it. In this section, the discussion will turn into more technical aspects since we will introduce the algorithms and the approximations on which we rely in order to practically solve the hadron spectrum.

4.3.1 Blankenbecler-Sugar reduction scheme of the Bethe-Salpeter equation

Let us start by considering the amplitude $\mathcal{M}$ describing the two-body interaction process given by (4.2.5) and let us write it in the center-of-mass frame:

$$\mathcal{M}(q,p;P) = \overline{K}(q,p;P) + \int d^4k\, \overline{K}(q,k;P)\, G_0(k;P)\, \mathcal{M}(k,p;P). \tag{4.3.1}$$

The conventions are the following. p is the initial relative four-momentum between the two-entering particles and P is the total four-momentum. Therefore, if the particle 1 is described by the four-momentum $p_1 =$

$(\omega_1, \vec{p}_1)$ in some Lorentz frame and the particle 2 by $p_2 = (\omega_2, \vec{p}_2)$, we have the usual center-of-mass relations

$$P = p_1 + p_2 = \left(\omega_1 + \omega_2, \vec{0}\right) = (\sqrt{s}, \vec{0}), \tag{4.3.2}$$

$$p = \frac{1}{2}(p_1 - p_2) = \left(\frac{\omega_1 - \omega_2}{2}, \vec{p}\right), \tag{4.3.3}$$

$$p_1 = \frac{P}{2} + p, \tag{4.3.4}$$

$$p_2 = \frac{P}{2} - p, \tag{4.3.5}$$

since $\vec{p}_1 = -\vec{p}_2 = \vec{p}$, $\omega_i = \sqrt{\vec{p}_i^{\,2} + m_i}$ with m_i the mass of the particle i, and $\sqrt{s}$ is the energy in the center-of-mass frame. Of course, q is the relative four-momentum for the two-outgoing particles and similar relations as those just aforementioned can be established.

Unfortunately, the four-dimensional equation (4.3.1) is difficult to solve and a three-dimensional reduction scheme is often used. Such schemes preserve the covariance of the BS equation and satisfy the relativistic elastic unitarity. However, it is not an unique procedure. In our case, we will only focus on the Blankenbecler-Sugar (Bbs) reduction scheme [Blan66], the most used in recent studies [Cabr07] [4].

Following these considerations, it can be shown that the BS equation (4.2.5) can be replaced by the two coupled operator equations [Thom70],

$$\mathcal{M} = \mathcal{W} + \mathcal{W} G_{RS} \mathcal{M}, \tag{4.3.6}$$

$$\mathcal{W} = \overline{K} + \overline{K}(G_0 - G_{RS})\mathcal{W}. \tag{4.3.7}$$

The second relation is usually simplified by $\mathcal{W} = \overline{K}$, which will be also assumed within this thesis, and G_{RS} is in general an arbitrary function of P and k. However, in the center-of-mass frame, it is chosen to be of the form

$$G_{RS}(k; \sqrt{s}) = \delta\left(k^0 - \frac{\omega_1 - \omega_2}{2}\right) G_{BbS}(\vec{k}\,; \sqrt{s}). \tag{4.3.8}$$

The role of the δ-function is especially to turn out the four-dimensional integral into a three-one. Only the positive energy part is kept in the propagator. The remaining part to determine is thus the structure of $G_{BbS}(\vec{k}\,; \sqrt{s})$.

It can be shown, after a tedious mathematical development [Mach89, Mine08], that $G_{BbS}(\vec{k}\,; \sqrt{s})$ for spinless particles reads

$$G_{BbS}(\vec{k}\,; \sqrt{s}) = m_1 m_2 \, \frac{\omega_1 + \omega_2}{2\,\omega_1 \omega_1} \frac{1}{\dfrac{s}{4} - \left(\dfrac{\omega_1 + \omega_2}{2}\right)^2 + i\dfrac{\epsilon}{4}}, \tag{4.3.9}$$

and (4.3.1) turns into the three-dimensional LS equation:

$$T(\vec{q}, \vec{p}; \sqrt{s}) = \overline{K}(\vec{q}, \vec{p}; \sqrt{s}) + \int \frac{d^3k}{(2\pi)^3} \, \overline{K}(\vec{q}, \vec{k}; \sqrt{s}) \, G_{BbS}(\vec{k}\,; \sqrt{s}) \, T(\vec{k}, \vec{p}; \sqrt{s}). \tag{4.3.10}$$

4. Note that we have also investigated the glueball sector within the Thompson reduction scheme and the differences observed in the glueball spectrum were really weak.

Note that $G_{BbS}(\vec{k}\,;\sqrt{s})$ has been computed without the explicit inclusion of a particle spin since we will use a potential that will not depend on it in our computations. So, (4.3.10) has the same general structure for all types of two-body processes that we will consider. Moreover, note that in this reduction scheme, virtual particle-antiparticle loops are neglected.

4.3.2 Interaction potential

Now that we have reduced the BS equation to (4.3.10), we must fix the kernel $\overline{K}(\vec{q},\vec{p};\sqrt{s})$. A common approximation that can be used is to restrict it to the lowest order in perturbation theory. This prescription is called the ladder (or the rainbow) approximation and it is schematically represented by

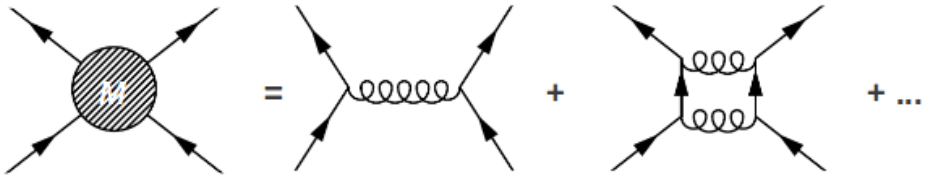

In this restriction, only the one-particle exchange is considered but it can happen an arbitrary number of times. It ensures the infinite number of interactions between particles and so, the possible existence of bound states and resonances.

In our case, we prefer to assume that $\overline{K}(\vec{q},\vec{p};\sqrt{s})$ is equal to an effective potential given by $V(\vec{q},\vec{p})$ [5]. Therefore, a key ingredient of the present approach is the two-body potential $V(\vec{q},\vec{p})$, encoding the interactions between the two particles.

Having in mind the building of an effective framework describing the deconfined phase of a non-abelian gauge theory, each particle composing the plasma should be in a given representation of the considered gauge group. It is thus reasonable to assume that the potential V between the two particles, respectively in the representations R_i and R_j of the gauge group, has the simplest possible colour-dependence. This corresponds to

$$V_{\{ij\}}(\vec{q},\vec{p}) = \tilde{M}_{R_i}\cdot\tilde{M}_{R_j}\alpha_S\,\bar{v}(\vec{q},\vec{p}), \tag{4.3.11}$$

where $\tilde{M}_R$ denotes the generator of the gauge algebra in the representation R, and where the real function $\bar{v}$ only depends on two momenta and possibly on the temperature (no dependence on the mass or other attributes of the particle). In the above definition, it has to be remembered that $\alpha_S = g^2/4\pi$ and that $g^2 = \lambda/C_2^{adj}$, adj being the adjoint representation of the gauge group under study and C_2^R being the value of the quadratic Casimir in the representation R. Note that in the case of SU(N_c), λ is the 't Hooft coupling (fixed in the large-N_c limit) [Hoof74].

5. The variable $\sqrt{s}$ is dropped off.

Introducing quadratic Casimirs, one can rewrite (4.3.11) as

$$V_{\{ij\}}(\vec{q},\vec{p}) = \frac{C_2^{\mathcal{C}} - C_2^{R_i} - C_2^{R_j}}{2}\,\alpha_S\,\bar{v}(\vec{q},\vec{p}) \equiv \kappa_{\mathcal{C};ij}\,v(\vec{q},\vec{p}), \tag{4.3.12}$$

with $\mathcal{C}$ the pair representation and

$$\kappa_{\mathcal{C};ij} = \frac{C_2^{\mathcal{C}} - C_2^{R_i} - C_2^{R_j}}{2\,C_2^{adj}}. \tag{4.3.13}$$

Again, the real function $v(\vec{q},\vec{p})$ is assumed to only depend on two momenta and possibly on the temperature. An explicit form for $v(\vec{q},\vec{p})$ at $T=0$ and $T>T_c$ will be given in Section 4.4.1 and Section 4.5.1. Let us note that in these cases, complicated multi-gluon and quark loop exchanges can occur since these potentials are directly extracted from lQCD.

Of course, the validity of the Casimir scaling is therefore questionable since our chosen interactions take into account many QCD processes and some of that are not scaled with the simple form (4.3.13), exhibited for instance by the one-gluon exchange processes. Already at the level of the lowest-order Feynman diagrams between two particles in QCD, it happens: The basic gluon-quark interaction is mediated by a quark exchange, which does not respect (4.3.13).

Nevertheless, it is worth mentioning that the Casimir scaling seems very well respected in lQCD. Indeed, the interaction potential between two static colour sources in the $T=0$ sector follows this scaling [Bali00] while computations in the $T>T_c$ sector show only slight deviations: The Casimir scaling seems partly violated (at most 20%) for short distances and temperatures near T_c [Gupt08]. In our work, we will thus assume that the Casimir scaling is satisfied.

Therefore, all hyperfine interactions are neglected. We miss for instance the annihilation contributions but we can expect that they are non-dominant. According to [Aitc82, Akhi65], the annihilations are expected to depend on the inverse square of the effective masses, involved in the process at the first perturbative order. So, it is a refinement in comparison to the associated scattering processes. Moreover, note that according to our choice of reduction scheme, annihilation processes can not be studied. Such refinements will be thus left for future works.

4.3.3 Masses and self-energies

To assess the presence of bound state, we need to study the T-matrix results below a threshold given by the sum of the particle masses. Therefore, the mass of the resulting bound state is seen as the mass of the threshold minus the binding energy. For heavy particles, this vision is not a problem but for light and massless particles, we need to define properly a threshold in order to have positive bound-state masses.

The procedure of acquiring an effective mass is a well-known process in the quantum field theory since a mass can be dynamically generated by self-energy effects. These effects will be taken into account in order to define a threshold. The real part of the self-energy Σ is reabsorbed in an effective mass for the particle, noted also here m_i (it will be discussed later), while the imaginary part enters the two-particle propagator by the following replacement [Cabr07]

$$\left[\frac{s}{4} - \left(\frac{\omega_1+\omega_2}{2}\right)^2 + i\frac{\epsilon}{4}\right]^{-1} \to \left[\frac{s}{4} - \left(\frac{\omega_1+\omega_2}{2}\right)^2 - i(\omega_1+\omega_2)\,\mathrm{Im}\,\Sigma\right]^{-1}. \tag{4.3.14}$$

For numerical purposes, $\mathrm{Im}\,\Sigma$ will be fixed to -0.01 GeV in all the computations, as in [Cabr07]. One can check that (4.3.9) and (4.3.14) reduce to the expressions given in [Cabr07] when $m_1 = m_2$.

4.3.4 Partial wave decomposition of the T-matrix

Before solving numerically (4.3.10), two tasks remain to do. Firstly, we have to Fourier-transform the two-body potentials that we will use since their expressions are defined in the configuration space. For a potential with spherical symmetry in the configuration space, the Fourier transform is given by

$$V(q,p,\theta_{q,p}) = 4\pi \int_0^\infty dr\, rV(r)\frac{\sin(Qr)}{Q}, \quad \text{where} \quad Q = \sqrt{q^2+p^2-2qp\,\cos\theta_{q,p}}, \tag{4.3.15}$$

and where $\theta_{q,p}$ is the angle between the momenta $\vec{q}$ and $\vec{p}$. Note that from now, q and p will indicate the norm of $\vec{q}$ and $\vec{p}$ and no more the 4-momenta.

Secondly, we have to decompose the two-body interactions in partial waves in order to get the correct $J^{P(C)}$ number [6] associated to each hadron. The partial-wave decomposition of the potential is given by

$$V(q,p,\theta_{q,p}) = \frac{1}{4\pi}\sum_L (2L+1)V_L(q,p)P_L(\cos\theta_{q,p}), \tag{4.3.16}$$

where

$$V_L(q,p) = 2\pi \int_{-1}^{1} dx P_L(x)V(q,p,x), \tag{4.3.17}$$

with P_L is the Legendre polynomial of order L and $x = \cos\theta_{q,p}$. Since the $J^{P(C)}$ states read (see Appendix B)

$$|J^{P(C)}\rangle = \sum_{L,S} C_{L,S}|^{2S+1}L_J\rangle, \tag{4.3.18}$$

it can be shown after a long and careful computation that

$$V_{J^{P(C)}}(q,p) = \sum_{L,S} |C_{L,S}|^2 V_L(q,p). \tag{4.3.19}$$

Different kinds of interactions will be considered within this work. They can be separated in two groups. The first one is made of $J^{P(C)}$ channels that can be described with a single partial wave. In our approach, this is for instance the case of the quark-antiquark interactions. The second group is made of a class of two-body interactions in which at least one particle is transverse. In this situation, the basis states are the helicity states given by Jacob and Wick's helicity formalism and the potentials for a given $J^{P(C)}$ channel are obtained by combination of different L-wave potential parts as expressed in (4.3.19). For further details about the way to build such states, cfr. Appendix B.

Once the potential in a given $J^{P(C)}$ scattering channel, *i.e.* $V_{J^{P(C)}}(q,p)$ is known, the off-shell T-matrix can be computed from (4.3.10) thanks to [Cabr07]:

$$T_{J^{P(C)}}(E;q,p) = V_{J^{P(C)}}(q,p) + \frac{1}{8\pi^3}\int_0^\infty dk\, k^2\, V_{J^{P(C)}}(q,k)\, G_{Bbs}(E;k)\, T_{J^{P(C)}}(E;k,p), \tag{4.3.20}$$

where E is the energy of the two particles in the center-of-mass frame. The two-body propagator reads

$$G_{BbS}(E,k) = m_1 m_2 \frac{\omega_1+\omega_2}{2\,\omega_1\omega_1}\frac{1}{\dfrac{E^2}{4} - \left(\dfrac{\omega_1+\omega_2}{2}\right)^2 - i(\omega_1+\omega_2)\,\mathrm{Im}\,\Sigma}, \tag{4.3.21}$$

6. As usual, $J = L + S$ is the total angular momentum where L is the orbital angular momentum and S is the spin. P is the parity and C the charge conjugaison.

where $\omega_i = \sqrt{k^2 + m_i^2}$ and $s \to E^2$.

Eventually, the on-shell T-matrix, $T_{J^{P(C)}}(E; q_E, q_E)$, is readily obtained by imposing the on-shell condition

$$q_E = \sqrt{\frac{1}{4E^2}(E^2 - (m_1 + m_2)^2)(E^2 - (m_1 - m_2)^2)}, \tag{4.3.22}$$

which comes from the inversion of $E = \omega_1(q_E) + \omega_2(q_E)$.

4.3.5 Haftel and Tabakin algorithm

Now that we have the equation to solve, *i.e.* (4.3.20), we need to compute it numerically in order to obtain the bound and scattering states. To these purposes, the Haftel and Tabakin algorithm [Haft70] is used. This latter consists of discretizing the momentum integration and converting (4.3.20) into a matrix equation,

$$\sum_{k=1}^{N} \mathcal{F}(E)_{ik} T(E)_{kj} = V_{ij}. \tag{4.3.23}$$

In this equation, $\mathcal{F}$ is schematically given by $\mathcal{F} = 1 - w\,V G_{BbS}$ where w denotes the integration weight. The solution for the T-matrix elements then follows from matrix inversion.

Note that it can be shown that the real part of the determinant of the transition function $\mathcal{F}$ (referred to as the Fredholm determinant) vanishes at the bound state and resonance energies. This property is particularly interesting since it provides us a simple and more manageable numerical criterion to solve the bound state problem than finding the localisation of the Dirac-delta peak.

The major part of this algorithm was implemented by D. Cabrera for the purposes of its paper [Cabr07]. We have thus used his Fortran code and adapted it for our computations.

4.4 QCD spectrum at zero temperature

4.4.1 Cornell potential and quasiparticle mass

Since all the theoretical and technical aspects are now discussed, we can exploit them to compute the $T = 0$ spectrum of QCD. This study essentially aims to fix the needful parameters for the finite-temperature developments. Indeed, the QCD spectrum at $T = 0$ is well investigated both in experiments [PDG] and in lQCD (*e.g.* [Fodo12]). Some comparisons can be thus established in order to guide us in the fitting of the parameters.

From quenched SU(3) lQCD, it is known that the potential between a static quark-antiquark pair is compatible with the funnel form [Bali01]

$$V_f(r) = \sigma r - \frac{4}{3}\frac{\alpha}{r}, \tag{4.4.1}$$

where standard values for α and σ are $\alpha = 0.4$ and $\sigma = 0.176$ GeV^2. The expression (4.4.1) is called the Cornell potential and is used as starting point of our computations.

As mentioned in Section 4.3.4, a first step to accomplish is to Fourier-transform the potential (4.4.1). Unfortunately, the Fourier's transformation of $V_f(r)$ is not defined. This flaw has to be cured. It is done by making it saturate at some value $V_{q\bar{q}}^{sb}$. This latter is then interpreted as a string-breaking value, that is the

energy above which a light quark-antiquark pair can be created from the vacuum and break the QCD string. This scale is then subtracted and the potential effectively taken into account is

$$V^0_{q\bar{q}}(r) = V_f(r) - V^{sb}_{q\bar{q}} \quad \text{for } r \leq r_{sb}, \tag{4.4.2}$$
$$= 0 \quad \text{for } r > r_{sb}, \tag{4.4.3}$$

while $V^{sb}_{q\bar{q}}/2$ is interpreted as an effective quark mass provided by self-energy effects and r_{sb} is defined such as $V_f(r_{sb}) = V^{sb}_{q\bar{q}}$. This effective mass is quadratically added to the bare quasiparticle mass m_0. The quasiquark mass is thus given by

$$m_q = \sqrt{m^2_{q,0} + \left(\frac{V^{sb}_{q\bar{q}}}{2}\right)^2}. \tag{4.4.4}$$

This standard procedure for a T-matrix approach is used in [Cabr07].

While the potential (4.4.2) can be directly used for a quark-antiquark pair, it has to be scaled in other cases. According to the colour scaling (4.3.13), the potential describing the interactions between two particles (p_1, p_2) at zero temperature is

$$V^0_{p_1p_2}(r) = \frac{\kappa_{\bullet;p_1p_2}}{\kappa_{\bullet;q\bar{q}}} V_f(r) - V^{sb}_{p_1p_2}. \tag{4.4.5}$$

For instance, for 2 gluons lying in the SU(3) gauge group, we have

$$V^0_{gg}(r) = \frac{9}{4} V_f(r) - V^{sb}_{gg}. \tag{4.4.6}$$

In this example, the string breaking scale should rather be interpreted as the energy scale necessary to form two gluelumps, a gluelump being a gluon bound in the colour field of a static adjoint source. It is known indeed that adjoint string breaking may be observed, and occurs at twice the lightest gluelump mass (~ 2 GeV) [Defo00]. The quasigluon mass naturally follows the same prescription as the quasiquark one.

4.4.2 Glueball spectrum

Using the general formula (4.4.5) for the effective interaction between the quasigluons, the glueball spectrum at zero temperature can be computed by looking at the pole of the T-matrix or, more precisely here, at the zeros of $\det \mathcal{F}$ as mentioned in Section 4.3.5. We only focus our study on the lightest glueballs [Morn99], namely the scalar 0^{++}, the pseudoscalar 0^{-+}, and the tensor 2^{++} ones. According to the equations (B.2.1) from Appendix B, giving the partial-wave decomposition of the two-gluon interactions for each channel, we have (after a Fourier's transformation)

$$V_{0^{++}}(q,q') = \frac{2}{3} V_0(q,q') + \frac{1}{3} V_2(q,q'), \tag{4.4.7}$$
$$V_{0^{-+}}(q,q') = V_1(q,q'), \tag{4.4.8}$$
$$V_{2^{++}}(q,q') = \frac{2}{5} V_0(q,q') + \frac{4}{7} V_2(q,q') + \frac{1}{35} V_4(q,q'), \tag{4.4.9}$$

where $V_0 \to V_4$ are the $L = 0 \to L = 4$ partial-wave part of (4.4.6).

The only free parameters that remain now in the computations, are V^{sb}_{gg} and $m_{g,0}$. A value of 2 GeV for V^{sb}_{gg} is used within this work. It is in agreement with lattice data showing that the mass of the lightest gluelump is given by $0.85(17)$ GeV [Bali04]. Concerning $m_{g,0}$, it is fixed to 0.7 GeV, which is an acceptable

value for the zero-momentum limit of the gluon propagator at zero temperature in view of previous studies locating this mass typically between 500 and 700 MeV, see *e.g.* [Corn82, Oliv11, Szcz96].

Using these parameter values, we obtain the results displayed in Table 4.1. They are compared with the zero temperature lQCD glueball spectrum [Morn99] and with the Coulomb gauge QCD (CGQCD) study [Szcz96]. Let us first focus on the fourth column (corresponding to the initial set of parameters). At least, in this case, the model is able to reproduce the mass hierarchy of the lightest glueballs observed in lQCD, as well as the typical mass scale of 2 GeV for those states. The accuracy of the model can be compared to CGQCD [Szcz96], sharing formally many similarities with our T-matrix approach.

State	Lattice [Morn99]	CGQCD [Szcz96]	T-matrix $\alpha = 0.4$	T-matrix $\alpha = 0.141$
0^{++}	1.73 (5)(8)	1.98	1.96	2.17
0^{-+}	2.59 (4)(13)	2.22	2.26	2.39
2^{++}	2.40 (2.5)(12)	2.42	2.21	2.34

Table 4.1: Masses (in GeV) of the lowest-lying glueball states at zero temperature with the gauge group SU(3). Our results (fourth and fifth columns), are compared to the lattice data of [Morn99] (second column) and to the Coulomb gauge QCD study [Szcz96] (third column). The fourth column is a T-matrix calculation with the standard value $\alpha = 0.4$, while the value $\alpha = 0.141$ is taken in the last column. In both cases, σ = 0.176 GeV^2.

In order to evaluate the effects of the temperature on the running coupling constant, we have also produced results with $\alpha = 0.141$ since it is the value chosen in our finite-temperature computations (cfr. Section 4.5.1). The existence of such a running coupling is well-known; see *e.g.* the pioneering work [Casw74], where $\alpha(T)$ comes from standard renormalization arguments, the temperature playing the role of the energy scale. Although no definitive conclusion can be drawn yet to our knowledge, it is tempting to assume that $\alpha(0)$ is finite and larger than $\alpha(T > T_c)$; fits on the lattice static potential in [Kacz02] actually favour such a saturation at zero temperature. In this case, the scalar glueball has a high mass in comparison with [Morn99]. It could be understood by the fact that this channel is dominantly a S-wave state and it should be particularly sensitive to the strength of the Coulomb term and to a possible running of α with the temperature. Note that, in the rest of this thesis, we will focus on the temperature interval $(1-3)\,T_c$, in which the running of α can be neglected as confirmed by the quality of the fit on the lattice data with the single value $\alpha = 0.141$ (see Section 4.5.1). Let us note also that the discrepancies between our results and those from the lattice for scalar and pseudoscalar states can also be partly due to the existence of a strong instanton interaction [Math09a] not taken into account here.

Finally, the extension of the above calculations to any gauge group is straightforward in our approach since $\kappa_{\bullet;gg} = -1$ for all gauge groups. The interested reader will find a discussion of such a generalization in [Buis11a], where it is shown that the lowest-lying glueball masses is gauge-group independent within a constituent framework. In particular, the lowest-lying glueball masses are found independent of N_c in [Buis11a], in agreement with what is observed on the lattice [Luci10]. That is why the T-matrix masses given in Table 4.1 are considered as valid for any gauge group too.

4.4.3 Meson spectrum

Adopting the same procedure as the one for gluons, the meson spectrum can also be computed. We only focus on states with an orbital angular momentum $L = 0$ or $L = 1$ whose quantum numbers are given in

Table 4.2. Several J^{PC} are obviously associated to $L = 0$ or $L = 1$. Since the potential (4.4.2) does not depend on other quantum numbers, all these states are degenerate within our approach.

J	L	S	P	C	J^{PC}
0	0	0	$-$	+	0^{-+}
	1	1	+	+	0^{++}
1	1	0	+	$-$	1^{+-}
	0	1	$-$	$-$	1^{--}
	1	1	+	+	1^{++}
2	1	1	+	+	2^{++}

Table 4.2: J^{PC} states allowed for $q\bar{q}$ with $L = 0$ or $L = 1$. The selection rule is $|J - S| \leq L \leq J + S$ where S is the spin of the two-particle states. Since the intrinsic spin of quarks is 1/2, a spin 0 or a spin 1 is allowed. The parity P of the state is given by $(-1)^{L+1}$, while the charge conjugaison C is $(-1)^{L+S}$.

We summarize in Table 4.3 the parameters we have to fix. There are essentially two main points to notice. Firstly, a shift of 0.3 GeV to the [PDG] quark "bare" mass is used. It is a common assumption within quasiparticle approaches since this shift corresponds to one third of the nucleon mass. Secondly, the string breaking depends on the quark flavour. This could be explained by the following argument: It is not the same region of the potential that contributes for all quark flavour. Indeed, light quarks are more sensitive to the linear part of the interaction, while the heavy-quark potential is dominated by the Coulomb part. According to this interpretation, $V_{q\bar{q}}^{sb}$ has to be higher for light quarks and has to decrease with heaviest quark flavour. It is exactly what we observe with the parameters chosen to fit the meson spectrum in Table 4.3.

Quark composition	$V_{q\bar{q}}^{sb}$	m_0^1	m_0^2
Light (l-l)	2.6	0.3	0.3
Strange (s-s)	2	0.4	0.4
Charm (c-c)	1	1.6	1.6
Beauty (b-b)	0.7	4.95	4.95
Kaon (l-s)	2.4	0.3	0.4

Table 4.3: Masses and string breaking (in GeV) for the different flavours of quarks.

In Table 4.4, our results are compared to experimental data extracted from [PDG]. In each case, we have associated the meson (with the same quark composition and quantum numbers) whose the mass is closest to the one that we have found within our T-matrix computations. As it can be noticed, a good agreement is reached provided that we do not consider the lightest pion and kaon *i.e.* $\pi(140)$ and $K(495)$. Indeed, the fact that the mass of these lightest mesons are not achievable can be explained by the theoretical origin of such states: The pion is the Goldstone boson resulting from the spontaneously breaking of the chiral symmetry. A so peculiar phenomenon can not be described within such simple effective model. Moreover, according to quasiparticle standard approaches, the spin effects are the weakest in a $S = 1$ channel. Since our computations do not take into account such effects, it is reasonable that our results for the $L = 0$ light meson are closed to the ρ instead of the π.

$L=0$	Exp.[PDG]	T-matrix	$L=1$	Exp.[PDG]	T-matrix
$\rho(u\bar{u},d\bar{d})$	0.77	0.72	$a_0(u\bar{u},d\bar{d})$	1.45	1.45
$\Phi(s\bar{s})$	1.02	1.08	$f_2'(s\bar{s})$	1.53	1.58
$K^*(l\text{-}s)$	0.89	0.89	$K(l\text{-}s)$	1.43	1.52
$J/\psi(c\bar{c})$	3.10	3.01	-		
$\Upsilon(b\bar{b})$	9.46	9.40	-		

Table 4.4: Masses (in GeV) of the $L=0$ and $L=1$ meson states at zero temperature with the gauge group SU(3). Our results (third and sixth columns), computed with $\alpha=0.4$ and $\sigma=0.176$ GeV^2, are compared to the experimental data of [PDG] (second and fifth columns).

Finally, let us add that, unlike in the glueball case, the $T=0$ meson mass depends on the gauge group since $\kappa_{\bullet;q\bar{q}}$ depends on it (see Appendix C). Within our approach, such study is not difficult to carry out. However, it is not one of our priorities and we have preferred to not dedicate time to establish the meson mass dependence in function of the gauge group. Indeed, as initially mentioned, the principal interest of the T-matrix computations at $T=0$ is to extract and to check the parameters we will use at $T\neq 0$ since, according to our knowledge, there is no available data concerning the QCD spectrum at finite-temperature regime.

4.5 QCD spectrum at finite temperature

Now that we have shown that the QCD spectrum at $T=0$ is quite well reproduced with our set of parameters, we can explore the finite-temperature regime in order to see whether or not such bound states survive above the critical temperature of deconfinement, T_c. This study requires a correct inclusion of the in-medium effects at the level of the potential, the masses and the propagator. This will be the point of the following discussion. The outcomes will be presented just hereafter.

4.5.1 Two-body potential and quasiparticle thermal mass

To fix the two-body potential and the quasiparticle mass at finite temperature, we have adopted a procedure similar to the one proposed in [Cabr07] in the case of heavy quark-antiquark bound states. The first step is to take some input from lQCD, from which accurate computations of the static free energy of a quark-antiquark pair bound in a colour singlet $F_1(r,T)$, are available. In particular, computations in quenched [7] SU(3) lQCD can be found in [Kacz02].

However, there is still debate on the proper potential term to use in phenomenological approaches, namely F_1 or the internal energy $U_1=F_1-T\partial_T F_1$. Spectral function analysis of heavy quarkonia from lQCD simulations of euclidean correlation functions typically suggest that the η_c and J/ψ states may survive up to about $2\,T_c$. Such values of the dissociation temperature can be accommodated if the singlet internal energy is used in potential model calculations [Albe05, Asak04, Riek10, Wong06]. That is the reason why we prefer developing an approach in which the internal energy extracted from lQCD [Kacz02] is the potential term, like in [Cabr07]. It is worth insisting on the fact that it is a choice to make in order to start the study.

7. In [Kacz05], results for unquenched SU(3) lQCD can also be found. The inclusion of quark loops is considered, which is an important refinement if one deals with mesons. Nevertheless, the free energy obtained is really closed to the quenched one, that is the reason why all our computations are done with the quenched form.

Nevertheless, the debate remains open and the following approach can be quite easily redone in function of its evolution.

For numerical convenience, it is preferable to deal with a fitted form of the potential, rather than with interpolations of the available points. To fit the data of [Kacz02], the analytic form proposed by Satz in [Satz06] is used:

$$F_1(r,T) = \frac{\sigma}{\mu(T)}\left[\frac{\Gamma(1/4)}{2^{3/2}\Gamma(3/4)} - \frac{\sqrt{\mu(T)r}}{2^{3/4}\Gamma(3/4)}K_{1/4}\left(\mu(T)^2r^2\right)\right] - \frac{4}{3}\frac{\alpha}{r}\left[\mathrm{e}^{-\mu(T)r} + \mu(T)r\right]. \quad (4.5.1)$$

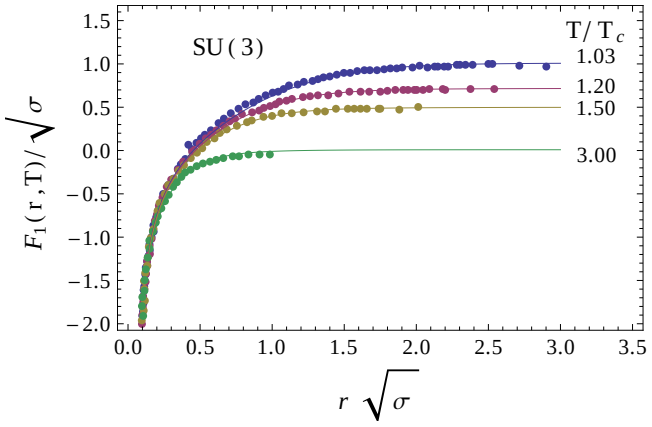

Figure 4.6: Static free energy $F_1(r,T)$ of a quark-antiquark pair bound in a colour singlet, computed in SU(3) quenched lattice QCD and plotted for different temperatures (symbols). Data are taken from [Kacz02] and expressed in units of $\sqrt{\sigma}$, with r the quark-antiquark separation. The fitted form (4.5.1) (solid lines) is compared to the lattice data.

The way of obtaining this formula is driven by the following physical idea. First, it is known that the static quark-antiquark energy at zero temperature is accurately fitted by a so-called funnel shape

$$F_1(r,0) = \sigma\, r - \frac{4}{3}\frac{\alpha}{r} = U_1(r,0), \quad (4.5.2)$$

as seen in Section 4.4.1. When $T > 0$, one can imagine that this potential is progressively screened by thermal fluctuations. An effective theory for studying the screening of a given potential is the Debye-Hückel theory [Deby23], in which the thermal fluctuations are all contained in a screening function $\mu(T)$, that modifies the zero-temperature potential and eventually leads to the form (4.5.1).

The explicit form of $\mu(T)$ is unknown *a priori* and has to be fitted on the lattice data. As it can be seen in Fig. 4.6, the form

$$\frac{\mu(T)}{\sqrt{\sigma}} \quad = \quad 0.537\frac{T}{T_c} + 0.644 + 0.112\ln\left(\frac{T}{T_c} - 0.967\right), \quad (4.5.3)$$

with $\alpha = 0.141$ and $\sigma = 0.176\ \mathrm{GeV}^2$, provides an accurate fit of the lattice data. A more complete fit should be such that $\mu(0) = 0$, but our model is not intended to be able to "cross" the phase transition in T_c. The

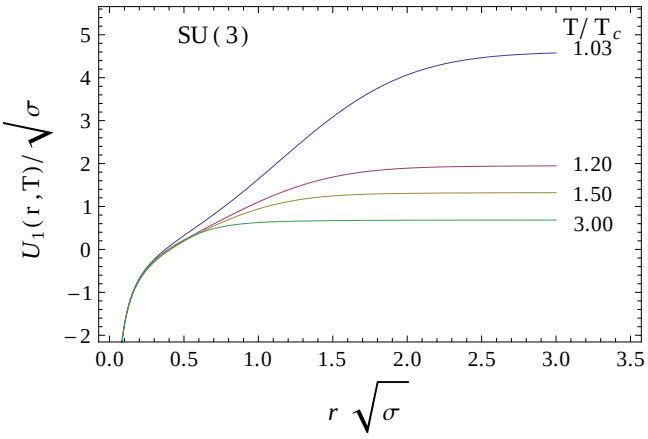

Figure 4.7: Internal energy $U_1(rT)$ of a quark-antiquark pair bound in a colour singlet, computed from the fitted form (4.5.1) and plotted for different temperatures (solid lines).

simple form (4.5.3) is already satisfactory. The corresponding internal energy $U_1 = F_1 - T\partial_T F_1$ is plotted in Fig. 4.7. Let us remark that $F_1(r,T)$ and $U_1(r,T)$ depend on T/T_c.

Now that a fitted form of potential is proposed in order to interpolate it between (1-3) T_c, we have to scale it to any two-body colour representation. Indeed, since we are above T_c, there is no reason to only consider colour-singlet representation. There is no more confinement. As at zero-temperature regime, we assume the Casimir scaling (4.3.13). Given $U_1(r,T)$ extracted from quenched SU(3) lattice data, the colour factor of the singlet quark-antiquark pair reads

$$\kappa_{\bullet;q\bar{q}} = -\frac{4}{9}. \tag{4.5.4}$$

According to (4.3.12), the potential (in position space) between two quasiparticles in the colour channel $\mathcal{C}$ is then given by

$$V(r,T) = \frac{\kappa_{\mathcal{C};p_1p_2}}{\kappa_{\bullet;q\bar{q}}}\left[U_1(r,T) - U_1(\infty,T)\right], \tag{4.5.5}$$

where the long-distance limit of the potential has to be normalized to zero in order to ensure the convergence of the scattering equation and to perform the Fourier's transformation. This is actually a standard procedure in finite-temperature calculations.

Moreover, considering the suggestion made in [Mocs05], the nonzero value of $U_1(\infty,T)$ should eventually be responsible of an effective in-medium contribution to the particle mass. The intuitive argument is that, when both particles are infinitely separated, they no longer interact. Therefore, the remaining potential energy should be seen as a manifestation of self-energy effects induced by the surrounding medium. These effects are encoded in the model as a mass shift to the "bare" quasiparticle mass, whose value has been fixed in Section 4.4.

Since $U_1(\infty,T)$ is then two times the in-medium SU(3) quark mass, the adaptation to any quasiparticle and to any gauge group must be done by extracting the correct colour-dependence. From Hard-Thermal-Loop (HTL) computations [Blai99], the quark self-energy colour dependence is given by C_2^q/C_2^{adj} at the

first order when it is added in the propagator as a mass term (m^2), that means here that

$$\frac{U_1(\infty,T)}{2} = \Delta(T)\,\sqrt{\frac{C_2^q}{C_2^{adj}}}\bigg|_{SU(3)}. \tag{4.5.6}$$

So,

$$\Delta(T) = \frac{3\,U_1(\infty,T)}{4}, \tag{4.5.7}$$

and $\Delta(T)$ is considered as an universal quantity within our approach.

For the cases under study, we finally have that the gluon thermal mass reads

$$\delta_g(T) = \sqrt{\frac{C_2^g}{C_2^{adj}}}\Delta(T) = \Delta(T), \tag{4.5.8}$$

since $C_2^g = C_2^{adj}$. So, $\delta_g(T)$ is gauge-group independent. For quark, we have

$$\delta_q(T) = \sqrt{\frac{C_2^q}{C_2^{adj}}}\Delta(T). \tag{4.5.9}$$

Instead of gluon, the in-medium effects are thus gauge-group dependent.

Finally, the effective in-medium gluon mass is given by

$$m_g(T)^2 = m_{g,0}^2 + \delta_g(T)^2, \tag{4.5.10}$$

while for quarks, it is

$$m_q(T)^2 = m_{q,0}^2 + \delta_q(T)^2, \tag{4.5.11}$$

in the same spirit as (4.4.4). δ_g and δ_q depend on T/T_c. The values $m_{g,0}$ and $m_{q,0}$ are taken from the zero-temperature analysis. Let us note that the values of V_{gg}^{sb} and $V_{q\bar{q}}^{sb}$ are not useful for the present study.

With lattice data taken from [Kacz02], the quasiparticle mass dependence on temperature is given in Fig. 4.8. As in standard quasiparticle approaches, the particle mass is rising quite sharply when $T \to T_c$ (with $T > T_c$) [Pesh96]. It is worth mentioning that in a recent work [Rugg12], it has been shown that the inclusion of a Polyakov loop dynamics leads to a gluon mass with a very smooth dependence on T. From HTL calculations, it is expected that at very high T, $m(T) \sim \sqrt{\alpha_S(T)}\,T$ [Blai99, Buis10b], with a quasilinear behaviour for $T \gtrsim 2\,T_c$. This is not the case in our model since our ansatz for the particle mass is not inspired from HTL theory but is instead completely driven – with no freedom – by data from [Kacz02], limited to $3\,T_c$. It could be interesting that new data above this temperature be computed in order to confirm or to infirm the decrease of $m(T)$.

It is obvious that the problem of the in-medium quasiparticle mass is far more complicated than the simple prescriptions (4.5.10) and (4.5.11), that have to be seen as valid in a first approximation only. A more refined mass should probably be momentum-dependent. There is indeed an increasing amount of evidences favouring the existence of a dynamically generated particle mass due to non-perturbative effects, at least at zero temperature. For the gluon, such a dynamically generated mass $m(p)$, with $m(\infty) = 0$ and $m(0)$ finite, is favoured by some lattice results in Landau gauge, see *e.g.* [Cucc10, Oliv11]. Also non-perturbative field-theoretical calculations, using for example the pinch technique, find a non-zero dynamically generated gluon and quark mass [Agui09, Bino09, Corn82]. It is also worth quoting the recent Coulomb gauge study [Rein11], which is a first step in view of understanding the behaviour of $m_g(p,T)$ at a non-perturbative level.

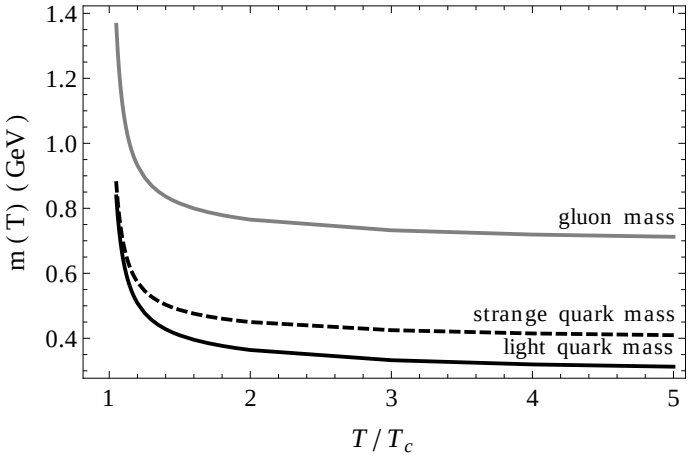

Figure 4.8: Thermal quasiparticle mass (GeV), given by (4.5.10) or (4.5.11) for a gauge group SU(3), as a function of the ratio T/T_c. Note that the gluon mass is independent of the gauge group.

From a different perspective, non-perturbative contributions to the gluon potential and mass are analysed at finite temperature in connection with the gluon condensates in [Megi07]. Such improvements of the particle masses can be in principle addressed within our approach by evaluating the self-energies from the T-matrix, see *e.g.* [Mann05]. This study is left for future works.

4.5.2 In-medium effects

As in [Cabr07], we have also added in-medium effects in our T-matrix computations: The Bose-enhancement and the Pauli blocking. According to [Prat94], these in-medium effects change the cross-section as follows,

$$\sigma^{med} = \sigma^{vac}(1 \pm f_{p_1})(1 \pm f_{p_2}), \tag{4.5.12}$$

where σ^{vac} and σ^{med} are respectively the cross-section in the vacuum and in the medium, and where f_p is the distribution function of the p-species. If the species is a boson,

$$f_p(\epsilon) = \frac{1}{e^{\beta(\epsilon-\mu)} - 1}, \tag{4.5.13}$$

while if the species is a fermion,

$$f_p(\epsilon) = \frac{1}{e^{\beta(\epsilon-\mu)} + 1}, \tag{4.5.14}$$

where μ is a possible chemical potential. The sign choice in (4.5.12) also depends on the nature of the particles: $+$ for bosons and $-$ for fermions. At the level of the T-matrix LS equation, the in-medium effects are then included as follows [Cabr07]

$$\begin{aligned} T_{J^{P(C)}}(E;q,p) &= V_{J^{P(C}}\,(q,p) + \frac{1}{8\pi^3}\int_0^\infty dk\, k^2\, V_{J^{P(C)}}(q,k)\, G_{BbS}(E;k) \\ &\times \; T_{J^{P(C)}}(E;k,p)\,[(1 \pm f_{p_1})(1 \pm f_{p_2})]\,. \end{aligned} \tag{4.5.15}$$

4.5.3 Glueball spectrum

Since all the modifications generated by the medium are now introduced, we can compute the lightest glueball spectrum at finite temperature by using the formula (4.5.15) with the potential (4.5.5)[8] and the threshold mass $2\,m_g(T)$, given by (4.5.10). T_c is fixed to 0.3 GeV in our computations, in agreement with the lQCD value [Yagi05]. The results are shown in Table 4.5 for the different allowed colour channels. Indeed, since there is no confinement any more, there is no more reason to only consider the colour-singlet representation. The results displayed in Table 4.5 were published in [Lacr13] without the inclusion of the Bose-enhancement. Nevertheless, it was checked that these results were slightly modified by the inclusion of the in-medium effects. So, this finding leads to the conclusion that the Bose-enhancement is negligible for these systems (see Section 4.5.4).

Channel		Singlet			Adjoint			(2,0)		
Group		All			SU($N_c \geq 3$)			G_2		
T/T_c	$2\,m_g$	0^{++}	0^{-+}	2^{++}	0^{++}	0^{-+}	2^{++}	0^{++}	0^{-+}	2^{++}
1.05	2.73	1.88 2.72	2.27	2.27	2.50	2.70	2.64	2.58	-	2.68
1.10	2.20	1.90	2.18	2.09	2.15	-	-	2.19		-
1.15	1.98	1.84	-	1.96	-			-		
1.20	1.86	1.80		-						
1.25	1.79	1.76								
1.30	1.74	1.73								
1.35	1.70	-								

Table 4.5: Masses (GeV) of lowest-lying glueballs above T_c ($T_c = 0.3$ GeV). A line mark the temperature at which a bound state is not detected any more.

We only consider in Table 4.5, the lightest glueball spectrum with SU(N_c) and G_2 gauge groups in order to not complicate the discussion. Indeed, some predictions for other gauge groups can be easily done by analysing the factor $\kappa_{\mathcal{C};gg}$. Since the lightest glueballs are J^{PC} symmetric, only the symmetric colour representations have to be taken into account here. Naturally, the singlet is one of them with $\kappa_{\bullet;gg} = -1$ for all the gauge groups. Moreover, the gluon mass is independent of N_c. This implies that the masses of the colour-singlet bound states are the same for all the considered gauge groups.

The evolution of the imaginary part of the on-shell T-matrix in the singlet scalar channel versus the temperature is displayed in Fig. 4.9: This gives an overall picture of the glueball progressive dissolution in the medium. The peak in the imaginary part, depicting a bound state, becomes smaller and smaller before melting into the continuum (and thus $\det \mathcal{F}$ does not vanish any more below threshold) as the temperature is increased. Still, for $T > T_{\text{dis}}$, T_{dis} being the dissociation temperature of the considered bound state, and above the threshold energy, one finds sizable strength from the bound state relic, the T-matrix exhibiting a resonant behaviour well beyond the Born approximation.

Concerning the pseudoscalar and the tensor channel, singlet bound states are found up to 1.10-1.15 T_c. Note that states in the pseudoscalar channels, which in our approach correspond to pure P-wave state, are just mildly bound due to the centrifugal barrier. The tensor states, having a S-wave component, lie between the scalar and pseudoscalar channels, regarding binding and dissociation temperatures.

8. Remember that a given J^{PC} glueball potential is a peculiar combination of partial-wave potentials, see Section 4.4.2.

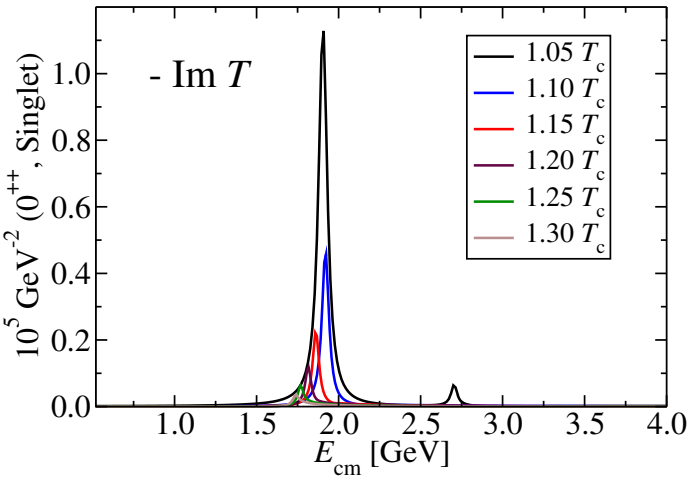

Figure 4.9: ImT for gg-scattering in the 0^{++} singlet channel for various T with $T_c = 0.3$ GeV.

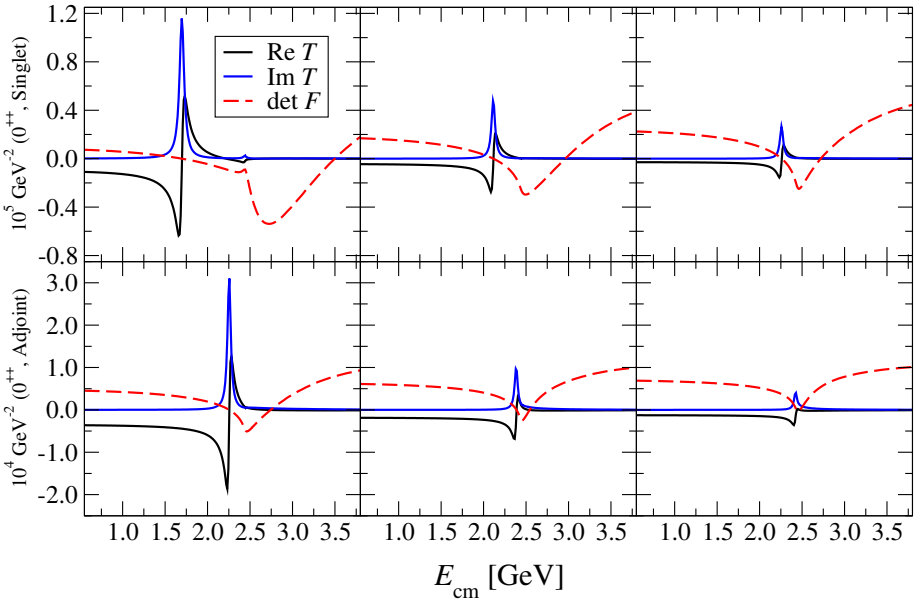

Figure 4.10: T-matrix for gg-scattering in the scalar singlet and scalar symmetric adjoint channels for SU($N_c \geq 3$). From left to right the temperatures are (1.05;1.10;1.15) T_c, with $T_c = 0.3$ GeV.

Bound states in the symmetric adjoint channel of SU($N_c \geq 3$) and $(2,0)^S$ of G_2 [9] are also studied (see Table 4.5), although they are less bound since $\kappa_{\mathcal{C};gg}$ is respectively $-1/2$ and $-5/12$. The scalar channel

9. The representations of SU(N_c) and G_2 are given in Appendix C.

disappears above 1.10 T_c, whereas in the pseudoscalar and tensor channels, bound states are lying right below the threshold energy at the lowest considered temperature (*i.e.* 1.05 T_c). The differences between the singlet and these two channels have to be attributed to the strength of the potential, which is two times smaller than in the colour singlet. The evolution of the T-matrix in the singlet and adjoint scalar channel versus the temperature is displayed in Fig. 4.10. One clearly sees the disappearance of this bound state at 1.15 T_c while the singlet state is still well bound at this temperature.

There are in general other coloured channels than the singlet and adjoint one. For SU(N_c) gauge groups in particular, the only one that could *a priori* lead to bound states (since the $(2, 0, \ldots, 0, 2)^S$ is repulsive) is the $(0, 1, 0, \ldots, 0, 1, 0)^S$ channel (see Appendix C), which is weakly attractive and exists only for $N_c > 3$. It has been checked that even the scalar state (the most attractive channel) is unbound at $N_c = 4$. Hence this colour channel does not admit bound states within our model.

Only a few papers are devoted to the existence of glueballs at finite temperature on the lattice [Ishi02, Meng09], and the interpretation of their results depends mostly on the way the glueball correlators are fitted: Either a single narrow pole, or a Breit-Wigner shape. Let us focus on the narrow pole fit, which identifies bound states in a way similar to ours. The main observation to be made from [Ishi02, Meng09] is that the glueball masses decrease above T_c with increasing temperature, with a mass near T_c that is similar to the zero temperature one. This non-trivial behaviour is well-checked within our approach. Two competing effects are responsible for the temperature evolution of the spectrum: reduction of the binding energy and downward shift of the threshold energy due to the decrease of the gluon mass. Overall, the singlet scalar bound state experiences a mild shift to lower energies and dissociates at $T_{\text{dis}} \approx 1.3\,T_c$. This is the value from which $\det \mathcal{F}$ does not vanish any more. Nevertheless, considerable strength remains at threshold up to about $1.5\,T_c$. This is in qualitative agreement with the spectral function analysis of Euclidean correlators by the CLQCD Collaboration [Meng09].

4.5.4 General QCD spectrum

In order to complete the two-body QCD spectrum at finite temperature, we have to consider much more states than the mesons, as done at $T = 0$. Indeed, since we are in the deconfinement range, the formation of bound states as qq, $\bar{q}\bar{q}$, qg and $\bar{q}g$ is also allowed. However, due to the assumed universality of our interaction, the procedure is almost the same as the one developed to analyse the glueball spectrum. Therefore, studying such states is just a matter of computational time.

In this section, we only show the outcomes with a gauge group SU(3). Even if within our approach, the generalization to any gauge group is straightforward (it just requires a careful enumeration of all the colour channels and the computation of all the associated mass and T-matrix files), this study is left for further developments. Indeed, the discussion is already quite dense due to the large number of two-body channels to consider.

In order to stay coherent with the lQCD data [Aoki06] concerning T_c, this value is moved to 0.15 GeV within our calculations while in the glueball sector, a value of 0.3 GeV was used. Since in-medium effects are included in the T-matrix (4.5.15), a change of T_c has to affect the glueball spectrum. Fortunately, if we draw a comparison between Table 4.5 and Table 4.6, we can notice that the effect of the Bose-enhancement is quite negligible as already mentioned. So, the all qualitative features discussed in Section 4.5.3 remain unchanged and the quantitative values are just slightly shifted.

The $q\bar{q}$, qq and $\bar{q}\bar{q}$ channels are also analysed for $L = 0$ or $L = 1$ as at $T = 0$; this generates all the states presented in Table 4.7. The meson sector has not to respect any Pauli's symmetry principle unlike the qq and $\bar{q}\bar{q}$ sectors with two same flavours of (anti)quarks, for which the selection rule is summarized in the following tables.

Channel		Singlet			Adjoint		
T/T_c	$2\,m_g$	0^{++}	0^{-+}	2^{++}	0^{++}	0^{-+}	2^{++}
1.05	2.73	1.90	2.29	2.29	2.52	2.71	2.65
1.10	2.20	1.92	2.19	2.10	2.16	-	-
1.15	1.98	1.87	-	1.97	-		
1.20	1.86	1.82		-			
1.25	1.79	1.78					
1.30	1.74	-					

Table 4.6: Masses (GeV) of lowest-lying SU(3) glueball spectrum above T_c ($T_c = 0.15$ GeV). A line mark the temperature at which a bound state is not detected any more.

u and d quarks		s quarks	
Colour	L, S, I	Colour	L, S
A	$(-1)^{L+S+I} = 1$	A	$(-1)^{L+S+1} = 1$
S	$(-1)^{L+S+I} = -1$	S	$(-1)^{L+S+1} = -1$

A new quantum number is added for the u and d quarks : I stands for the isospin.

$q\bar{q}$ sector						qq and $\bar{q}\bar{q}$ sector				
J	L	S	P	C	J^{PC}	J	L	S	P	J^P
0	0	0	$-$	+	0^{-+}	0	0	0	+	0^+
	1	1	+	+	0^{++}		1	1	$-$	0^-
1	1	0	+	$-$	1^{+-}	1	1	0	$-$	1^-
	0	1	$-$	$-$	1^{--}		0	1	+	1^+
	1	1	+	+	1^{++}		1	1	$-$	1^-
2	1	1	+	+	2^{++}	2	1	1	$-$	2^-

Table 4.7: Allowed J^P states for $q\bar{q}$, qq and $\bar{q}\bar{q}$

The Tables 4.8 and 4.9 summarize all our data for the lightest quarks. Several comments can be done. Unlike to the glueball sector, the two-body finite-temperature spectrum made of (anti)quarks is poor. Only states with $L = 0$ survive in all the attractive channels. This is coherent with what we have observed for glueballs. Indeed, only states with a large S-wave proportion survive quite well above T_c. Nevertheless, they melt here quickly inside the medium even if considerable strength remains at threshold up to about 1.3 T_c. Only the strange meson is still present at 1.10 T_c, the last temperature before the melting of all the bound states. This observation could be understood by the comparison of the $\kappa_{\mathcal{C}}$ magnitude. Indeed, $\kappa_{\bullet;gg} = -1$, which is more than two times the magnitude of a $\kappa_{\mathcal{C}}$ involved in the interactions between (anti)quarks.

Another interesting remark to do at this stage is the sameness of the bound-state masses for all the type of interactions: light-light, strange-strange or light-strange. This can be understood by remembering that the mass of the quasiparticle is given by (4.5.11). Indeed, within this formula, the bare light (0.3 GeV) and strange (0.4 GeV) quark masses are really close to each other and so, significant differences as observed

in the $T = 0$ spectrum can not be reached here. Moreover, unlike the glueball sector, no meson masses around T_c are close to the $T = 0$ ones. Since it does not exist any results about the meson spectrum at finite temperature, we have no check of this feature.

Concerning the qg and $\bar{q}g$, the building of the J^P states requires the helicity formalism since the gluon is transverse. The states on which we focus are given in Appendix B. Due to their partial-wave decomposition, the potential reads

$$(J1)\ V_{\frac{1}{2}^+}(q,q') = V_1(q,q'), \tag{4.5.16}$$

$$(J2)\ V_{\frac{3}{2}^-}(q,q') = \frac{1}{6}V_0(q,q') + \frac{5}{6}V_2(q,q'), \tag{4.5.17}$$

$$(J3)\ V_{\frac{3}{2}^-}(q,q') = \frac{1}{2}V_0(q,q') + \frac{1}{2}V_2(q,q'), \tag{4.5.18}$$

$$(J4)\ V_{\frac{1}{2}^-}(q,q') = \frac{2}{3}V_0(q,q') + \frac{1}{3}V_2(q,q'), \tag{4.5.19}$$

$$(J5)\ V_{\frac{3}{2}^+}(q,q') = \frac{7}{10}V_1(q,q') + \frac{3}{10}V_3(q,q'), \tag{4.5.20}$$

$$(J6)\ V_{\frac{3}{2}^+}(q,q') = \frac{9}{10}V_1(q,q') + \frac{1}{10}V_3(q,q'). \tag{4.5.21}$$

Note that the parity is given for qg and has to be reversed for $\bar{q}g$. The nomenclature $J1 \to J6$ is used for simplicity.

From Table 4.9, similar comments can be done and can explain the quick melting of these bound states inside the plasma. Therefore, the main conclusion of this study is that only glueballs seem to significantly survive above T_c.

Nevertheless, it is worth quoting the works of [Hees09, Mann05] in which a Brueckner many-body T-matrix approach similar to ours is used to evaluate elastic heavy-quark-light-quark scattering amplitudes and to study the properties of light (anti-) quarks in a QGP at moderate temperatures, $T \sim$ 1-2 T_c. Heavy-quark-light-quark meson and diquark channel resonance states seem to be formed for temperatures up to $\sim 1.5\, T_c$. Moreover, it is also important to remember that heavy quarkonia, as η_c and J/ψ, may survive up to about $2\, T_c$ [Albe05, Asak04, Cabr07, Riek10, Wong06]. This studies are left for further developments within our approach.

Light quark sector									
Channel		$q\bar{q}$ $(L=0)$		$q\bar{q}$ $(L=1)$		$qq/\bar{q}\bar{q}$ $(L=0)$		$qq/\bar{q}\bar{q}$ $(L=1)$	
$\kappa_{\mathcal{C}}$		-4/9	1/18	-4/9	1/18	1/9	-2/9	1/9	-2/9
T/T_c	$2\,m_l$								
1.05	1.67	1.51	-	-	-	-	1.67	-	-
1.10	1.28	-					-		
Strange quark sector									
Channel		$q\bar{q}$ $(L=0)$		$q\bar{q}$ $(L=1)$		$qq/\bar{q}\bar{q}$ $(L=0)$		$qq/\bar{q}\bar{q}$ $(L=1)$	
$\kappa_{\mathcal{C}}$		-4/9	1/18	-4/9	1/18	1/9	-2/9	1/9	-2/9
T/T_c	$2\,m_s$								
1.05	1.76	1.57	-	-	-	-	1.74	-	-
1.10	1.38	1.38					-		
1.15	1.23	-							
Light-strange quark sector									
Channel		$q\bar{q}$ $(L=0)$		$q\bar{q}$ $(L=1)$		$qq/\bar{q}\bar{q}$ $(L=0)$		$qq/\bar{q}\bar{q}$ $(L=1)$	
$\kappa_{\mathcal{C}}$		-4/9	1/18	-4/9	1/18	1/9	-2/9	1/9	-2/9
T/T_c	$m_l + m_s$								
1.05	1.71	1.54	-	-	-	-	1.71	-	-
1.10	1.33	-					-		

Table 4.8: Masses (GeV) of lowest-lying SU(3) QCD spectrum above T_c ($T_c = 0.15$ GeV). A line mark the temperature at which a bound state is not detected anymore.

Light (anti)quark - gluon sector										
Channel		$J1$			$J2$			$J3$		
$\kappa_{\mathcal{C}}$		-1/2	1/6	-1/6	-1/2	1/6	-1/6	-1/2	1/6	-1/6
T/T_c	$m_l + m_g$									
1.05	2.20	-	-	-	-	-	-	2.13	-	-
1.10	1.74							-		
Channel		$J4$			$J5$			$J6$		
$\kappa_{\mathcal{C}}$		-1/2	1/6	-1/6	-1/2	1/6	-1/6	-1/2	1/6	-1/6
T/T_c	$m_l + m_g$									
1.05	2.20	2.06	-	-	-	-	-	-	-	-
1.10	1.74	-								
Strange (anti)quark - gluon sector										
Channel		$J1$			$J2$			$J3$		
$\kappa_{\mathcal{C}}$		-1/2	1/6	-1/6	-1/2	1/6	-1/6	-1/2	1/6	-1/6
T/T_c	$m_s + m_g$									
1.05	2.24	2.31	-	-	-	-	-	2.17	-	-
1.10	1.79	-						-		
Channel		$J4$			$J5$			$J6$		
$\kappa_{\mathcal{C}}$		-1/2	1/6	-1/6	-1/2	1/6	-1/6	-1/2	1/6	-1/6
T/T_c	$m_s + m_g$									
1.05	2.24	2.10	-	-	-	-	-	-	-	-
1.10	1.79	-								

Table 4.9: Masses (GeV) of lowest-lying SU(3) QCD spectrum above T_c ($T_c = 0.15$ GeV). A line mark the temperature at which a bound state is not detected anymore.

Chapter 5

Thermodynamics of the QCD Deconfined Phase

Within this chapter, we will study the thermodynamics of the QCD deconfined phase by resorting to the Dashen, Ma and Berstein's (DMB) formalism [Dash69]. Such a formalism is particularly well suited for systems whose microscopic constituents behave according to relativistic quantum mechanics. The QGP is indeed identified here to a quantum gas of gluons and quarks, which are seen as the effective degrees of freedom propagating in the plasma [1]. This assumption is actually common to all the so-called quasiparticle approaches, see e.g. [Buis10a, Gore95]. The particularity of our work is that it is *a priori* possible to investigate the behaviour of the QGP just above the critical temperature of deconfinement T_c, in the strongly-interacting regime. In this temperature range, the interactions between the particles remain still important and so, are possibly sufficient to bound quasiparticles; Remember the T-matrix computations [2] driven in Chapter 4.

However, the concept of quasiparticle itself could become questionable in such a strongly-interacting regime. Indeed, such interactions could cause large width. A consensus seems to exist about the relevance of this notion for plasma above $3\,T_c$, but the situation is less clear below [Blai05]. A first encouraging remark is that the notion of quasiparticles has been successful in condensed matter physics where strongly-correlated systems are well described by effective field theories. This does not prove that the situation is similar in hot QCD, but this kind of approach has already produced very good results [Blum11]. It has also been suggested that the assumed smooth crossover between confinement and deconfinement may make it possible to approximate the QCD thermodynamics near crossover in terms of the quasiquarks and quasigluons [Fuku13]. In order to perform a coherent description of the QGP, it is possible to compute the width of the quasiparticles by a self-consistent procedure [Mann05, Tolo08]. This more sophisticated task can be by-passed by the use of a constant width to estimate the effect of a quasiparticle self-energy [Vanh08, Hugg12], as done in Section 4.3.3.

In the first section of this chapter, we will expose the main principles of the DMB formalism, and we will directly apply it to QCD. A restriction to the two-body interactions will be used and some considerations about the Born approximation will be also presented.

1. Remember that the hadronic degrees of freedom can not describe any more thermodynamics above a certain temperature, called the Hagedorn temperature, T_h (see Chapter 3).

2. Such a metastable phase in which hadron, quark and gluon degrees of freedom coexist, is allowed between T_c and T_h (see Chapter 3).

Then, we will study different thermodynamic situations. The first case will be the gluon plasma. This latter is interesting for several reasons. Firstly, from technical point of view, we have only to take care of one particle species. It simplifies drastically the problem while the main feature of the description, *i.e.* the explicit inclusion of interactions in a quasiparticle approach, is kept. Secondly, the pure-gauge thermodynamic features (in particular, the EoS) are well-known in lQCD; This will allow an accurate comparison between our phenomenological approach and the lQCD calculations. Finally, with this simple case, we will be also able to study the generalization of the formalism to any gauge group. A particular attention will be dedicated to SU(N_c) and the large-N_c limit, and to G_2. All these results are developed in our paper [Lacr13].

Another thermodynamic situation of interest will be naturally the study of the full QGP. A plasma with two light species will be firstly studied in order to identify the main features of the quark inclusion. Then, we will discuss the 2 + 1 QGP [3]. Of course, our data will be compared to lQCD ones. These latter are mainly available at zero or weak baryonic potential μ. These two areas will be thus investigated. This last work is planned to be presented in a future paper.

5.1 Dashen, Ma and Bernstein's formalism applied in QCD

5.1.1 Generalities

The DMB formalism [Dash69] is a formulation of statistical mechanics in terms of S-matrix (or equivalently, T-matrix) elements which is built to study gaseous systems of
(non-)relativistic particles. The main outcome is a prescription to compute the grand canonical potential Ω defined in (2.1.4), for such systems. This latter, expressed as an energy density, is given by

$$\Omega = \Omega_0 + \sum_\nu \left[\Omega_\nu - \frac{\mathrm{e}^{\beta\vec{\mu}\cdot\vec{N}}}{2\pi^2\beta^2} \int_{M_\nu}^{\infty} \frac{d\epsilon}{4\pi i}\, \epsilon^2\, K_2(\beta\epsilon)\ \mathrm{Tr}_\nu \left(\mathcal{S} S^{-1} \overleftrightarrow{\partial_\epsilon} S \right) \Big|_c \right]. \tag{5.1.1}$$

This prescription simply reduces to the calculation of virial coefficients in the non-relativistic case.

In the above equation, the first term Ω_0, is the grand canonical potential of the free relativistic particles, *i.e.* the remaining part of the grand canonical potential if the interactions are turned off. The second term accounts for interactions in the plasma and is a sum running on all the species, the number of particles included, and the quantum numbers necessary to fix a channel. The characteristics of all these channels is generically denoted ν. The vectors $\vec{\mu} = (\mu_1, \mu_2, \dots)$ and $\vec{N} = (N_1, N_2, \dots)$ contain the chemical potentials and the particle number of each species taking part in a given scattering channel.

Despite the fact that the T-matrix allows an unified treatment of bound and scattering states, we will follow precisely the procedure of [Dash69] and consider separately the contributions below and above the threshold [4] M_ν. Below the threshold, one has Ω_ν, the grand canonical potential coming from bound states in the channel ν, seen as free additional species in the plasma, and appearing as poles of the T-matrix. Above the threshold, one has the scattering contribution, where the trace is taken in the center-of-mass frame of the channel ν and where S is the S-matrix, depending in particular on the total energy ϵ. The symmetrizer $\mathcal{S}$ enforces the Pauli's principle when a channel involving identical particles is considered, and the subscript c means that only the connected scattering diagrams are taken into account. Notice that $K_2(x)$ is the modified Bessel function of the second kind, and that the notation $A\overleftrightarrow{\partial_x}B = A(\partial_x B) - (\partial_x A)B$ is used.

By definition, $S = 1 - 2\pi i\, \delta(\epsilon - H_0)\, T$, where T is the off-shell T-matrix and where H_0 is the free Hamiltonian of the system. A convenient way to compute the T-matrix is to solve the LS equation for the

3. 2+1 means two light quark flavours (u and d) and one strange quark (s).
4. Within this approach, the threshold is the summation on the masses of all the particles included in a given channel ν.

off-shell T-matrix as seen and carried out in Chapter 4. Once the T-matrix is known, the plasma EoS is obtained from (5.1.1) and the pressure is simply given by (recall Section 2.1.1)

$$p = -\Omega. \tag{5.1.2}$$

The other thermodynamic observables can derived from p, like the entropy density or the trace anomaly ($\Delta = e - 3\,p$, where e is the energy density).

For later convenience, the thermodynamic quantities will be normalized to the SB pressure, which is defined as

$$p_{SB} = -\lim_{m_i \to 0} \Omega_0, \tag{5.1.3}$$

m_i being the masses of the particles propagating in the medium. This is a standard way to present results, especially in lQCD. Moreover, the normalized trace anomaly can be computed by the following formula

$$\frac{\Delta}{p_{SB}} = -\beta \left(\partial_\beta \frac{p}{p_{SB}} \right)_{\beta\mu}. \tag{5.1.4}$$

5.1.2 Application in QCD

Let us now particularize the general formalism presented in the previous section to QCD. The bosonic degrees of freedom propagating in the plasma are then the quasigluons while the fermionic ones are the quasiquarks. According to standard formulas in statistical mechanics, one has that the grand canonical potential for free relativistic particles is

$$\begin{aligned} \Omega_0^{\rm QCD} &= \underbrace{2 \dim adj\, \omega_0^B(m_g, \mu_g)}_{gluons} \\ &+ \underbrace{2 \sum_{n=1}^{N_f} \dim q_n\, \omega_0^F(m_{q_n}, \mu_{q_n})}_{quarks} + \underbrace{2 \sum_{n=1}^{N_f} \dim q_n\, \omega_0^F(m_{q_n}, -\mu_{q_n})}_{antiquarks}, \end{aligned} \tag{5.1.5}$$

where the quasigluons [5] g are *a priori* supposed to have a mass m_g and the quasiquarks q_n, a mass m_{q_n}. μ_g and μ_{q_n} are respectively the chemical potential of the gluon and the considered quark flavour. The particle degrees of freedom are the following. The gluon is a transverse spin-1 (so, two spin projections) boson lying in the adjoint representation of the gauge group, while the quark (resp. antiquark), existing in N_f different flavours, is a spin-1/2 fermion belonging in the fundamental (resp. conjugate) gauge-group representation. The grand canonical potential per degree of freedom associated to a bosonic species $\omega_0^B(m,\mu)$, and to a fermionic species $\omega_0^F(m,\mu)$, with mass m are given by

$$\omega_0^B(m,\mu) = \frac{1}{2\pi^2\beta} \int_0^\infty dk\, k^2 \ln\left(1 - \mathrm{e}^{-\beta\left(\sqrt{k^2+m^2}-\mu\right)}\right), \tag{5.1.6}$$

$$\omega_0^F(m,\mu) = -\frac{1}{2\pi^2\beta} \int_0^\infty dk\, k^2 \ln\left(1 + \mathrm{e}^{-\beta\left(\sqrt{k^2+m^2}-\mu\right)}\right). \tag{5.1.7}$$

5. The term "quasiparticle" enforces the fact that the particle acquires effective properties. However, the prefix "quasi" will be given up in the following, in order to not overload the notation.

Equation (5.1.3) leads to

$$p_{SB} = \frac{\pi^2}{45\beta^4}\left[\dim adj \; + \frac{7}{4}\sum_{n=1}^{N_f}\dim q_n\right]. \tag{5.1.8}$$

Concerning the second and third terms in (5.1.1), the sum $\sum_\nu$ now explicitly reads $\sum_{(n_g,n_q,n_{\bar{q}})}\sum_{\mathcal{C}}\sum_{J^P}$, where n_g, n_q, $n_{\bar{q}}$ are respectively the number of gluons, quarks and antiquarks involved in the interaction process. As soon as $n_g > 2$ (and in minor measure, n_q,$n_{\bar{q}} > 2$), the determination of the allowed colour channels and of the correct symmetrized gluon states generally becomes a painful task, to which the problem of finding the T-matrix in many-body scattering must be added. Intuitively, one can nevertheless expect the dominant scattering processes to be two-body ones. These processes are the only ones considered here.

After simplification, the grand canonical potential (5.1.1) eventually reads

$$\begin{aligned}\Omega_{(2)}^{\rm QCD} &= \Omega_0^{\rm QCD} \\ &+ \sum_{n_g+n_q+n_{\bar{q}}=2} e^{\beta(\mu_1+\mu_2)}\sum_{\mathcal{C}}\sum_{J^P}\dim\mathcal{C}\,(2J+1)\Big\{\omega_0^{B/F}(M^{BS}_{\mathcal{C},J^P}) \\ &+ \frac{1}{2\pi^2\beta^2}\int_{m_1+m_2}^{\infty} d\epsilon\,\epsilon^2\,K_2(\beta\epsilon)\,{\rm Tr}_{\mathcal{C},J^P}\Big[(\delta{\rm Re}T)' \\ &- 2\pi\Big((\delta{\rm Re}T)(\delta{\rm Im}T)' - (\delta{\rm Im}T)(\delta{\rm Re}T)'\Big)\Big]\Big\},\end{aligned} \tag{5.1.9}$$

where the summation is restricted to two-body channels *i.e.* gg, qq, $\bar{q}\bar{q}$, $q\bar{q}$, gq and $g\bar{q}$. m_1 and m_2 are the masses of the two considered particles while μ_1 and μ_2 are the associated chemical potential The subscript "prime" is the derivative respective to the energy and $M^{BS}_{\mathcal{C},J^P}$ are the masses of the two-body bound states (if they exist) with colour $\mathcal{C}$ and quantum numbers J^P. In the remaining trace, it is understood that the T-matrix is computed in a given two-body channel with colour $\mathcal{C}$ and quantum numbers J^P, and that the Dirac δ reads $\delta(\epsilon-\epsilon_1(q)-\epsilon_2(q))$, with the dispersion relation $\epsilon_i(q)=\sqrt{q^2+m_i^2}$. These T-matrices are computed thanks to the method detailed in the previous chapter.

It is more convenient to express (5.1.9) as

$$\Omega_{(2)}^{\rm QCD} = \Omega_0^{\rm QCD} + \Omega_{bs}^{\rm QCD} + \Omega_s^{\rm QCD}, \tag{5.1.10}$$

with

$$\Omega_{bs}^{\rm QCD} = \sum_{n_g+n_q+n_{\bar{q}}=2} e^{\beta(\mu_1+\mu_2)}\sum_{J^P}(2J+1)\sum_{\mathcal{C}}\dim\mathcal{C}\,\omega_0^{B/F}(M^{BS}_{\mathcal{C},J^P}), \tag{5.1.11}$$

is the contribution of bound states inside the plasma while $\Omega_s^{\rm QCD}$ is the scattering part given by

$$\begin{aligned}\Omega_s^{\rm QCD} &= \sum_{n_g+n_q+n_{\bar{q}}=2} e^{\beta(\mu_1+\mu_2)}\sum_{\mathcal{C}}\sum_{J^P}\frac{\dim\mathcal{C}}{2\pi^2\beta^2}\,(2J+1)\int_{M_{\mathcal{C},J^P}}^{\infty} d\epsilon\,\epsilon^2\,K_2(\beta\epsilon) \\ &\times \; {\rm Tr}_{\mathcal{C},J^P}\left[(\delta{\rm Re}T)' - 2\pi\Big((\delta{\rm Re}T)(\delta{\rm Im}T)' - (\delta{\rm Im}T)(\delta{\rm Re}T)'\Big)\right].\end{aligned} \tag{5.1.12}$$

To produce numerical data, it is thus necessary to express $\Omega_s^{\rm QCD}$ in momentum space. Using the following definitions concerning the trace of an operator A in momentum space

$${\rm Tr}A = \frac{1}{(2\pi)^3}\int_{-\infty}^{\infty} d\vec{q}\,\langle\vec{q}|A|\vec{q}\rangle, \tag{5.1.13}$$

the partial-wave expansion

$$\langle \vec{q}|A|\vec{q}'\rangle = A(q,q',\hat{q}.\hat{q}') = \frac{1}{4\pi}\sum_l (2l+1)A_l(q,q')P_l(\hat{q}.\hat{q}'), \tag{5.1.14}$$

where $P_l(x)$ is the Legendre polynomial of order l, and the fact that a general J^P state is a combination of $|^{2S+1}L_J\rangle$ states, (5.1.12) reads after a tedious calculation

$$\begin{aligned}
\Omega_s^{\rm QCD} &= \frac{1}{64\pi^5\beta^2}\sum_{n_g+n_q+n_{\bar{q}}=2} e^{\beta(\mu_1+\mu_2)}\sum_{J^P}(2J+1)\sum_{\mathcal{C}}{\rm dim}\mathcal{C} \\
&\Bigg(\beta\int_{m_1+m_2}^{\infty} d\epsilon\,\epsilon^2\,\omega(\epsilon)\,\Lambda(\epsilon)K_1(\beta\epsilon)\,{\rm Re}T_{\mathcal{C},J^P}(\epsilon;\omega(\epsilon),\omega(\epsilon)) \\
&-\frac{1}{16\pi^2}\int_{m_1+m_2}^{\infty} d\epsilon\,\epsilon^2\,\omega(\epsilon)^2\,\Lambda(\epsilon)^2K_2(\beta\epsilon) \\
&\qquad\times\left[{\rm Re}T_{\mathcal{C},J^P}(\epsilon;\omega(\epsilon),\omega(\epsilon))\left({\rm Im}T_{\mathcal{C},J^P}(\epsilon;\omega(\epsilon),\omega(\epsilon))\right)'\right] \\
&+\frac{1}{16\pi^2}\int_{m_1+m_2}^{\infty} d\epsilon\,\epsilon^2\,\omega(\epsilon)^2\Lambda(\epsilon)^2K_2(\beta\epsilon) \\
&\qquad\times\left[\left({\rm Re}T_{\mathcal{C},J^P}(\epsilon;\omega(\epsilon),\omega(\epsilon))\right)'{\rm Im}T_{\mathcal{C},J^P}(\epsilon;\omega(\epsilon),\omega(\epsilon))\right]\Bigg),
\end{aligned} \tag{5.1.15}$$

where $\omega(\epsilon)$ and $\Lambda(\epsilon)$ are given by

$$\omega(\epsilon) = \frac{\sqrt{(\epsilon^2-(m_1+m_2)^2)(\epsilon^2-(m_1-m_2)^2)}}{2\epsilon}, \tag{5.1.16}$$

$$\Lambda(\epsilon) = \frac{\epsilon^4-(m_1^2-m_2^2)}{\epsilon^3}, \tag{5.1.17}$$

and where $T_{\mathcal{C},J^P}(\epsilon;\omega(\epsilon),\omega(\epsilon))$ is the on-shell $T_{\mathcal{C},J^P}$-matrix.

Finally, it is worth noticing that, in connection with nuclear many-body approaches, (5.1.9) can be rewritten in terms of a weighted thermal average of scattering phase shifts by means of unitarity of the S-matrix [Beth35]. It is also important to add that annihilation processes are not explicitly taken into account within our approach (remember Section 4.3.2).

5.1.3 Born approximation

The equation (5.1.10) can be considerably simplified by using the Born approximation, *i.e.* by noticing that if the interactions are weak enough, $T = V + \mathrm{O}(V^2)$. Such conditions are generally expected to be valid at high enough temperatures, where the typical interaction energy is small with respect to the typical thermal energy of the particles. In this temperature range, $\Omega_{bs}^{\rm QCD}$ is simply zero since no bound state longer exists and $\Omega_s^{\rm QCD}$ is drastically reduced (see (5.1.18)). Note also that, according to the chosen scaling of the interactions in function of the gauge-group representation of the particle (remember Section 4.3.2), this approximation can be relevant when the factor $\kappa_{\mathcal{C};p_1p_2}$ is negligible, irrespective of the temperature. Such cases will be encountered when the gauge group is SU(N_c) (cfr. Appendix C).

To the first order in V, (5.1.12) becomes

$$\begin{aligned}\Omega_s^{\rm QCD} &= \frac{1}{64\pi^5\beta}\sum_{n_g+n_q+n_{\bar q}=2} e^{\beta(\mu_1+\mu_2)}\sum_{J^P}(2J+1)\sum_{\mathcal{C}}\dim\mathcal{C} \\ &\times \int_{m_1+m_2}^{\infty} d\epsilon\,\epsilon^2\,\omega(\epsilon)\,\Lambda(\epsilon)K_1(\beta\epsilon)\,V_{\mathcal{C},J^P}(\epsilon;\omega(\epsilon),\omega(\epsilon)).\end{aligned} \tag{5.1.18}$$

A useful remark to be done at this stage is that the pairwise structure of V given by (4.3.11), causes $V|_c$ in (5.1.1) to be always vanishing excepted in two-body channels. Here, at the Born approximation, we have formally to only consider two-body interactions.

After having extracted the colour dependence of the potential as seen in (4.3.12), we have

$$\begin{aligned}\Omega_s^{\rm QCD} &= \frac{1}{64\pi^5\beta}\sum_{n_g+n_q+n_{\bar q}=2} e^{\beta(\mu_1+\mu_2)}\sum_{J^P}(2J+1)\sum_{\mathcal{C}}\dim\mathcal{C}\,\kappa_{\mathcal{C};p_1p_2} \\ &\times \int_{m_1+m_2}^{\infty} d\epsilon\,\epsilon^2\,\omega(\epsilon)\,\Lambda(\epsilon)K_1(\beta\epsilon)\,v_{J^P}(\epsilon;\omega(\epsilon),\omega(\epsilon)),\end{aligned} \tag{5.1.19}$$

where v_{J^P} is the potential with the quantum numbers of the considered channel. Among the various summations to be performed, two are of particular interest: The one over the different interacting species, that can be denoted $\sum_{(p_2,p_2)}$, and the one over the colour representations appearing in $R_{p_1}\otimes R_{p_2}$, that is $\sum_{\mathcal{C}}$. Expression (5.1.19) is thus proportional to a factor $\sum_{\mathcal{C}}\dim\mathcal{C}\,\kappa_{\mathcal{C},p_1p_2}$ for a given pair (p_1,p_2) in a given J^P channel. When the combination of species does not have to respect a symmetry principle, this last sum runs on all the representations appearing in $R_{p_1}\otimes R_{p_2}$. One can then show that

$$\sum_{\mathcal{C}}\dim\mathcal{C}\,\kappa_{\mathcal{C},p_1p_2}=0. \tag{5.1.20}$$

In other words, the average scattering contribution provided by two different species is zero at the Born approximation, within the prescription of the Casimir scaling.

Indeed, it is known in group theory that the second order Dynkin indices I^R in a tensor product obey a sum rule that can be rewritten using our notations as $I^{R_{p_1}}\dim R_{p_2}+I^{R_{p_2}}\dim R_{p_1}=\sum_{\mathcal{C}}I^{\mathcal{C}}$ [Fuch97]. Using $C_2^R=(\dim adj/\dim R)I^R$ [Fuch97], one straightforwardly shows that (5.1.20) holds. Note that (5.1.19) and (5.1.20) are thus *a priori* non-zero when a symmetry principle has to be respected: The summation is not performed on all possible colour representations.

5.2 Thermodynamics of the Yang-Mills plasma

5.2.1 Model description

The first case we investigate with the model described in the above section, is the Yang-Mills plasma for arbitrary gauge groups. It is a plasma only made of gluons, viewed here as particles belonging in the adjoint gauge-group representation. The two-body contributions to consider in (5.1.9) are thus drastically reduced: Only the gg-interactions in different J^{PC} and colour channels have to be included. It is worth noticing that since the J^{PC} summation is infinite, a cut-off is needed. In this section, we follow the channel selection adopted in [Lacr13] and we only take into account the lightest glueball channels *i.e.* 0^{++}, 0^{-+} and 2^{++},

also present in the confined phase. Nevertheless, a criterion based on the cross-section will be developed in Section 5.3.2 and the YM plasma EoS will be recomputed with it.

The basic ingredient underlying the present study is the static quark-antiquark potential computed in finite-temperature quenched lQCD (see Section 4.5.1). The assumed one-gluon-exchange-like nature of the two-particle interactions leads to the universality of the momentum-dependent part of the potential, and to a well-defined prescription for its gauge-group dependence. Similarly, the gluon thermal mass given by (4.5.10), has a peculiar colour scaling originating in its interpretation as a self-energy term.

More freedom is left for the other numerical parameters at our disposal. First, by dimensional analysis, it can be checked that our results can all be expressed in terms of the ratios T/T_c, $T_c/\sqrt{\sigma}$ and $m_{g,0}/\sqrt{\sigma}$ provided that the Bose-enhancement and the Pauli-blocking are not taken into account at the level of the T-matrix. However and as already mentioned, these effects can be neglected since they only generate slight changes on the T-matrix computations.

About the ratio $m_{g,0}/\sqrt{\sigma}$, it is worth mentioning the work [Maas11], in which it is shown that the non-perturbative gluon propagator at zero temperature (thus $m_{g,0}$ in particular) shows no significant quantitative differences when expressed in units of the string tension for the groups SU(N_c) and G_2. It is thus tempting to say that the ratio $m_{g,0}/\sqrt{\sigma}$ may be gauge-group independent also: This was assumed in the previous bound state analysis. The value $m_{g,0}/\sqrt{\sigma} = 1.67$ obtained from the zero-temperature glueball spectrum was retained.

Concerning $T_c/\sqrt{\sigma}$, the glueball gas models with a Hagedorn spectrum describing the high-lying glueball states (remember (3.3.5) and the discussion in Section 3.4.2) give

$$\frac{T_h}{\sqrt{\sigma}} = \sqrt{\frac{3}{2\pi}} = 0.69. \tag{5.2.1}$$

This temperature is here interpreted as the deconfinement one. It is worth saying, as discussed in Section 3.3, that it leads to an EoS in very good agreement with lattice results [Case11, Hage65, Meye09] below T_c. In this picture, the ratio $T_c/\sqrt{\sigma}$ is gauge-group independent: This is only valid in a first approximation since, for example, there are lattice evidences showing that $T_c/\sqrt{\sigma}$ is only constant up to $1/N_c^2$ corrections [Luci04]. Nevertheless, such deviation are beyond the scope of this exploratory work. Note that according to [Brau10], the critical temperature is found to be pretty close to 0.3 GeV up to fluctuation of about 10% for the gauge groups SU(N_c), $Sp(2)$, and E_7. So, that is the reason why we fixed $T_c = 0.3$ GeV in our calculations for all the gauge group. This value is in good agreement with (5.2.1) for the value $\sigma = 0.176$ GeV^2 chosen for $T = 0$ calculations (see Section 4.4.1).

5.2.2 Considerations about thermodynamic observables with SU(N_c) and G_2

5.2.2.1 SU(N_c) Case

To evaluate the colour dependence of $\Omega_{(2)}^{\mathrm{QCD}}$ (given by (5.1.9)) for the YM plasma, we have to analyse the colour dependence of the different terms. In the free part Ω_0, the colour dependence is only included in the degrees of freedom to take into account and possibly in the thermal mass $m_g(T)$. Nevertheless, this last one is assumed to be $\mathrm{O}(1)$ with respect to the number of colours (see (4.5.10)).

Concerning, the two-body interacting part expressed in terms of the T-matrix elements, the all colour dependence actually comes from the two-gluon interaction potential only. More precisely, it is included in the factor (4.3.13), reading in the present case

$$\kappa_{\mathcal{C};gg} = \frac{C_2^{\mathcal{C}} - 2N_c}{2N_c}, \tag{5.2.2}$$

since $C_2^g = C_2^{adj} = N_c$ in the SU(N_c) case.

As it can be found and explained in Appendix C, a gauge-group representation of SU(N_c) is denoted by $(a_1, \ldots, a_k, \ldots, a_{N_c-1})$ and corresponds to a Young diagram with a_k columns of length k. In the present case, the adjoint representation of SU(N_c), to which the gluons belong, can be written as the (N_c-1)-component vector $(1, 0, \ldots, 0, 1)$ in a highest weight representation corresponding to a Young diagram with 1 column of length $N_c - 1$ and 1 column of length 1. The tensor product of the adjoint representation by itself gives the allowed two-gluon colour channels:

$$\begin{aligned} & \bullet^S \oplus (1,0,\ldots,0,1)^A \oplus (2,0,\ldots,0,2)^S \\ \oplus \quad & (1,0,\ldots,0,1)^S \oplus (0,1,0,\ldots,0,2)^A \oplus (2,0,\ldots,1,0)^A \\ \oplus \quad & (0,1,0,\ldots,0,1,0)^S. \end{aligned} \tag{5.2.3}$$

The superscript S/A denotes a symmetric/antisymmetric channel. The first/second/third line exists as soon as $N_c \geq$ 2/3/4. Note that in the special case $N_c = 2$, the above tensor product reduces to $(2) \otimes (2) = (0)^S \oplus (2)^A \oplus (4)^S$, and one recovers the usual spin-coupling rules. The dimensions and colour factors of the representations appearing in (5.2.3) can be found in Appendix C.

In the singlet channel, one has $\kappa_{\bullet;gg} = -1$ for any N_c. It is such that $T = \mathrm{O}(1)$ since $V = \mathrm{O}(1)$. Consequently, the properties of glueballs in singlet above the deconfinement temperature are not dependent of N_c, in agreement with [Buis11b], where it is suggested that this argument is even gauge-group independent. The singlet finally brings a contribution $\mathrm{O}(1)$ to $\Omega_{(2)}^{\mathrm{QCD}}$ since its dimension is 1.

Using the same arguments as for the singlet, one finds that the adjoint channels also lead to a T-matrix that is N_c-independent. Bound states can be formed since the potential is attractive, though less strongly than for the singlet (see Section 4.5.3). Note that the symmetric adjoint channel is actually absent for $N_c = 2$. In this channel, $T = \mathrm{O}(1)$ since $V = \mathrm{O}(1)$ but, unlike the singlet, its contribution to $\Omega_{(2)}^{\mathrm{QCD}}$ is $\mathrm{O}(N_c^2)$ since $\dim(1, 0, \ldots, 0, 1) = N_c^2 - 1$.

The two remaining channels with non-zero $\kappa_{\mathcal{C};gg}$, namely the $(2, 0, \ldots, 0, 2)$ (the 27^S for SU(3)) and the $(0, 1, 0, \ldots, 0, 1, 0)$ (only when $N_c > 3$), have in common that they are symmetric and that their colour factor scales in $1/N_c$, thus vanishes in the large-N_c limit. The fact that $V = \mathrm{O}(1/N_c)$ in both cases leads to the exact large-N_c result

$$T = V + V\, G_0\, V + \mathrm{O}(N_c^{-3}), \tag{5.2.4}$$

or

$$T = \pm \frac{1}{N_c} v + \frac{1}{N_c^2} v\, G_0\, v + \mathrm{O}(N_c^{-3}), \tag{5.2.5}$$

the $\pm$ coming from one channel or another. Because of the weakness of V at large-N_c, one can reasonably suppose that even the attractive channel $(0, 1, 0, \ldots, 0, 1, 0)$ does not lead to the formation of bound states (as seen in Section 4.5.3). For the two channels under consideration,

$$\left(S S^{-1} \overleftrightarrow{\partial_\epsilon} S \right)\Big|_c \propto \partial_\epsilon \mathrm{Re} \left(\pm \frac{v}{N_c} + \frac{v G_0 v}{N_c^2} \right) + \mathrm{O}(N_c^{-3}). \tag{5.2.6}$$

One sees in (5.1.9) that the contributions of both channels have to be summed and, since they are symmetric, the sums on the allowed J^{PC} is identical in both cases. This causes the term in $1/N_c$ to vanish in the trace at large-N_c limit, the first non-trivial one being in $1/N_c^2$, leading to an overall contribution to $\Omega_{(2)}^{\mathrm{QCD}}$ scaling as N_c^2 because the dimension of both channels scale as N_c^4.

Although the colour singlet is relevant in view of studying glueballs, it does not bring any contribution to the EoS at large-N_c. So, the large-N_c EoS is dominated by free gluons and scattering processes above

threshold in coloured channels. The more N_c is large, the more important is the gap between the confined phase and the deconfined one, whose EoS scales respectively as 1 and N_c^2. It is indeed known that the large N_c-case corresponds to a strongly first-order phase transition ($N_c = 3$ is already weakly first order) [Luci05].

5.2.2.2 G_2 Case

Another interesting group under consideration is G_2 which is also the best studied gauge group in lQCD so far beyond SU(N_c). The main features of this group are summarized in Appendix C and are discussed in what follows.

The adjoint representation of G_2 has dimension 14, and reads $(0,1)$ in a highest weight representation. The two-gluon channels are then given by

$$(0,1) \otimes (0,1) = \bullet^S + (0,1)^A + (0,2)^S + (2,0)^S + (3,0)^A \tag{5.2.7}$$

or, in terms of the dimensions, $14 \otimes 14 = 1 + 14 + 77' + 27 + 77$. Using the same normalization than in the SU(N_c) case, the colour factors respectively read $\kappa_{\mathrm{C};gg} = -1$, $-1/2$, 1/4, $-5/12$, and 0 [Buis11a, Lipt08]. The colour factors in the singlet and adjoint channels are equal to those of SU(N_c), so the glueball properties are unchanged in the singlet and antisymmetric adjoint channels. The symmetric $(2,0)^S$ channel is almost as attractive as the adjoint one: It lead to bound states [Lacr13].

5.2.2.3 Scaling relations for SU(N_c) and G_2

Some interesting relations about the scaling of the EoS can be deduced thanks to the T-matrix. Let us write the on-shell T-matrix as $T = \sum_k a_k \, \kappa_{\mathcal{C};gg}^k$ where all a_k do not depend on the colour but rather on the other quantum numbers involved. The colour dependence of the thermodynamic observables is then given by the quantities $\sum_{\mathcal{C};A/S} \dim \mathcal{C} \, \kappa_{\mathcal{C};gg}^k$. Using the results of Appendix C and of Section 5.2.2.2, one can check that, for SU(N_c) and G_2,

$$\sum_{\mathcal{C};\mathcal{S}} \dim \mathcal{C}_{gg} \kappa_{\mathcal{C};gg} = \frac{1}{2} \dim adj, \tag{5.2.8}$$

$$\sum_{\mathcal{C};\mathcal{S}} \dim \mathcal{C}_{gg} \kappa_{\mathcal{C};gg}^2 = \frac{3}{4} \dim adj, \tag{5.2.9}$$

$$\sum_{\mathcal{C};\mathcal{S}} \dim \mathcal{C}_{gg} \kappa_{\mathcal{C};gg}^3 = -\frac{1}{8} \dim adj, \tag{5.2.10}$$

$$\sum_{\mathcal{C};\mathcal{A}} \dim \mathcal{C}_{gg} \kappa_{\mathcal{C};gg}^k = \left(-\frac{1}{2}\right)^k \dim adj. \tag{5.2.11}$$

For SU(N_c) at large-N_c, the previous relations can be written

$$\sum_{\mathcal{C};\mathcal{S}} \dim \mathcal{C}_{gg} \kappa_{\mathcal{C};gg}^k = N_c^2 \left[\left(-\frac{1}{2}\right)^k + \delta_{k,1} + \frac{1}{2}\delta_{k,2} \right] + \mathrm{O}(1), \tag{5.2.12}$$

$$\sum_{\mathcal{C};\mathcal{A}} \dim \mathcal{C}_{gg} \kappa_{\mathcal{C};gg}^k = N_c^2 \left(-\frac{1}{2}\right)^k + \mathrm{O}(1). \tag{5.2.13}$$

Again that means that the expected scaling like N_c^2 (actually like dim adj)[6] of the EoS is found using the present approach. This can be viewed as a confirmation of the relevance of the chosen colour scaling (4.3.11).

5.2.3 Equations of state

5.2.3.1 Pressure

Now that we have theoretically studied what happens with the thermodynamic observables for a SU(N_c) or G_2 gauge group, let us compute the EoS. In Fig. 5.1, the normalized pressure p/p_{SB} obtained by our approach in the SU(3) case is displayed. Its different contributions are also analysed: That is to say the normalized pressure provided by the free gluon gas with the thermal mass (4.5.10), as well as the ones from bound-state and from scattering parts using the potential (4.5.5). The situation is similar for the other gauge groups.

At low temperature ($T \leq 1.3\,T_c$), the bound-state and the scattering parts both give thermodynamic contributions that modify the free gas pressure, but the effect of the bound-state part is very small. For $T > 1.3\,T_c$, only the scattering part keeps to contribute. As it can be observed in Fig. 5.1, the main global effect of the interactions, resulting from the combination of various positive and negative contributions, is to decrease the pressure.

If each contribution is analysed, we can notice that the bound-state formation increases the pressure. This is due to the fact that the bound states are simply added as new species and do not interact with the other particles inside the plasma. Indeed, when a glueball melts into the plasma for a given temperature $T_{\rm dis}$, its contribution to the pressure disappears abruptly for $T = T_{\rm dis}$. As the global effect of bound states is very small, this situation is not really disturbing. It is more problematic for the computation of other observables, as we will see in the next section.

Concerning the two-gluon scattering part, the sign of the pressure contribution can not be analytically predicted at each temperature. Only at the Born approximation, one can observe that attractive (repulsive) channels increase (decrease) the pressure. Indeed, for two identical particles, $\Omega_s^{\rm YM}$ is given at the Born approximation by

$$\Omega_s^{\rm YM} = \frac{1}{64\pi^5\beta}\sum_{J^P}(2J+1)\sum_{\mathcal{C},g}\dim\mathcal{C}\,\kappa_{\mathcal{C},gg}\int_{2m_g}^{\infty}d\epsilon\,\epsilon^3\sqrt{\frac{\epsilon^2}{4}-m_g^2}\,K_1(\beta\epsilon)\,v_{J^P}. \tag{5.2.14}$$

In an attractive (repulsive) channel, the sign of the potential is negative (positive). Since $\Omega_s^{\rm YM}$ is the scattering contribution to the grand canonical potential, it can be deduced that attractive (repulsive) channels increase (decrease) the pressure at the Born approximation, that is to say here, at large temperature. In the present SU(3) case, the only repulsive channel is the $(2,2)^S$. That means that the decreasing of the pressure in our approach compared with the free gas pressure is only driven by the $(2,2)^S$ channel.

It is also worth wondering whether some other considerations arise or not from the high-temperature limit of our framework concerning the behaviour of the two-body interactions. Using (5.2.8) and (5.2.14) since the Born approximation is relevant, one can write

$$\Omega_{s,0^{++}}^{\rm YM} \quad\sim\quad \frac{1}{64\pi^5\beta}\frac{\dim adj}{2}\int_{2m_g}^{\infty}d\epsilon\,\epsilon^3\sqrt{\frac{\epsilon^2}{4}-m_g^2}K_1(\beta\epsilon)\,v_{0^{++}}. \tag{5.2.15}$$

6. This scaling is the one of the SB thermodynamics, which is the behaviour expected for the YM plasma at large temperature.

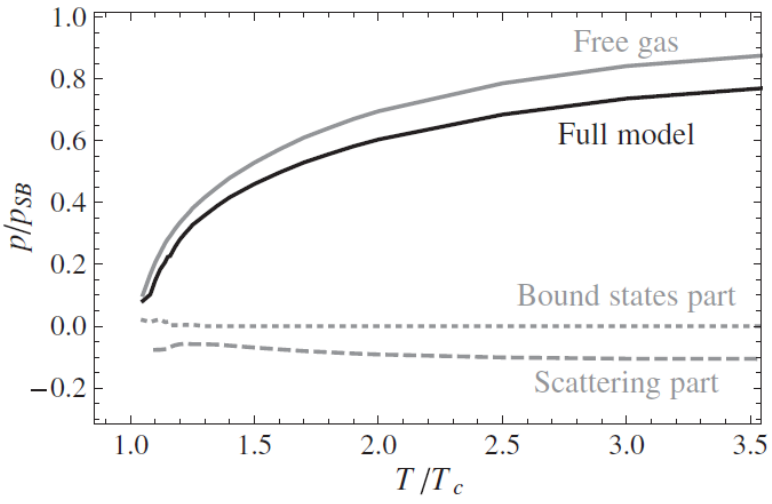

Figure 5.1: Normalized pressure p/p_{SB} versus temperature in units of T_c (with $T_c = 0.3$ GeV), computed for the gauge group SU(3) in the free gluon gas case and in the full approach. The bound state and scattering contributions are also indicated. The black curve is the sum of all the gray curves.

Only the scalar channel has been taken into account for the sake of clarity, but the following argument can be extended to any spin. According to HTL results, it is relevant to assume a simple Yukawa form for the potential v_0 at high temperature [Blai99]. Then,

$$\Omega^{\mathrm{YM}}_{s,0^{++}} \quad \sim \quad \frac{\alpha}{64\pi^5\beta^4}\frac{\dim adj}{2}\int_{2\beta m_g}^{\infty} dx\, x^3 K_1(x)\, \frac{\sqrt{\frac{x^2}{4}-\beta^2 m_g^2}}{\frac{x^2}{4}-\beta^2 m_g^2+\beta^2 M^2}, \tag{5.2.16}$$

where M is the screening mass of the theory and α is the running coupling constant, *a priori* both temperature-dependent. Still in HTL theory, it is found that, because of the running of the strong coupling constant,

$$\lim_{\beta\to 0}\beta m_g = \lim_{\beta\to 0}\beta M = 0. \tag{5.2.17}$$

More precisely, the quark and gluon thermal masses are found to behave as $\sqrt{\alpha_s(T)}\,T$. Consequently, at high enough temperatures, it is found that

$$\Omega^{\mathrm{YM}}_{s,0^{++}} \quad \sim \quad \alpha\,\frac{\dim adj}{32\pi^5\beta^4}, \tag{5.2.18}$$

i.e. a scattering contribution that has the same behaviour with respect to the temperature as the free part, ensuring a well-defined large-temperature limit. Notice that our fit of the screening mass does not follow the

constraints (5.2.17), but it is designed to fit the static potential below $3\,T_c$. A more involved form would be needed to reach the HTL predictions at high temperatures, but it is not the scope of the present work.

In Fig. 5.2, the normalized pressure p/p_{SB} is presented for different gauge groups: SU(2), SU(3), SU(∞) and G_2. Several remarks can be done. First, the free gluon thermodynamic contribution is gauge-group invariant once normalized to p_{SB}. The gauge-group dependence is only present in the bound-state and scattering sectors. The number of allowed colour channels (*i.e.* the symmetric ones since we only consider the 0^{++}, 0^{-+} and 2^{++} J^{PC} states) depends on the gauge group (see Appendix C) and determines the allowed maximum number of bound states and the number of scattering channels. For clearness, these channels are listed in Table 5.1 and their numbers are given just below.

Channels to consider			
SU(2)	SU(3)	SU($N_c > 3$)	G_2
0^{++} in $\bullet^S$			
0^{-+} in $\bullet^S$			
2^{++} in $\bullet^S$			
0^{++} in $(2,0,\ldots,0,2)^S$			$(2,0)^S$
0^{-+} in $(2,0,\ldots,0,2)^S$			$(2,0)^S$
2^{++} in $(2,0,\ldots,0,2)^S$			$(2,0)^S$
-	0^{++} in $(1,0,\ldots,0,1)^S$		$(0,2)^S$
-	0^{-+} in $(1,0,\ldots,0,1)^S$		$(0,2)^S$
-	2^{++} in $(1,0,\ldots,0,1)^S$		$(0,2)^S$
-	-	0^{++} in $(0,1,\ldots,0,1,0)^S$	-
-	-	0^{-+} in $(0,1,\ldots,0,1,0)^S$	-
-	-	2^{++} in $(0,1,\ldots,0,1,0)^S$	-

Table 5.1: Channels taken into account in the EoS of the YM plasma for different gauge groups.

Total number of channels			
SU(2)	SU(3)	SU($N_c > 3$)	G_2
6	9	12	9

Note that the small bound-state thermodynamic contribution comes from two effects: The number and the mass of the existing glueballs. Because of the glueball dissociation, this contribution is only taken into account up to the temperature of dissociation (see Table 4.5). One can observe in Fig. 5.2 that the produced EoS are not very sensitive to the gauge group. The most important difference occurs between 1.05 and $1.35\,T_c$ (see Fig. 5.3): In this range, the gluon-gluon interactions have a maximal strength. When the

temperature increases, the Born approximation becomes more and more valid and the pressure then scales as dim adj as just previously seen. Thus the normalized pressure tends to be universal.

In Fig. 5.2, it is also worth noticing that the EoS computed in our approach favourably compares with lQCD data for gauge groups SU(3-8) [Pane09] where such universal curves seem to appear (note that lattice data exist also for very high values of T/T_c but only for SU(3) [Bors12a]). Concerning G_2, no lattice data about EoS are currently available but a new effective matrix model describing pure YM thermodynamics has been proposed in [Dumi12]. These last results are also compared to ours in Fig. 5.2.

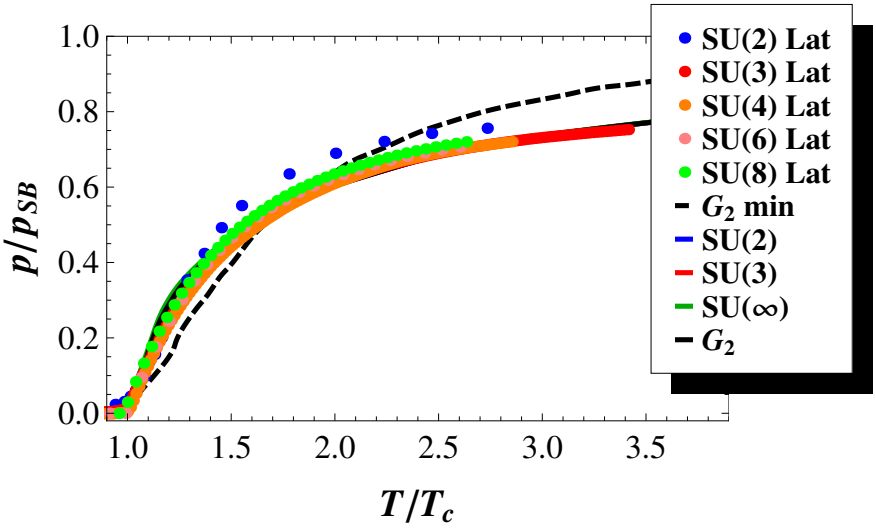

Figure 5.2: Normalized pressure p/p_{SB} versus temperature in units of T_c (with $T_c = 0.3$ GeV), computed for the gauge groups SU(2,3,∞) and G_2 (solid lines). Note that all the curves are nearly indistinguishable. Our results are compared to the lattice data of [Enge89] for SU(2) (dots), and of [Pane09] for SU(3,4,6,8) (dots). Concerning G_2, no lQCD is nowadays available and a comparison with the minimal model of [Dumi12] is therefore presented (dashed line). Note that all lattice data have been normalized to the lattice SB pressure [Enge89, Pane09].

5.2.3.2 Trace anomaly

A relevant observable which measures the non-ideal character of the deconfined medium is the trace anomaly $\Delta = e - 3\,p$, where e is the energy density. We have computed this quantity in the framework of our model, but the results obtained can only be considered as preliminary for the two reasons explained below.

Firstly, the normalized trace anomaly can be computed from the pressure thanks to the thermodynamic relations (remember (5.1.4)):

$$\frac{\Delta}{p_{SB}} = -\beta \left(\partial_\beta \frac{p}{p_{SB}} \right)_{\beta\mu} . \tag{5.2.19}$$

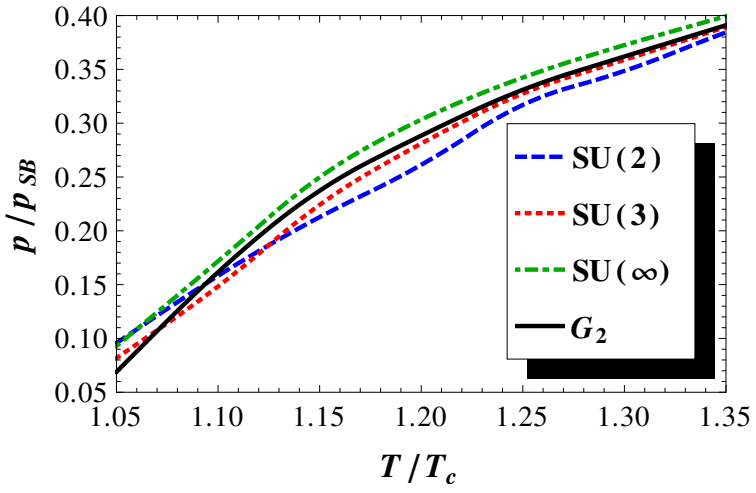

Figure 5.3: Normalized pressure p/p_{SB} versus temperature in units of T_c (with $T_c = 0.3$ GeV), computed for the gauge groups SU(2), SU(3), G_2, and SU(∞). The temperature range is the one where the differences between the curves are the most important.

As the Hamiltonian considered explicitly depends on the temperature, these relations must be used with some cautions. For instance, in the case of free particles with a temperature-dependent dispersion relation, several procedures exist to compute the observables keeping the usual thermodynamic relations [Brau09, Gore95]. With temperature-dependent masses and interactions as in our model, all observables obtained by derivation of the grand canonical potential must be examined with caution. Here, we will simply use the relation (5.1.4) but a self-consistent procedure is needed and will be investigated in the future.

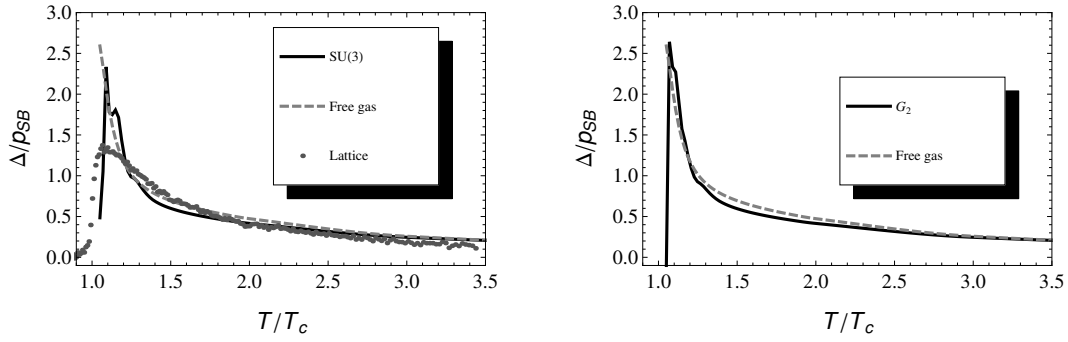

Figure 5.4: Normalized trace anomaly Δ/p_{SB} versus temperature in units of T_c (with $T_c = 0.3$ GeV) computed for the gauge groups SU(3) (left) and G_2 (right). The models (black solid line) are compared with the free gas (dashed grey line) and the lattice data from [Pane09] in the SU(3) case (dark grey dots).

Secondly, as mentioned in the previous section, the glueball contributions to the pressure disappear abruptly at the melting temperature. The derivative of the pressure for this temperature is then not defined. At first sight, one could argue that the contribution of the glueballs to the pressure is so weak that it can be safely neglected. But, this does not mean a small contribution to the derivative of the pressure. Moreover, the glueballs exist in a domain of temperature where the deviation from the non-ideal character of the gluon plasma is expected to be large. Thus, a smooth transition between a bound state with a finite width and a scattering state of two gluons is worthwhile. It could be obtained by an unified treatment of the T-matrix results in the computation of the grand canonical potential. This would imply a strong modification of the formalism developed in [Dash69]. Here, we will simply not take into account the glueball contributions in (5.1.4), leaving a detailed study for another work.

The normalized trace anomaly computed with (5.1.4) for SU(3) and G_2, without the bound state contributions, are compared in Fig. 5.4 with the (gauge-independent) normalized trace anomaly computed for the free gluon gas with the thermal mass (4.5.10) and with the lattice data from [Pane09] in the SU(3) case. The G_2 trace anomaly is not significantly different from its SU(3) counterpart, just as the pressure is. The situation is similar for the other gauge groups. The peak near T_c results from the combination of various negative and positive channel contributions. This explains its non-standard structure. One can see that this peak is not in good agreement with the lattice data. This discrepancy could be cured by a correct treatment of the bound state contributions and melting. However, the peak cannot be obtained with the free part only and the behaviour above $2\,T_c$ is in agreement with lQCD data: These are probably the most important features of our model concerning the trace anomaly. Improved calculations are necessary to clarify the situation.

5.3 Thermodynamics of the QGP

5.3.1 Model description

Now that the pure-gauge sector has been studied, we will naturally add quarks and try to extract EoS with baryonic potential. This implies the change of the critical temperature since lQCD calculations seem to find it around 150 MeV [Aoki06]. Thus, T_c is now fixed to 150 MeV while the other parameters remain unchanged.

In what follows, we will firstly investigate the QGP with 2 light flavours of quarks. In this case, the quark thermal mass is given by (4.5.11) where $m_{q,0} = 0.3$ GeV (fixed to the $T = 0$ spectrum). Then, one strange quark flavour will be added in order to study the 2 + 1 QGP. Its thermal mass naturally respects the same prescription as for the light quarks but $m_{q,0} = 0.4$ GeV.

For these two thermodynamic situations, the number of channels to consider is huge since we have no limitation due to confinement. Therefore, gg, qq, $\bar{q}\bar{q}$, $q\bar{q}$, qg and $\bar{q}g$ two-body interactions are included and also extracted from the potential (4.5.5). The colour channels for each two body interactions are given in Appendix C. Furthermore, a isospin number is added because of the two light quarks. Obviously, the Pauli's symmetry principle has to be respected when it is needed.

Concerning the J^P channels to take into account, the question is much more delicate as already mentioned. Indeed, we need a correct cut-off since this summation is formally infinite. This will be the point of the following discussion.

5.3.2 Criterion for selecting J^P channels

Using the formalism of [Tayl83], but adapted for a relativistic kinematics, it can be shown that the differential elastic cross-section for a two-body interaction is given by

$$\frac{d\sigma}{d\Omega}(\vec{p} \leftarrow \vec{p}_0) = (2\pi)^4 \mu(E)^2 \left|\langle \vec{p}|T_{\mathcal{C}}(E+i0)|\vec{p}_0\rangle\right|^2, \tag{5.3.1}$$

where $|\vec{p}_0| = |\vec{p}|$, $\mu(E) = \Lambda(E)/4$ (cfr. (5.1.17)) and E is the center-of-mass frame energy. The notation $i0$ means that we have formally to take the limit where the imaginary part tends to zero. The matrix element is evaluated for each colour channel.

As expected, in the non-relativistic limit, $\mu(E)$ tends to the reduced mass. By integration on the angles, one obtains

$$\sigma = (2\pi)^5 \mu(E)^2 \int_{-1}^{+1} d(\hat{p}\cdot\hat{p}_0) \left|\langle \vec{p}|T_{\mathcal{C}}(E+i0)|\vec{p}_0\rangle\right|^2. \tag{5.3.2}$$

The ket $|\vec{p}\rangle$ is a plane wave state containing all possible partial components. By decomposing this state into helicity states, we obtain the cross-section $\sigma_{\mathcal{C},J^P}$ for a given colour-isospin-J^P channel

$$\sigma_{\mathcal{C},J^P} = 4\pi^3 \mu(E)^2 \left|T_{\mathcal{C},J^P}(E)\right|^2. \tag{5.3.3}$$

Our purpose is to compare the contributions from various channels to the grand potential at a given temperature for all possible values of the center-of-mass energy. So, we define a kind of mean cross-section $\bar{\sigma}_{\mathcal{C},J^P}$ by integrating (5.3.3) on the energy,

$$\bar{\sigma}_{\mathcal{C},J^P} = 4\pi^3 \int_{m_1+m_2}^{\infty} dE\, \mu(E)^2 \left|T_{\mathcal{C},J^P}(E)\right|^2 \left[1 \pm f^1(\epsilon_1(E))\right]\left[1 \pm f^2(\epsilon_2(E))\right]. \tag{5.3.4}$$

The in-medium effects are taken into account, depending on the bosonic or fermionic nature of the two interacting particles. According to the Born approximation, when $E \to \infty$, we have

$$T_{\mathcal{C},J^P}(E; q, q') \to V_{\mathcal{C},J^P}(q, q'). \tag{5.3.5}$$

In our model, $V_{\mathcal{C},J^P}(q,q')$ is essentially the Fourier's transform of a Yukawa interaction which behaves like q^{-2}. So, the mean cross-section, which depends only on the temperatures, is finite since $\left|T_{\mathcal{C},J^P}(E)\right|^2 \sim E^{-4}$ when $E \gg m_1 + m_2$. We have decided to estimate the relative contributions of two channels J^P and $J'^{P'}$ by computing the ratios $\bar{\sigma}_{J^P}/\bar{\sigma}_{J'^{P'}}$, the reference being the channel with the largest cross-section.

Each two-body channel is analysed separately and the following considerations are used to determine the selection criterion on which we rely on. When the total spin J increases, the average value $\left\langle \vec{L}^2 \right\rangle$ increases also. This is obvious for ordinary spin states, and this is shown in Appendix B for helicity states. For a bound state, this means the increase of the mass, and then a reduced contribution to the grand potential. Moreover, in a naive non-relativistic picture, the strength of the orbital barrier increases with $\left\langle \vec{L}^2 \right\rangle$ in a scattering process, which reduces the value of the corresponding T-matrix. So, we have decided to restrict the summation over J^P channels to the lowest values of $\left\langle \vec{L}^2 \right\rangle$. More precisely, the selection rule is the following: The $\bar{\sigma}_{J^P}/\bar{\sigma}_{J'^{P'}}$ has to be higher than 25% for at least one $T \geq 1.2\,T_c$. We have checked that the imposition of such criterion is reasonable.

Indeed, in the gg case, the J^{PC} channels that we have to take into account are displayed in Table 5.2. The $J'^{P'C'}$ reference is the most attractive channel, *i.e.* 0^{++}. An analysis of this table shows that only the

T/T_c	gg: $\sigma_{J^{PC}}/\sigma_{0^{++}}$					
	0^{++}	0^{-+}	2^{++}	1^{++}	1^{-+}	2^{++}
1.2	1.00	0.25	0.41	0.32	0.19	0.19
1.5	1.00	0.31	0.47	0.38	0.24	0.24
2	1.00	0.30	0.47	0.39	0.23	0.23
5	1.00	0.20	0.43	0.34	0.14	0.14

Table 5.2: Ratio of the cross-sections for different gg channels. Selection criterion: Ratio > 25 % for at least one $T \geq 1.2\,T_c$. The gg channels are compared with the octet-colour representation of the SU(3) gauge group since it is the only representation common to symmetric and antisymmetric channels. Other colour channels have been tested.

0^{++}, 0^{-+}, 2^{++} and 1^{++} states must be included in our thermodynamic computations. We have thus tested that including much more channels in the YM plasma does not change significantly the EoS. For instance, the inclusion of all gg states up to $\left\langle \vec{L}^2 \right\rangle = 8$ brings very weak modifications to the normalized pressure (see Fig. 5.5). The value of 25% is thus a good compromise between accuracy and computational effort.

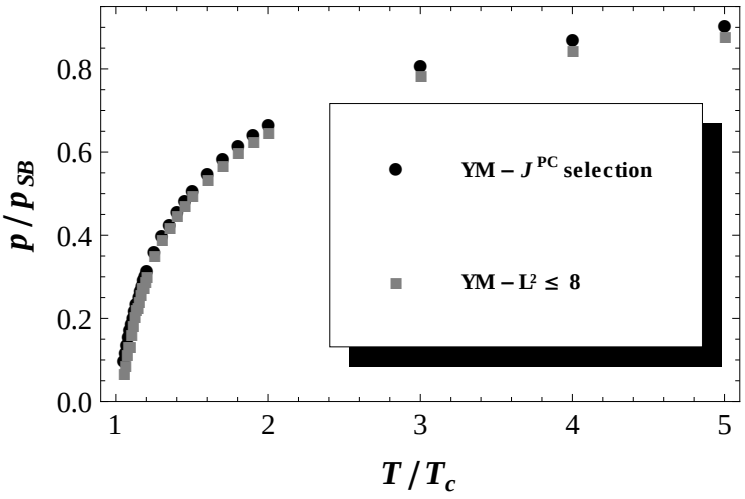

Figure 5.5: Normalized pressure p/p_{SB} versus temperature in units of T_c (with $T_c = 0.3$ GeV) computed for the gauge groups SU(3). The dots correspond to the normalized pressure obtained thanks to the inclusion of gg states according to our J^{PC} selection criterion, while the squares correspond to the inclusion of gg channels up to $\left\langle \vec{L}^2 \right\rangle = 8$.

Concerning the quark sector, we can study the qq and $\bar{q}\bar{q}$ on the same footing since we start by computing the T-matrices without baryonic potential [7]. These results as well as the meson ones are given in Table 5.3.

7. As we will see in Section 5.3.4, the influence of the baryonic potential on the T-matrix computations is negligible

The conclusion is that only the $L = 0$ and $L = 1$ channels must be retained.

T/T_c	qq (or $\bar{q}\bar{q}$) : $\sigma_L/\sigma_{L=0}$				$q\bar{q}$: $\sigma_L/\sigma_{L=0}$			
	$L=0$	$L=1$	$L=2$	$L=3$	$L=0$	$L=1$	$L=2$	$L=3$
1.2	1.00	0.26	0.13	0.07	1.00	0.22	0.10	0.06
1.5	1.00	0.27	0.13	0.07	1.00	0.26	0.12	0.06
2	1.00	0.27	0.12	0.06	1.00	0.27	0.12	0.06
5	1.00	0.21	0.07	0.02	1.00	0.21	0.07	0.02

Table 5.3: Ratio of the cross-sections for different qq (or $\bar{q}\bar{q}$) and $q\bar{q}$ channels. Selection criterion: Ratio > 25 % for at least one $T \geq 1.2\,T_c$. The qq (or $\bar{q}\bar{q}$) channels are compared with the sextet-colour representation of the SU(3) gauge group while the $q\bar{q}$ are compared with the singlet one, just to give an example.

Finally, the qg (or $\bar{q}g$) cross-sections are shown in Table 5.4. The reference is named $J4$ within our nomenclature (see Appendix B). In this sector, we conclude that all the states given in Table 5.4 have to be included in the QGP. In summary, for the QGP with two light quarks, the total number of channels, and so T-matrix computations, is 82 while 190 T-matrix files are required for the 2 + 1 QGP.

T/T_c	$g\tilde{g}$: σ_J/σ_{J4}					
	$J4$	$J1$	$J2$	$J3$	$J5$	$J6$
1.2	1.00	0.34	0.24	0.64	0.24	0.31
1.5	1.00	0.42	0.29	0.69	0.29	0.37
2	1.00	0.42	0.29	0.70	0.29	0.38
5	1.00	0.33	0.22	0.67	0.21	0.29

Table 5.4: Ratio of the cross-sections for different qg (or $\bar{q}g$) channels. Selection criterion: Ratio > 25 % for at least one $T \geq 1.2\,T_c$. The qg (or $\bar{q}g$) channels are compared with the singlet-colour representation of the SU(3) gauge group, just to give an example. The nomenclature used is given in Appendix B.

5.3.3 Equations of state

5.3.3.1 QGP with two light quark flavours

Now that we have established which J^P channels for each two-body interactions we have to take into account, we can compute the EoS of the QGP with two light quarks. In Fig. 5.6, the normalized pressure is shown. As it can be noticed in the left panel, the interactions do not contribute: The major part is given by the free gas. Therefore, in order to realise why the scattering part is so small (for the bound-state contribution, a nearly-zero value is not surprising as in the YM case), we have separated the different scattering contributions in the right panel.

Without surprise, the $q\bar{q}$, qg and $\bar{q}g$ channels asymptotically tend to zero as expected at the Born approximation since the relation (5.1.20) holds. The qq and $\bar{q}\bar{q}$ channels generate a global increase of the normalized pressure while it is the contrary for the gg sector. Thus, it seems that not only these two effects are weak but in addition, they contribute in opposite directions, leading to a global suppression of the two-body interactions in average.

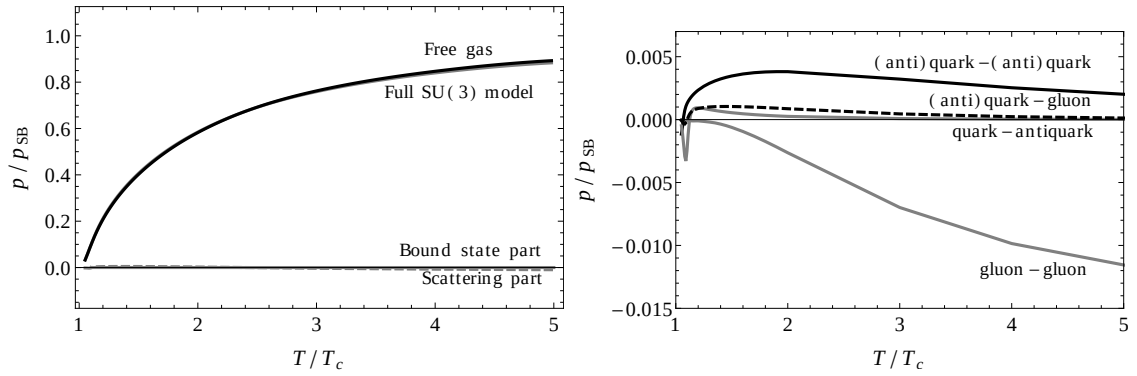

Figure 5.6: QGP with two light quark flavours. (Left) Normalized pressure p/p_{SB} versus temperature in units of T_c (with $T_c = 0.15$ GeV), compared to the free part, bound state and scattering contribution. (Right) Different scattering contributions to the normalized pressure p/p_{SB} versus temperature in units of T_c (with $T_c = 0.15$ GeV).

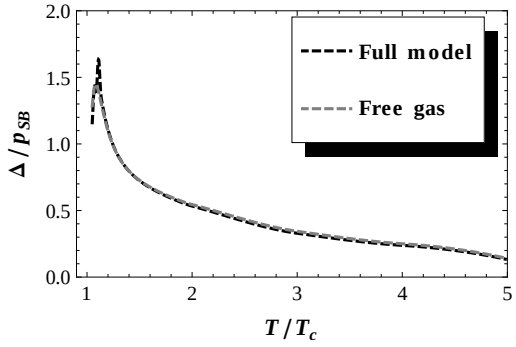

Figure 5.7: QGP with two light quark flavours. Normalized trace anomaly Δ/p_{SB} (without bound states) versus temperature in units of T_c (with $T_c = 0.15$ GeV), compared to the free part contribution.

In Fig. 5.7, we display the normalized trace anomaly (without bound states) compared to the free gas part. A peak structure is here exhibited even in the free gas contribution. Therefore, it seems that not only the interactions create the peak, unlike in the YM sector. The nature of this latter is really difficult to establish since few variations of the pressure can drastically change the shape of the trace anomaly.

The main conclusion that seems to emerge from our approach (looking at the normalized trace anomaly as well as at the normalized pressure) is that the leading behaviour of the QGP is driven by gluon and (anti)quark degrees of freedom that interact weakly. Nevertheless, it does not mean that the interactions have no impact on the EoS. Indeed, the particle thermal mass is extracted from it, leading to a self-energy contribution for the particle.

5.3.3.2 2 + 1 QGP

A similar analysis as the one proposed in the previous subsection can be applied in the 2 + 1 QGP case. Since similar results and features can be deduced from it, we will not repeat it again and focus more on the comparisons between our model and lQCD extracted from [Bors14]. Indeed, lQCD collaborations have recently reached the physical quark masses in their computations of the EoS, making their results more and more reliable for comparisons.

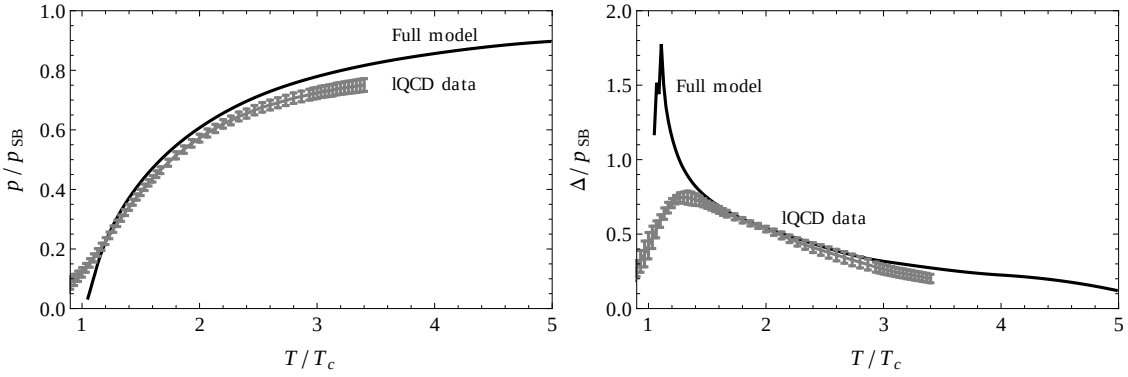

Figure 5.8: 2 + 1 QGP. (Left) Normalized pressure p/p_{SB} versus temperature in units of T_c (with $T_c = 0.15$ GeV), compared to lQCD data from [Bors14]. (Right) Normalized trace anomaly Δ/p_{SB} (without bound states) versus temperature in units of T_c (with $T_c = 0.15$ GeV), compared to lQCD data from [Bors14].

As we can observe in Fig. 5.8, our data are qualitatively in agreement with lQCD ones. The lQCD normalized pressure is slightly overestimated as well as the asymptotic behaviour of the normalized trace anomaly. On the other hand, its peak structure is very different of ours quantitatively. As already mentioned and debated, this latter is really difficult to obtain due to several reasons in our approach: problems in the treatment of the bound states and restriction to two-body interactions. Even in lQCD, different collaborations find different quantitative behaviours for the trace anomaly peak up to now. The possible discrepancies can arise from the choice of the fermionic lattice action, the lattice spacing, the considered quark masses, the extrapolation to the continuum limit,... Only, a good agreement in the behaviour of the decreasing tail is reached by the different lQCD groups according to [Bors14]. Nevertheless, it is worth mentioning that the disagreements observed in the quantitative value of the peak structure in various lQCD results (mainly due to a computation with no physical quark masses) seem to reduce, and the shape of the lQCD trace anomaly tends to the one depicted in Fig. 5.8, and firstly given by the BMW collaboration [Ratt14].

Therefore, except for the normalized trace anomaly peak structure, our data are in correct agreement with lQCD ones. As discussed in the previous subsection, this agreement seems to be reached by only including a quasiparticle thermal mass: The contributions of the two-interacting channels are minor. Nevertheless, it is worth insisting on the fact that the thermal mass effects are extracted from the two-body lQCD interaction potential (4.5.5) within our model. So, the two-body interactions are not useless to understand the behaviour of the QGP around T_c. Moreover, a more appropriate treatment for the bound-state inclusion is needed and could change significantly the structure of the trace anomaly.

Finally, let us compare in Fig 5.9 the normalized pressure and trace anomaly for a QGP with $N_f = 2$

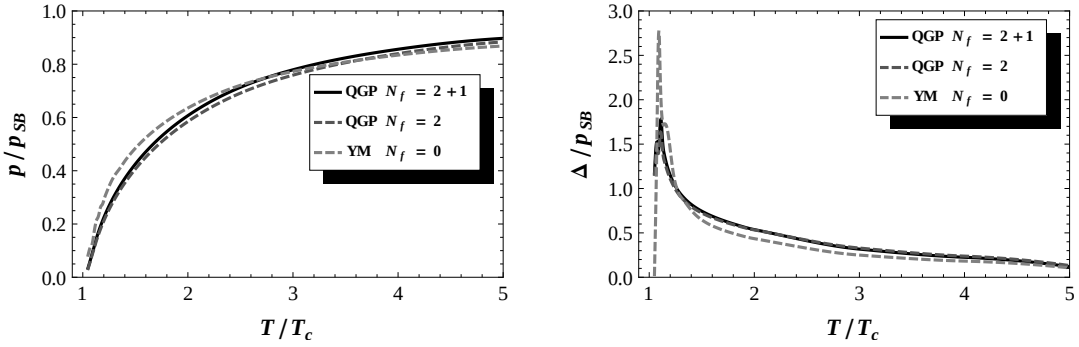

Figure 5.9: (Left) Normalized pressure p/p_{SB} versus temperature in units of T_c (with $T_c = 0.15$ GeV for QGP and $T_c = 0.3$ GeV for YM). (Right) Normalized trace anomaly Δ/p_{SB} (without bound states) versus temperature in units of T_c (with $T_c = 0.15$ GeV for QGP and $T_c = 0.3$ GeV for YM).

and $N_f = 2 + 1$ ($T_c = 0.15$ GeV) to the ones of the YM plasma ($T_c = 0.3$ GeV). We can notice that the normalized pressure curves are almost superimposed and that the decreasing trend of the trace anomaly is nearly the same in all the considered theories. The maximum of the deviation between these curves is around $1.2\,T_c$, at the localisation of the trace anomaly peak. It is nevertheless important to remember that the critical temperature and the normalization are not the same in all the EoS, see (5.1.8). However within these units, a universality at large temperature ($\geq 3\,T_c$) seems to emerge.

5.3.4 Adding baryonic potential

Now that the EoS for the QGP are computed and favourably compared with lQCD, we can investigate the non-zero baryonic regime. As already mentioned, this latter deserves a lot of interests, especially in the area of the neutron star physics. Indeed, since pioneering works [Coll75] about the existence of a deconfined phase in QCD, it was assumed that the core of the heaviest neutron star should be probably filled by a medium with a high nuclear density and in which the significant degrees of freedom should be the quarks. Therefore, getting the QCD EoS at finite μ could shed some light in this field.

Up to now, this task still remain difficult from first QCD principles. Remember that even in lQCD [Yagi05], some conceptual troubles appear (cfr. sign problem) and only perturbations around $\mu = 0$ are meaningful. Therefore, it seems appealing to check whether or not quasiparticle approaches could help. Unfortunately at the present stage, some problems also appear in our formalism. The main reasons are the following.

First, the DMB formalism that we have used to compute EoS is based on a virial expansion in terms of $e^{\beta\mu\mathcal{N}}$. We are thus limited by construction to small baryonic potentials. Indeed, increasing the baryonic potential is the same as increasing the screening between particles: The many-body interactions are more and more likely to contribute. So, the reduction to two-body interactions make no more sense *a priori* and some problems, other than a careful computation of all the channels, arise. Let us mention for instance, the absence of a helicity formalism for many-body systems and the necessity to resort to Faddeev and higher equations for more than two-body interactions [Joac75].

Another peculiar problem is the building of a coherent interaction in presence of baryonic potential. Already at $\mathcal{N} = 2$, no lQCD data are available to our knowledge. It is not only important to define the

potential between particles but also the quasiparticle mass, which seems to read out the main behaviour of the EoS at $\mu = 0$. A way to circumvent this problem could be to use the HTL expressions for the particle thermal mass but it was not the bias adopted within this study. Indeed, the actual shape of our thermal masses are not the ones extracted from HTL.

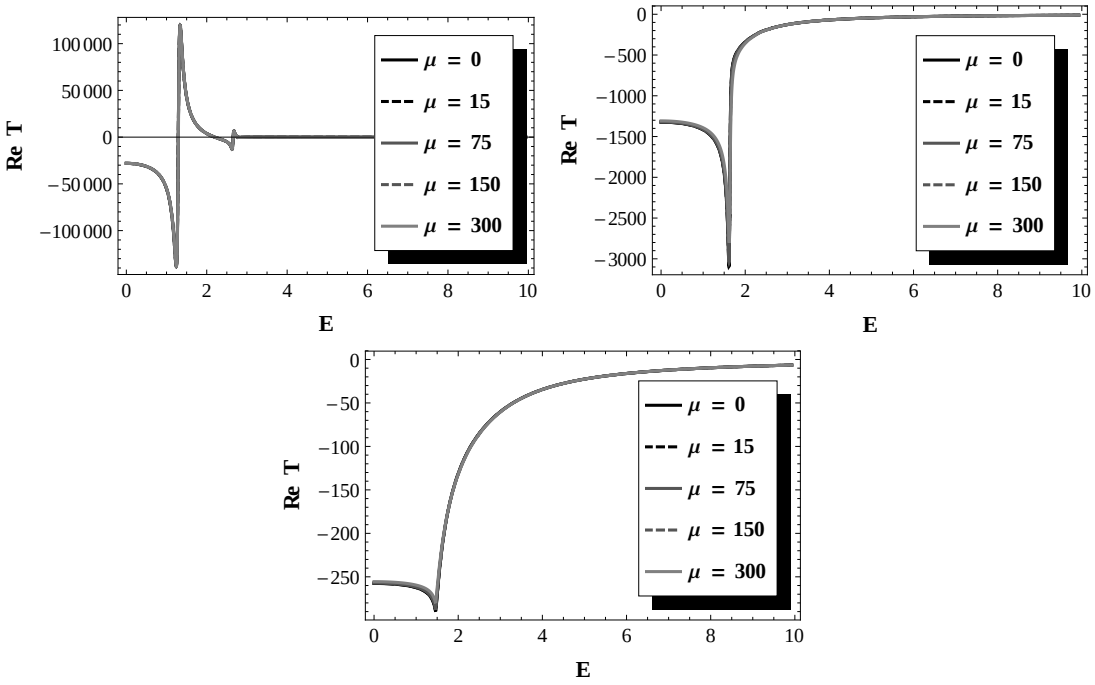

Figure 5.10: Real part of the T-matrix ($q\bar{q}$ in $L = 0$, here given as an example) in function of the energy for T = 0.105 GeV (left), T = 0.150 GeV (middle) and T = 0.300 GeV (right) at different μ (MeV) with T_c = 0.15 GeV.

For all these reasons, the study that follows will be only limited to small baryonic potentials. We will thus keep the restriction to two-body interactions which can make sense in such a μ-range. Moreover, the interaction potential and the quasiparticle thermal masses are the same as the ones used up to now, without the inclusion of the baryonic potential. Of course, the obtained results must be considered as preliminary and are just intended to draw a general tendency. The baryonic potential enters thus at two levels in our computations: in the T-matrices because of the in-medium effects and as multiplicative factors to all the EoS contributions. Fortunately as for the T_c-impact, it seems that the μ-dependence on the T-matrix calculations is negligible (see Fig. 5.10). Therefore, these latter do not have to be recomputed at each μ, which drastically reduces the computational time.

In Fig. 5.11, we have plotted the normalized pressure and trace anomaly at different μ for a QGP with two light quarks. Naturally, the gluon chemical potential is zero and the quark one is such that $\mu_u = \mu_d = \mu$. The normalization is given by (5.1.8), that is to say at $\mu = 0$. We realize in Fig. 5.11 that increasing μ is the same as increasing the normalized pressure. This latter is especially driven by the increase of the ideal quark gas contribution given in Fig. 5.12. Indeed, as in the $\mu = 0$ case, the leading contributions to the normalized

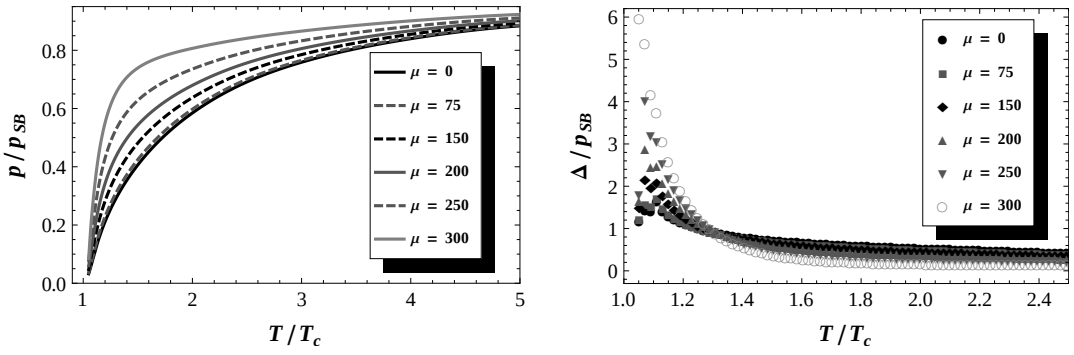

Figure 5.11: QGP with two light quarks. (Left) Normalized pressure p/p_{SB} versus temperature in units of T_c (with $T_c = 0.15$ GeV) at different μ (MeV). (Right) Normalized trace anomaly Δ/p_{SB} (without bound states) versus temperature in units of T_c (with $T_c = 0.15$ GeV) at different μ (MeV).

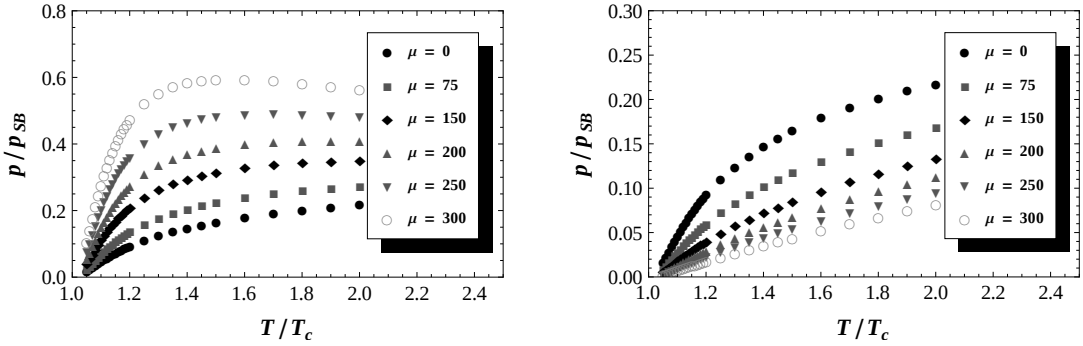

Figure 5.12: QGP with two light quarks. (Left) Ideal quark gaz contribution to the total normalized pressure p/p_{SB} versus temperature in units of T_c (with $T_c = 0.15$ GeV) at different μ (MeV). (Right) Ideal antiquark gaz contribution to the total normalized pressure p/p_{SB} versus temperature in units of T_c (with $T_c = 0.15$ GeV) at different μ (MeV).

pressure are the free part ones since the impact of the interactions is small as observed in Fig. 5.13. Moreover, the decrease of the ideal antiquark gas contribution is slower than the increase of the ideal quark gas one, explaining the total increasing behaviour of the normalized pressure.

Concerning the normalized trace anomaly, it is much more difficult to understand the μ-dependence. The only ascertainments that we can do is that the trace anomaly peak structure becomes higher and higher with the increase of μ and seems to disappear at large μ as observed for $\mu = 300$ MeV. Moreover, we can notice that the convergence to zero is faster with large μ.

As already mentioned, the scattering contributions are small. Nevertheless in Fig. 5.13, we can observe a significant dependence in terms of μ. The qq and qg scattering contributions obviously increase with μ, respectively as $e^{2\beta\mu}$ and $e^{\beta\mu}$, while the $\bar{q}\bar{q}$ and $\bar{q}g$ ones go in opposite way. However, as in the ideal gas case, the increase is higher than the decrease, leading *in fine* to a more important contribution of the scattering

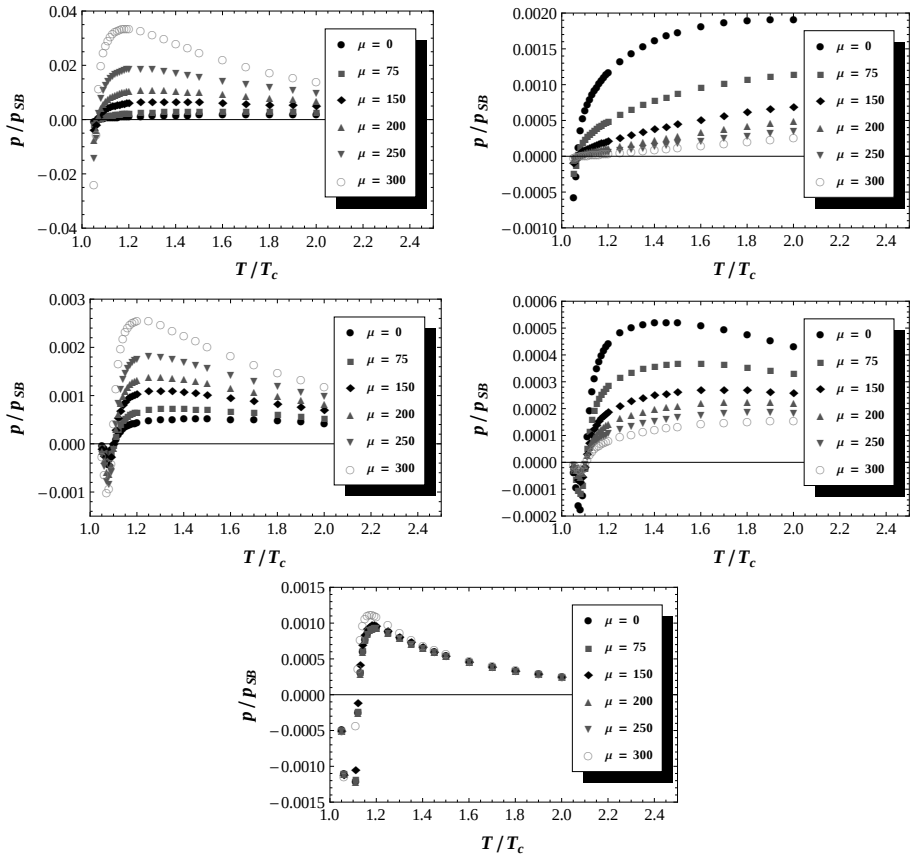

Figure 5.13: QGP with two light quarks. (Left, top) qq-scattering contribution to the total normalized pressure p/p_{SB}. (Right, top) $\bar{q}\bar{q}$-scattering contribution to the total normalized pressure p/p_{SB}. (Left, middle) qg-scattering contribution to the total normalized pressure p/p_{SB}. (Right, middle) $\bar{q}g$-scattering contribution to the total normalized pressure p/p_{SB}. (Bottom) $q\bar{q}$-scattering contribution to the total normalized pressure p/p_{SB}. All the scattering contributions are presented versus temperature in units of T_c (with $T_c = 0.15$ GeV) at different μ (MeV).

parts to the total normalized pressure. To be complete, the $q\bar{q}$ scattering contribution is stable since there is no μ-dependence at the level of the EoS: Indeed, we have $e^{\beta(\mu-\mu)} = 1$. Moreover, since the gg sector is also stable regarding μ, increasing μ means increasing the impact of the quark sector within the QGP.

Finally, we close this study by comparing, in Fig. 5.14, our preliminary results to the lQCD ones given by [Bors12b]. Within this paper, they deal with a QGP with $N_f = 2 + 1$ and with a small baryonic potential μ_B. Each flavour of quarks is considered to carry one third of μ_B. Therefore, we analyse the 2 + 1 QGP with $\mu_u = \mu_d = \mu_s = \mu_B/3$. As for the $\mu = 0$ case, we sightly overestimate the normalized pressure and we miss the peak of the normalized trace anomaly. Therefore, it seems that these differences have mainly the same origin as at $\mu = 0$, and our extrapolations at small μ is compatible with lQCD.

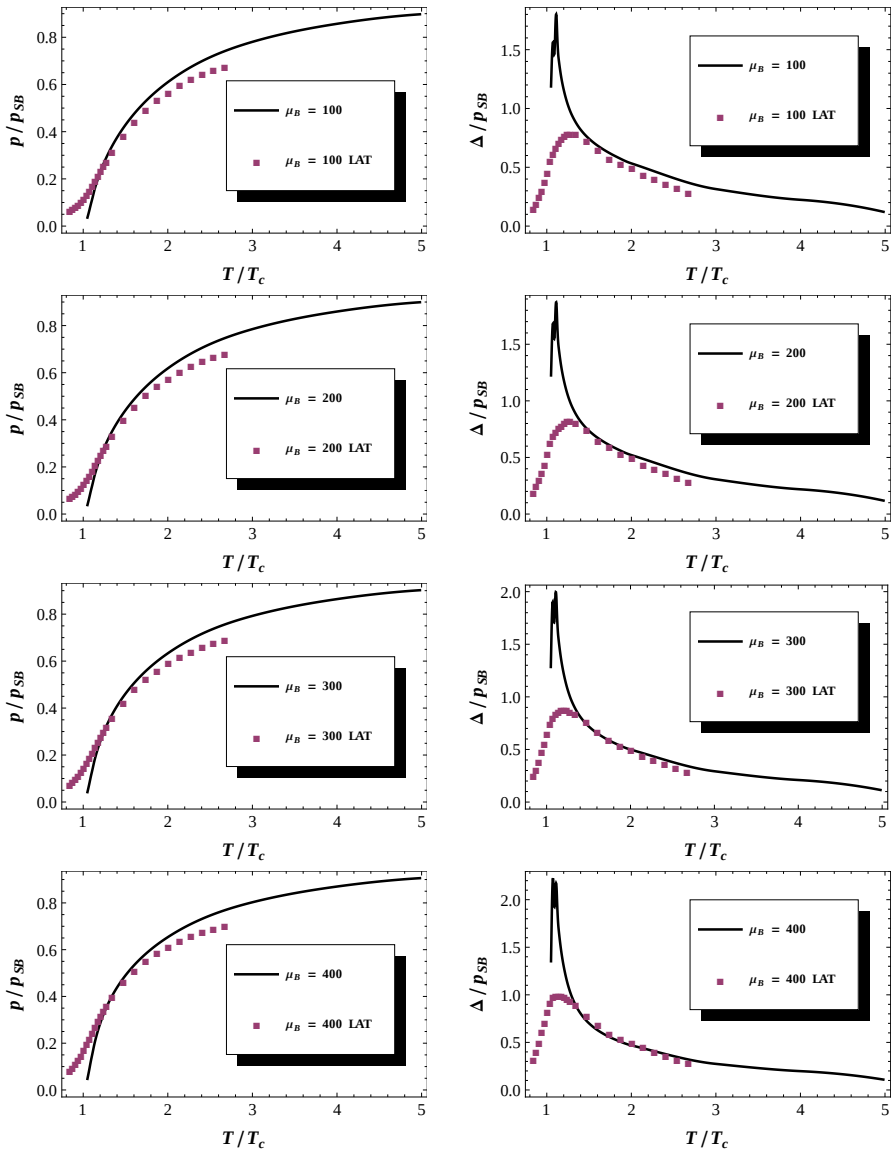

Figure 5.14: QGP with $N_f = 2+1$. (Left) Normalized pressure p/p_{SB} compared to lattice QCD [Bors12b] versus temperature in units of T_c (with $T_c = 0.15$ GeV) at different μ_B (MeV). (Right) Normalized trace anomaly Δ/p_{SB} compared to lattice QCD [Bors12b] versus temperature in units of T_c (with $T_c = 0.15$ GeV) at different μ_B (MeV).

Chapter 6

The $\mathcal{N} = 1$ SUSY Yang-Mills Plasma

Up to now, we have investigated the phenomenology related to the QCD confinement/deconfinement phase transition. However, several extensions can be considered. Among these latter, a particularly challenging case is the Yang-Mills plasma with one flavour of massless Majorana fermions in the adjoint representation of the gauge group. Such a theory is actually supersymmetric and is the $\mathcal{N} = 1$ [1] SUSY YM theory [Sala74], the adjoint quarks being called the gluinos.

In the present chapter, we aim at studying the bound-state spectrum and the EoS of the $\mathcal{N} = 1$ supersymmetric (SUSY) YM theory by resorting to the T-matrix approach developed in Chapter 4 and the thermodynamic formalism presented in Chapter 5. To our knowdlege, this subject has been poorly studied up to now. Only some lQCD calculations at finite temperature [Berg14] have been carried out concerning the Polyakov loop (indicator of the deconfinement) and the chiral condensate susceptibility (indicator of the chiral symmetry restoration).

The chapter will be organized as follows. The first section will recall the general concepts on which SUSY YM theories relied on. Then, the bound-state spectrum at $T = 0$ as well as at finite temperature will be presented and the SUSY EoS will be computed. Finally, the orientifold equivalence will be introduced and computationally checked. Note that these results are available on ArXiv [Lacr14a, Lacr14b].

6.1 General background

The central idea of SUSY theories is to postulate the existence of a supersymmetry that relates bosons and fermions. Each particle is then associated with another one whose spin differs by a half-integer. Such couples form superpartner pairs.

In a theory with a perfectly unbroken supersymmetry, each pair of superpartners shares the same mass and internal quantum numbers except for the spin. For instance, a "squark" (spin 0) is a boson similar to the quark and the gluino (spin 1/2) is the fermionic counterpart of the gluon. However, since no superpartners have been observed yet, supersymmetry must be spontaneously broken if it exists, and the superpartner mass of each particles has to be higher than the particle mass to which it is associated.

As already mentioned, the behaviour of each quantum field theory is predicted by its β-function. For our case of interest, that is to say the $\mathcal{N} = 1$ SUSY YM theory, the β-function has been exactly computed from

1. $\mathcal{N}$ indicates the number of supersymmetric generators.

instanton calculus [Novi83]. As an illustration, it is worth giving its form for an SU(N_c) theory,

$$\beta(g) = -\frac{g^3}{16\pi^2}\frac{3N_c}{1-\frac{g^2N_c}{8\pi^2}}. \tag{6.1.1}$$

This form is compatible with asymptotic freedom as in QCD. Moreover, the $\mathcal{N} = 1$ SUSY YM theory exhibits a confined phase as well as a spontaneously broken chiral symmetry driven by a non-vanishing expectation value of the gluino condensate at $T = 0$ [Armo03]. Several studies have been devoted to compute its spectrum with the gauge groups SU(N_c) (see for instance [Berg13, Camp99, Demm10, Farc04, Farr98, Feo04]).

Because of the asymptotic freedom, a deconfined medium is expected at high temperature. Recent lattice results indicate that it is indeed the case, at least for SU(2) [Berg14]. Moreover, this might be the case for an arbitrary gauge group too [Anbe14]. At very high temperatures finally, the deconfined phase should behave as a free gas of gluons and gluinos [Amat88].

Finally, a peculiarity of SU(N_c) $\mathcal{N} = 1$ SUSY YM is that it is equivalent to one-flavour QCD at large N_c provided that quarks are in the two-indice antisymmetric representation of the gauge group, which is isomorphic to the fundamental one at $N_c = 3$. This duality is called "orientifold equivalence" and has attracted a lot of attention since the pioneering work [Armo03].

6.1.1 $\mathcal{N} = 1$ SUSY Yang-Mills spectrum at $T = 0$

Let us first discuss the $\mathcal{N} = 1$ SUSY YM spectrum at $T = 0$. Since it is the minimal SUSY extension of the YM theory, it only contains gluons g, and gluinos $\tilde{g}$. Within our approach, we assume that the gluons and the gluinos have the same mass and quantum numbers except for the spin. Therefore, if we consider the formation of two-body bound states, the SUSY theory allows the production of gg, $\tilde{g}\tilde{g}$ and $g\tilde{g}$ at $T = 0$. Indeed, the singlet representation, that is to say the only one allowed in the confinement regime, appears in the tensor product of the adjoint representation by itself (see Appendix C); the gluino lying also in the adjoint representation of the gauge group.

For the gg channels, the study developed in Section 4.4.2 remains naturally valid. In this discussion, we thus only focus on the $\tilde{g}\tilde{g}$ and $g\tilde{g}$ channels. Concerning the $\tilde{g}\tilde{g}$-bound states, the allowed J^{PC} states are the same as the meson ones (cfr. Table 4.2) with a restriction driven by the Pauli's symmetry principle. Therefore, for $\tilde{g}\tilde{g}$ systems, the parity is given by $P = (-)^{L+1}$ and the charge conjugation by $C = (-)^{L+S}$, as in $q\bar{q}$ pairs and the Pauli principle implies that (anti)symmetric colour $\tilde{g}\tilde{g}$ states are characterized by $L + S$ even (odd) and $C = +\ (-)$ [Zuk83]. As we analyse the confined regime and because the colour-singlet representation is symmetric (see Appendix C), only symmetric J^{PC} channels can exist at $T = 0$. These channels are displayed in Table 6.1.

J	L	S	P	C	J^{PC}
0	0	0	-	+	0^{-+}
	1	1	+	+	0^{++}
	1	1	+	+	1^{++}
2	1	1	+	+	2^{++}

	T-matrix
$L = 0$	1.58
$L = 1$	2.26

Table 6.1: (Left) J^{PC} states allowed for $\tilde{g}\tilde{g}$ with $L = 0$ or $L = 1$ at $T = 0$. (Right) Masses (in GeV) of the $L = 0$ and $L = 1$ $\tilde{g}\tilde{g}$-states at $T = 0$ with the gauge group SU(N_c).

The $\tilde{g}\tilde{g}$-potential is given by (4.4.6) and the gluino mass as well as the string breaking are the same as the gluon ones. The results are presented in Table 6.1. Naturally, similarly to the meson spectrum, the model is not able to distinguish bound states with different spin numbers. These states are degenerate. The $L = 0$ $\tilde{g}\tilde{g}$-state is lighter than the lightest glueball since it is a pure S-wave while the $L = 1$ $\tilde{g}\tilde{g}$-state has exactly the same mass as the 0^{+-} glueball because they share the same partial-wave decomposition.

Concerning the $g\tilde{g}$ channels, the building of the J states requires the helicity formalism since the gluon is transverse. The states on which we focus are given in Appendix B. Due to their partial-wave decomposition, the potential reads

$$(J1)\ V_{\frac{1}{2}}(q,q') = V_1(q,q'), \tag{6.1.2}$$

$$(J2)\ V_{\frac{3}{2}}(q,q') = \frac{1}{6}V_0(q,q') + \frac{5}{6}V_2(q,q'), \tag{6.1.3}$$

$$(J3)\ V_{\frac{3}{2}}(q,q') = \frac{1}{2}V_0(q,q') + \frac{1}{2}V_2(q,q'), \tag{6.1.4}$$

$$(J4)\ V_{\frac{1}{2}}(q,q') = \frac{2}{3}V_0(q,q') + \frac{1}{3}V_2(q,q'), \tag{6.1.5}$$

$$(J5)\ V_{\frac{3}{2}}(q,q') = \frac{7}{10}V_1(q,q') + \frac{3}{10}V_3(q,q'), \tag{6.1.6}$$

$$(J6)\ V_{\frac{3}{2}}(q,q') = \frac{9}{10}V_1(q,q') + \frac{1}{10}V_3(q,q'). \tag{6.1.7}$$

Note that the parity is not defined for such states [Zuk83]. Therefore, in order to have a clear nomenclature, we prefer using the notation $J1 \to J6$. Because a $g\tilde{g}$ channel has no symmetry principle to respect, all the above states can exist in the colour-singlet representation. The $T = 0$ spectrum is given in Table 6.2.

	T-matrix		T-matrix
$J1$	2.26	$J4$	1.96
$J2$	2.40	$J5$	2.40
$J3$	2.13	$J6$	2.31

Table 6.2: Masses (in GeV) of the $g\tilde{g}$-states at $T = 0$ with the gauge group SU(N_c).

Of course, the $J1$ and $J4$ states have respectively the same mass as the 0^{-+} and 0^{++} glueballs (see the partial-wave decomposition). Moreover, the mass hierachy naturally follows the proportion of low L-wave in the potential: The S-wave being the most attractive channel. To be complete, as in the gg case, all the results given in Table 6.1 and in Table 6.2 are valid for any gauge group since $\kappa_{\bullet;gg} = -1$.

Let us now compare this spectrum to current known results in the field. It is known from effective Lagrangians that supersymmetry is not expected to be broken at the level of the bound-state spectrum. Hence the lightest states should form two supermultiplets [Farr98]. Since hyperfine corrections (spin-spin, spin-orbit, etc.) are neglected in the present work, we expect these supermultiplets to be observable but only approximately degenerated.

The first supermultiplet can be seen in the first three lines of Table 6.3. As expected from [Farr98], it contains the pseudoscalar $\tilde{g}\tilde{g}$ state, also known as the $a - \eta'$ (the adjoint η'), a spin $1/2$ state and the scalar glueball. The last two states are degenerate, but not the $a - \eta'$ which is lighter. This is mainly a consequence of the approach used here: The $a - \eta'$ being a pure S-wave, it is maximally sensitive to the attractive Coulomb interaction and its mass is logically smaller than the other state ones. The degeneracy

could be recovered by including for example spin-orbit terms that would decrease the mass of the $J4$ and 0^{++} states only, but this is out of the scope of the present calculations.

Content	State	Mass
$\tilde{g}\tilde{g}$	0^{-+}	1.58
$g\tilde{g}$	$J4$	1.96
gg	0^{++}	1.96
$\tilde{g}\tilde{g}$	0^{++}	2.26
$g\tilde{g}$	$J1$	2.26
gg	0^{-+}	2.26
$g\tilde{g}$	$J3$	2.13
gg	2^{++}	2.21
$\tilde{g}\tilde{g}$	$\{1,2\}^{++}$	2.26
$g\tilde{g}$	$J6$	2.31

Table 6.3: Masses (in GeV) of the lowest-lying bound states at $T = 0$ with the gauge group SU(N_c) in $\mathcal{N} = 1$ SUSY YM. J^{PC} is indicated for gg and $\tilde{g}\tilde{g}$ states. The notation defined in Appendix B is used to characterize the $g\tilde{g}$ states.

The second supermultiplet is shown in the lines four to six of Table 6.3: The masses are equal as expected from supersymmetry. We have also listed other states with higher spins: They are absent of low-energy effective actions but straightforwardly computed within our formalism.

Our spectrum is actually very similar to what is observed in lattice studies, see for example [Farc04, Demm10, Berg13]. In these studies also, the three lightest states are not exactly degenerate although very close up to the error bars, and the $a - \eta'$ is the lightest state. It is an indication that exact supersymmetry is still not reached on the lattice, as in our model. Smaller lattice sizes would be needed in order to draw definitive conclusions on the structure of the spectrum [Berg13], so the agreement between our model and the lattice data should be, in our opinion, restricted to qualitative considerations.

We finally mention the work [Feo04], in which information on the $\mathcal{N} = 1$ SUSY YM spectrum is obtained by resorting to the orientifold duality between the theory under study and QCD with one quark flavour. In such an approach, the $a - \eta'$ could be the lightest state of the theory without being degenerated with the other states of the aforementioned supermultiplet. So the zero-temperature mass spectrum is still an open problem in our opinion.

6.1.2 $\mathcal{N} = 1$ SUSY YM at finite temperature

Let us now have a look to the $\mathcal{N} = 1$ SUSY YM spectrum at finite temperature by using the same parameters as the ones given in Section 4.5.3: The gluino thermal mass thus follows the formula (4.5.10) and the finite-temperature potential between quasiparticles is given by (4.5.5). Concerning T_c, we prefer to fix it to 245 MeV (see Section 6.2.1 for further explanations and motivations). This change is not significant here since the T_c-dependence of the results is marginal [2]. The gg-spectrum is therefore recomputed in Table 6.4 for the sake of accuracy. Nevertheless, its main features remain unchanged.

2. Indeed, T_c enters only in the Bose-enhancement or in the Pauli-blocking and we have seen that these effects are negligible in the T-matrix computations.

Channel		Singlet			Adjoint			(2,0)		
Group		All			SU($N_c \geq 3$)			G_2		
T/T_c	$2\,m_g$	0^{++}	0^{-+}	2^{++}	0^{++}	0^{-+}	2^{++}	0^{++}	0^{-+}	2^{++}
1.05	2.73	1.90	2.29	2.29	2.50	2.71	2.65	2.59	-	2.68
		2.72								
1.10	2.20	1.91	2.19	2.09	2.16	-	-	2.18		-
1.15	1.98	1.86	-	1.96	-			-		
1.20	1.86	1.80		-						
1.25	1.79	1.77								
1.30	1.74	-								

Table 6.4: Masses (GeV) of lowest-lying glueballs above T_c ($T_c = 0.245$ GeV). A line mark the temperature at which a bound state is not detected any more.

Concerning the $\tilde{g}\tilde{g}$-bound states, the same selection rule that the one used in the $T = 0$ case can be applied for the J^{PC} numbers. However, much more states are allowed since there is no more confinement. All these channels are thus displayed in Table 6.5 with L up to one.

The results of the T-matrix computations for $\tilde{g}\tilde{g}$ states are given in Table 6.6 . It is important to mention that because of the gluino fermionic nature, the in-medium effect takes into account here is the Pauli-blocking. Moreover, the study is carried out for a SU(N_c) and G_2 gauge group. The channels that produce bound states are only the singlet, the adjoint representation and the $(2,0)^S$ of G_2. As in the glueball case, the $\tilde{g}\tilde{g}$-masses are close to their zero value in 1.05 T_c and the $L = 0$ $\tilde{g}\tilde{g}$ states in singlet are the lightest ones. It is obvious since these latter are pure S-waves in the most attractive colour channel. Furthermore, they naturally survive longer, up to 1.4 T_c.

J	L	S	P	C	J^{PC}	$\mathcal{S}_\mathcal{C}$
0	0	0	-	+	0^{-+}	S
	1	1	+	+	0^{++}	S
1	1	0	+	-	1^{+-}	A
	0	1	-	-	1^{--}	A
	1	1	+	+	1^{++}	S
2	1	1	+	+	2^{++}	S

Table 6.5: J^{PC} states allowed for $\tilde{g}\tilde{g}$ with $L = 0$ or $L = 1$ at finite temperature. $\mathcal{S}_\mathcal{C}$ represents the required symmetry of the colour representation.

Finally, the results for $g\tilde{g}$ are displayed in Table 6.7. Since there is no symmetry principle to respect, all the gauge group representations are allowed. Without surprise, states with a strong S-wave in singlet survive longer, up to 1.3 T_c and the mass at 1.05 T_c is nearly equal to that at $T = 0$.

In summary, our computations show that two-body bound states can exist in the gluino-gluon plasma for any species in the range (1-1.30) T_c, contrary to the pure QCD case with 2 (+ 1) quark flavours in which only glueballs significantly survive above T_c. The picture developed in the pioneering work [Shur04], where the importance of binary bound states on some features of the quark-gluon plasma was stressed, seems thus to be valid in a supersymmetric extension of YM theory too. A more detailed look at the dissociation tables

Channel		Singlet		Adjoint		$(2,0)$	
Group		All		All		G_2	
T/T_c	$2\,m_g$	$L=0$	$L=1$	$L=0$	$L=1$	$L=0$	$L=1$
1.05	2.73	1.30	2.29	2.33	2.71	2.44	-
		2.65					
1.10	2.20	1.66	-	2.08	-	2.13	
1.15	1.98	1.72		1.96		-	
1.20	1.86	1.73		-			
1.25	1.79	1.72					
1.30	1.74	1.71					
1.35	1.70	1.70					
1.40	1.67	-					

Table 6.6: Masses (GeV) of lowest-lying $\tilde{g}\tilde{g}$ states above T_c ($T_c = 0.245$ GeV). A line mark the temperature at which a bound state is not detected anymore.

Channel		Singlet					
Group		All					
T/T_c	$2\,m_g$	$J1$	$J2$	$J3$	$J4$	$J5$	$J6$
1.05	2.73	2.29	2.57	2.15	1.90	2.52	2.37
		2.72					
1.10	2.20	2.19	-	2.04	1.92	-	-
1.15	1.98	-		1.94	1.87		
1.20	1.86			-	1.82		
1.25	1.79				1.78		
1.30	1.74				-		

Channel		Adjoint					
Group		All					
T/T_c	$2\,m_g$	$J1$	$J2$	$J3$	$J4$	$J5$	$J6$
1.05	2.73	2.71	-	2.60	2.52	-	2.72
1.10	2.20	-		-	2.16		-
1.15	1.98				-		

Channel		$(2,0)$					
Group		G_2					
T/T_c	$2\,m_g$	$J1$	$J2$	$J3$	$J4$	$J5$	$J6$
1.05	2.73	-	-	2.65	2.59	-	-
1.10	2.20			-	2.19		
1.15	1.98				-		

Table 6.7: Masses (GeV) of lowest-lying $g\tilde{g}$ states above T_c ($T_c = 0.245$ GeV). A line mark the temperature at which a bound state is not detected anymore.

shows that the behaviour of a given bound-state mass with the temperature is not systematic: It can either increase or decrease before the dissociation. We have pointed out in [Lacr13] that the observed behaviour in the glueball sector is in qualitative agreement with the lattice study [Meng09]. As soon as gluinos are involved, there are, to our knowledge, no study to which our results can be compared.

6.2 Thermodynamics of the $\mathcal{N} = 1$ SUSY Yang-Mills

6.2.1 Model description

Let us now particularize the general formalism presented in Section 5.1.1 to the $\mathcal{N} = 1$ SUSY extension of the gluon plasma *i.e.* a plasma made of two species of quasiparticles: the gluons and its supersymmetric partners, the gluinos. As already discussed in Section 6.1.2, we treat here a case in which the gluon and the gluino share the same properties, except for the spin naturally. The finite-temperature potential between quasiparticles is given by (4.5.5) and the thermal mass formula is (4.5.10).

Concerning T_c, we have already mentioned that this value is moved to 245 MeV. The reasons are the following. As seen in Section 5.2 for the non-SUSY YM case, identifying the critical temperature to the Hagedorn temperature of a bosonic closed string theory in $(3+1)$-dimensions agrees well with currently known lattice data. Correspondingly, in the $\mathcal{N} = 1$ SUSY YM, we conjecture that the Hagedorn temperature should be that of a non-critical (*i.e.* well-defined in a 4-dimensional spacetime) closed superstring theory. Such a theory has been studied in particular in [Cham91], where the usual Hagedorn temperature is recovered for the bosonic case and where the ratio

$$\frac{T_c(\text{SUSY})}{T_c(\text{non-SUSY})} = \sqrt{\frac{2}{3}} \approx 0.8 \tag{6.2.1}$$

is found for the superstring. Interestingly, the same value has been recently observed in a SU(2) lattice simulation of $\mathcal{N} = 1$ SUSY YM thermodynamics [Berg14]. Equation (6.2.1) thus provides an explanation to this value, finally leading us to set

$$\frac{T_c(\text{SUSY})}{\sqrt{\sigma}} = \frac{1}{\sqrt{\pi}} \approx 0.6, \tag{6.2.2}$$

and so, $T_c = 245$ MeV since $\sigma = 0.176$ GeV^2.

For the $J^{(PC)}$ channels considered inside the plasma, the selection rules proposed in Section 5.3.2 to retain a channel in the computations, are used and the results are summarized in Table 6.8. Moreover, since we are in the deconfinement range, all the colour representations provided by the tensor product of two adjoint representations (given in Appendix C) are allowed *modulo* the respect of the Pauli's principle if it is needed. These considerations characterize the summation appearing in (5.1.9). For memory, the SU(2) thermodynamics requires the computation of 35 different T-matrix files, for SU(3) and G_2, 48 files are needed, while 61 are necessary for the SU(N_c) case.

Regarding the free part of (5.1.9), we have here

$$\Omega_0^{\text{SUSY}} = 2 \dim\, adj\, \left(\omega_0^B(m_g, 0) + \omega_0^F(m_{\tilde{g}}, 0)\right) \tag{6.2.3}$$

where ω_0^B and ω_0^F are respectively defined in (5.1.6) and (5.1.7). In our work, $m_g = m_{\tilde{g}}$. Moreover, the normalization of the thermodynamic quantities is given by

$$p_{SB} = \frac{\pi^2}{45\beta^4}\left(1 + \frac{7}{8}\right) \dim\, adj = \frac{\pi^2}{24\beta^4} \dim\, adj. \tag{6.2.4}$$

gg	$\tilde{g}\tilde{g}$	$g\tilde{g}$
0^{++}	0^{-+}	$J1$
0^{-+}	1^{--}	$J2$
2^{++}	0^{++}	$J3$
1^{++}	1^{++}	$J4$
-	2^{++}	$J5$
-	1^{+-}	$J6$

Table 6.8: $J^{(PC)}$ channels considered inside the $\mathcal{N} = 1$ SUSY plasma and provided by the selection results summarized in Table 6.9

T/T_c	gg: $\sigma_{J^{PC}}/\sigma_{0^{++}}$						$\tilde{g}\tilde{g}$: $\sigma_L/\sigma_{L=0}$			
	0^{++}	0^{-+}	2^{++}	1^{++}	1^{-+}	2^{++}	$L=0$	$L=1$	$L=2$	$L=3$
1.2	1.00	0.25	0.41	0.33	0.19	0.19	1.00	0.42	0.19	0.11
1.5	1.00	0.30	0.46	0.37	0.23	0.23	1.00	0.17	0.07	0.04
2	1.00	0.29	0.47	0.38	0.23	0.23	1.00	0.21	0.09	0.05
5	1.00	0.19	0.43	0.33	0.14	0.14	1.00	0.20	0.07	0.02

T/T_c	$g\tilde{g}$: σ_J/σ_{J4}					
	$J4$	$J1$	$J2$	$J3$	$J5$	$J6$
1.2	1.00	0.46	0.33	1.03	0.32	0.41
1.5	1.00	0.30	0.21	0.62	0.20	0.27
2	1.00	0.34	0.24	0.66	0.23	0.30
5	1.00	0.29	0.19	0.65	0.18	0.25

Table 6.9: Ratio of the cross-sections for the SUSY channels. Selection criterion: Ratio > 25 % for at least one $T \geq 1.2\,T_c$. The gg channels are compared in the octet-colour representation of the SU(3) gauge group while the $\tilde{g}\tilde{g}$ L-channels as well as the $g\tilde{g}$ J-channels are analysed with the singlet-colour representation. Similar results are obtained from other colour channels.

The inclusion of the bound-state and scattering contributions are computed in the same way as $\Omega_{bs}^{\rm QCD}$ and $\Omega_{s}^{\rm QCD}$ but of course, adapted to the SUSY bound states and degrees of freedom. So,

$$\Omega_{(2)}^{\rm SUSY} = \Omega_{0}^{\rm SUSY} + \Omega_{bs}^{\rm SUSY} + \Omega_{s}^{\rm SUSY}. \tag{6.2.5}$$

As in the QCD case, annihilation contributions will be neglected.

6.2.2 Equations of state

6.2.2.1 Pressure

With the above description, we are now in position to compute the normalized pressure of the $\mathcal{N} = 1$ SUSY YM plasma. The three different parts of $\Omega_{(2)}^{\rm SUSY}$, namely the free, the bound-state and the scattering terms, are displayed in Fig. 6.1. The global structure is the same as the one presented in the pure YM case. The bound-state contribution is weak at every computed temperature but it is logically maximal around 1.2

T_c, where the trace anomaly appears to be maximal (see Fig. 6.3). The scattering part is also maximal around 1.2 T_c and the repulsive channels are dominant at higher temperatures, leading to decrease the free gas pressure. Nevertheless, as in the pure YM case, the effect of two-body interactions on the pressure is a minor contribution to the total pressure. The slight differences are the following. The bound-state sector is richer since $\tilde{g}\tilde{g}$ and $g\tilde{g}$ bound states also exist up to 1.4 T_c in their most attractive channel (see Section 6.1.2).

Concerning the high temperature limit, our model should be accurately described within the Born approximation, $\mathcal{T} = V + \mathrm{O}(V^2)$. It has been shown in Section 5.1.3 that the interactions between two different species vanish within this approximation because of an identity relating the colour factors: $\sum_{\mathcal{C}} \dim \mathcal{C}\ \kappa_{\mathcal{C},ij} = 0$ (see (5.1.20)). In conclusion, gluons and gluinos does not interact with each other at high temperature in average. However, the interactions between gluons only and gluinos only are still present.

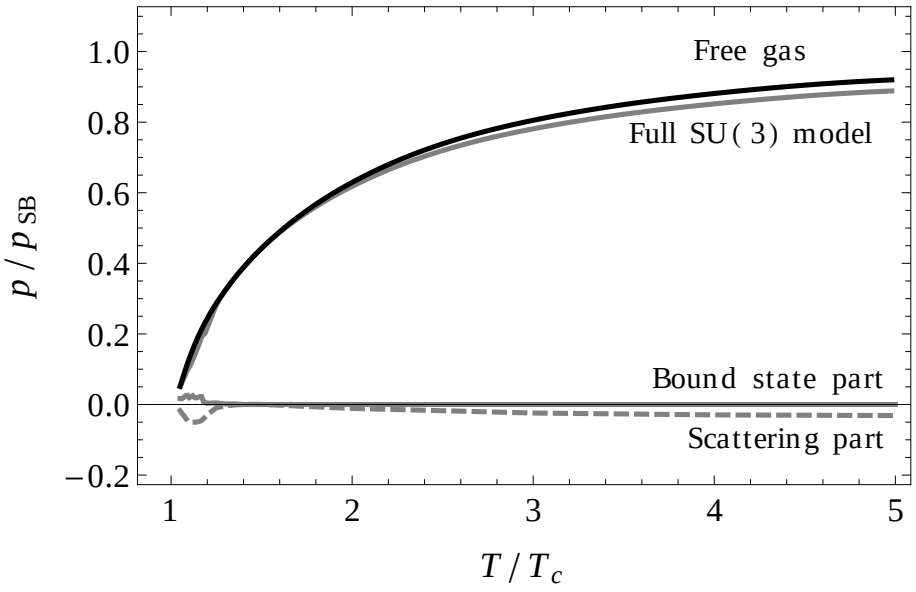

Figure 6.1: $\mathcal{N} = 1$ SUSY plasma. Normalized pressure p/p_{SB} versus temperature in units of T_c (with $T_c = 0.245$ GeV), computed for the gauge group SU(3). The free, the bound-state and the scattering contributions are also indicated.

In Fig. 6.2, the SU(N_c) gauge structure of the normalized total pressure is shown. Again in this case, an asymptotically SU(N_c) gauge-group independent pressure seems to emerge: The maximum deviation of the gauge universality is just above T_c. This is in agreement with the scaling relations presented in Section 5.2.2.3. Indeed, if we expand the T-matrix in terms of V, the colour dependence of the total pressure (without considering bound states) is in dim adj up to $O(V^3)$. This factor is thus cancelled by the same one in the normalization pressure and so, the gauge-group independence is obtained at high temperature since such expansion of the T-matrix becomes more and more valid with an increase of T. Moreover, it is worth adding that this peculiarity of our model is due to the Casimir scaling and to the prescription that we have used for the gluon and gluino thermal masses. Indeed, these latter are gauge-group independent in our framework.

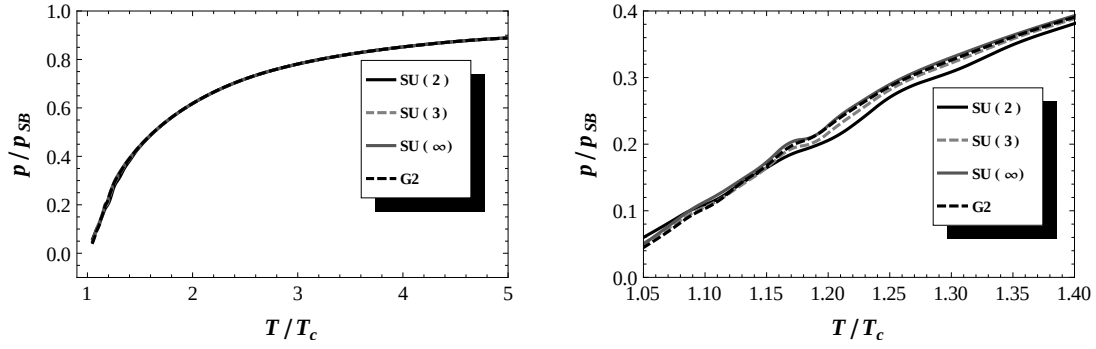

Figure 6.2: $\mathcal{N} = 1$ SUSY plasma. (Left) Normalized pressure p/p_{SB} versus temperature in units of T_c (with $T_c = 0.245$ GeV), computed for SU(N_c) and G_2 gauge groups. (Right) Zoom near T_c.

6.2.2.2 Trace anomaly

The behaviour of the total normalized trace anomaly is displayed in Fig. 6.3. Again, we find appropriate to compute it without bound state (since the treatment of bound states requires a more refined study as already mentioned), and to compare it to the normalized free gas part of $\Omega^{\rm SUSY}_{(2)}$. We also observe in this case that the interactions provide the peak structure and that the trace anomaly tends to zero at high temperature. This last observation is in agreement with [Amat88] in which a $\mathcal{N} = 1$ SUSY theory is expected to behave at high temperature as a gas of free gluinos and gluons. Concerning the peak structure, a quantitative measure is naturally lost since all the two-body bound states that should appear around T_c are not taken into account. This study is left for further developments.

Finally, the last thermodynamic quantities that we want to discuss in this section is the normalized trace anomaly for SU(N_c) and G_2 groups, presented in Fig. 6.4. The asymptotic gauge-group universality is, without surprise, observed and follows the same justification as the normalized pressure. The behaviour around T_c exhibits some slight differences according to the gauge group. This can be understood by the fact that the number of channels to include in the computation depends on the gauge group (see Appendix C).

6.2.3 Comparison to pure Yang-Mills theory

At this stage, it is natural to wonder whether the inclusion of gluinos has a strong impact or not on the EoS compared to pure YM theory. In other words: How far the EoS of the supersymmetric and non-supersymmetric cases are ? Since our framework has already proven to describe satisfactorily the lattice EoS of pure YM theory with gauge groups SU(N_c), we are in position to compare these previous results with the new ones. This is done in Fig. 6.5. It is readily seen that the SU(3) pressure computed in the non-SUSY case on the lattice is surprisingly close to the SUSY EoS. As in the QCD case, an universality between the different pressures seem to emerge once they are normalized to their own SB pressure and presented in units of T/T_c with the appropriate T_c for each theory.

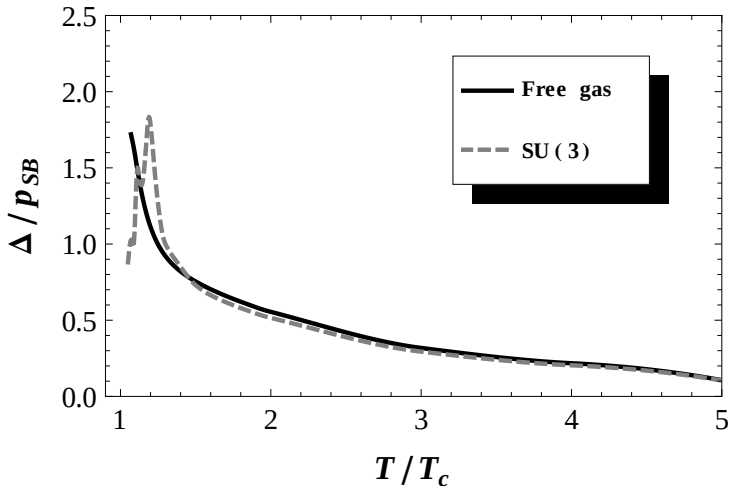

Figure 6.3: $\mathcal{N} = 1$ SUSY plasma. (Left) Normalized trace anomaly Δ/p_{SB} versus temperature in units of T_c (with $T_c = 0.245$ GeV), compared to the normalized free gas part of $\Omega^{(2)}$.

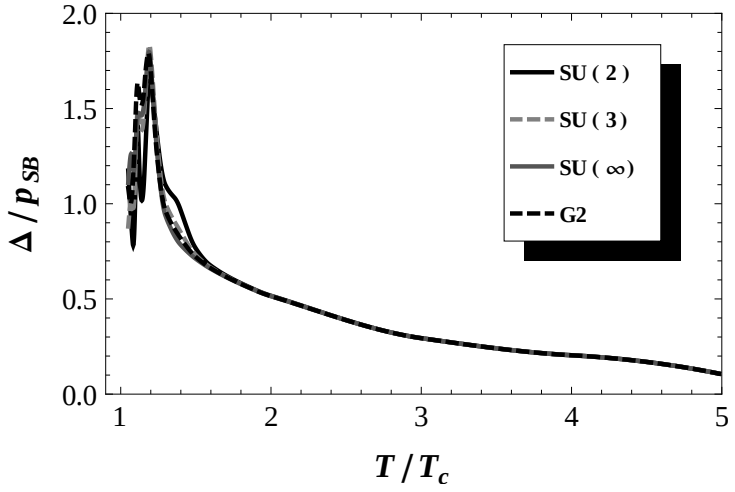

Figure 6.4: $\mathcal{N} = 1$ SUSY plasma. (Left) Normalized trace anomaly Δ/p_{SB} versus temperature in units of T_c (with $T_c = 0.245$ GeV) for different SU(N_c) gauge groups.

6.2.4 Orientifold planar equivalence

Let us now denote by QCD$_{AS}$ a SU(N_c) YM theory with N_f Dirac fermions in the two-index anti-symmetric representation, and QCD$_{adj}$ a SU(N_c) YM theory with N_f Majorana flavours in the adjoint representation. The so-called orientifold equivalence states that QCD$_{AS}$ and QCD$_{adj}$ are equivalent at large

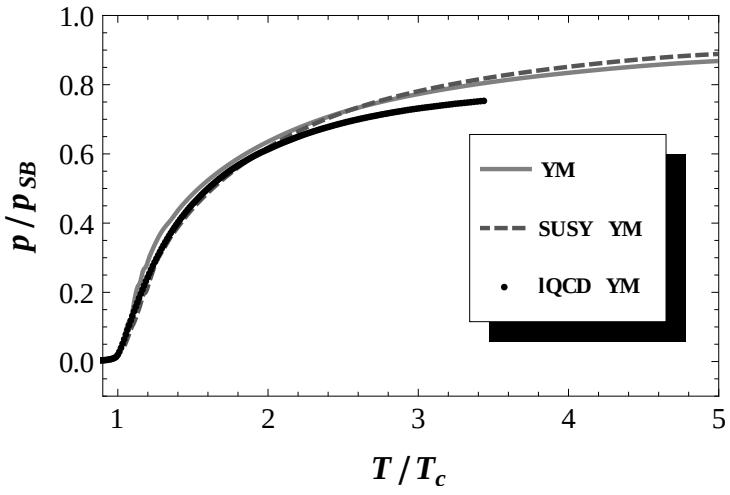

Figure 6.5: Normalized pressure p/p_{SB} versus temperature in units of T_c for the gauge group SU(3) in the $\mathcal{N} = 1$ SUSY YM case ($T_c = 0.245$ GeV, dashed line) and pure YM case ($T_c = 0.3$ GeV, solid line). Lattice data of [Pane09] corresponding to the pure SU(3) YM case are also indicated for comparison (dots).

N_c in the bosonic sector [Armo03]. This equivalence is particularly appealing when $N_f = 1$ since in this case QCD$_{adj}$ is actually the $\mathcal{N} = 1$ SUSY YM. Moreover, QCD$_{AS}$ reduces to standard one-flavour QCD (vanishing isospin) for $N_c = 3$.

Within our framework, it is possible to show that the orientifold equivalence holds, and to compute how far one-flavour QCD deviates for the large-N_c limit. This is the purpose of the present section where we notice that the meaning of the symbol $\cong$ will be "equal at the limit $N_c \to \infty$". Moreover, q_A ($\bar{q}_A$) will denote a(n) (anti)quark in the two-index antisymmetric representation $(0, 1, \ldots, 0, 0)$ (resp. $(0, 0, \ldots, 1, 0)$).

First, we have to check that the masses of the particles coincide since the free-gas contribution is important. The gluon thermal mass is common to QCD$_{AS}$ and QCD$_{adj}$ since the gluonic sector is identical in both theories. An assumption of our model is that the function $\Delta(T)$ is gauge-group independent. Hence, $\delta_{\tilde{g}}(T) = \delta_g(T) = \Delta(T)$. Using the colour factors listed in Appendix C, one gets following (4.5.6),

$$\delta_{q_A}(T) = \delta_{\bar{q}_A}(T) = \sqrt{\frac{N_c^2 - N_c - 2}{N_c^2}}\Delta(T), \tag{6.2.6}$$

which is not equal to $\Delta(T)$ in general. Nevertheless, $\delta_{q_A}(T) = \delta_{\bar{q}_A}(T) \cong \delta_{\tilde{g}}(T)$ as expected. Coherently assuming that $m_{0,q_A} = m_{0,\bar{q}_A} = m_{0,\tilde{g}}$, we obtain that the thermal masses $m_{\tilde{g}}(T)$, $m_{q_A}(T)$ and $m_{\bar{q}_A}(T)$ are equal at large N_c. The free gluinos thus bring a contribution

$$\Omega_0(\tilde{g}) = 2(N_c^2 - 1)\omega_0^F(m_{\tilde{g}}, 0) \tag{6.2.7}$$

to the grand potential, while the free quarks and antiquarks bring a corresponding contribution

$$\Omega_0(q_A, \bar{q}_A) = 2\frac{N_c(N_c - 1)}{2}\omega_0^F(m_{q_A}, 0) + 2\frac{N_c(N_c - 1)}{2}\omega_0^F(m_{\bar{q}_A}, 0). \tag{6.2.8}$$

It is then straightforwardly checked that

$$\Omega_0(\tilde{g}) \cong \Omega_0(q_A, \bar{q}_A). \tag{6.2.9}$$

After the equivalence of the free part, we have to show the equivalence of the two-body contributions. The gg channels are trivially equal in QCD$_{AS}$ and QCD$_{adj}$, so only the $\tilde{g}\tilde{g}$ and $g\tilde{g}$ channels have to be investigated.

The $\tilde{g}\tilde{g}$ channels are bosonic. Their contribution should thus be equivalent to that of the q_Aq_A, $\bar{q}_Aq_A$ and $\bar{q}_A\bar{q}_A$ ones. The colour singlet appears in $\tilde{g}\tilde{g}$ and $q_A\bar{q}_A$; the corresponding contributions to the pressure are different because the Pauli's principle has to be applied in the first one, not in the second one. This discrepancy is irrelevant at large N_c because the singlet contribution is of order 1, not N_c^2. The symmetric and antisymmetric adjoint channels in $\tilde{g}\tilde{g}$ bring a pressure contribution which is equal to the adjoint channel appearing in $q_A\bar{q}_A$: All the possible helicity states are allowed in both cases. The $(2, 0, \ldots, 1, 0)$ and $(0, 1, \ldots, 0, 2)$ channels in $\tilde{g}\tilde{g}$ have no equivalent in the quark case, but they bring no contribution to the EoS since $\kappa_{\mathcal{C}} = 0$. The remaining colour channels in $\tilde{g}\tilde{g}$ are the symmetric $(2, 0, \ldots, 0, 2)$ and $(0, 1, \ldots, 1, 0)$ ones, that should match with the symmetric $(0, 0, 0, 1, 0 \ldots, 0)$ and $(0, \ldots, 0, 1, 0, 0, 0)$ ones in q_Aq_A and $\bar{q}_A\bar{q}_A$. This is actually the case. Indeed, Pauli's principle asks the $\tilde{g}\tilde{g}$ states to have $L + S$ even, just as for the q_Aq_A and $\bar{q}_A\bar{q}_A$ states. Moreover, the Born approximation is valid at large N_c for all those channels since $\kappa_{\mathcal{C}} = O(1/N_c)$. The contributions of the $\tilde{g}\tilde{g}$ channels to the grand potential is thus proportional to $\sum_{\mathcal{C}} \dim \mathcal{C}\ \kappa_{\mathcal{C}} = (N_c^2 - 1)/2$, as well as the q_Aq_A, $\bar{q}_A\bar{q}_A$, $q_A\bar{q}_A$ ones for which $\sum_{\mathcal{C}} \dim \mathcal{C}\ \kappa_{\mathcal{C}} + \sum_{\bar{\mathcal{C}}} \dim \bar{\mathcal{C}}\ \kappa_{\bar{\mathcal{C}}} = (N_c^2 - 1)(N_c - 2)/(2N_c)$. Both factors are equal at large N_c, leading to equivalent contributions to the EoS.

Finally, the $g\tilde{g}$ contribution should be equivalent to the q_Ag and $\bar{q}_Ag$ ones. The same kind of arguments apply, so we will not perform the full analysis. Let us just mention that the two adjoint channels in $g\tilde{g}$ bring equivalent contributions to the grand potential than the $(2, 0, \ldots, 0)$ and $(0, 1, 0, \ldots, 0)$ channels in q_Ag an $\bar{q}_Ag$. Similarly, the $(2, 0, \ldots, 0, 2)$ and $(0, 1, \ldots, 1, 0)$ channels in $g\tilde{g}$ match with the $(1, 1, 0, \ldots, 0, 1)$ and $(0, 0, 1, 0, \ldots, 0, 1)$ one in q_Ag an $\bar{q}_Ag$.

The above discussion shows that QCD$_{AS} \cong$ QCD$_{adj}$. The orientifold equivalence is checked within our framework. This can be seen as a strong validation of the various assumptions made in the building of the model.

Now, we can compare the accuracy of the orientifold equivalence at finite N_c, namely $N_c = 3$. The pressure and trace anomaly of SU(3) $\mathcal{N} = 1$ SUSY YM is compared to the EoS of SU(3) one-flavour QCD in Fig. 6.6 and Fig. 6.7. Note that the free part of this latter is given by,

$$\Omega_0 = 2(N_c^2 - 1)\omega_B(m_g, 0) + 2N_c(N_c - 1)\omega_F(m_{q_A}, 0), \tag{6.2.10}$$

for SU(N_c) gauge groups, and that 70 T-matrix files are necessary to compute the bound-states and scattering contributions. These plots show how far one-flavour QCD is from the $\mathcal{N} = 1$ SUSY YM theory at the level of the EoS. As far as the pressure is concerned, both theories are very similar. The trace anomaly however reveals some differences around 1.2 T_c. Note that each case is normalized to its own SB pressure, that of QCD$_{AS}$ reading

$$p_{SB} = \frac{\pi^2 T^4}{45}(N_c - 1)\left(\frac{15}{8}N_c + 1\right) \tag{6.2.11}$$

for SU(N_c) gauge groups.

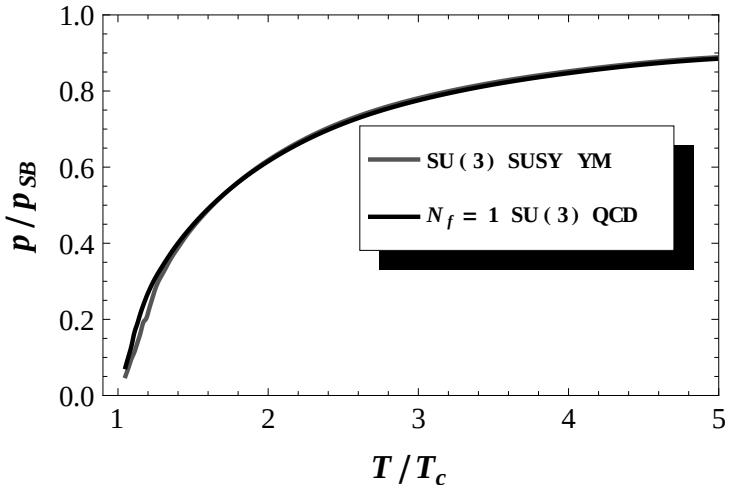

Figure 6.6: (Left) Normalized pressure p/p_{SB} versus temperature in units of T_c ($T_c = 0.245$ GeV), computed for SU(3) QCD with $N_f = 1$ and $\mathcal{N} = 1$ SU(3) SUSY YM.

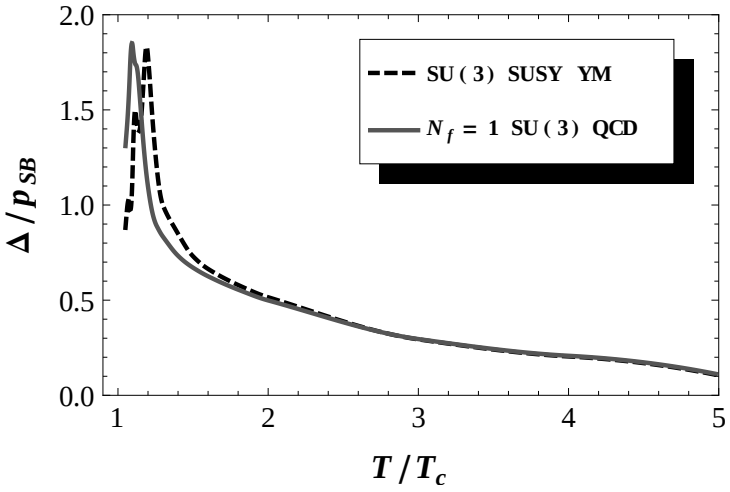

Figure 6.7: Normalized trace anomaly Δ/p_{SB} versus temperature in units of T_c ($T_c = 0.245$ GeV), computed for SU(3) QCD with $N_f = 1$ and $\mathcal{N} = 1$ SU(3) SUSY YM.

Chapter 7

Large-N_c PNJL Model with Explicit Z_{N_c} Symmetry

As already mentioned, the structure of the QCD phase diagram is intimately related to our understanding of QCD fundamental features, like for example confinement dynamics and chiral symmetry breaking, and to their interplay with in-medium effects like a non-zero temperature or quark density. Among the various effective frameworks used to study the QCD phase diagram (see *e.g.* the reviews [Fuku11, Step06]), we will mostly focus on two of them: The Polyakov-loop effective models for the pure-gauge part of QCD, and the Nambu-Jona-Lasinio (NJL) model for the quark part. The main idea of our work is to build a Polyakov-Nambu-Jona-Lasinio (PNJL) model in which the Polyakov-loop potential is explicitly Z_{N_c} symmetric in order to mimic a Yang-Mills theory with a gauge group SU(N_c). Then, thanks to this approach, we will be able to discuss the structure of the QCD phase diagram at large N_c.

This chapter is based on [Buis12] and will be organized as follows. In the first section, we will explain how we build the Z_{N_c}-symmetric potential. Then, we will develop the PNJL model related to it. Finally, the issues of deconfinement and chiral symmetry restoration in the 't Hooft's large-N_c limit when varying T and μ are addressed in the third section as well as the obtained phase diagram.

7.1 Polyakov-loop effective models for the pure-gauge sector

7.1.1 Explicit Z_{N_c}-symmetry

As already seen in Section 2.3.2, the Polyakov loop is a precious tool to study the phase structure of a given YM theory. Indeed, $\langle L(T,\vec{x})\rangle = 0\ (\neq 0)$ when the theory is in a (de)confined phase [Suss79, Svet82]. In the particular case of SU(N_c), deconfinement might thus be driven by the breaking of a global Z_{N_c}-symmetry. The order parameter of the deconfinement phase transition should then be the traced Polyakov loop

$$\phi = \frac{1}{N_c}\mathrm{Tr}_c L, \tag{7.1.1}$$

where the trace Tr_c is taken over the colour indices.

The thermodynamic properties of pure-gauge SU(3) QCD can be successfully studied by resorting to an

effective scalar field theory where the potential energy density is Z_3-symmetric, with *e.g.* the form [Pisa00]

$$U = T^4 \lambda \left[-\frac{b_2(T)}{2}|\phi|^2 + \frac{b_4}{4}|\phi|^4 + \frac{b_3}{6}(\phi^3 + \phi^{*3}) \right]. \tag{7.1.2}$$

The coefficients b_i can be fitted on lQCD data. Various applications of this formalism can be found for example in [Dumi01]. Note that, in the following, ϕ and L will be indifferently called Polyakov loop.

The simplest effective potential energy density depending on ϕ, defined in (7.1.1), and being explicitly Z_{N_c}-invariant has been proposed in [Sann05] and reads

$$V_g(T, N_c, \phi, \phi^*) = A(T, N_c)\,|\phi|^2 + B(T, N_c)\,|\phi|^4 + C(T, N_c)\,(\phi^{N_c} + \phi^{*N_c}). \tag{7.1.3}$$

It is formally valid for any value of ϕ, but one may restrict oneself to $|\phi| \in [0, 1]$ in a mean-field approximation [1]. The above expression contains the basic blocks that could be expected to build a non-trivial theory: A mass term ($|\phi|^2$), an interaction term ($|\phi|^4$), and the term in $\phi^{N_c} + \phi^{*N_c}$ accounting for the explicit Z_{N_c}-symmetry [2]. Terms scaling like $|\phi|^6, |\phi|^8, \ldots, |\phi|^{N_c-2}$, *etc.* could be added, but then the number of arbitrary functions would become too large to be efficiently constrained. Moreover, such higher-order terms would mostly be interaction terms that are already present in their simplest form in the $|\phi|^4$ term. The expression (7.1.3) is thus particularly convenient since it contains the minimal number of terms needed to perform the present study. The real coefficients A, B, and C appearing in (7.1.3) are functions of T and N_c, and their explicit form will be specified just hereafter. Note that ϕ, which depends on T, N_c, and $\vec{x}$ *a priori*, is here assumed to be independent of $\vec{x}$.

Beyond the polynomial form (7.1.3), logarithmic shapes can actually be shown to emerge from a Haar integration on the gauge group in a strong coupling expansion. One can find such a form in [Fuku04], or for example in [Roes07], where a potential schematically given by

$$\frac{\mathcal{U}}{T^4} = A(T)|\phi|^2 + B(T)\ln\left[1 - 6|\phi|^2 + 4(\phi^3 + \phi^{*3}) - 3|\phi|^4\right] \tag{7.1.4}$$

is used for $N_c = 3$ computations. Instead of computing a similar potential at arbitrary N_c, we keep the ansatz (7.1.3) in the following; It is indeed particularly convenient for the calculations that are to be performed and still contains the Z_{N_c}-symmetry that we want to take into account.

Various parametrizations of Z_3-symmetric potentials, fitted on pure-gauge lattice data, have been proposed so far [Fuku04, Polo82, Ratt06]. Here, we are rather interested in obtaining an effective potential valid at large N_c. Therefore, the following expected qualitative constraints have to be imposed in order to obtain the shape of the functions A, B, and C:

- The pressure $p_g = -\min_\phi(V_g)$ is proportional to $N_c^2\,T^4$ at large N_c and high T in order to recover asymptotically the SB limit of a free gluon gas.

- The norm $|\phi_0|$, of the optimal value of the Polyakov loop, $\phi_0 = |\phi_0|\,\mathrm{e}^{i\delta_0}$, must be N_c-independent at the dominant order. This condition results from the implementation of the previous one concerning the pressure. This N_c-independence at the dominant order is in agreement with large-N_c scaling rules

1. In the mean-field approximation, the fields are replaced by their expectation values. Nevertheless, we keep the notation ϕ and ϕ^* for simplicity.

2. $Z(N_c)$ is the group of unity roots: $z = e^{2\pi i\,n/N_c}\mathbb{1}$ with $n = 0, 1, \ldots, N_c - 1$. As pointed out in [Sann05], the term $\phi^{N_c} - \phi^{*N_c}$ possesses the same symmetry but violates charge conjugation, which is also a symmetry of the effective theory under consideration.

for ϕ_0. The first corrections, scaling as $1/N_c^2$, are neglected in the present approach. More results on large-N_c features of Wilson and Polyakov loops can be found for example in [Make02]. $|\phi_0| = 0$ in the confined phase, and > 0 in the deconfined phase. Also, $|\phi_0|$ tends toward unity at very large T.

- There exists a critical temperature T_c signalling a first-order phase transition, *i.e.* the potential must have two different minima whose depth changes with the temperature in order to modify discontinuously the localisation of the absolute minimum. At the critical temperature, $|\phi_0| = 0$ and $1/2$ are two degenerate minima of V_g. This last value is chosen so that it will ensure a good compatibility between our model and existing lattice data but it has only to be non-zero in order to lead to a deconfined phase. T_c has to be seen as a typical value for the deconfinement temperature in SU(N_c) YM theory since the deconfinement temperature appears to be N_c-independent up to corrections in $1/N_c^2$ [Brau10, Luci05].

Obviously, the above constraint does not apply to $N_c = 2$, where the transition is of second-order [Yagi05]. This is not problematic since we eventually look for a model valid at large-N_c. Moreover, the value $|\phi_0| = 1/2$ may not be the exact value of the Polyakov loop in T_c: Recent lattice results find it to be around 0.4 [Gupt08], while a more recent renormalization-group-based approach leads to values closer to 0.6 for the Polyakov loop at the deconfinement temperature [Brau10]. The value 1/2 then appears to be relevant because it falls in the typical range of the existing results and because it simplifies the calculations performed in the following.

The above constraints are actually satisfied by the Lagrangian

$$V_g = N_c^2 T^4\, a(T) \left[|\phi|^2 - 4|\phi|^4 + \frac{l(T)^{2-N_c}}{N_c} [8l(T)^2 - 1](\phi^{N_c} + \phi^{*N_c}) \right], \tag{7.1.5}$$

where

$$a(T) > 0, \quad l(T) > \frac{1}{\sqrt{8}}, \quad l(T_c) = \frac{1}{2}, \quad \partial_T l(T) > 0, \quad l(\infty) = 1. \tag{7.1.6}$$

Explicit forms of $a(T)$ and $l(T)$ will be given in the next subsection. All these conditions are required in order to have the existence of two degenerate minima and the correct behaviour of the Polyakov loop in the mean-field approximation. It can be shown that the potential (7.1.5) has the following absolute minimum: $\phi_0(T < T_c) = 0$ and $\phi_0(T \geq T_c) = |\phi_0(T)|\, \mathrm{e}^{2i\pi k/N_c}$, where $k = 0, \ldots, N_c - 1$ and where $|\phi_0(T)|$ is a solution of

$$1 - 8|\phi_0(T)|^2 + l(T)^{2-N_c} \left[8l(T)^2 - 1 \right] |\phi_0(T)|^{N_c - 2} = 0. \tag{7.1.7}$$

It is straightforwardly checked that

$$|\phi_0(T)| = l(T) \tag{7.1.8}$$

actually solves (7.1.7).

A more compact expression for the optimal value of the Polyakov loop is thus

$$\phi_0 = l(T)\, \mathrm{e}^{2i\pi k/N_c}\, \Theta(T - T_c), \tag{7.1.9}$$

where Θ is the Heaviside function. As seen from (7.1.7), $|\phi_0|$ only depends on T as required.

Restricting ourselves to the values $\phi = |\phi|\, \mathrm{e}^{2i\pi k/N_c}$, we get at the limit $N_c \to \infty$ a quite simple shape for the effective potential (7.1.5), namely

$$\begin{aligned} \frac{V_g}{N_c^2 T^4} \equiv \frac{\omega_g}{T^4} \quad &= a(T)\, |\phi|^2 (1 - 4|\phi|^2) && |\phi| \leq l(T), \\ &\to +\infty && |\phi| > l(T). \end{aligned} \tag{7.1.10}$$

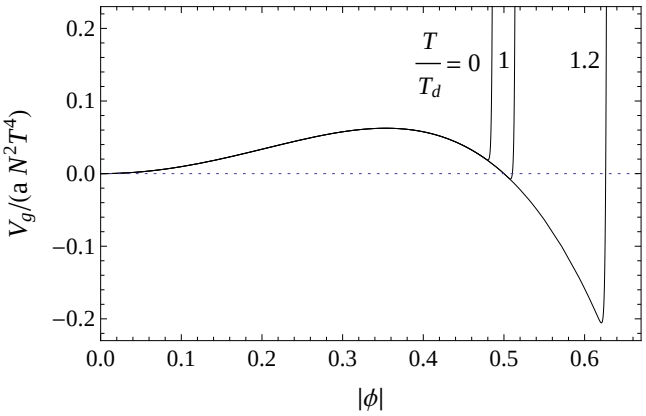

Figure 7.1: Schematic evolution of the effective potential (7.1.10) versus the temperature (solid lines). $T_d = T_c$ on the graph. The parametrization (7.1.12) is used to compute (7.1.10).

Hence, a U(1) invariance is recovered at infinite N_c as a limiting case of the Z_{N_c}-symmetry. The schematic evolution of the large-N_c limit of V_g with the temperature is plotted in Fig. 7.1; The behaviour (7.1.10) is readily observed, as well as the change of global minimum in $T = T_c$. Finally, the large-N_c limit of the pressure reads

$$p_g(T, N_c) = N_c^2 T^4\, a(T)\, l(T)^2 \left[4l(T)^2 - 1\right]. \tag{7.1.11}$$

Provided that $l(\infty) = 1$ according to the large-T behaviour of the Polyakov loop, p_g would tend toward the SB limit for a free gluon gas if $a(\infty) = \pi^2/135$

7.1.2 Numerical data

The function $l(T)$ is constrained by the relations (7.1.6) in order to have the required behaviour for the structure of the potential and its evolution with the temperature. Moreover, $l(T)$ is equal to the norm of the Polyakov loop as soon as $T > T_c$. Those physical constraints are not sufficient to write down an explicit expression for $l(T)$. A possible way of proceeding, that we choose here, is to fit $l(T)$ on available lattice computations of the Polyakov loop in pure YM theory. To our knowledge, large-N_c values have not been obtained so far, but accurate SU(3) ones have been computed in [Gupt08]. Since the Polyakov loop should not depend on N_c at the dominant order, it is relevant to fit $l(T)$ on SU(3) data; The *ad hoc* form

$$l(T) = 0.74 - 0.26\,\tanh\left[2.10\left(\frac{T_c}{T}\right)^3 - 0.60\frac{T}{T_c}\right] \tag{7.1.12}$$

leads to a satisfactory parametrization of the results of [Gupt08] as it can be seen in Fig. 7.2. It is also worth noting that Fig. 7.1 has been obtained using the form (7.1.12) for $l(T)$.

It is important to remark at this stage that the calculations that we perform are done in the mean-field approximation. In this scheme, the Polyakov loop is always lower than 1: Values larger than 1 are due to quantum fluctuations and are *de facto* beyond the mean-field treatment. That is why we have restricted our fit to lattice data lower than unity ($T < 2.4\ T_c$). We miss the overshoot due to quantum fluctuations, but we stay coherent with the mean-field approximation, and reach moreover $l(\infty) = 1$. As a consequence, our

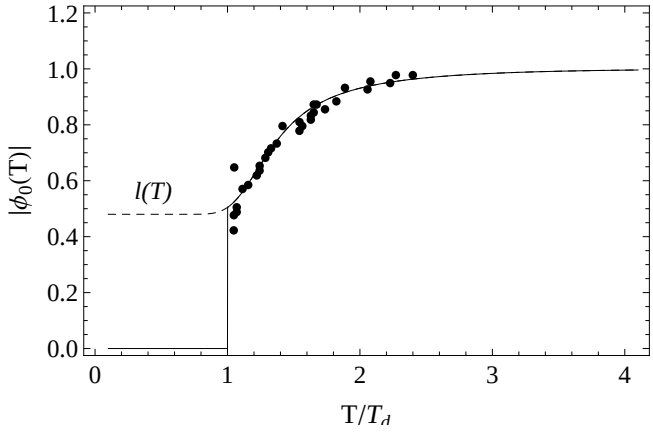

Figure 7.2: Norm of the Polyakov loop minimizing the potential (7.1.5) versus the temperature in units of T_d (solid line). The function $l(T)$ (dashed line) given by (7.1.12) and the norm of the Polyakov loop computed in pure-gauge SU(3) lQCD (points) have been added for comparison. Lattice data are given for temperatures lower than 2.4 T_d; Data are taken from [Gupt08]. $T_d = T_c$ in the graph.

results should be mostly trusted below $T < 2.4\ T_c$ but this is not a flaw since, in the following, we will be concerned with the phase structure of the theory and no phase transition will appear at energy scales above this upper limit.

The positive-definite function $a(T)$ is only present as an overall factor in V_g, so it does not come into play in the qualitative features of the effective potential. However, it is relevant in view of reproducing the absolute value of the pressure in pure-gauge QCD, for which lattice data are known at $N_c = 3$, 4, 5, 6, 8 and ∞, through an extrapolation of these data [Pane09]. The empirical choice

$$a(T) = \frac{1}{l(T)^4}\left(\frac{\pi^2}{135} - \frac{0.029}{\ln(T/T_c + 1.5)}\right) \tag{7.1.13}$$

leads to a good agreement between the lattice data of [Pane09] and formula (7.1.11), as shown in Fig. 7.3. Notice that the value $a(\infty)$ is such that the SB limit is reached at large temperatures.

It is worth summarizing what has been done at this stage. Starting from Lagrangian (7.1.3), we have shown that the three arbitrary functions of T and N_c that it contains can be strongly constrained by demanding that the averaged Polyakov loop and the pure-gauge pressure have a relevant behaviour in T_c, at large T, and in the large-N_c limit. Explicit forms for the two remaining unconstrained functions of T can then be found by asking the present model to be in agreement with current pure-gauge lattice data. One is finally left with a fully determined Lagrangian with explicit Z_{N_c}-symmetry at finite N_c and U(1) symmetry in the large-N_c limit. This Lagrangian, just as the previous ones like (7.1.2), is obviously not predictive concerning the thermodynamics of the pure-gauge sector since it is built using its properties. However, its knowledge is a necessary step in view of making predictions concerning the quark sector, whose inclusion is discussed in the next section.

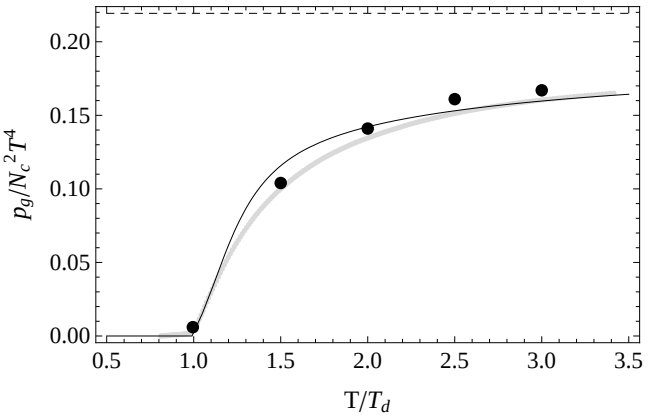

Figure 7.3: Large-N_c pure gauge pressure computed from (7.1.11) thanks to (7.1.12) and (7.1.13) and normalized to $N_c^2T^4$ (solid line). The corresponding lattice data, taken from [Pane09], are plotted for comparison in the case $N_c = 3$ (gray points) and $N_c \to \infty$ (black points). $T_d = T_c$ in the graph.

7.2 PNJL model

In order to include quarks, we consider the NJL model which is based on the Lagrangian [Namb61]

$$\mathcal{L}_{NJL} = \bar{q}(i\gamma^\mu\partial_\mu - m_q)q + \frac{G}{2}\left[(\bar{q}q)^2 + (\bar{q}i\gamma_5\vec{\tau}q)^2\right], \tag{7.2.1}$$

where q is the quark field, m_q the mass matrix, G a coupling constant, and $\vec{\tau}$ the Pauli matrices when a SU(2) flavour symmetry is considered. The interaction terms are such that the Lagrangian is chirally symmetric. The NJL model is designed to model chiral symmetry breaking and study many related phenomenological problems; The interested reader may consult the review [Klev92] for more information.

In the original NJL model, fermions are not coupled to the gauge field: As shown in [Fuku04], the coupling of this model to the Polyakov loop can be achieved by minimally coupling the quark field to a gauge field of the form $A_\mu = A_0\,\delta_{\mu 0}$, that formally appears as an imaginary quark chemical potential. The so-called PNJL model resulting in this coupling has motivated a lot of studies devoted to the QCD phase diagram (*e.g.* [Ratt06]), including cases with a non-zero magnetic field (*e.g.* [Fuku10]) or non-local extensions (*e.g.* [Cont08]).

Here, we follow [Fuku04] and make appear the Polyakov loop in the quark grand canonical potential. In the mean-field approximation, one is led indeed to the quark potential

$$\frac{V_q(\mu,T,\sigma,L,L^\dagger)}{N_c\,N_f} = \frac{\sigma^2}{2g} - 2\int\frac{d^3p}{(2\pi)^3}\times \tag{7.2.2}$$
$$\left\{E_p + \frac{T}{N_c}\mathrm{Tr}_c\ln\left[1 + L\,\mathrm{e}^{-(E_p-\mu)/T}\right] + \frac{T}{N_c}\mathrm{Tr}_c\ln\left[1 + L^\dagger\,\mathrm{e}^{-(E_p+\mu)/T}\right]\right\}.$$

In the above equality,

$$E_p = \sqrt{\vec{p}^2 + (m_q - \sigma)^2} \tag{7.2.3}$$

is the quark dispersion relation, where m_q is the quark bare mass and σ is related to the chiral condensate as follows

$$\sigma = G \langle \bar{q}\, q \rangle \,. \tag{7.2.4}$$

The coupling G has to scale as $(N_c\, N_f)^{-1}$ in order for the potential (7.2.2) to scale as $N_c\, N_f$, so it is convenient to define the coupling g as

$$g = G\, N_c\, N_f. \tag{7.2.5}$$

Although N_f is *a priori* arbitrary, our results are mostly valid at $N_f = 2$. For higher values of N_f, the axial anomaly (not present in this formalism) should be taken into account in order to get a reliable model. In what follows, $N_f = 2$ will be implicitly understood, although we keep the notation N_f so that the quark contributions appear more clearly.

Since the pure-gauge part of the potential only involves the traced Polyakov loop ϕ, it is interesting to express V_q in terms of ϕ rather than L. Terms of the form $\mathrm{Tr}_c \ln\left[1 + z\, L\right]$ can be expressed as functions of $\mathrm{Tr}_c L \propto \phi$, $\mathrm{Tr}_c L^2$, $\mathrm{Tr}_c L^3$, ... through a Taylor expansion. A possible way of proceeding is to expand the quark potential at the first order in L. This eventually leads to formulas in which only ϕ appears in V_q [McLe09]. This scheme has the advantage of being independent of the parametrization of L. Here we adopt an inequivalent procedure. As a first step, we notice that there exists in general a gauge in which the Polyakov loop L is a diagonal element of SU(N_c):

$$L = \mathrm{diag}(\mathrm{e}^{i\theta_1}, \mathrm{e}^{i\theta_2}, \ldots, \mathrm{e}^{i\theta_{N_c-1}}, \mathrm{e}^{-i\sum_{j=1}^{N_c-1}\theta_j}). \tag{7.2.6}$$

The $N_c - 1$ parameters θ_j are real so that $L^\dagger L = \mathbf{1}$ and $\mathrm{det} L = 1$ as demanded for a SU(N_c) element. In the special case of $N_c = 3$, there is a one-to-one correspondence between the parameters θ_1, θ_2 and the Polyakov loop degrees of freedom ϕ, ϕ^* (see [Fuku04]). This is not the case at large N_c however, where the number of independent parameters in the Polyakov loop goes to infinity. As a consequence, an exact computation of the colour traces appearing in (7.2.2) is not possible unless simplifying assumptions are made. As a second step to reach this goal, we propose the following ansatz:

$$\begin{aligned} L &= \mathrm{diag}(\underbrace{\mathrm{e}^{i\theta}, \ldots, \mathrm{e}^{i\theta}}_{(N_c-1)/2}, 1, \underbrace{\mathrm{e}^{-i\theta}, \ldots, \mathrm{e}^{-i\theta}}_{(N_c-1)/2}) \qquad \mathrm{odd} - N_c, \\ &= \mathrm{diag}(\underbrace{\mathrm{e}^{i\theta}, \ldots, \mathrm{e}^{i\theta}}_{N_c/2}, \underbrace{\mathrm{e}^{-i\theta}, \ldots, \mathrm{e}^{-i\theta}}_{N_c/2}) \qquad \mathrm{even} - N_c. \end{aligned} \tag{7.2.7}$$

It reduces to the mean-field parametrization of [Fuku04] at $N_c = 3$, but the price to pay is that the number of degrees of freedom in L is drastically reduced to a single real parameter θ. It is then readily computed that

$$\begin{aligned} \phi &= \frac{1}{N_c}\left[1 + (N_c - 1)\cos\theta\right] \qquad \mathrm{odd} - N_c, \\ &= \cos\theta \qquad\qquad\qquad\qquad\qquad\quad \mathrm{even} - N_c, \end{aligned} \tag{7.2.8}$$

by using of the ansatz (7.2.7) in (7.1.1). We thus have an ansatz that "looks like" the SU(3) case and that

reduces to $\phi = \cos\theta$ at large-N_c. Moreover, one can compute that

$$\begin{aligned}
\mathrm{Tr}_c \ln\left[1 + L\,\mathrm{e}^{-(E_p-\mu)/T}\right] &= \ln\det{}_c\left[1 + L\,\mathrm{e}^{-(E_p-\mu)/T}\right] \\
&= \frac{N_c-1}{2}\ln\left[1 + 2\frac{N_c\phi - 1}{N_c-1}\mathrm{e}^{-(E_p-\mu)/T} + \mathrm{e}^{-2(E_p-\mu)/T}\right] \\
&\quad + \ln\left[1 + \mathrm{e}^{-(E_p-\mu)/T}\right] \qquad \mathrm{odd} - N_c, \\
&= \frac{N_c}{2}\ln\left[1 + 2\phi\mathrm{e}^{-(E_p-\mu)/T} + \mathrm{e}^{-2(E_p-\mu)/T}\right] \\
&\qquad\qquad \mathrm{even} - N_c, \qquad (7.2.9)
\end{aligned}$$

and, taking into account a cutoff for the momentum integration of the vacuum term, one finally arrives at the quark potential, whose large-N_c limit is given by

$$\begin{aligned}
\omega_q(\mu, T, \sigma, \phi) &\equiv \frac{V_q(\mu, T, \sigma, \phi)}{N_c\, N_f} \\
&= \frac{\sigma^2}{2g} - \frac{1}{\pi^2}\int_0^\Lambda dp\, p^2 E_p \\
&- \frac{T}{2\pi^2}\int_0^\infty dp\, p^2 \left\{\ln\left[1 + 2\phi\mathrm{e}^{-(E_p-\mu)/T} + \mathrm{e}^{-2(E_p-\mu)/T}\right]\right. \\
&+ \left.(\mu \to -\mu)\right\}. \qquad (7.2.10)
\end{aligned}$$

This last potential formally reduces to the genuine NJL potential once $\phi = 1$, as observed in previous studies [Fuku04, McLe09]. The total potential of the large-N_c PNJL model under study is finally given by

$$\mathcal{V}(\mu, T, \sigma, \phi) = N_c^2 \omega_g(T, \phi) + N_c\, N_f\, \omega_q(\mu, T, \sigma, \phi). \qquad (7.2.11)$$

In the confined phase, where $\phi = 0$, one observes a term in $\ln\left[1 + \mathrm{e}^{-2(E_p-\mu)/T}\right]$ in the potential (7.2.10), so it could be tempting to associate such a term with diquark degrees of freedom in the confined phase. However, in the limit $T \to 0$, one exactly recovers the zero temperature NJL potential, expressed in terms of the quark degrees of freedom. So the confined degrees of freedom are still quarks in the present approach.

7.3 Phase diagram at large N_c

To study the phase diagram at large N_c, we adopt the 't Hooft limit. In this latter, the number of quark flavours N_f stays finite and $\mathcal{V}$ is dominated by the gluonic contribution. Consequently, when N_c becomes infinite, the optimal value ϕ_0 can be found by minimizing ω_g only. According to (7.1.9), the large-N_c solution reads

$$\phi_0(T) = l(T)\,\Theta(T - T_c). \qquad (7.3.1)$$

The physical value of σ, denoted σ_0 and depending on T and μ, is then such that it minimizes the quantity $\omega_q(T, \mu, \sigma, \phi_0(T))$. ω_g does not depend on σ. Since $\sigma \propto \langle\bar{q}q\rangle$, chiral symmetry is present when $\sigma_0 = 0$ and broken when $\sigma_0 \neq 0$. As a consequence of (7.3.1), the deconfined phase appears as soon as $T > T_c$, independently of the value of μ: As pointed out in [McLe07], quarks have no influence on the deconfinement phase transition at large-N_c because of the suppression of internal quark loops in this limit.

As a consequence of the large-N_c limit, the confined/deconfined phases are straightforwardly identified in our model. The situation is less simple as far as chiral symmetry is concerned; Numerical computations are needed. As a first step, the parameters of the model have to be fixed. The values

$$m_q = 5.5 \text{ MeV},\ g = 60.48 \text{ GeV}^{-2},\ \Lambda = 651 \text{ MeV},\ T_c = 270 \text{ MeV}, \tag{7.3.2}$$

used in the PNJL study [Ratt06], will be taken in the following also. The first three parameters have been fitted so that the zero-temperature pion mass and decay constant are reproduced within the standard NJL model with $N_c = 3$ and $N_f = 2$ [Hats94, Klev92]. T_c is a typical value for the deconfinement temperature in SU(N_c) YM theory.

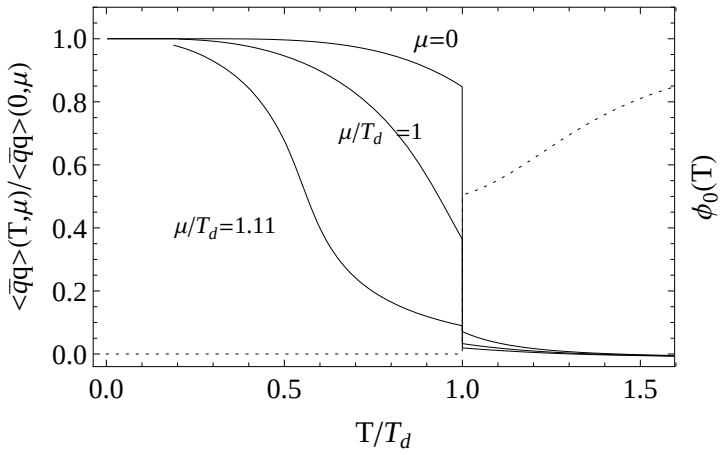

Figure 7.4: Chiral condensate at large-N_c ($N_c \to \infty$), normalized to its zero temperature value, versus T in units of T_d, and plotted for $\mu/T_d = 0$, 1, and 1.11 (solid lines). The optimal value of the Polyakov loop is also plotted (dotted line). $T_d = T_c$ in this graph.

Using the parameters (7.3.2), the optimal value σ_0 can now be computed for any couple (μ, T), and can be linked to the quark condensate thanks to (7.2.4)

$$\langle \bar{q}q \rangle (\mu, T) = \frac{N_c\, N_f}{g} \sigma_0(\mu, T). \tag{7.3.3}$$

In the limit where T and μ both tend toward zero, we get

$$\lim_{\mu, T \to 0} \langle \bar{q}q \rangle (\mu, T) = -N_c\, N_f\, 5.29\, 10^6 \text{ MeV}^3, \tag{7.3.4}$$

corresponding to a quite common value of $-(317 \text{ MeV})^3$ for $N_c = 3$ and $N_f = 2$.

The large-N_c chiral condensate versus the temperature is plotted in Fig. 7.4 for some values of the quark chemical potential. The most salient feature of this plot is the simultaneity of the first-order deconfinement phase transition and of the restoration of chiral symmetry through a first-order phase transition occurring at $T_\chi = T_c$. However, when $\mu/T_c \gtrsim 0.8$ ($\mu \gtrsim 200$ MeV), the quick decrease of the chiral condensate

suggests a progressive restoration of chiral symmetry through a crossover at temperatures smaller than T_c (see also in advance Fig. 7.5). As shown in [Fuku04], the crossover temperature can be computed thanks to the determination of the peak position in the dimensionless quark susceptibility reading, at large-N_c,

$$\chi_{qq}(T,\mu) = \frac{\Lambda\, T}{\partial_\sigma^2 \omega_q|_{\sigma=\sigma_0}}. \tag{7.3.5}$$

We have chosen to follow the definition of [Fuku04] for the quark susceptibility, although a more standard way of defining the susceptibility is rather $\partial^2_{m_q}\omega_q(T,\mu)$, see *e.g.* [Cont10]. In both cases, a peak in the quark susceptibility signals a phase transition.

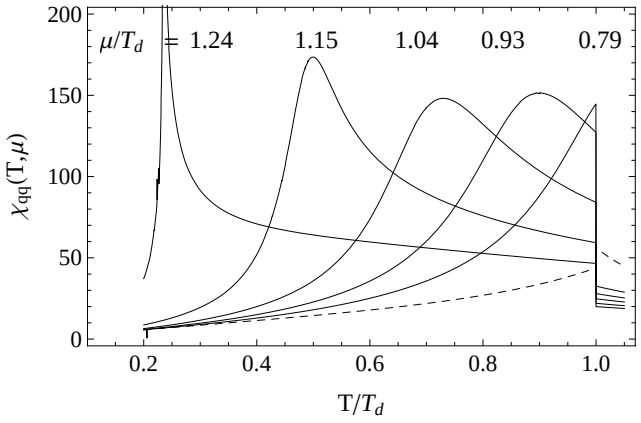

Figure 7.5: Dimensionless quark susceptibility (7.3.5) versus the temperature in units of T_d (solid lines) with, from left to right, μ/T_d =1.24, 1.15, 1.04, 0.93, 0.79. $\chi_{qq}(T,0)$ is also plotted for completeness (dashed line). Computations were done for $N_c \to \infty$. $T_d = T_c$ in the graph.

A plot of $\chi_{qq}(T,\mu)$ for some values of μ/T_c is given in Fig. 7.5. Several observations can be made by looking at this figure together with Fig. 7.4. First, the peak of the quark susceptibility is located in T_c when $\mu/T_c \leq 0.79$. This corresponds to a first-order-type chiral symmetry restoration in the deconfined phase. The point $(0.79, 1) \times T_c$ actually corresponds to a triple point in the (μ, T)-plane. At large μ, the peak of χ_{qq} is located below T_c. A larger μ corresponds to a lower peak position, leading to the existence of a confined phase in which chiral symmetry is progressively restored through a crossover. A careful look at σ_0 actually shows that the chiral phase transition below T_c becomes of first order when $\mu/T_c \geq 1.24$: There exists thus a critical-end-point that we find to be $(1.23, 0.26) \times T_c$ in the (μ, T)-plane. Apart from the susceptibility, the position of the chiral phase transition could have been alternatively determined by computing the zero of $\partial_T^2 \sigma_0(T,\mu)$. We have checked that the chiral temperatures computed using that method agree with those computed from the peak in the susceptibility up to 5%. For an exploratory study such as the present one, this agreement is satisfactory.

Gathering all these observations, the phase diagram of our model in the (μ, T)-plane can be established. It is shown in Fig. 7.6. The three phases we find correspond to those found in [McLe09], see Fig. 7.7, but the structure of the chiral phase transition is a bit more involved under T_c: The chemical potential at which chiral symmetry is restored now depends on T, and there exists a critical-end-point at large enough μ. Although the deconfining phase transition corresponds to what is expected in the large-N_c limit of QCD from

generic arguments [McLe07], the critical line $T_\chi(\mu)$ that we find under T_c quite resembles to what can be observed within previously known $N_c = 3$ PNJL studies [Fuku04, Ratt06]. The similarity between our way of including the Polyakov loop in the NJL model and the way of [Fuku04] – our ansatz is a straightforward generalization of the one used in this last work – might actually be at the origin of the similarities between the phase diagrams that we find. The same reason, combined to the fact that we chose for our parameters values fitted on the SU(3) case, might explain why the values we find for *e.g.* the chiral condensate are similar to those of [Fuku04].

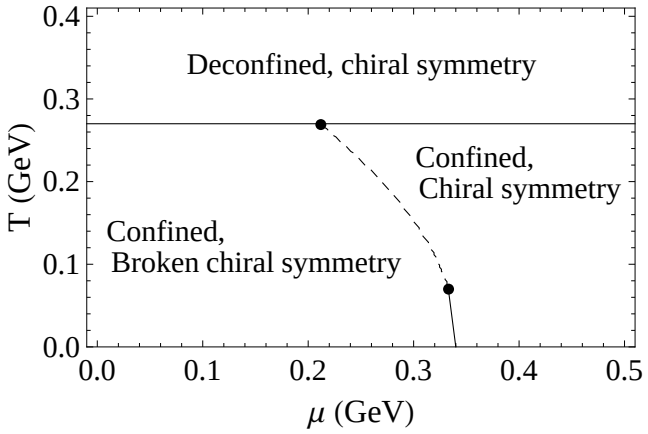

Figure 7.6: Phase diagram of the large-N_c PNJL model (7.2.11) with explicit Z_{N_c} symmetry, obtained for $N_c \to \infty$. The solid lines denote first-order phase transitions while the dashed line denotes a crossover. The triple point (0.212, 0.270) GeV and the critical end-point (0.335, 0.063) GeV have been also plotted. The end of the lower curve is reached at (0.343, 0) GeV.

We notice that, at large but finite values of N_c, the full potential (7.2.11) has to be minimized and quark contributions (presumably in $1/N_c$) will cause the Polyakov loop to be different from $l(T)$. Hence, the chiral condensate will also be modified, and the whole phase diagram will be affected. We nevertheless choose here to focus on the large-N_c limit of the model, since it has been designed to be relevant in this limit mostly.

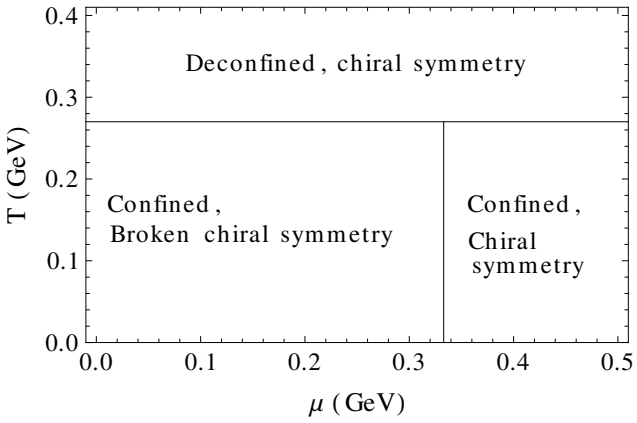

Figure 7.7: Phase diagram obtained by taking the large-N_c limit ($N_c \to \infty$) of the PNJL model used in [McLe09]. The solid lines signal first-order phase transitions

Conclusions and Perspectives

Within this thesis, we mainly focus on the study of the QCD spectrum at finite temperature and on the establishment of the EoS for different types of QCD matter. Four articles discussing this topic and related areas were published [Buis10a, Buis11b, Buis12, Lacr13]. Other papers are being submitted [Lacr14a, Lacr14b] and a last one, based on Section 4.4.3, Section 4.5.4 and Section 5.3, is in preparation. Moreover, two articles about the LMM in momentum space were published [Lacr11, Lacr12]. In these few last pages, we will thus draw some conclusions about the contributions brought by these several works and we will sketch some perspectives that could be considered.

Let us start by our conclusions. Firstly, in the confined phase, we have highlighted that the EoS for hadronic matter, provided by lQCD, can be correctly reproduced within a HRG model. In the particular case of the Yang-Mills medium, it has been shown that the abundance of the high-lying glueball states can be approximated by a Hagedorn spectrum; This latter leading to the existence of a limiting temperature for the hadronic matter. Our original work was to extend this picture to any gauge group. The main observation that we can extract from this work is that the EoS for the different considered gauge groups are gathered in a same window delimited by A_1 and E_6, surrounding the SU(3) lQCD data. Moreover, the orbifold equivalence, *i.e.* the large-N_c equivalence between SU(N_c) and SO($2N_c$) is checked within our model.

Secondly, the study of the Yang-Mills matter above T_c has been addressed. Its main ascertainments are the following. Glueballs survive inside the medium above T_c according to our T-matrix approach. Their melting is around 1.3-1.5 T_c for the colour-singlet channels while the coloured ones dissolve just around T_c. This observation is the same for all the gauge groups that we have studied. From a thermodynamic point of view, we have used the DMB formulation of statistical mechanics to compute the EoS. Our approach has thus the peculiarity to include explicitly the interactions between particles inside the plasma. Our study is restricted to the inclusion of the two-body interactions; These latter being computed thanks to a T-matrix formalism. Correct agreements between our EoS and the ones given in lQCD are reached. Nevertheless, the computation of the trace anomaly requires some refinements, mainly because of the way whose the bound states are included within the DMB formalism. An universality between the normalized EoS, performed with SU(N_c) and G_2 gauge groups, seems to emerge. This feature also appears in lQCD for SU(N_c) gauge groups. It is worth noticing that this universality can be analytically proven at the Born approximation in our approach.

Two extensions to this Yang-Mills plasma have been then analysed. The first one is naturally the full QGP with 2 (+1) flavours of quarks. In these cases, much more interaction channels were taken into account and so, much more bound states survive above T_c. However, unlike the glueballs, other two-body states melt quickly around T_c. The EoS were then computed and compared to lQCD ones. The main qualitative features are reproduced even if the pressure is slightly overestimated and the same issues concerning the trace anomaly peak appear. These EoS for the pressure were also compared to the Yang-Mills plasma one. A striking conclusion is that, once these pressures are normalized and expressed in terms of T/T_c, with

their own T_c, a kind of universality between the curves seem to emerge, leading to think that the same main mechanisms are at work to characterize the thermodynamic of the deconfined medium. Again, for the trace anomaly, the observation is less clear because of the peak structure.

An exploratory work at finite baryonic potential were eventually carried out since it is a challenging predictive area. Indeed, as already discussed, lQCD results in this phase diagram region are limited because of several deep problems in the baryonic-potential implementation on lattice. Unfortunately, our approach is also limited since the DMB formalism is based on a virial expansion. Therefore, our restriction to two-body interactions becomes more questionable. Moreover, we have no consistent two-body interactions including the effects of baryonic potential. For all these reasons, only expansions at small baryonic potentials were considered. Nevertheless, it is worth noticing that the obtained EoS agree well with the ones computed in lQCD, up to the remarks already done at zero baryonic potential.

The second extension addressed in this thesis were the study of the SUSY matter at finite temperature. Predictive results about the SUSY spectrum at finite temperature were presented. In this case, all the two-body states significantly survive above T_c; The most attractive channel for each kind of interactions not melting before about 1.3-1.5 T_c. The EoS for different gauge groups were also produced. Again, once normalized, an universality in function of the gauge groups seems to emerge. Let us also add that the orientifold planar equivalence, *i.e.* an equivalence between QCD$_{AS}$ and QCD$_{adj}$ at large-N_c, has been analytically checked within our model provided that the quark and the gluino bare masses are assumed to be the same. Moreover, an extrapolation to $N_c = 3$ of this equivalence gives good results. Therefore, since QCD$_{AS}$ is isomorphic to QCD at $N_c = 3$, we have that QCD with one quark flavour and SUSY with one generator thermodynamics share the same features. This particular relation can thus be a crucial tool to obtain information about one theory from the other and *vice versa*.

Finally, this thesis work ends with the building of a PNJL model in which the Polyakov-loop potential is explicitly Z_{N_c}-symmetric in order to mimic a Yang-Mills theory with a gauge group SU(N_c). Different phases of this resulting PNJL model were discussed in the 't Hooft's large-N_c limit. Three phases are found, in agreement with previous studies resorting to effective approaches of QCD. When the temperature is larger than T_c, the system is in a deconfined, chirally symmetric, phase for any quark chemical potential μ. When $T < T_c$ however, the system is in a confined phase in which chiral symmetry is either broken or not. The critical line $T_\chi(\mu)$, signalling the restoration of chiral symmetry, has the same qualitative features than what can be obtained within a standard $N_c = 3$ PNJL model.

Now that we have exposed and summed up the main teaching extracting from our researches, let us discuss some perspectives. The first one is definitely a better inclusion of the bound-state contributions to the EoS. Indeed, with the DMB formalism, this sector is completely decoupled from the scattering one; the bound states being added as free additional species. The main issue is that once these bound states melt inside the medium, they totally disappear from the EoS. For the pressure computations, this behaviour is not dramatic: The bound-state contributions are small. However, for the trace anomaly, it is not the same since it is obtained from a derivative of the pressure respecting to the temperature: Small fluctuations can thus become important and the step-function behaviour of the bound-state inclusion can generate unphysical oscillations. A possible way to cure this problem could be to use the peculiarity of the T-matrix to deal with bound and scattering states in a whole framework. Therefore, a reformulation of the DMB formalism in order to directly integrate the whole energy range, without dividing it by a threshold energy, is needed.

A second interesting direction that could be explored is the modification of the thermodynamic relations under the constraint that the Hamiltonian explicitly depends on some intensive variables like the temperature or the chemical potential. Indeed, within this thesis, we make the implicit assumption that these relations are not modified despite the fact that our chosen interactions depend on the temperature and that derivatives in function of the temperature are used. This assumption is currently employed in quasiparticle approaches

since the particle generally acquires a mass term from the in-medium effects; this mass being a function of the temperature and the chemical potential, as in HTL formulas. At first sight, it seems that such study will thus require a reformulation of the thermodynamic relations from first principles in statistical physics, especially at the level of the introduction of the Lagrange multipliers.

A third way to consider, maybe more straightforward, could be the computations of the gluonic and mesonic correlators. Indeed, we practically have at our disposal all the needed background to do it since such correlators can be extracted from our T-matrix computations. Schematically, we have $G = G_0 + G_0 T G_0$ with G_0, the lowest-order correlation function [Cabr07]. This information is particularly interesting in order to have a comparison with the spectral function given in lQCD. It could be a direct manner to check the validity of our potential choice used to take into account the two-body interactions between particles inside the medium.

Another natural extension to our researches is the explicit inclusion of the three-body interactions within our approach in order to estimate their impacts. Even if it is natural and expected to be small, it is not straightforward to implement. Indeed, we have first to extend the Jacob and Wick's helicity formalism to three-body systems, which is *a priori* not direct. Then, we have to adapt our T-matrix computations by using for instance Faddeev's equations. Finally, we have to carefully take into account all the possible channels inside the medium and compute the third term of the DMB formalism, after having expressed it in momentum space.

Among the different possible directions which may result from our current researches, the computation of the quark susceptibilities is also one of them. This latter requires a careful data acquisition and an adaptation of the code in order to extract derivatives in terms of small baryonic potentials. This investigation is particularly interesting since lQCD collaborations (especially the BMW) is nowadays working on it in order to have a direct check with the experiments.

Finally, let us mention that our EoS could be naturally used as starting point for hydrodynamic computations. In this sense, a calculation of the ratio viscosity over entropy can be considered in order to characterize the plasma that we have built. A small value of this ratio, as observed in experiments, could enforce the validity of the model that we have developed.

As you can notice it, the extensions and perspectives to our researches are not missing. It is always the same in physics: Every time a research is finished, a lot of questions come in mind and numerous and different directions are open. Nevertheless, *carpe diem* and let us see what tomorrow will bring.

Appendix A

Conventions

It is important to specify the general conventions that we have used within this thesis. Therefore, in what follows, the units [PDG] and the space-time notations are fixed as well as the acronyms and abbreviations that we have employed.

A.1 Unit system

Concerning the units, a scale in which $\hbar = 1 = c$ is chosen. Under these conditions, it thus remains only a free unit which is the energy and that we can express in multiple of electron-volt (eV); the MeV (10^6 eV) and the GeV (10^9 eV) being well-adapted units in hadronic physics. The masses have then the same dimensions as the energy. The length and time dimensions are in GeV^{-1}. Moreover, in the thermodynamic relations, we fix the Boltzmann constant k_B to unity. Therefore, the temperatures are also expressed in energy units.

To be complete, we mention some conversion factors to link our conventions to the international system:

- 1 GeV = 1.602176487(40) 10^{-10} J,
- 1 kg/c^2 = 1.782661758(44) 10^{-45} GeV,
- k_B = 8.617343(15) 10^{-14} GeV K^{-1},
- $\hbar c = 0.1973269631(49)$ GeV.fm.

A.2 Space-time characterization

The space-time metric is the Minskowski one $\eta_{\mu\nu}$, with the $(-,+,+,+)$ signature. The length element is given by

$$ds^2 = -dt^2 + dx^2 + dy^2 + dz^2.$$

The Dirac's matrices γ^μ, are defined by the anticommutation relations $\{\gamma^\mu, \gamma^\nu\} = 2\eta^{\mu\nu}$ whose one representation is

$$\gamma^0 = \begin{pmatrix} \mathbb{1}_2 & 0 \\ 0 & -\mathbb{1}_2 \end{pmatrix}, \gamma^j = \begin{pmatrix} 0 & \sigma_j \\ -\sigma_j & 0 \end{pmatrix}, \tag{A.2.1}$$

where the σ_j are the Pauli's matrices

It is also interesting to express some quantities in the euclidean space-time. In this case, the Dirac's matrices are denoted Γ^μ and have to check the anticommutation relations $\{\Gamma^\mu, \Gamma^\nu\} = 2\delta^{\mu\nu}$. They are given by

$$\Gamma^0 = i\gamma^0 = i\begin{pmatrix} \mathbb{1}_2 & 0 \\ 0 & -\mathbb{1}_2 \end{pmatrix}, \Gamma^j = \gamma^j = \begin{pmatrix} 0 & \sigma_j \\ -\sigma_j & 0 \end{pmatrix}. \tag{A.2.2}$$

A.3 List of acronyms and abbreviations

- AGS: Alternating Gradient Synchrotron
- ALEPH: Apparatus for LEP Physics (LEP experiment)
- BbS: Blankenbecler-Sugar
- BMW: Budapest-Marseille-Wuppertal
- BNL: Brookhaven National Laboratory
- BS: Bethe-Salpeter
- CERN: Organisation européenne pour la Recherche Nucléaire
- CKM: Cabibbo-Kobayashi-Maskawa
- CLQCD: China Lattice QCD
- DESY: Deutsches Elektronen-Synchrotron
- DMB: Dashen, Ma and Bernstein
- EoS: Equation(s) of State
- Fermilab: Fermi National Accelerator Laboratory
- HERA: Hadron Electron Ring Accelerator
- HRG: Hadron Resonance Gas
- HTL: Hard Thermal Loop

- LEP: Large Electron Positron collider
- LHC: Large Hadron Collider
- LMM: Lagrange-Mesh Method
- lQCD: Quantum Chromodynamics on lattice
- LS: Lippmann-Schwinger
- MC: Monte Carlo
- NJL: Nambu-Jona-Lasinio
- NLO: Next-to-leading order
- N^3LO: (Next-to)^3-leading order
- PETRA: Positron-Electron Tandem Ring Accelerator
- PNJL: Polyakov-Nambu-Jona-Lasinio
- QCD: Quantum Chromodynamics
- QED: Quantum Electrodynamics
- QGP: Quark-Gluon Plasma
- RHIC: Relativistic Heavy Ion Collider
- SB: Stefan-Boltzmann
- SLAC: Stanford Linear Accelerator Center
- SPEAR: Stanford Positron Electron Asymmetric Rings
- SPS: Super Proton Synchrotron
- YM: Yang-Mills

Appendix B

Helicity Formalism for Spin-1/2 and Transverse Spin-1 Particles

B.1 Generalities

The proper way to manage two-body states containing gluons, gluinos or quarks is to use the Jacob and Wick's helicity formalism [Jaco59], since a gluon is a transverse spin-1 particle and a quark or a gluino is a spin-1/2 particle. A two-body state with total spin J, with helicities λ_1 and λ_2, and with a given parity P can be written

$$\left|J^P, M; \lambda_1, \lambda_2, \epsilon\right\rangle = \frac{1}{\sqrt{2}} \left[|J, M; \lambda_1, \lambda_2\rangle + \epsilon \, |J, M; -\lambda_1, -\lambda_2\rangle\right], \tag{B.1.1}$$

with $\epsilon = \pm 1$ and $|J, M; \lambda_1, \lambda_2\rangle$, a two-particle helicity state in the rest frame of the system. The parity is given by $P = \epsilon \, \eta_1 \eta_2 (-1)^{J - s_1 - s_2}$ with η_i and s_i, the intrinsic parity and spin of particle i. Moreover, $J \geq |\lambda_1 - \lambda_2|$. The helicity states can be expressed as particular linear combinations of usual normalized basis states $\left|^{2S+1}L_J\right\rangle$, which is very convenient to perform the computations [Jaco59]

$$\begin{aligned} |J, M; \lambda_1, \lambda_2\rangle \quad = \quad & \sum_{L,S} \left[\frac{2L+1}{2J+1}\right]^{1/2} \langle L, S; 0, \lambda_1 - \lambda_2 | J, \lambda_1 - \lambda_2\rangle \\ & \times \langle s_1, s_2; \lambda_1, -\lambda_2 | S, \lambda_1 - \lambda_2\rangle \left|^{2S+1}L_J\right\rangle . \end{aligned} \tag{B.1.2}$$

The sum (B.1.2) involves all the $\{L, S\}$ couples such that $\vec{S} = \vec{s}_1 + \vec{s}_2$ and $\vec{L} + \vec{S} = \vec{J}$. The symbols $\langle a, b; c, d | e f\rangle$ denote the well-known Clebsch-Gordan coefficients.

In this present thesis, it is sufficient to recall that four families of helicity states can be found, separated in helicity singlets,

$$\left|S_\pm; J^P\right\rangle = |J^P, M; \lambda_1, \lambda_2, \pm 1\rangle \text{ with } \lambda_1 \lambda_2 > 0, \tag{B.1.3}$$

and doublets,

$$\left|D_\pm; J^P\right\rangle = |J^P, M; \lambda_1, \lambda_2, \pm 1\rangle \text{ with } \lambda_1 \lambda_2 < 0. \tag{B.1.4}$$

This notation follows the pioneering work [Barn81] and is used in [Math09a]. In the special case of identical particles, the helicity states must also be eigenstates of the operator $\hat{\mathcal{S}} = \left[1 + (-1)^{2s} P_{12}\right]$, which is the

projector on the symmetric (s integer) or antisymmetric (s half-integer) part of the helicity state. It can be seen that the states [Math09a]

$$\left|J^P, M; \lambda_1, \lambda_2, \epsilon, \rho\right\rangle = \frac{1}{2}\left\{\left|J^P, M; \lambda_1, \lambda_2, \epsilon\right\rangle + \rho\left|J^P, M; \lambda_2, \lambda_1, \epsilon\right\rangle\right\}, \tag{B.1.5}$$

with $\rho = \pm 1$, are eigenstates of $\hat{\mathcal{S}}$ with the eigenvalues $1 + \rho(-1)^J$.

B.2 Two transverse spin-1 particles

The generic form of transverse spin-1 two-particle states (in this work, two-gluon states) has been presented in [Math09a]. Some properties are given in Table B.1, as well as the average value of some operators, computed with these states.

State	S	A	$\left\langle \vec{L}^2 \right\rangle$	$\left\langle \vec{S}^2 \right\rangle$	$\left\langle \vec{L}\cdot\vec{S} \right\rangle$
$\left\|S_+; J^P\right\rangle$	(even-$J \geq 0$)$^+$	(odd-$J \geq 1$)$^-$	$J(J+1)+2$	2	-2
$\left\|S_-; J^P\right\rangle$	(even-$J \geq 0$)$^-$	(odd-$J \geq 1$)$^+$	$J(J+1)+2$	2	-2
$\left\|D_+; J^P\right\rangle$	(even-$J \geq 2$)$^+$	(odd-$J \geq 3$)$^-$	$J(J+1)-2$	6	-2
$\left\|D_-; J^P\right\rangle$	(odd-$J \geq 3$)$^+$	(even-$J \geq 2$)$^-$	$J(J+1)-2$	6	-2

Table B.1: Symmetrized (S) and antisymmetrized (A) transverse spin-1 two-particle helicity states, following the notation of [Barn81, Math09a], with the corresponding quantum numbers and some averaged operators.

We give here the explicit form of the states considered in this work; the number between braces being the value of $\left\langle \vec{L}^2 \right\rangle$. The first symmetric states are:

$$\left|S_+; 0^+\{2\}\right\rangle = \left[\frac{2}{3}\right]^{1/2}\left|{}^1S_0\right\rangle + \left[\frac{1}{3}\right]^{1/2}\left|{}^5D_0\right\rangle, \tag{B.2.1}$$

$$\left|S_-; 0^-\{2\}\right\rangle = -\left|{}^3P_0\right\rangle, \tag{B.2.2}$$

$$\left|D_+; 2^+\{4\}\right\rangle = \left[\frac{2}{5}\right]^{1/2}\left|{}^5S_2\right\rangle + \left[\frac{4}{7}\right]^{1/2}\left|{}^5D_2\right\rangle + \left[\frac{1}{35}\right]^{1/2}\left|{}^5G_2\right\rangle. \tag{B.2.3}$$

The first antisymmetric states are:

$$\left|S_+; 1^-\{4\}\right\rangle = \left[\frac{2}{3}\right]^{1/2}\left|{}^1P_1\right\rangle - \left[\frac{2}{15}\right]^{1/2}\left|{}^5P_1\right\rangle + \left[\frac{1}{5}\right]^{1/2}\left|{}^5F_1\right\rangle, \tag{B.2.4}$$

$$\left|S_-; 1^+\{4\}\right\rangle = \left[\frac{1}{3}\right]^{1/2}\left|{}^3S_1\right\rangle - \left[\frac{2}{3}\right]^{1/2}\left|{}^3D_1\right\rangle, \tag{B.2.5}$$

$$\left|D_-; 2^-\{4\}\right\rangle = -\left[\frac{4}{5}\right]^{1/2}\left|{}^5P_2\right\rangle - \left[\frac{1}{5}\right]^{1/2}\left|{}^5F_2\right\rangle. \tag{B.2.6}$$

All other states are characterized by $\left\langle \vec{L}^2 \right\rangle \geq 8$.

B.3 States containing one transverse spin-1 particle

The generic form of states containing one transverse spin-1 particle (in this work, states containing one gluon) can also be expressed as particular linear combinations of usual basis states $\left|^{2S+1}L_J\right\rangle$, following the procedure given in [Math09a]. Some properties are given in Table B.2, as well as the average value of some operators, computed with these states.

State	J min	$\left\langle \vec{L}^2 \right\rangle$	$\left\langle \vec{S}^2 \right\rangle$	$\left\langle \vec{L}\cdot\vec{S} \right\rangle$
$\left\vert S_\pm; J^P \right\rangle$	$\frac{1}{2}$	$J(J+1)+\frac{5}{4}$	$\frac{7}{4}$	$-\frac{3}{2}$
$\left\vert D_\pm; J^P \right\rangle$	$\frac{3}{2}$	$J(J+1)-\frac{3}{4}$	$\frac{15}{4}$	$-\frac{3}{2}$

Table B.2: Helicity states containing one transverse spin-1 particle, following the notation of [Barn81, Math09a], with the corresponding quantum numbers and some averaged operators.

We give here the explicit form of the states considered in this work; the number between braces being the value of $\left\langle \vec{L}^2 \right\rangle$. The first qg states are:

$$\left|S_+; \frac{1}{2}^+ \{2\}\right\rangle = \left[\frac{2}{3}\right]^{1/2} \left|^2P_{\frac{1}{2}}\right\rangle - \left[\frac{1}{3}\right]^{1/2} \left|^4P_{\frac{1}{2}}\right\rangle, \tag{B.3.1}$$

$$\left|S_-; \frac{1}{2}^- \{2\}\right\rangle = \left[\frac{2}{3}\right]^{1/2} \left|^2S_{\frac{1}{2}}\right\rangle - \left[\frac{1}{3}\right]^{1/2} \left|^4D_{\frac{1}{2}}\right\rangle, \tag{B.3.2}$$

$$\left|D_+; \frac{3}{2}^- \{3\}\right\rangle = \left[\frac{1}{2}\right]^{1/2} \left|^4S_{\frac{3}{2}}\right\rangle + \left[\frac{1}{2}\right]^{1/2} \left|^4D_{\frac{3}{2}}\right\rangle, \tag{B.3.3}$$

$$\left|D_-; \frac{3}{2}^+ \{3\}\right\rangle = -\left[\frac{9}{10}\right]^{1/2} \left|^4P_{\frac{3}{2}}\right\rangle - \left[\frac{1}{10}\right]^{1/2} \left|^4F_{\frac{3}{2}}\right\rangle, \tag{B.3.4}$$

$$\left|S_+; \frac{3}{2}^- \{5\}\right\rangle = \left[\frac{1}{6}\right]^{1/2} \left|^4S_{\frac{3}{2}}\right\rangle + \left[\frac{2}{3}\right]^{1/2} \left|^2D_{\frac{3}{2}}\right\rangle - \left[\frac{1}{6}\right]^{1/2} \left|^4D_{\frac{3}{2}}\right\rangle, \tag{B.3.5}$$

$$\left|S_-; \frac{3}{2}^+ \{5\}\right\rangle = \left[\frac{2}{3}\right]^{1/2} \left|^2P_{\frac{3}{2}}\right\rangle + \left[\frac{1}{30}\right]^{1/2} \left|^4P_{\frac{3}{2}}\right\rangle - \left[\frac{3}{10}\right]^{1/2} \left|^4F_{\frac{3}{2}}\right\rangle. \tag{B.3.6}$$

All other states are characterized by $\left\langle \vec{L}^2 \right\rangle \geq 8$. The parity is reversed for $\bar{q}g$ states. It is not relevant for $\tilde{g}g$

states [Zuk83]. Within the nomenclature defined in Section 4 and Section 6, we have the following relation:

$$(J1) \quad \rightarrow \quad \left| S_+; \frac{1}{2}^+ \{2\} \right\rangle, \tag{B.3.7}$$

$$(J2) \quad \rightarrow \quad \left| S_+; \frac{3}{2}^- \{5\} \right\rangle, \tag{B.3.8}$$

$$(J3) \quad \rightarrow \quad \left| D_+; \frac{3}{2}^- \{3\} \right\rangle, \tag{B.3.9}$$

$$(J4) \quad \rightarrow \quad \left| S_-; \frac{1}{2}^- \{2\} \right\rangle, \tag{B.3.10}$$

$$(J5) \quad \rightarrow \quad \left| S_-; \frac{3}{2}^+ \{5\} \right\rangle, \tag{B.3.11}$$

$$(J6) \quad \rightarrow \quad \left| D_-; \frac{3}{2}^+ \{3\} \right\rangle. \tag{B.3.12}$$

Appendix C

Gauge Group Factors

In this appendix, we summarize all the useful gauge factors entering in the diverse approaches developed within this thesis. The representations of the different two-body tensor products of interest, their dimension, their symmetry (when it is defined) as well as their values of $\kappa_{\mathcal{C}}$ given by (4.3.13) are displayed in the following tables. Note that the software LIE has been used and their conventions are followed for the enumeration of the fundamental weights of the various algebras associated to the gauge groups.

C.1 SU(N) gauge groups

In order to correctly interpret the tables below, it is important to mention some conventions and remarks. First of all, a representation $\mathcal{C}$ of the considered gauge groups is denoted $(a_1, \ldots, a_k, \ldots, a_{N-1})$ and corresponds to a Young diagram with a_k columns of length k. The notation of its conjugate representation is simply obtained by reversing the numbers; For example, the conjugate representation of $(2, 0, \ldots, 1, 0)$ is $(0, 1, \ldots, 0, 2)$.

Some interesting relations can be employed to check the different values given in what follows. Indeed, the dimension of each representation $\mathcal{C}_i$, appearing in the tensor product of $\mathcal{C}_1$ and $\mathcal{C}_2$, has to respect

$$\dim \mathcal{C}_1 \times \dim \mathcal{C}_2 = \sum_i \dim \mathcal{C}_i. \tag{C.1.1}$$

Moreover, in group theory [Fuch97], the second order Dynkin indices $I^{\mathcal{C}}$ in a tensor product obey a sum rule that can be rewritten using our notations as

$$\sum_{\mathcal{C}} \dim \mathcal{C}\ \kappa_{\mathcal{C}} = 0. \tag{C.1.2}$$

A general method for computing the quadratic Casimir of SU(N), needed to obtain the value of $\kappa_{\mathcal{C}}$ given by (4.3.13), can be found in *e.g.* [Luci01].

Since the background of this thesis is essentially the QCD, let us associate to the standard particles, their gauge group representation.

Particle	Representation	Dimension	Quadratic Casimir
g	$(1,0,\ldots,0,1)$	N^2-1	N
q	$(1,0,\ldots,0,0)$	N	$\frac{N^2-1}{2N}$
$\bar{q}$	$(0,0,\ldots,0,1)$	N	$\frac{N^2-1}{2N}$
q_A	$(0,1,\ldots,0,0)$	$\frac{N(N-1)}{2}$	$-1-\frac{2}{N}+N$
$\bar{q}_A$	$(0,0,\ldots,1,0)$	$\frac{N(N-1)}{2}$	$-1-\frac{2}{N}+N$

This notation will be used just hereafter within the tables in which the condition of existence, the symmetry (if it is meaningful), the dimension ($\dim \mathcal{C}$) and the colour factor ($\kappa_{\mathcal{C}}$) of the colour channels ($\mathcal{C}$) appearing in the considered tensor product are given. The SU(3) case is also indicated. Moreover, since the particle and its antiparticle share the same properties, they generate the same numbers in the tables below. That is the reason why we will not double the tables. It is just necessary to replace the representation notation by its conjugate one.

	gg				
SU(N)	•	$(1,0,\ldots,0,1)$	$(2,0,\ldots,0,2)$	$(2,0,\ldots,1,0)$ $(0,1,\ldots,0,2)$	$(0,1,0,\ldots,0,1,0)$
SU(3)	•	(1,1)	(2,2)	(0,3), (3,0)	-
$N \geq$	2	$2_A, 3_S$	2	3	4
Symmetry	S	A, S	S	A	S
$\dim \mathcal{C}$	1	N^2-1	$\frac{N^2(N+3)(N-1)}{4}$	$\frac{(N^2-4)(N^2-1)}{4}$	$\frac{N^2(N-3)(N+1)}{4}$
$\kappa_{\mathcal{C}}$	-1	$-\frac{1}{2}$	$\frac{1}{N}$	0	$-\frac{1}{N}$

	qq		$q\bar{q}$	
SU(N)	$(2,0,\ldots,0)$	$(0,1,0,\ldots,0)$	•	$(1,0,\ldots,0,1)$
SU(3)	$(2,0)$	$(0,1)$	•	$(1,1)$
$N \geq$	2	2	2	2
Symmetry	S	A	-	-
$\dim \mathcal{C}$	$\frac{N(N+1)}{2}$	$\frac{N(N-1)}{2}$	1	N^2-1
$\kappa_{\mathcal{C}}$	$\frac{N-1}{2N^2}$	$-\frac{N+1}{2N^2}$	$-\frac{N^2-1}{2N^2}$	$\frac{1}{2N^2}$

	qg		
SU(N)	$(1,0,\ldots,0)$	$(2,0,\ldots,0,1)$	$(0,1,\ldots,0,1)$
SU(3)	$(1,0)$	$(2,1)$	$(0,2)$
$N \geq$	2	2	3
$\dim \mathcal{C}$	N	$\frac{(N+2)N(N-1)}{2}$	$\frac{(N+1)N(N-2)}{2}$
$\kappa_{\mathcal{C}}$	$-\frac{1}{2}$	$\frac{1}{2N}$	$-\frac{1}{2N}$

	$q_A q_A$		
SU(N)	$(0,2,0,\ldots,0)$	$(1,0,1,0\ldots,0)$	$(0,0,0,1,0,\ldots,0)$
SU(3)	$(0,2)$	$(1,0)$	-
$N \geq$	2	3	4
Symmetry	S	A	S
$\dim \mathcal{C}$	$\frac{N^2(N^2-1)}{12}$	$\frac{N(N^2-1)(N-2)}{8}$	$\frac{N(N-1)(N-2)(N-3)}{24}$
$\kappa_{\mathcal{C}}$	$\frac{N-2}{N^2}$	$-\frac{2}{N^2}$	$-\frac{2(N+1)}{N^2}$

	$q_A \bar{q}_A$		
SU(N)	•	$(1,0,\ldots,0,1)$	$(0,1,0,\ldots,0,1,0)$
SU(3)	•	$(1,1)$	-
$N \geq$	2	3	4
$\dim \mathcal{C}$	1	N^2-1	$\frac{(N-3)N^2(N+1)}{4}$
$\kappa_{\mathcal{C}}$	$-\frac{(N-2)(N-1)}{N^2}$	$\frac{-N^2+2N+4}{2N^2}$	$\frac{2}{N^2}$

	$q_A g$			
SU(N)	$(2,0,\ldots,0)$	$(0,1,0\ldots,0)$	$(1,1,0,\ldots,0,1)$	$(0,0,1,0,\ldots,0,1)$
SU(3)	$(2,0)$	$(0,1)$	$(1,2)$	-
$N \geq$	2	3	3	4
$\dim \mathcal{C}$	$\frac{N(N+1)}{2}$	$\frac{N(N-1)}{2}$	$\frac{N^2(N^2-4)}{3}$	$\frac{N(N^2-1)(N-3)}{6}$
$\kappa_{\mathcal{C}}$	$-\frac{N-2}{2N}$	$-\frac{1}{2}$	$\frac{1}{2N}$	$-\frac{1}{N}$

C.2 G_2 gauge group

Another interesting group under consideration is G_2 which is also the best studied gauge group so far beyond SU(N). The adjoint representation of G_2 has dimension 14, and reads $(0,1)$ in a highest weight representation. Since we only consider the gauge-group dependence in the Yang-Mills sector, it is only necessary to look at the tensor product of two gluons. The useful numbers are then given in the table below, following the canvas proposed for the SU(N) tables.

	gg				
G_2	$\bullet$	$(0,1)$	$(0,2)$	$(2,0)$	$(3,0)$
Symmetry	S	A	S	S	A
$\dim \mathcal{C}$	1	14	77	27	77
$\kappa_{\mathcal{C}}$	-1	$-1/2$	1/4	$-5/12$	0

Appendix D

Lagrange-Mesh Method

The Lagrange-mesh method (LMM) is initially a powerful procedure, expressed in configuration space, to solve eigenproblems mainly associated to a two-body Schrödinger equation [Baye86, Baye95, Baye06, Vinc93] or a semi-relativistic Hamiltonian [Buis05, Sema01]. It is very simple to implement and very accurate. The trial eigenstates are expanded in a basis of well chosen functions, the regularized Lagrange functions which vanish at the origin and at all mesh points except one. Using their special properties and a Gauss quadrature rule, the method requires only the evaluation of the potential at the mesh points. Mean values of observables can then be easily obtained as well as the Fourier transform of the configuration space wave functions [Lacr11].

Afterward, the LLM has been adapted to solve eigenequations written directly in momentum space [Lacr12]. It has been shown in [Lacr12] that the convenience and the accuracy of the original technique are preserved. In particular, the kinetic operator is a diagonal matrix. Mean values of observables and wave functions expressed in configuration space can also be easily computed with a good accuracy using only eigenfunctions computed in the momentum space.

This appendix is based on a short compilation of the papers [Lacr11, Lacr12]. Only the philosophy of the method in configuration and in momentum space will be summarized. The numerical results demonstrating the efficiency of the LMM will not be exposed here. Interested readers can refer to all the articles mentioned in this introduction to realize its efficiency.

D.1 Method in configuration space

D.1.1 Lagrange functions

The basic tools for the LMM are a N-point mesh $\{x_i\}$ associated with an orthonormal set of N indefinitely derivable functions $f_j(x)$, called the Lagrange functions and satisfying [Baye86, Baye95, Vinc93]

$$f_j(x_i) = \lambda_i^{-1/2}\delta_{ij}. \tag{D.1.1}$$

This condition means that it vanishes at all mesh points except one. The x_i and λ_i are respectively the abscissae and the weights of a Gauss quadrature formula,

$$\int_0^\infty g(x)dx \approx \sum_{k=1}^{N} \lambda_k g(x_k). \tag{D.1.2}$$

As we usually work with the radial part of wave functions, we consider the case of the Gauss-Laguerre quadrature because the domain of interest is $[0, \infty[$. Nevertheless, it is worth mentioning that a general procedure for deriving other Lagrange meshes related then to orthogonal and non-orthogonal bases has also been developed in [Baye02]. The Gauss formula (D.1.2) is exact when $g(x)$ is a polynomial of degree $2N-1$ at most, multiplied by $\exp(-x)$. The Lagrange-Laguerre mesh points are the zeros of a Laguerre polynomial of degree N: $L_N(x_i) = 0$ [Baye86] while the weights can be computed by the following formula [Baye02]:

$$\ln \lambda_i = x_i - \ln x_i + 2 \ln \Gamma(N+1) - \sum_{j \neq i=1}^{N} \ln(x_i - x_j)^2. \tag{D.1.3}$$

For physical purposes, it is preferable to use the regularized Lagrange functions whose explicit form is given by

$$f_i(x) = (-1)^i x_i^{-1/2} x (x - x_i)^{-1} L_N(x) \exp(-x/2). \tag{D.1.4}$$

Besides nullifying at x_j with $j \neq i$, such a function also vanishes at the origin while checking (D.1.1).

D.1.2 Eigenvalue problems

With the LMM, the solution of a quantum equation (as for instance, the Schrödinger equation or a semi-relativistic Hamiltonian) reduces to the determination of eigensolutions of a given matrix. Let us consider the eigenvalue equation

$$\left[T(\vec{p}^{\,2}) + V(r)\right] |\psi\rangle = E\, |\psi\rangle, \tag{D.1.5}$$

where $T(\vec{p}^{\,2})$ is the kinetic energy term of the Hamiltonian and $V(r)$ the potential which depends only on the radial coordinate $r = |\vec{r}|$. A trial state $|\psi\rangle$, approximation of the genuine eigenstate, is expanded on a basis of the regularized Lagrange functions (D.1.4)

$$|\psi\rangle = \sum_{j=1}^{N} C_j |f_j\rangle \quad \text{with} \quad \langle \vec{r} | f_j \rangle = \frac{f_j(r/h)}{\sqrt{h} r} Y_{lm}(\hat{r}), \tag{D.1.6}$$

with $\hat{r} = \vec{r}/r$. The coefficients C_j are linear variational parameters and the scale factor h is a non-linear parameter aimed at adjusting the mesh to the domain of physical interest. Contrary to some other mesh methods, the wave function is also defined between mesh points by (D.1.4) and (D.1.6).

Basis states $|f_i\rangle$ built with the regularized Lagrange functions are orthogonal only at the Gauss approximation, *i.e.* $\langle f_j | f_i \rangle = \delta_{ji}$. So, all mean values has to be performed using the Gauss quadrature formula (D.1.2). The potential matrix elements are then given by

$$\langle f_i | V(r) | f_j \rangle = V(h x_i)\, \delta_{ij}. \tag{D.1.7}$$

The potential matrix is both simple to obtain and diagonal.

The only non-trivial part to compute is the matrix elements $\langle f_i | T | f_j \rangle \approx T_{ij}$. Let us first look at the matrix P whose elements are $P_{ij} = \langle f_i | \vec{p}^{\,2} | f_j \rangle$. With (D.1.2), these matrix elements are given by

$$P_{ij} = \frac{1}{h^2} \left(t_{ij} + \frac{l(l+1)}{x_i^2} \delta_{ij} \right), \tag{D.1.8}$$

where l is the orbital angular momentum quantum number, and where

$$t_{ij} = \int_0^\infty f_i(x) \left(-\frac{d^2}{dx^2} \right) f_j(x)\, dx \approx -\lambda_i^{1/2} f_j''(x_i). \tag{D.1.9}$$

This compact expression is exact for some Lagrange meshes. This is not the case for the regularized Laguerre mesh. An exact expression for t_{ij} can easily be obtained (see Appendix in [Vinc93]). However, as shown in [Baye95], it is preferable to use the approximation (D.1.8)-(D.1.9). The kinetic matrix elements are then even easier to obtain and read [Baye95]

$$t_{ij} = \begin{cases} (-)^{i-j}(x_i x_j)^{-1/2}(x_i + x_j)(x_i - x_j)^{-2} & (i \neq j), \\ (12x_i^2)^{-1}[4 + (4N+2)x_i - x_i^2] & (i = j). \end{cases} \tag{D.1.10}$$

For a non-relativistic Hamiltonian, $T_{ij} = \frac{1}{2\mu} P_{ij}$, where μ is the reduced mass of the system. For a more general operator $T(\vec{p}^{\,2})$, the calculation is much more involved (think for instance to the kinetic part of a spinless Salpeter equation $2\sqrt{\vec{p}^{\,2} + m^2}$). The idea is to use a four-step method suggested in [Fulc94] and applied in [Sema01]:

1. Computation of the matrix P whose elements are $P_{ij} = \langle f_i | \vec{p}^{\,2} | f_j \rangle$, given by (D.1.8)-(D.1.10).
2. Diagonalization of the matrix P. If P^D is the diagonal matrix formed by the eigenvalues of P, we have
$$P = S\, P^D\, S^{-1}, \tag{D.1.11}$$
where S is the transformation matrix composed of the normalized eigenvectors.
3. Computation of T^D, a diagonal matrix obtained by taking the function $T(x)$ of all diagonal elements of P^D.
4. Determination of the kinetic matrix T in the original basis by using the transformation (D.1.11)
$$T = S\, T^D\, S^{-1}. \tag{D.1.12}$$

The elements T_{ij} computed with (D.1.12) are of course approximations of the numbers $\langle f_i | T(\vec{p}^{\,2}) | f_j \rangle$. However, it has been shown in [Sema01], that this four-step procedure can give very good results for physical problems.

Now, let us apply the variational method to (D.1.5). It provides a system of N mesh equations

$$\sum_{j=1}^{N} [T_{ij} + V(hx_i)\, \delta_{ij} - E\, \delta_{ij}]\, C_j = 0. \tag{D.1.13}$$

It is worth noticing that the Hamiltonian matrix elements in (D.1.13) are computed at the Gauss approximation. So, the variational character of the method cannot be guaranteed, except if an exact quadrature is performed. In practice, for a sufficiently high number of basis states, the method is often variational and, in most cases, a very high accuracy can be achieved in the framework of the Gauss approximation. Nevertheless, the mathematical reasons for this high efficiency of the LMM are not well known yet [Baye02].

The accuracy of the eigensolutions depends on two parameters: The number of mesh points N and the value of the scale parameter h. For a sufficiently high value of N (which can be as low as 20 or 30), the eigenvalues present a large plateau as a function of h. This is a great advantage since the non-linear parameter must not be determined with a high precision. Nevertheless, if h is too small, a significant part of the wave function is not covered by the points of the Lagrange mesh and when h is too large, all mesh points are located in its asymptotic tail. Therefore, a procedure to directly estimate a reasonable value of h is necessary. We have remarked that the best results are obtained when the last mesh points are located "not too far" in the asymptotic tail. So, if we choose a point $r_{\max}$ in the tail of the wave function, the value of h can be obtained by $h = r_{\max}/x_N$, where x_N is the last mesh point. A methode to evaluate $r_{\max}$ has been developed but will not be detailed here. Interested readers can refer to [Brau98, Lacr11].

D.1.3 Mean values of radial observables

The mean value of the operator $U(r)$ for a trial state $|\psi\rangle$ is given by

$$\langle\psi|U(r)|\psi\rangle = \sum_{i,j=1}^{N} C_i\, C_j\, \langle f_i|U(r)|f_j\rangle. \tag{D.1.14}$$

Using the Lagrange condition (D.1.1) and the Gauss quadrature (D.1.2), this integral reduces to

$$\langle\psi|U(r)|\psi\rangle = \sum_{j=1}^{N} C_j^2\, U(hx_j). \tag{D.1.15}$$

If U is the identity, we recover the normalization condition as expected. A very high accuracy can be obtained with this simple procedure [Baye06, Hess99].

D.1.4 Mean values of momentum-dependent observables

As previously, the mean value of the operator $K(p)$ for a trial state $|\psi\rangle$ is given by

$$\langle\psi|K(p)|\psi\rangle = \sum_{i,j=1}^{N} C_i\, C_j\, \langle f_i|K(p)|f_j\rangle. \tag{D.1.16}$$

The matrix elements $\langle f_i|K(p)|f_j\rangle$ can be determined by a procedure identical to the one used to compute $\langle f_i|T(\vec{p}^{\,2})|f_j\rangle$. An intermediate step is the calculation of the matrix K^D, a diagonal matrix obtained by taking the function $K(\sqrt{x})$ of all diagonal elements of P^D (remember that P is linked to the matrix elements of $\vec{p}^{\,2}$, not $p = |\vec{p}|$). The numbers $\langle f_i|K(p)|f_j\rangle$ are well approximated by the elements of the matrix K obtained by using the transformation: $K = S\, K^D\, S^{-1}$. As it can be seen in [Lacr11], a very good accuracy can be reached for the mean values $\langle K(p)\rangle$.

D.1.5 Fourier's transform

For some particular problems, it can be useful to compute the Fourier's transform of a wave function in the position space in order to obtain the corresponding wave function in the momentum space. The Fourier's transform $\phi^{\text{FT}}(\vec{p})$ of a wave function $\phi(\vec{r})$ is defined by

$$\phi^{\text{FT}}(\vec{p}) = \frac{1}{(2\pi)^{3/2}} \int \phi(\vec{r})\, e^{-i\vec{p}.\vec{r}} d\vec{r}. \tag{D.1.17}$$

Using the spherical representation of the wave function

$$\phi(\vec{r}) = R_{nl}(r)\, Y_{lm}(\hat{r}), \tag{D.1.18}$$

and expanding $e^{-i\vec{p}.\vec{r}}$ in spherical waves [Vars88], it can be shown that

$$\phi^{\text{FT}}(\vec{p}) = R_{nl}^{\text{FT}}(p)\, \tilde{Y}_{lm}(\hat{p}), \tag{D.1.19}$$

where $p = |\vec{p}|$ and $\hat{p} = \vec{p}/p$, and where

$$R_{nl}^{\text{FT}}(p) = (-1)^l \sqrt{\frac{2}{\pi}} \int_0^\infty R_{nl}(r)\, j_l(p\, r)\, r^2\, dr, \tag{D.1.20}$$

$$\tilde{Y}_{lm}(\hat{p}) = i^l\, Y_{lm}(\hat{p}). \tag{D.1.21}$$

$j_l(x)$ is a spherical Bessel function [Abra65] and $\tilde{Y}_{lm}(\hat{x})$ is called a modified spherical harmonic [Vars88].

Using (D.1.6), the radial part $R(r)$ of the trial function is given by

$$R(r) = \sum_{j=1}^{N} C_j \frac{f_j(r/h)}{\sqrt{h} r}. \tag{D.1.22}$$

The Fourier's transform $R^{\text{FT}}(p)$ of this radial function is defined by (D.1.20). It is tempting to use the Gauss quadrature rule (D.1.2) with the Lagrange condition (D.1.1) to perform this calculation. The problem is that spherical Bessel functions are rapidly oscillating functions. It is then not obvious that such a procedure could work. Actually, we have checked that the Fourier's transform of a unique regularized Lagrange function, which is also a rapidly oscillating function, can not be obtained in this way with a good accuracy. Fortunately, the radial part of a wave function has a much smoother behaviour. Its Fourier's transform can be easily obtained in the framework of the LMM by taking benefit of the very special properties of the regularized Lagrange function [Lacr11]. Using (D.1.2) with (D.1.1), the integral (D.1.20) simply reduces to

$$\bar{R}^{\text{FT}}(p) = (-1)^l \sqrt{\frac{2}{\pi}}\, h^{3/2} \sum_{i=1}^{N} C_i\, \sqrt{\lambda_i}\, x_i\, j_l(h\, x_i\, p), \tag{D.1.23}$$

where we use the "bar" to indicate that this is not the exact Fourier's transform $R^{\text{FT}}(p)$. For a sufficiently high value of N (which can be as low as 50), $\bar{R}^{\text{FT}}(p)\, \tilde{Y}_{lm}(\hat{p})$ can be a very good approximation of the genuine eigenstate in the momentum space for values of $p \in [0, p_{\text{max}}]$, where p_{max} can be determined with the procedure used to compute r_{max} [Brau98, Lacr11]. For values of $p \gtrsim p_{\text{max}}$, $\bar{R}^{\text{FT}}(p)$ can present large unphysical rapid oscillations.

D.2 Method in momentum space

D.2.1 Eigenvalue problems

Let us go back to the eigenequation (cfr. (D.1.5))

$$\left[T(\vec{p}^{\,2}) + V(r)\right] |\phi\rangle = E\, |\phi\rangle. \tag{D.2.1}$$

We have shown in the previous section that the wave functions in configuration space $\phi_r(\vec{r}) = \langle \vec{r} | \phi \rangle$ and in momentum space $\phi_p(\vec{p}) = \langle \vec{p} | \phi \rangle$ can be written using the spherical representation (we could use the notation R_{nl}^{FT} in (D.2.3) but we prefer to keep the notation of [Lacr12])

$$\phi_r(\vec{r}) = \mathcal{R}_{nl}(r)\, Y_{lm}(\hat{r}), \tag{D.2.2}$$

$$\phi_p(\vec{p}) = \mathcal{P}_{nl}(p)\, \widetilde{Y}_{lm}(\hat{p}), \tag{D.2.3}$$

and linked by the following Fourier's transforms [Saku93]

$$\phi_p(\vec{p}) = \frac{1}{(2\pi)^{3/2}} \int \phi_r(\vec{r})\, e^{-i\vec{p}\cdot\vec{r}}\, d\vec{r}, \tag{D.2.4}$$

$$\phi_r(\vec{r}) = \frac{1}{(2\pi)^{3/2}} \int \phi_p(\vec{p})\, e^{+i\vec{p}\cdot\vec{r}}\, d\vec{p}. \tag{D.2.5}$$

These equations lead to [Lacr11]

$$\mathcal{P}_{nl}(p) = (-1)^l \sqrt{\frac{2}{\pi}} \int_0^\infty \mathcal{R}_{nl}(r)\, j_l(p\,r)\, r^2\, dr, \tag{D.2.6}$$

$$\mathcal{R}_{nl}(r) = (-1)^l \sqrt{\frac{2}{\pi}} \int_0^\infty \mathcal{P}_{nl}(p)\, j_l(p\,r)\, p^2\, dp. \tag{D.2.7}$$

Written in the momentum space, (D.2.1) takes the following form

$$T(\vec{p}^{\,2})\, \phi_p(\vec{p}) + \int V_{\rm FT}(\vec{p}-\vec{p}\,')\, \phi_p(\vec{p}\,')\, d\vec{p}\,' = E\, \phi_p(\vec{p}) \tag{D.2.8}$$

with $V_{\rm FT}(\vec{p}-\vec{p}\,')$, the Fourier's transform of $V(r)$, given by

$$V_{\rm FT}(\vec{p}-\vec{p}\,') = \frac{1}{(2\pi)^3} \int V(r)\, e^{-i(\vec{p}-\vec{p}\,')\cdot\vec{r}} d\vec{r}. \tag{D.2.9}$$

This potential is a continuous function of the momentum, even if parts of the interaction in configuration space present discontinuities. One can think of square well or Dirac delta function. As the potential depends only on r, we have $V_{\rm FT}(\vec{p}-\vec{p}\,') = V_{\rm FT}(|\vec{p}-\vec{p}\,'|)$ and (D.2.9) becomes [Grad80]

$$V_{\rm FT}(k) = \frac{1}{2\pi^2 k} \int_0^\infty V(r)\, \sin(k\,r)\, r\, dr. \tag{D.2.10}$$

Using the standard decomposition of an angular function [Vars88], the eigenvalue equation (D.2.8) takes the form of an integral equation for the wave function $\mathcal{P}_{nl}(p)$

$$T(p^2)\, \mathcal{P}_{nl}(p) + \int_0^\infty V_l(p,p')\, \mathcal{P}_{nl}(p')\, p'^{\,2}\, dp' = E\, \mathcal{P}_{nl}(p) \tag{D.2.11}$$

with the partial potentials

$$V_l(p,p') = 2\pi \int_{-1}^{+1} P_l(t)\, V_{\rm FT}\left(\sqrt{p^2 + p'^{\,2} - 2pp't}\right) dt. \tag{D.2.12}$$

The Legendre polynomial $P_l(t)$ depends on the variable $t = \hat{p}\cdot\hat{p}'$.

Within this formulation, the action of the kinetic operator is just an ordinary multiplication. So, non-relativistic and semi-relativistic systems are computed with the same manner. Moreover, more complicated kinetic parts, with momentum-dependent masses [Agui11, Llan00, Szcz96], can be equally treated. Though the formulations in the configuration and momentum spaces are completely equivalent, this does not mean that the technical difficulties to solve the eigenequations are the same in both spaces.

To express the integral equation (D.2.11) within LMM, the idea is to expand the wave function $\mathcal{P}_{nl}(p)$ with the regularized Lagrange functions in such a way that a trial state $|\psi\rangle$ is written

$$|\psi\rangle = \sum_{j=1}^{N} C_j \, |f_j\rangle \quad \text{with} \quad \langle \vec{p}|f_j\rangle = \frac{f_j(p/h)}{\sqrt{h}\, p} \, \widetilde{Y}_{lm}(\hat{p}). \tag{D.2.13}$$

This formula is identical to (D.1.6) with just two differences: the replacement of the variable r by p and the dimension of the parameter h (a dimension of a momentum versus a dimension of a distance). For a good value of h and a sufficiently high value of N, the function

$$\bar{\mathcal{P}}_{nl}(p) = \sum_{j=1}^{N} C_j \, \frac{f_j(p/h)}{\sqrt{h}\, p} \tag{D.2.14}$$

can also be a good approximation of the exact function $\mathcal{P}_{nl}(p)$. We have checked that the method in momentum space keeps the advantage of a large plateau for the determination of h. It is sufficient that this value be located within a given interval. However, the generalization of an automatic procedure for determining the value of h, as developed in the configuration space, is very difficult to obtain due to the non-local nature of the interaction in (D.2.11). A study of the convergence of the method as a function of the scale parameter h and the number of mesh points N for non-relativistic and semi-relativistic kinematics has been done in [Lacr12].

Inserting expansion (D.2.14) in (D.2.11) gives

$$T(h^2x^2) \sum_{j=1}^{N} C_j \, \frac{f_j(x)}{x} + \sum_{j=1}^{N} C_j \, h^3 \, \sqrt{\lambda_j} \, x_j \, V_l(h\,x_j, h\,x) = E \sum_{j=1}^{N} C_j \, \frac{f_j(x)}{x}, \tag{D.2.15}$$

where $x = p/h$ is a dimensionless variable. We can now multiply this equation by $x\, f_j(x)$ and integrate on $[0, \infty[$ with again the Gauss quadrature formula (D.1.2). Finally, we obtain

$$\sum_{j=1}^{N} C_j \left[T(h^2 x_i^2)\, \delta_{ij} + h^3 \, \sqrt{\lambda_i \, \lambda_j} \, x_i \, x_j \, V_l(h\,x_i, h\,x_j) - E\, \delta_{ij} \right] = 0. \tag{D.2.16}$$

The Hamiltonian matrix is symmetric since $V_l(p,p') = V_l(p',p)$. A similar expression is obtained for calculations with the LMM in the configuration space for a non-local potential [Hess02].

In [Lacr12], we have cross-checked our results by comparing eigenvalues and mean values of observables computed with the LMM in both configuration and momentum spaces. The Fourier's transform is naturally used to pass from one space to another.

D.2.2 Mean values of momentum-dependent observables

As the analogue case in the configuration space, the mean value of the operator $U(p)$ for a trial state $|\psi\rangle$ is given by

$$\langle \psi|U(p)|\psi\rangle = \sum_{i,j=1}^{N} C_i \, C_j \, \langle f_i|U(p)|f_j\rangle. \tag{D.2.17}$$

It naturally reduces to the simple expression

$$\langle\psi|U(p)|\psi\rangle = \sum_{j=1}^{N} C_j^2\, U(h\, x_j). \tag{D.2.18}$$

If U is the identity, we recover the normalization condition as expected.

D.2.3 Mean values of radial observables

The mean value of the operator $K(r)$ for a trial state $|\psi\rangle$ is given by

$$\langle\psi|K(r)|\psi\rangle = \sum_{i,j=1}^{N} C_i\, C_j\, \langle f_i|K(r)|f_j\rangle. \tag{D.2.19}$$

The method to compute matrix elements $\langle f_i|K(r)|f_j\rangle$ relies on the fact that $\vec{r}^{\,2} = -\vec{\nabla}_{\vec{p}}^{\,2}$ in the momentum space [Luch90]. If we look at the matrix R whose elements are $R_{ij} = \langle f_i|\vec{r}^{\,2}|f_j\rangle$, we find similar expressions as the one developed in Section D.1.2. This case is therefore analogue at the computation of momentum-dependent observables in the configuration space.

D.2.4 Fourier's transform

The Fourier's transform of the wave function computed in momentum space is of course given by

$$\bar{\mathcal{R}}_{nl}(r) = (-1)^l \sqrt{\frac{2}{\pi}}\, h^{3/2} \sum_{i=1}^{N} C_i\, \sqrt{\lambda_i}\, x_i\, j_l(h\, x_i\, r). \tag{D.2.20}$$

This formula is identical to (D.1.23) with just the replacement of the variable r by p. The same conclusions as the ones drawn in the configuration space can be done here.

List of Publications

Master thesis

- F. Buisseret and G. Lacroix, Eur. Phys. J. C **70**, 1051 (2010).
- F. Buisseret and G. Lacroix, *Proceedings*, Few-Body Systems **53**, 53 (2012).

Chapter 3

- F. Buisseret and G. Lacroix, Phys. Lett. B **705**, 405 (2011).

Chapter 4 and Chapter 5

- D. Cabrera, G. Lacroix, C. Semay, and F. Buisseret, *Proceedings*, Sixth International Conference on Quarks and Nuclear Physics (2012).
- G. Lacroix, C. Semay, D. Cabrera, and F. Buisseret, Phys. Rev. D **87**, 054025 (2013).
- G. Lacroix, C. Semay, D. Cabrera, and F. Buisseret, *Proceedings*, Xth Quark Confinement and the Hadron Spectrum (2013).
- G. Lacroix, C. Semay and F. Buisseret, article in preparation concerning the inclusion of quarks in the QGP (2014).

Chapter 6

- G. Lacroix, C. Semay and F. Buisseret, arXiv:1408.0958 (2014).
- G. Lacroix, C. Semay and F. Buisseret, arXiv:1408.4979 (2014).

Chapter 7

- F. Buisseret and G. Lacroix, Phys. Rev. D **85**, 016009 (2012).

Appendix D

- G. Lacroix and C. Semay, Phys. Rev. E **84**, 036705 (2011).
- G. Lacroix, C. Semay, and F. Buisseret, Phys. Rev. E **86**, 026705 (2012).

List of Communications and Stays Abroad

Year 2011

03/22: *Statistical approach of the quark-gluon plasma*, Poster, La Matinée des Chercheurs (UMONS).

04/06: *A minimal quasiparticle approach for the QGP and its large-Nc limits*, Seminar, Conference "30 years of strong interactions : a three-day meeting in honor of Joseph Cugnon and Hans-Jürgen Pirner".

05/25: *Statistical approach of the quark-gluon plasma*, Poster, Belgian Physical Society meeting.

09/13: *Statistical approach of the quark-gluon plasma*, Poster, EJC Ph.D. School.

11/20-12/03: Stay in Universidad Complutense de Madrid, Spain.

11/30: *Phenomenological approaches characterizing the pure-glue phase transition in QCD*, Seminar, Universidad Complutense de Madrid.

Year 2012

05/01-06/10: Stay in ECT*, Trento, Italy.

05/25: *Phenomenological approaches characterizing the pure-glue phase transition in QCD*, Seminar, ECT*.

10/09: *Characterization of the pure-glue phase in QCD*, Seminar, Xth Quark Confinement and the Hadron Spectrum.

Year 2013

01/06-02/10: Stay in ECT*, Trento, Italy.

01/29: *Glueballs and the Yang-Mills plasma in a T-matrix approach*, Seminar, ECT*.

03/12: *Glueballs and the Yang-Mills plasma*, Poster, La Matinée des Chercheurs (UMONS), Prize of the best poster for Complexys Institute.

05/14: *Glueballs and the Yang-Mills plasma*, Seminar, ECT* Doctoral Training Progam.

03/28: *La Chromodynamique Quantique : Théorie physique entre particules colorées*, Seminar, Séminaire pour jeunes chercheurs (UMONS).

06/09-14: Stay in Frankfurt Institute for Advanced Studies, Germany.

06/09: *From a white to a coloured world : QGP with quasiparticle approaches*, Seminar, Frankfurt Institute for Advanced Studies.

09/30: *Glueballs and the Yang-Mills plasma*, Poster, EJC Ph.D. School.

Year 2014

01/06-01/19: Stay in ECT*, Trento, Italy.

03/21-04/12: Stay in Indiana University, Bloomington, USA.

03/28: *Characterization of the pure-glue phase in QCD*, Seminar, Indiana University.

05/22: *Glueballs and the Yang-Mills plasma*, Seminar, Annual meeting of the PandA Ph.D. school (ULB).

05/28: *Glueballs and the Yang-Mills plasma*, Poster, Belgian Physical Society meeting

08/28: *Characterization of the pure-glue phase and its $\mathcal{N} = 1$ SUSY extension*, Seminar, Mons Meeting 2014.

Bibliography

[Abra65] M. Abramowitz and I. A. Stegun, *Handbook of Mathematical Functions* Dover, New York (1965).

[Agui09] A. C. Aguilar, D. Binosi, J. Papavassiliou, and J. Rodriguez-Quintero, Phys. Rev. D **80**, 085018 (2009); A. C. Aguilar, D. Binosi, and J. Papavassiliou, JHEP **1007**, 002 (2010).

[Agui11] A. C. Aguilar, D. Binosi, and J. Papavassiliou, Phys. Rev. D **84**, 085026 (2011).

[Aitc82] I. J. R. Aitchison and A. J. G. Hey, *Gauge Theories in Particle Physics*, Adam Hilger LTD, Bristol (1982).

[Akhi65] A. I. Akhiezer and V. B. Berestetskii, *Quantum Electrodynamics*, Interscience Publishers, New-York (1965).

[Albe05] W. M. Alberico, A. Beraudo, A. De Pace, and A. Molinari, Phys. Rev. D **72**, 114011 (2005).

[Amat88] D. Amati, K. Konishi, Y. Meurice, G. C. Rossi, and G. Veneziano, Phys. Rep. **162**, 169 (1988).

[Anbe14] M. M. Anber, E. Poppitz, and B. Teeple, arXiv:1406.1199 (2014).

[Aoki06] Y. Aoki, Z. Fodor, S. D. Katz, and K. K. Szabo, Phys. Lett. B **643** (2006); Y. Aoki, S. Borsanyi, S. Durr, Z. Fodor, S. D. Katz, S. Krieg, and K. K. Szabo, J. High Energy Phys. **0906** (2009).

[Armo03] A. Armoni, M. Shifman, and G. Veneziano, Phys. Rev. Lett. **91**, 191601 (2003).

[Asak04] M. Asakawa and T. Hatsuda, Phys. Rev. Lett. **92**, 012001 (2004).

[Bali00] G. S. Bali, Phys.Rev. D **62**, 114503 (2000).

[Bali01] G. S. Bali, Phys. Rep. **343**, 1 (2001); C. Semay, Eur. Phys. J. A **22**, 353 (2004); M. Cardoso and P. Bicudo, Phys. Rev. D **78**, 074508 (2008).

[Bali04] G. S. Bali and A. Pineda, Phys. Rev. D **69**, 094001 (2004).

[Bann95] V. M. Bannur, Phys. Lett. B **362**, 7 (1995).

[Barn81] T. Barnes, Z. Phys. C **10**, 275 (1981).

[Baye86] D. Baye and P.-H. Heenen, J. Phys. A **19**, 2041 (1986).

[Baye95] D. Baye, J. Phys. B **28**, 4399 (1995).

[Baye02] D. Baye, M. Hesse, and M. Vincke, Phys. Rev. E **65**, 026701 (2002).

[Baye06] D. Baye, Phys. Stat. Sol. (b) **243**, 1095 (2006); D. Baye and K. D. Sen, Phys. Rev. E **78**, 026701 (2008).

[Baza09] A. Bazavov (Arizona U.) *et al.*, Phys. Rev. D **80**, 014504 (2009).

[Baza10] A. Bazavov and P. Petreczky, J. Phys. Conf. Ser. **230**, 012014 (2010).

[Bere66] F. A. Berezin, *The Method of Second Quantization*, Academic Press (1966).

[Berg13] G. Bergner, I. Montvay, G. Münster, U. D. Özugurel, and D. Sandbrink, JHEP **1311**, 061 (2013).

[Berg14] G. Bergner, P. Giudice, G. Mü nster, S. Piemonte and D. Sandbrink, ArXiv:1405.3180.

[Beth35] E. Beth and G. E. Uhlenbeck, Physica **3**, 729 (1936); Physica **4**, 915 (1937).

[Beth07] S. Bethke, Prog. Part. Nucl. Phys. **58**, 351 (2007).

[Beth09] S. Bethke, Eur. Phys. J. C **64**, 689 (2009).

[Bino09] D. Binosi and J. Papavassiliou, Phys. Rep. **479**, 1 (2009).

[Blai99] J.-P. Blaizot, E. Iancu, and A. Rebhan, Phys. Lett. B **470**, 181 (1999); Phys. Rev. D **63**, 065003 (2001).

[Blai05] J.-P. Blaizot, Nucl. Phys. A **751**, 139 (2005).

[Blan66] R. Blankenbecler and R. Sugar, Phys. Rev. **142**, 1051 (1966).

[Blum11] M. Bluhm, B. Kämpfer, and K. Redlich, Phys. Rev. C **84**, 025201 (2011).

[BMW08] Budapest-Marseille-Wuppertal Collaboration, Science Vol. **322** no. **5905**,1224 (2008).

[Bors10] S. Borsányi *et al.*, JHEP **1011**, 077 (2010); S. Borsanyi *et al.*, Nucl. Phys. A **855**, 253 (2011).

[Bors11] S. Borsányi, G. Endrödi, Z. Fodor, S.D. Katz, and K.K. Szabo, arXiv:1104.0013.

[Bors12a] S. Borsányi, G. Endrödi, Z. Fodor, S. D. Katz, and K. K. Szabo, JHEP **07**, 056 (2012).

[Bors12b] S. Borsányi, *et al.*, JHEP **08**, 053 (2012).

[Bors14] S. Borsányi *et al.*, Phys. Lett. B **370**, 99 (2014).

[Braa90] E. Braaten and R.D. Pisarski, Nuclear Physics B **337**, 569 (1990).

[Brau98] F. Brau and C. Semay, J. Comput. Phys. **139**, 127 (1998).

[Brau09] F. Brau and F. Buisseret, Phys. Rev. D **79**, 114007 (2009).

[Brau10] J. Braun, A. Eichhorn, H. Gies, and J. M. Pawlowski, Eur. Phys. J. C **70**, 689 (2010).

[Brin06] B. Bringoltz and M. Teper, Phys. Rev. D **73**, 014517 (2006).

[Bron04] W. Broniowski, W. Florkowski, and L. Y. Glozman, Phys. Rev. D **70**, 117503 (2004).

[Buis05] F. Buisseret and C. Semay, Phys. Rev. E **71**, 026705 (2005); F. Buisseret and C. Semay, Phys. Rev. E **75**, 026705 (2007).

[Buis09] F. Buisseret, V. Mathieu, and C. Semay, Phys. Rev. D **80**, 074021 (2009).

[Buis10a] F. Buisseret and G. Lacroix, Eur. Phys. J. C **70**, 1051 (2010).

[Buis10b] F. Buisseret, Eur. Phys. J. C **68**, 473 (2010).

[Buis11a] F. Buisseret, Eur. Phys. J. C **71**, 1651 (2011).

[Buis11b] F. Buisseret and G. Lacroix, Phys. Lett. B **705**, 405 (2011).

[Buis12] F. Buisseret and G. Lacroix, Phys. Rev. D **85**, 016009 (2012).

[Cabr07] D. Cabrera and R. Rapp, Phys. Rev. D **76**, 114506 (2007).

[Camp99] I. Campos *et al.* [DESY-Münster Collaboration], Eur. Phys. J. C **11**, 507 (1999).

[Case11] M. Caselle, L. Castagnini, A. Feo, F. Gliozzi, and M. Panero, JHEP **1106**, 142 (2011).

[Casw74] W. E. Caswell, Phys. Rev. Lett. 33, 244 (1974).

[CERN] CERN website, www.cern.ch.

[CERNco] http://cerncourier.com.

[Cham91] A. H. Chamseddine, Phys. Lett. B **258**, 97 (1991); S. D. Odintsov, Phys. Lett. B **274**, 338 (1992).

[Chen06] M. Cheng *et al.*, Phys. Rev. D **74**, 054507 (2006); Y. Aoki *et al.*, JHEP **0906**, 088 (2009).

[Cher11] A. Cherman, M. Hanada, and D. Robles-Llana, Phys. Rev. Lett. **106**, 091603 (2011).

[Cley11] J. Cleymans and D. Worku, arXiv:1103.1463.

[Clos80] F. E. Close, *An Introduction to Quarks and Partons*, Academic Press, third edition (1980).

[Cohe06] T. D. Cohen, Phys. Lett. B **637**, 81 (2006).

[Cohe10] T. D. Cohen, JHEP **1006**, 098 (2010).

[Coll75] J. C. Collins and M. J. Perry, Phys. Rev. Lett. **34**, 1353 (1975); E. V. Shuryak, Phys. Rep. **61**, 71 (1980).

[Cont08] G. A. Contrera, D. Gomez Dumm, and N. N. Scoccola, Phys. Lett. B **661**, 113 (2008).

[Cont10] G. A. Contrera, M. Orsaria, and N. N. Scoccola, Phys. Rev. D **82**, 054026 (2010).

[Corn82] J. M. Cornwall, Phys. Rev. D **26**, 1453 (1982).

[Coss11] G. Cossu, web page: http://www.jicfus.jp/en/promotion/pr/mj/guido-cossu/ (2011).

[Cucc10] A. Cucchieri and T. Mendes, Phys. Rev. D **81**, 016005 (2010).

[Dash69] R. Dashen, S.-K. Ma, and H. J. Bernstein, Phys. Rev. **187**, 345 (1969).

[Deby23] P. Debye and E. Hückel, Physikalische Zeitschrift **24**, 185 (1923).

[Defo00] P. de Forcrand and O. Philipsen, Phys. Lett. B **475**, 280 (2000).

[Deld02] L. Del Debbio, H. Panagopoulos, P. Rossi, and E. Vicari, JHEP **0201**, 009 (2002).

[Demm10] K. Demmouche, F. Farchioni, A. Ferling, I. Montvay, G. Münster, E. E. Scholz, and J. Wuilloud, Eur. Phys. J. C **69**, 147 (2010).

[Diak11] D. Diakonov and V. Petrov, AIP Conf. Proc. 1343, 69 (2011) and references therein.

[Dien94] K. R. Dienes and J. -R. Cudell, Phys. Rev. Lett. **72**, 187 (1994).

[Dies14] J. Diestel and A. Spalsbury, *The Joys of Haar Measure*, American Mathematical Society (2014).

[Dumi01] A. Dumitru and R. D. Pisarski, Phys. Lett. B **504**, 282 (2001); E. S. Fraga, R. D. Pisarski and J. Schaffner-Bielich, Phys. Rev. D **63**, 121702 (2001); O. Scavenius, A. Dumitru and J. T. Lenaghan, Phys. Rev. C **66**, 034903 (2002).

[Dumi12] A. Dumitru, Y. Guo, Y. Hidaka, C. P. K. Altes, and R. D. Pisarski, Phys. Rev. D **86**, 105017 (2012).

[Enge89] J. Engels, J. Fingberg, K. Redlich, H. Satz, and M. Weber, Z. Phys. C **42**, 341 (1989).

[Fade67] L. D. Faddeev and V. N. Popov, Phys. Lett. **25B**, 29 (1967).

[Fade80] L. D. Faddeev and A. A. Slavnov, *Gauge fields*, Benjamin/Cummings (1980).

[Farc04] F. Farchioni and R. Peetz, Eur. Phys. J. C **39**, 87 (2005).

[Farr98] G. R. Farrar, G. Gabadadze, and M. Schwetz, Phys. Rev. D **58**, 015009 (1998); G. Veneziano and S. Yankielowicz, Phys. Lett. B **113**, 231 (1982).

[Fava12] L. Favart, Lecture notes, *Physique auprès des collisionneurs*, Chapter 3 (2012).

[Feo04] A. Feo, P. Merlatti, and F. Sannino, Phys. Rev. D **70**, 096004 (2004).

[Feyn48] R. P. Feynman, Rev. Mod. Phys. **20**, 367 (1948).

[Fodo12] Z. Fodor and C. Hoelbling, Rev. Mod. Phys. **84**, 449 (2012).

[Frau71] S. C. Frautschi, Phys. Rev. D **3**, 2821 (1971).

[Frim11] B. Friman *et al.*, *The CBM Physics Book*, Lecture Notes in Physics, Vol. **814** (2011).

[Frit73] H. Fritzsch, M. Gell-Mann, and H. Leutwyler, Phys. Lett. B **47**, 365 (1973).

[Fuch97] J. Fuchs and C. Schweigert, *Symmetries, Lie Algebras and Representations*, Cambridge University Press (1997).

[Fuku04] K. Fukushima, Phys. Lett. B **591**, 277 (2004).

[Fuku10] K. Fukushima, M. Ruggieri, and R. Gatto, Phys. Rev. D **81**, 114031 (2010).

[Fuku11] K. Fukushima and T. Hatsuda, Rep. Prog. Phys. **74**, 014001 (2011).

[Fuku13] K. Fukushima and C. Sasaki, arXiv:1301.6377.

[Fulc94] L. P. Fulcher, Phys. Rev. D **50**, 447 (1994) and references therein.

[Gatt10] C. Gattringer and C. B. Lang, *Quantum Chromodynamics on the Lattice*, Springer (2010).

[Gelm06] B. A. Gelman, E. V. Shuryak and I. Zahed, Phys. Rev. C **74**, 044908 (2006); Phys. Rev. C **74**, 044909 (2006).

[Gers10] V. D. Gershun and A. I. Pashnev, Theor. Math. Phys. **73**, 1227 (1987); V. D. Gershun and D. J. Cirilo-Lombardo, J. Phys. A **43**, 305401 (2010).

[Gieb85] D. R. Giebink, Phys. Rev. C **32**, 502 (1985).

[Golo93] V. Goloviznin and H. Satz, Z. Phys. C **57**, 671 (1993).

[Gore95] M. I. Gorenstein and S. N. Yang Phys. Rev. D **52**, 5206 (1995).

[Grad80] I. S. Gradshteyn and I. M. Ryzhik, *Tables of Integrals, Series, and Products*, Academic Press, New York (2007).

[Grei99] W. Greiner and J. Reinhardt, *Quantum Electrodynamics*, Springer-Verlag, New York (1999).

[Gros73] D. J. Gross and F. Wilczek, Phys. Rev. Lett. **30**, 1343 (1973).

[Gupt08] S. Gupta, K. Hübner, and O. Kaczmarek, Phys. Rev. D **77**, 034503 (2008).

[Haft70] M. I. Haftel and F. Tabakin, Nucl. Phys. **A158**, 1 (1970).

[Hage65] R. Hagedorn, Nuovo Cim. Suppl. **3**, 147 (1965).

[Hage68] R. Hagedorn, Nuovo Cim. A **56**, 1027 (1968).

[Hash11] S. Hashimoto, J. Laiho, and S.R. Sharpe, PDG, section 17 (2011).

[Hats94] T. Hatsuda and T. Kunihiro, Phys. Rep. **247**, 221 (1994).

[Hees09] H. van Hees, M. Mannarelli, V. Greco, and R. Rapp, Eur. Phys. J. C **61**,799 (2009).

[Heis29] W. Heisenberg and W. Pauli, Z. Phys. **56**, 1 (1929); Z. Phys **59**, 168 (1930).

[Hess99] M. Hess and D. Baye, J. Phys. B **32**, 5605 (1999).

[Hess02] M. Hesse, J. Roland, and D. Baye, Nucl. Phys. A **709**, 184 (2002).

[Hoof74] G. 't Hooft, Nucl. Phys. **72**, 461 (1974).

[Hugg12] K. Huggins and R. Rapp, Nucl. Phys. A **896**, 24 (2012)

[Huss00] D. Husson, *Les quarks, histoire d'une découverte*, Ellipses (2000).

[Isgu85] N. Isgur and J. E. Paton, Phys. Rev. D **31**, 2910 (1985).

[Ishi02] N. Ishii, H. Suganuma, and H. Matsufuru, Phys. Rev. D **66**, 094506 (2002).

[Jaco59] M. Jacob and G. C. Wick, Annals Phys. **7**, 404 (1959).

[Jicf] http://www.jicfus.jp/en/promotion/pr/mj/guido-cossu/ (2014).

[Joac75] C. J. Joachain, *Quantum Collision Theory* (North-Holland, New-York, 1975).

[Kacz02] O. Kaczmarek, F. Karsch, P. Petreczky, and F. Zantow, Phys. Lett. B **543**, 41 (2002).

[Kacz05] O. Kaczmarek and F. Zantow, arXiv:0506019 (2005).

[Kapu06] J. I. Kapusta and C. Gale, *Finite-Temperature Filed Theory*, Cambridge Monographs, second edition (2006).

[Kars00] F. Karsch, E. Laermann, and A. Peikert, Phys. Lett. B **478**, 447 (2000).

[Kars03] F. Karsch, K. Redlich, and A. Tawfik, Eur. Phys. J. C **29**,549 (2003).

[Klev92] S. P. Klevansky, Rev. Mod. Phys. **64**, 649 (1992).

[Kovt04] P. Kovtun, D. T. Son, and A. O. Starinets, Phys. Rev. Lett. **94**, 111601 (2005).

[Kura14] Y. Kuramashi, web page, http://labs.aics.riken.jp/kuramashi.html.

[Lacr11] G. Lacroix and C. Semay, Phys. Rev. E **84**, 036705 (2011).

[Lacr12] G. Lacroix, C. Semay, and F. Buisseret, Phys. Rev. E **86**, 026705 (2012).

[Lacr13] G. Lacroix, C. Semay, D. Cabrera, and F. Buisseret, Phys. Rev. D **87**, 054025 (2013).

[Lacr14a] G. Lacroix, C. Semay and F. Buisseret, arXiv:1408.0958 (2014).

[Lacr14b] G. Lacroix, C. Semay and F. Buisseret, arXiv:1408.4979 (2014).

[Lang10] J. Langelage and O. Philipsen, JHEP **1004**, 055 (2010).

[LeBe96] M. Le Bellac, *Thermal Field Theory*, Cambridge University Press (1996).

[Leva98] P. Levai and U. Heinz, Phys. Rev. C **57**, 1879 (1998).

[Liao06] J. Liao and E. V. Shuryak, Nucl. Phys. A **775**, 224 (2006); Phys. Rev. D **73**, 014509 (2006); Phys. Rev. C **75**, 054907 (2007).

[Lipt08] L. Lipták and Š. Olejník, Phys. Rev. D **78**, 074501 (2008); B. H. Wellegehausen, A. Wipf, and C. Wozar, Phys. Rev. D **83**, 016001 (2011).

[Llan00] F. J. Llanes-Estrada and S. R. Cotanch, Phys. Rev. Lett. **84**, 1102 (2000).

[Luch90] W. Lucha, Mod. Phys. Lett. A **5**, 2473 (1990).

[Luci01] B. Lucini and M. Teper, Phys. Rev. D **64**, 105019 (2001).

[Luci04] B. Lucini, M. Teper, and U. Wenger, JHEP **0401**, 061 (2004).

[Luci05] B. Lucini, M. Teper and U. Wenger, JHEP **0502**, 033 (2005).

[Luci10] B. Lucini, A. Rago, and E. Rinaldi, JHEP **1008**, 119 (2010).

[Maas11] A. Maas, JHEP **1102**, 076 (2011).

[Mach89] R. Machleidt, Adv. Nucl. Phys. **19**, 189 (1989).

[Make02] Y. Makeenko, *Methods of contemporary gauge theory*, Cambridge University Press (2002).

[Mald98] J. Maldacena, Adv. Theor. Math. Phys. **2**, 231 (1998).

[Mann05] M. Mannarelli and R. Rapp, Phys. Rev. C **72**, 064905 (2005).

[Math09a] V. Mathieu, F. Buisseret, and C. Semay, Phys. Rev. D **77**, 114022 (2008); F. Buisseret, V. Mathieu, and C. Semay, Phys. Rev. D **80**, 074021 (2009).

[Math09b] V. Mathieu, N. Kochelev, and V. Vento, Int. J. Mod. Phys. E **18**, 1 (2009), and references therein.

[Mats86] T. Matsui and H. Satz, Phys.Lett. B **178**, 416 (1986).

[McLe07] L. McLerran and R. D. Pisarski, Nucl. Phys. A **796**, 83 (2007).

[McLe09] L. McLerran, K. Redlich, and C. Sasaki, Nucl. Phys. A **824**, 86 (2009).

[Megi07] E. Megias, E. R. Arriola, and L. L. Salcedo, Phys. Rev. D **75**, 105019 (2007); Phys. Rev. D **80**, 056005 (2009).

[Meng09] X.-F. Meng *et al.*, Phys. Rev. D **80**, 114502 (2009).

[Metr53] N. Metropolis *et. al.*, J. Chem. Phys. **21**, 1087 (1953).

[Meye09] H. B. Meyer, Phys. Rev. D **80**, 051502 (2009).

[Mine08] H. Mineo, J. A. Tjon, K. Tsushima, and Shin Nan Yang, Phys. Rev. C **77**, 055203 (2008).

[Mocs05] A. Mocsy and P. Petreczky, Phys. Rev. D **73**, 074007 (2006).

[Morn99] C. J. Morningstar and M. J. Peardon, Phys. Rev. D **60** , 034509 (1999); Y. Chen *et al.*, Phys. Rev. D **73**, 014516 (2006).

[Muta10] T. Muta, *Foundations of quantum chromodynamics*, World Scientific, third edition (2010).

[Namb61] Y. Nambu, G. Jona-Lasinio, Phys. Rev. **122**, 345 (1961); Y. Nambu, G. Jona-Lasinio, Phys. Rev. **124**, 246 (1961).

[Novi83] V. A. Novikov, M. A. Shifman, A. I. Vainshtein, and V. I. Zakharov, Nucl. Phys. B **229**, 381 (1983).

[Ohnu78] Y. Ohnuki and T. Kashiwa, Prog. Theor. Phys. **60**, 548 (1978).

[Oliv11] O. Oliveira and P. Bicudo, J. Phys. G **38**, 045003 (2011).

[Pane09] M. Panero, Phys. Rev. Lett. **103**, 232001 (2009).

[Pari81] G. Parisi and Y. Wu, Sci. Sinica **24**, 483 (1981).

[PDG] Particle Data Group (2013).

[Pepe07] M. Pepe and U.-J. Wiese, Nucl. Phys. B **768**, 21 (2007).

[Pesh96] A. Peshier, B. Kämpfer, O. P. Pavlenko, and G. Soff, Phys. Rev. D **54**, 2399 (1996).

[Pisa00] R. D. Pisarski, Phys. Rev. D **62**, 111501 (2000); C. Ratti, M. A. Thaler, and W. Weise, Phys. Rev. D **73**, 014019 (2006).

[Poli01] G. Policastro, D. T. Son, and A. O. Starinets, Phys. Rev. Lett. **87**, 081601 (2001).

[Poli74] H. D. Politzer, Phys. Rep. **14**, 129 (1974).

[Polo82] J. Polónyi and K. Szlachányi, Phys. Lett. B **110**, 395 (1982); M. Gross, Phys. Lett. B **132**, 125 (1983).

[Prat94] S. Pratt and W. Bauer, arXiv: 9404027 (1994).

[Plum11] S. Plumari, W. M. Alberico, V. Greco, and C. Ratti, arXiv:1103.5611 (2011).

[Rafe82] J. Rafelski and B. Muller, Phys. Rev. Lett. **48**, 1066 (1982).

[Ratt06] C. Ratti, M. A. Thaler, and W. Weise, Phys. Rev. D **73**, 014019 (2006).

[Ratt14] C. Ratti, Informal discussions during the Mons Meeting 2014.

[Rein11] H. Reinhardt, D. R. Campagnari, and A. P. Szczepaniak, Phys. Rev. D **84**, 045006 (2011).

[Riek10] F. Riek and R. Rapp, Phys. Rev. C **82**, 035201 (2010).

[Roes07] S. Roessner, C. Ratti, and W. Weise, Phys. Rev. D **75**, 034007 (2007).

[Rugg12] M. Ruggieri, P. Alba, P. Castorina, S. Plumari, C. Ratti, and V. Greco, Phys. Rev. D **86**, 054007 (2012).

[Sark10] S. Sarkar, H. Satz, and B. Sinha, *The Physics of the Quark-Gluon Plasma*, Lecture Notes in Physics, Vol. **785** (2010).

[Saku93] J. J. Sakurai, *Modern Quantum Mechanics*, Addison Wesley (1993).

[Sala74] A. Salam and J. A. Strathdee, Phys. Lett. B **51**, 353 (1974).

[Sann05] F. Sannino, Phys. Rev. D **72**, 125006 (2005).

[Satz06] H. Satz, hep-ph/0602245; V. V. Dixit, Mod. Phys. Lett. A **5**, 227 (1990).

[Schw51] J. Schwinger, Proc. Nat. Acad. Sci. **37**, 452 (1951).

[Sema01] C. Semay, D. Baye, M. Hesse, and B.Silvestre-Brac, Phys. Rev. E **64**, 016703 (2001); F. Brau and C. Semay, J. Phys. G: Nucl. Part. Phys. **28**, 2771 (2002).

[Shos03] A. I. Shoshi, F. D. Steffen, H. G. Dosch, and H. J. Pirner, Phys. Rev. D **68**, 074004 (2003).

[Shur04] E. V. Shuryak and I. Zahed, Phys. Rev. D **70**, 054507 (2004).

[SLAC] SLAC website.

[Step06] M. A. Stephanov, Proc. Sci., LAT2006 (2006).

[Stoe05] H. Stoecker, Nucl. Phys. A **750**,121 (2005).

[Surf] http://www.surfability.com

[Suss79] L. Susskind, Phys. Rev. D **20**, 2610 (1979); N. Weiss, Phys. Rev. D **24**, 476 (1981); N. Weiss, Phys. Rev. D **25**, 2668 (1982).

[Svet82] B. Svetitsky and L. G. Yaffe, Nucl. Phys. B **210**, 423 (1982); Phys. Rev. D **26**, 963 (1982).

[Szcz96] A. Szczepaniak, E. S. Swanson, C. -R. Ji, and S. R. Cotanch, Phys. Rev. Lett. **76**, 2011 (1996); A. P. Szczepaniak and E. S. Swanson, Phys. Lett. B **577**, 61 (2003).

[Tayl83] J. R. Taylor, *Scattering Theory*, Dover Publications (1983).

[Thom70] R. H. Thompson, Phys Rev D **1**, 110 (1970).

[Tolo08] L. Tolós, D. Cabrera, and A. Ramos, Phys. Rev. C **78**, 045205 (2008).

[Vanh08] H. van Hees, M. Mannarelli, V. Greco, and R. Rapp, Phys. Rev. Lett. **100**, 192301 (2008).

[Vars88] D. A. Varshalovich, A. N. Moskalev, and V. K. Khersonskii, *Quantum Theory of Angular Momentum*, World Scientific, Singapore (1988).

[Vinc93] M. Vincke, L. Malegat, and D. Baye, J. Phys. B **26**, 811 (1993).

[West96] G. B. West, Phys. Rev. Lett. **77**, 2622 (1996).

[Witt79] E. Witten, Nucl. Phys. B **160**, 57 (1979).

[Wong06] C.-Y. Wong and H. W. Crater, Phys. Rev. D **75**, 034505 (2007).

[Yagi05] K. Yagi, T. Hatsuda and Y. Miake *Quark-Gluon Plasma*, Cambridge Monographs, first edition (2005).

[Zuk83] J. Zuk, G. C. Joshi, and J. W. G. Wignall, Phys. Rev. D **28**, 1706 (1983).

[Zwie04] B. Zwiebach (2004), *A First Course in String Theory* (Cambridge University Press, second edition, 2009).